QUANTUM LIQUIDS AND QUANTUM CRYSTALS

Localization of helium around microscopic impurities in liquid helium

E. B. Gordon*

Branch of the Institute of Energy Problems of Chemical Physics, Russian Academy of Sciences, 142432 Chernogolovka, Moscow District, Russia

A. F. Shestakov**

Institute of Problems of Chemical Physics, Russian Academy of Sciences, 142432 Chernogolovka, Moscow District, Russia

The structure and properties of the environment of impurity atoms Im immersed in liquid helium are examined. It is demonstrated that there are two qualitatively different types of structure of the layer of helium atoms nearest to Im: structures characterized by attraction and repulsion. In the structures with attraction toward the center (for strong Im–He interaction) the Im–He distance is greater than the equilibrium distance for the Im–He pair potential, and the density and localization of helium atoms are greater than in the bulk. Here the number of helium atoms n in the layer is almost independent of the external pressure. In structures with repulsion, which exist for alkali metal atoms, the Im–He distances are shorter than the equilibrium ones, while the density is lower than in bulk helium. For $T \sim 1$ K several states with different n are populated, with energies differing only by ~ 0.1 K, and n decreases substantially as the pressure is increased. On the basis of this analysis an interpretation is given for the optical and ESR spectra of atoms implanted in liquid and solid helium. A simple model is proposed for determining the characteristics of the helium environment from the experimental pressure dependence of the shifts of the atomic lines in the absorption and emission spectra. It is predicted that in ^{3}He–^{4}He mixtures the structure with attraction should be strongly enriched with ^{4}He atoms, while the structures with repulsion should be enriched with ^{3}He. The possible existence of phase transitions in the helium shells surrounding impurity atoms is discussed. © *2000 American Institute of Physics.* [S1063-777X(00)00101-8]

The main motivation for embedding atoms, molecules, and clusters in liquid and solid helium has been the effort to set them into the most inert host matrix (the absence of chemical interactions, the lowest polarizability, the highest-lying electronic energy levels) with a characteristic low-temperature ''freezing in'' of the internal degrees of freedom of the impurities. It has turned out, however, that such host matrices are not entirely inert—on account of the quantum nature of condensed helium, the interaction of the impurity particles with the surrounding helium and with one another has a very specific character and leads to a number of strong effects. This has motivated further research activity in this area, and some new experimental methods have recently been developed for introducing and studying various types of impurities in liquid and solid helium.

The first review article on this topic was published in 1997,[1] and during the preparation of this paper two more review articles dealing with research on the properties of atoms and molecules in condensed helium appeared in print.[2,3] In the present article our goal is therefore not to give a detailed discussion of the experimental and theoretical research in the field, but rather to concentrate on the peculiari-

ties of the behavior of microscopic objects in a quantum medium—liquid and solid helium. We attempt to explain the basic regularities observed under these conditions and explore the possibility of observing specific new effects experimentally.

The success of the bubble model, which correctly describes the behavior and the energy spectrum of an excess electron in liquid helium,[4,5] has led researchers to attempt a description of the environment of impurity atoms in liquid and even solid helium in terms of ''bubbles.'' However, the behavior of liquid helium around a free electron is fundamentally different from that around an atom or molecule: the very existence of an ''electron bubble'' is due, on the one hand, to the large ''size'' ($\lambda_{dB} = h/m_e V_e$) of a thermalized electron and, on the other, to the large zero-point kinetic energy (the large amplitude of the zero-point vibrations) of the liquid helium surrounding the electron. At the same time, electrons in atoms and molecules are spatially localized on account of the strong coupling with the nuclei, and this makes for a much smaller amplitude of the zero-point radial modes of the helium atoms surrounding the impurity.[6]

A logically consistent ''bubble'' approach requires con-

sidering the problem of the perturbation of an electron–helium bubble when a positively charged atomic core is introduced into it. It is clear, however, that the nearly free state of the electron is a poor zeroth approximation for describing a bound state of an optical electron in an atom.[1)] Therefore, for a numerical solution of such a complicated problem there can be nonphysical artifacts, such as, for example, the formation of ultradense helium droplets in the neighborhood of the atomic core,[8] which contains two helium atoms in a spherical volume with a radius of 0.8 atomic units, i.e., a density >40 g/cm^3. Furthermore, because of the strong coupling of the electron with the atomic core, the polarizational asymptotic behavior of the interaction with helium atoms is lost. At the same time, since the effects of the Im–He–He three-body interaction can be neglected,[6] the numerical solution of the electron problem for a fixed distribution function of the helium atoms can be obtained directly and more economically by summing the Im–He pair potentials, which implicitly contain all the important electronic effects associated with the relaxation of the wave functions of the outer electron shells. This approach does not, of course, eliminate the need of calculating the effects of the significant zero-point kinetic energy of the helium atoms, which in all the ''simple'' approaches is in one way or another parametrized in accordance with the properties of liquid helium. A ''potential'' approach retaining the continuum description of helium is also possible[9] through the use the density functional for liquid helium,[10,11] but it requires a numerical solution of the problem.

It should be noted that the continuum approach, which is also referred to as the ''bubble'' model in the literature, permits a satisfactory interpretation of the experimental results, most of which pertain to alkali, alkaline-earth, and transition-metal impurity atoms in helium. The reason for this is not hard to understand. Indeed, even if one starts from the ''bubble'' concept in an analysis of the helium environment of an impurity atom in liquid helium, then of the four energy terms used to estimate it (the potential energy of the impurity plus the energy of surface tension plus the work of displacement of the liquid plus the zero-point kinetic energy of the structure), the last term, even for the largest atoms (rubidium and cesium), is always small, and the electronic state of the impurity atom is perturbed weakly by interaction with the medium.[12] Thus the state of the helium environment in the ''bubble'' model is actually determined by the impurity–helium interaction and the interaction between helium atoms in the surface layer, which in the continuum approximation is the surface energy. As expected, the results of the calculations show that the size of the cavity is close to the van der Waals dimension of an atom, and its compressibility (which is actually the compressibility of the impurity atom) is extremely small compared to that of an electron ''bubble.''[12] The possibility of obtaining a fair description of the optical spectra of impurity atoms in liquid[12] and solid[13] helium means that in an approach based on the known macroscopic characteristics of condensed helium, viz., the density, compressibility, and surface tension, which are determined by its quantum properties, one can subsequently treat the condensed helium as a classical object.
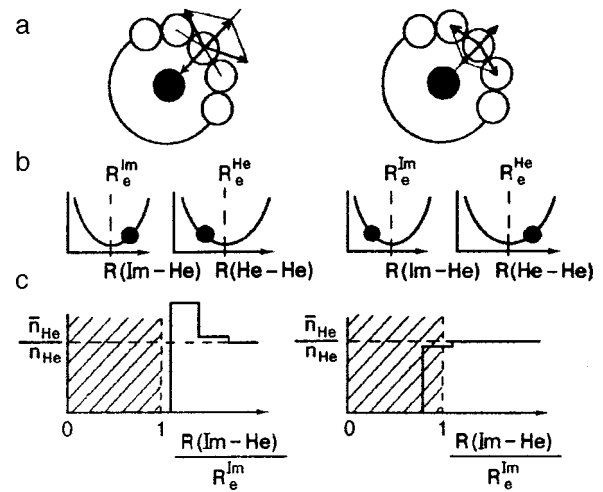

FIG. 1. Two types of structure of the helium environment of an impurity atom. a: Diagram of force equilibrium. b: Positions of the helium atoms in the shell relative to the minima of the impurity–helium and helium–helium pair interaction potentials. c: Layer histogram of the helium density in the shell; the region occupied by the impurity atom is shaded.

It is intuitively clear that in the case of weakly interacting alkali metal atoms in liquid helium the properties of the helium layer adjacent to the impurity atom should not differ strongly from its bulk properties, and therefore the aforementioned ''bubble'' approach can be valid. However, this is by no means the case for microparticles which interact more strongly with liquid helium, with an interaction energy $U >10$ K.[14]

On account of the inertness of helium the interaction of any impurities with it will have the character of unsaturated and short-range $(U \sim R^{-6})$ van der Waals forces.[2)] Therefore, the influence of an impurity center on the second-nearest layer of helium is small, and the properties of the helium in that layer should not differ appreciably from the properties of helium in the bulk. This in turn means that the ''bubble'' approach is in principle applicable for strongly interacting particles as well, but beginning with the second layer (i.e., for an impurity particle in the form of a single-layer cluster, ImHe$_n$). It follows from the results of both quantum calculations[15] and calculations by the density-functional method[9] that there always exists a distinguished layer of helium localized around an impurity with a strong Im–He interaction.

Nevertheless, for designing experiments and for understanding the general relationships it is of interest to analyze the problem as a whole, and not on the basis of specific examples.

The physical nature of the localization of helium around an impurity is demonstrated in Fig. 1, which shows the qualitative structure of the shell (a), the equilibrium positions of the helium atoms making up the shell relative to the minima of the Im–He and He–He interaction potentials (b), and also histograms of the density (number) of helium atoms as a function of the distance from the impurity center (c).

If the Im–He interaction is stronger than the He–He interaction, we have a case in which the attraction of the He atoms toward the center is counterbalanced by the mutual

repulsion of the He atoms. Naturally, in this case the number of He atoms in the shell is greater than would follow from the equilibrium distance between them. However, for heavy alkali metal atoms (it is known that Rb and Cs atoms are not wet by helium[14]) a second case is possible, in which the repulsion of the He atoms from the center is compensated by the attraction arising between helium atoms in the shell; in this case the density of helium atoms in the shell should be lowered.

Even this qualitatively treatment shows how appreciably the structure of the helium shell around an impurity differs from the intuitive idea of a ''bubble.'' For the case of attraction toward the center the Im–He distances exceed the equilibrium distances for the Im–He interaction, while the distances between He atoms in the shell are less than the equilibrium distance, as is characteristic for a ''snowball;'' as will be clear from what follows, the interhelium distance in the first layer can even turn out to be smaller than in solid helium. In any case the description of the interaction between He atoms in the shell with the aid of surface tension is a poor approximation here. Indeed, the physical manifestation of surface tension is an excess energy (or lowered density) in the surface layer. At the same time, the enhanced density of He atoms in the surface layer means that the ''coefficient of surface tension'' is formally negative.

For the case of repulsion from the center the radius of the He surface layer is even smaller than the Im–He distance, but its structure more closely resembles a bubble. To understand the scale of the variations of the dimensions of the cavity and the density of the helium shell as functions of the characteristics of the impurity in liquid helium, it is advisable to first choose a simple model that will admit an analytical solution.

SIMPLE MODEL OF AN IMPURITY–HELIUM CLUSTER ($T=0, P=0$)

An isolated helium cluster may be a fair model for describing the structure of the environment of an impurity in liquid helium. In particular, this is suggested by calculations in the density-functional approach, from which it follows that the shape and amplitude of the first maximum of the radial distribution function of the helium atoms around an impurity remains practically constant as N increases just after $N > N_0$, where N and N_0 are the numbers of atoms in the cluster and in the first layer of the cluster, respectively.[9]

In the general case the problem of finding the structure of an ImHe$_n$ cluster reduces to one of minimizing its total energy E as a function of its radius R, the distance d between adjacent helium atoms in the shell, and the number n of atoms in the shell, which is a parameter of the problem. For a spherical single-layer shell of n He atoms the total energy of the system in the pair interaction approximation is

$$E(R,n) = n E_{\mathrm{ImHe}}(R) + \frac{nm}{2} \widetilde{E}_{\mathrm{He}}(d(R)), \qquad (1)$$

where $E_{\mathrm{ImHe}}(R)$ is the corresponding pair potential, $\widetilde{E}_{\mathrm{He}}(d)$ is the energy of the helium shell per interacting pair of He atoms, and m is the average number of neighboring He atoms

in the shell. The number m can take on values from 3 to 6 (these are the limiting values for small and large n: $m=3$ for a tetrahedron or a cube, $m=4$ for cubo-octahedron, $m=5$ for an icosahedron, and $m=6$ for a plane), and $d(R)$ is the average distance between neighboring He atoms in a shell of radius R. It follows from simple geometric considerations that

$$d(R) = 2R \frac{\sqrt{\sin(\omega/2m)\sin(2\pi/m - \omega/2m)}}{\sin(\pi/m)}$$

$$\approx 2R \left(\frac{\omega}{m\tan(\pi/m)} \right)^{1/2} = \frac{RC_m}{\sqrt{n}},$$

where $\omega = 4\pi/n$ is the solid angle per He atom in the shell. Then

$$\frac{d}{R} = C_m \frac{1}{\sqrt{n}}, \quad C_m = 2 \left(\frac{4\pi}{m\tan(\pi/m)} \right)^{1/2}. \qquad (2)$$

Besides the indeterminacy in the choice of the parameter m, which is not very important and, as we shall discover, can be eliminated, there is a more fundamental difficulty. While the impurity–helium interaction is described reliably by a pair potential, it is quite a complicated matter to describe the collective helium–helium interaction in such a manner, since the zero-point kinetic energy is high and on account of the possibility of quantum-mechanical exchange the function $\widetilde{E}_{\mathrm{He}}(d)$ is fundamentally different from the true He–He pair potential and, generally speaking, depends on whether the cluster is found in a liquid or in vacuum. Qualitatively, however, it is clear that the function $\widetilde{E}_{\mathrm{He}}(d)$ has a minimum (the depth of which is equal to ε_0) at a certain $d=r_e$ and that it goes to zero as $d \to \infty$. Since we are interested in deviations of d from r_e which are not too large, for the analytical solution of the problem we consider only an effective energy in the form of a Lennard–Jones potential:

$$\widetilde{E}_{\mathrm{He}}(d) = \varepsilon_0 \left[\left(\frac{r_e}{d} \right)^{12} - 2 \left(\frac{r_e}{d} \right)^{6} \right]. \qquad (3)$$

As to the Im–He interaction, there is no question that it can be validly represented by the potential curves of the Lennard–Jones potential:

$$E_{\mathrm{ImHe}}(R) = U \left[\left(\frac{R_e}{R} \right)^{12} - 2 \left(\frac{R_e}{R} \right)^{6} \right]. \qquad (4)$$

The solution of the problem of the structure and optimum composition of an isolated ImHe$_n$ cluster,

$$\frac{\partial E}{\partial R} = 0; \quad \frac{\partial E}{\partial n} = 0,$$

where E is given by Eq. (1) with allowance for Eqs. (2)–(4), gives the following expression for the radius R^* of the shell, the number n^* of He atoms, and the total energy E^* of the cluster:

$$R^* = R_e \left[\frac{\gamma + f^2(\gamma)}{\gamma + F(\gamma)} \right]^{1/6} \qquad (5)$$

$$n^* = n_0 f^{1/3}(\gamma); \quad n_0 \equiv \left(\frac{C_m R_e}{r_e}\right)^2, \tag{6}$$

$$E^* = = -\frac{n^* m \varepsilon_{\mathrm{He}}}{2} \frac{[\gamma + f(\gamma)]^2}{\gamma + f^2(\gamma)}. \tag{7}$$

Here the parameter

$$\gamma = \frac{2U}{m\varepsilon_0} \tag{8}$$

is the dimensionless depth of the Im–He potential (the values of γ for several atoms are given in Table I), and the function $f(\gamma)$ is given implicitly by the equation

$$\frac{\gamma + 7f}{\gamma + f} = \frac{6f^2}{\gamma + f^2} \tag{9}$$

and has the approximate espression $f(\gamma) = (0.72 + \sqrt{0.461 + 0.2\gamma})/(1 - 0.288\gamma^{-1})$. As can be seen from Eq. (2), n_0 is the number of helium atoms in a hypothetical shell in which the helium–center and helium–helium distances have their equilibrium values for the Im–He and He–He pair potentials used, respectively. Of course, the radius of this shell is R_e, the distance between helium atoms in it is r_e, and the total energy is described by the expression

$$E_0 = -n_0 U - \frac{n_0 m}{2} \varepsilon_0 = -\frac{n_0 m}{2} \varepsilon_0 (1 + \gamma).$$

The results of the calculations are presented in Figs. 2 and 3. One notices first of all that for impurity atoms that interact strongly with helium ($\gamma \gg 1$) the radius of the shell is slightly larger than the equilibrium distance R_e for the pair potential, and for large U it is practically independent of the well depth (Fig. 2a).

For impurity centers that interact weakly with helium (in particular, alkali metal atoms) the parameter γ for ^{4}He becomes less than unity (see Table I). However, in the model considered, there is no stable state of an isolated single-layer cluster for $\gamma < \gamma_{\mathrm{cr}} = 343/(71 + 66\sqrt{11}) = 1.183$: the total energy decreases monotonically with n, and $R^* \to \infty$ for
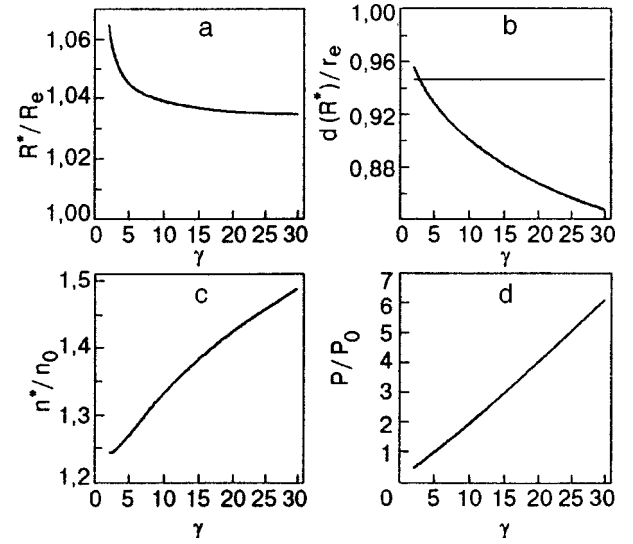

FIG. 2. Characteristics of an isolated helium cluster ImHe$_n$, normalized to the characteristics of a hypothetical equilibrium cluster (see text), as functions of the dimensionless interaction energy for Im–He, $\gamma \equiv 2U/(m\varepsilon_0)$ for $m = 5$. Analytical model. a: Shell radius. b: Distance between helium atoms in the shell (the horizontal straight line is the He–He distance upon the bulk solidification of helium for $T = 0$). c: Number of helium atoms in the shell. d: Radial pressure in the cluster.

$d \approx r_e$. This is a reflection of the fact that an isolated spherical impurity–helium cluster is physically unrealizable—in the case of unwettability the stable state is a helium "droplet" with an atom on the surface.

The distance d between He atoms in the shell obeys the relation

$$d(R^*) = r_e \left[\frac{\gamma + f^2(\gamma)}{\gamma f(\gamma) + f^2(\gamma)}\right]^{1/6}.$$

The decrease of d in comparison with r_e for $\gamma > 1$ is sufficient that the force of mutual repulsion of the atoms gives rise to a stable shell of "compressed" He atoms. As can be seen from Fig. 2b, the relative decrease of d in com-

TABLE I. Parameters of the interaction of various atoms with helium for $m = 5$.

Atom	Characteristics of potential		Isotope ^{4}He	Isotope ^{3}He
	R_e, Å	U, K	γ	γ
Ne	3.03	21.24	7.13	29.5
Ar	3.48	30.05	10.09	29.0
Kr	3.70	30.98	10.10	29.90
Xe	3.98	29.01	9.74	28.0
N	3.44	33.19	11.14	32.0
Li	6.033	1.64	0.549	1.58
Na	6.408	1.73	0.581	1.67
K	7.181	1.408	0.473	1.36
Rb	7.334	1.415	0.475	1.36
Cs	7.731	1.206	0.405	1.16

Note: For the inert-gas atoms and for Li the data shown are the experimental data of Refs. 16 and 17. The rest of the data are the results of calculations: our estimates for N and the calculation of Ref. 18 for the atoms Na–Cs. The data of Ref. 19 were used for converting to ^{3}He.
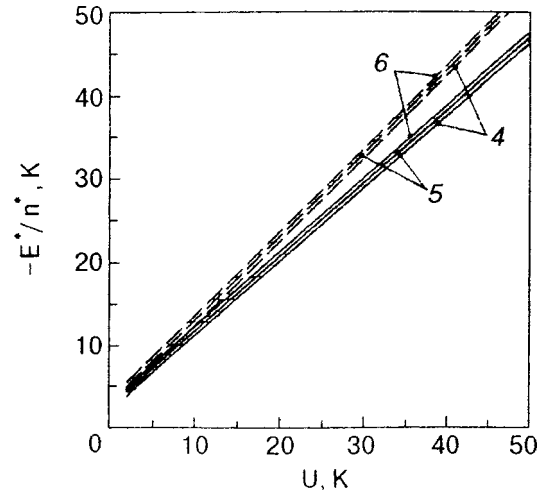

FIG. 3. Total energy of an isolated cluster per helium atom versus the parameter U. The dashed lines are the data for a hypothetical equilibrium cluster ($-E_0/n_0$). The numbers labeling the curves are the values of the parameter m.

TABLE II. Parameters of impurity–helium clusters $ImHe_n$ for $m=5$ (analytical model).

Im	Isotope ^{4}He				^{3}He			
	R^*, Å	n^*	E^*, K	σK/Å^2	R^*, Å	n^*	E^*, K	σK/Å^2
Ne	3.16	10.2	-221.9	-1.77	3.14	9.3	-182.5	-1.47
Ar	3.62	13.8	-407.8	-2.48	3.60	12.8	-347.2	-2.13
Kr	3.84	15.7	$-475.$	-2.56	3.83	14.5	-405.4	2.20
Xe	4.14	18.1	-515.4	2.40	4.12	16.6	-437.3	-2.05
N	3.57	13.6	-439.3	-2.74	3.56	12.6	-377.1	-2.37

Note: The surface tension was determined from the (negative) pressure P exerted by the helium shell on the center, according to the relation $\sigma = R^*P/2$.

parison with the equilibrium distance r_e is of the same scale as for the shell radius R. However, if one assumes for estimation that the equilibrium distance between helium atoms in the shell and their effective interaction energy are the same as in bulk liquid helium, i.e., if one takes $V_{He}=45.476$ Å^3 and $\varepsilon_{He}=7.15$ K for the atomic volume and energy of liquid ^{4}He at $T,P=0$ (Ref. 20) and $r_e=(\sqrt{2}V_{He})^{1/3}=4.02$ Å and $\varepsilon_0=\varepsilon_{He}/6=1.19$ K (on the assumption that the most probable number of nearest neighbors is 12, as for solid helium),[21] then even for $\gamma \geqslant 3$ the interhelium distance in the shell becomes smaller than the value corresponding to the onset of bulk solidification of helium. As a result, the number of He atoms in the shell is substantially larger than that which would follow from the density of liquid helium (see Fig. 2c). Therefore, it can be assumed that for $\gamma>3$ the effective pressure in the helium shell is more than 25 bar (the pressure of solidification of helium at $T=0$).[3] In order to estimate the variability of the characteristics of an impurity–helium cluster under an external influence it is sensible to estimate the value of the external pressure that would correspond to the force of attraction of the helium shell to the central atom: these forces are counterbalanced by the negative pressure exerted by the helium shell on the impurity center, which is given by

$$P = \frac{1}{4\pi R^{*2}} \left. \frac{\partial n^* E_{ImHe}(R)}{\partial R} \right|_{R=R^*}$$

$$= \frac{mC_m^2 \varepsilon_0}{4\pi R_e r_e^2} \gamma f^{4/3}(\gamma)[f(\gamma)-1] \left\{ \frac{[\gamma+F(\gamma)]^3}{[\gamma+F^2(\gamma)]^5} \right\}^{1/2},$$

where $P_0=6n_0 m\varepsilon_0/(4\pi R_e^3)$. The value $P_0=86$ bar for $R_e=r_e$ and $m=5$. A plot of $P(\gamma)$ is shown in Fig. 2d. The effective pressure turns out to be extremely large, amounting to more than 150 bar for atoms of Xe and N. Figure 3 shows a plot of the energy per helium atom $-E^*/n^*$ as a function of the depth of the Im–He potential in comparison with the case of the hypothetical equilibrium cluster. We see that the "binding energy" of each helium atom to the center is slightly less than U and is much larger than kT at $T=1-2$ K; this makes for stability of the cluster at the typical temperatures of most experiments.

The high level of internal stresses in an impurity–helium cluster formed around an atom which interacts rather strongly with helium is the reason why the liquid helium surrounding the atom does not have a noticeable effect on the characteristics of the cluster, at least at external pressures

$P_0<1$ bar. However, alkali metal atoms are a special case; for them the shell owes its very existence to the surrounding liquid.

One can thus consider two different types of environment of impurity atoms in condensed helium: structures with attraction (strong interaction with helium) and structures with repulsion (weak interaction). The characteristics of stable single-layer impurity–helium clusters are given in Table II. An analytical solution is useful because it permits a systematic analysis. In calculations for specific systems by numerical methods the interaction energy in (1) need not be given by Lennard–Jones potentials. In particular, the He–He interaction at pressures above 1 bar is not described very well by expression (3), and it would be logically more correct to describe them directly by proceeding from the equation of state $\varepsilon(V)$ of liquid helium, which is valid for any He–He distances:

$$\tilde{E}_{He}(d) = \frac{1}{6}\varepsilon\left(\frac{d^3}{\sqrt{2}}\right).$$

Using this form of the interaction between helium atoms, we can determine for any particular case the accuracy of the analytical description of an isolated $ImHe_n$ cluster having a structure with attraction and we can also compare the results obtained in the approximation we have adopted with the results of calculations done by the density-functional method.[9]

As a convenient object for calculation we choose xenon–helium clusters $XeHe_n$, for which data from density-functional calculations are available. Following Ref. 11, we write the equation of state of helium in the form

$$\varepsilon(V) = \frac{b}{2V} + \frac{c_2}{2V^2} + \frac{c_3}{3V^3}, \tag{10}$$

where $b=-719.99$ K·Å^3, $c_2=-2411.857$ K·Å^6, and $c_3=1858496$ K·Å^9. In addition, by virtue of of the linearity of the energy with respect to m, we have eliminated the indeterminacy in the choice of the parameter m, having taken m equal to its maximum possible value at the given n. An analysis shows that this gives the relation $m=6-12/n$. This formula describes exactly the cases of regular polyhedra with $m=3$, 4, and 5 for $n=4$, 6, and 12, respectively. Here we have the following relation connecting the distance between He atoms and the radius of the shell:
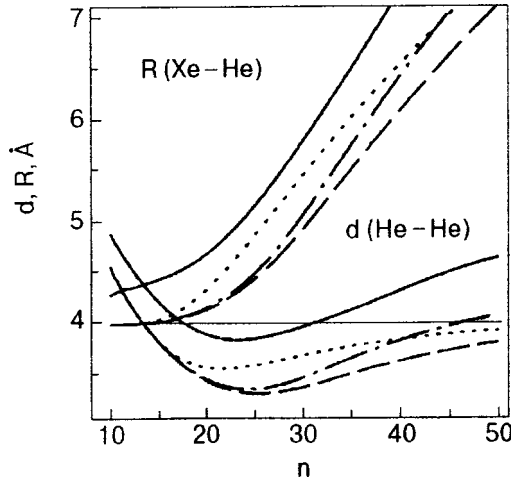
FIG. 4. Radius R of an isolated XeHe$_n$ cluster and the distance d between helium atoms in the shell versus n. Analytical model with $m=5$ ($\cdots$); calculation based on Eq. (12) ($---$); calculation based on Eq. (14), with the kinetic and potential energies treated separately ($-\cdot-\cdot$); calculation with allowance for the delocalization of helium (———).

$$d_n(R) = 2R\left\{1 - \left(2\sin\frac{\pi n}{6(n-2)}\right)^{-2}\right\}^{1/2}. \tag{11}$$

As a result, the energy of an isolated cluster is described by the expression

$$E(R,n) = nE_{\text{ImHe}}(R) + (3n-6)\varepsilon\left(\frac{d_n^3(R)}{\sqrt{2}}\right). \tag{12}$$

and for the Xe–He pair potential, which is well described by a Lennard–Jones potential, expression (4) is used, as before. We see from Figs. 4 and 5 that the results of the analytical calculation (the dotted curves) and the calculation with expression (12) are qualitatively close to each other.

The density-functional method enables one to calculate rather exactly the total energy of a system without separating it into potential and kinetic parts. In our approach, based on Eq. (1), the kinetic energy and especially the zero-point
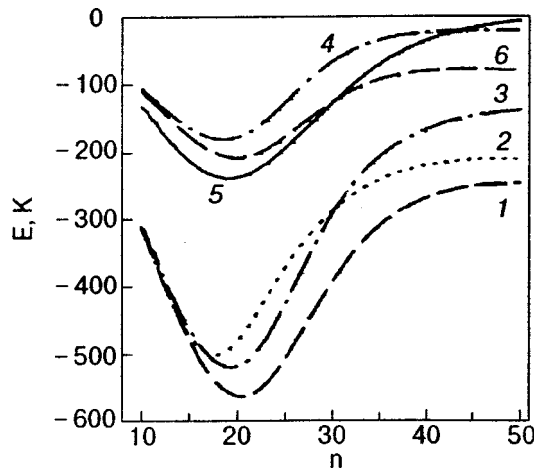

FIG. 5. Total energy of a XeHe$_n$ cluster versus n without (curves *1,2,3*) and with (*4,5,6*) allowance for the zero-point radial modes for different models (the numbering is the same as in Fig. 4).

energy of the radial vibrational modes, as will become clear below, is described with less than complete rigor. However, we proceeded deliberately by taking the interatomic interactions explicitly into account, since the goal of our analysis is to describe the optical and ESR spectra of impurity centers in liquid helium, for which it is necessary to know the spectrum of elementary excitations not only in the bulk of the liquid helium but also those localized in the nearest neighborhood of an impurity center. Therefore we require a separate description of the kinetic and potential energies. The density-functional method does not in itself permit one to do this.

TAKING THE KINETIC ENERGY INTO ACCOUNT

In our model the zero-point modes of the helium shell are effectively taken into account by virtue of the adopted parametrization in terms of the properties of liquid helium, which depend on its zero-point kinetic energy. This way of taking the zero-point vibrations into account is approximate on account of the presence of a potential energy relief, which distorts the dynamical properties of liquid helium, in the neighborhood of an impurity. To estimate the accuracy of the approximation used, let us take into account separately the contributions of the kinetic T and potential U energies to the energy of liquid helium, $\varepsilon(V) = T(V) + U(V)$.

According to the analysis of Ref. 22, a good approximation for T is the expression

$$T\left(\frac{R^3}{\sqrt{2}}\right) = \frac{T_0}{(R/L-1)^2}, \tag{13}$$

$T_0 = 8.266$ K, $L = 2.295$ Å. Then the potential energy per van der Waals bond in liquid helium is given by

$$U_{\text{He}}(d) = \frac{1}{6}\left[\varepsilon\left(\frac{d^3}{\sqrt{2}}\right) - \frac{T_0}{(d/L-1)^2}\right].$$

Assuming that the helium in the shell around an impurity center is delocalized in the same way as in liquid helium of the corresponding density, we get the following expression for the energy of an ImHe$_n$ cluster, which already includes the zero-point lateral modes of He, the total number of which is equal to $2n-3$:

$$E(R,n) = nE_{\text{ImHe}}(R) + (3n-6)U_{\text{He}}(d_n(R))$$
$$+ \frac{2n-3}{3}\frac{T_0}{\{2R\arcsin[d_n(R)/2R]/L-1\}^2}. \tag{14}$$

The radial modes of the helium shell are taken into account in the harmonic approximation:

$$E(R,n) \approx E(R^*,n) + \frac{k(n)}{2}(R-R^*)^2.$$

Then for an ImHe$_n$ cluster with the wave function of the completely symmetric mode, as we have shown previously,[6] satisfies the harmonic oscillator equation[4]

$$\left[-\frac{\hbar^2}{2m_{\text{He}}}\frac{d^2}{dQ^2} + \frac{Q^2}{2n}k(n)\right]R\Psi = \frac{\omega_0(n)}{2}R\Psi, \tag{15}$$

where $Q = R - R^*$, $\hbar^2/m_{He} = 12.119$ K·Å², and $\omega_0(n) = \hbar[k(n)/(nm_{He})]^{1/2}$. We have neglected the frequency dispersion for the different radial modes (it follows from a numerical calculation that for $n = 12$ this is a reasonable approximation).[6] The total energy of the system in this approximation is $E(R^*, n) + n\omega_0(n)/2$. The radial distribution function of the He atoms then takes the form

$$\rho(R) = \frac{n}{4\pi R^2 \sqrt{\pi a}} \exp\left[-\left(\frac{R - R^*}{a}\right)^2\right], \quad (16)$$

where $a(n) = [\hbar\sqrt{n/(k(n)m_{He})}]^{1/2}$ are the amplitudes of the radial modes.

Figures 4 and 5 show the results obtained when the above-described method of explicit inclusion of the radial modes of the helium shell is applied to isolated XeHe$_n$ clusters. It follows from these figures that taking the kinetic and potential energies of the system separately into account has little effect on the structure of the helium shell: while a calculation using formula (12) gave the cluster energy, the optimum number of helium atoms, the radius of the shell, and the distance between helium atoms in it as $E = -563$ K, $n = 20$, $R^* = 4.12$ Å, and $d^* = 3.42$ Å, the corresponding values are now $E = -519$ K, $n = 19$, $R^* = 4.10$ Å, and $d^* = 3.48$ Å, respectively. At the same time, the presence of radial modes of the helium shell, calculated using Eq. (15), noticeably alters the energy of the system. It increases to -181 K (while n retains its value of 19), but the radius of the shell and the distances between He atoms in it are practically unchanged, equalling 4.10 Å and 3.48 Å, respectively.

One notices that the energies obtained from expressions (12) and (14) are close; this may be due to the closeness of the coefficients $(3n-6)/6$ and $(2n-3)/3$ with which the kinetic energy of the helium atoms appears in these expressions, respectively. Thus one can propose a simpler way of taking the radial modes of the helium shell into account—by the use of the unmodified expression for the energy (12) in the solution of the vibrational problem (15). This approach gives practically identical results: $n = 20$, $E = -208$ K, $R = 4.12$ Å, $d = 3.42$ Å, $a = 0.58$ Å, and $\omega_0 = 35$ K.

At first glance these results differ substantially from the characteristics obtained by Dalfovoa[9] for XeHe$_n$ clusters by the density-functional method (see Fig. 6). For example, for its radial density distribution the maximum density at the first peak is 3(!) times larger than the density of liquid helium (in our calculation the number of helium atoms in the first layer is only 30% greater than would be the case for liquid helium). However, as we shall show below, the differences are only apparent ones, and the two calculations give basically the same results.
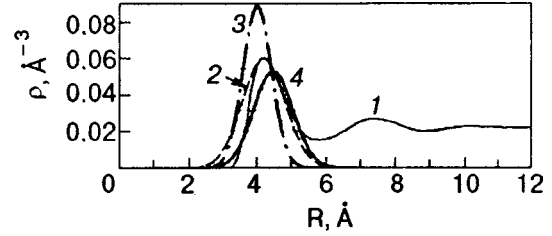

FIG. 6. Radial distribution functions of the helium density around a xenon atom: density-functional method for liquid helium (*1*), approximation of the first peak of curve *1* by a Gaussian (*2*), and the data obtained with the energy represented in the form given in Eq. (12) (*3*) and Eq. (21) (*4*).

Indeed, integration of the density corresponding to the first peak on curve *1* of Fig. 6 gives a value of 21 for the number of atoms in the first layer.[9] If the distribution in the first peak is represented by a Gaussian curve (16), then from the position R_{max} of the maximum on the curve one can estimate the amplitude of the zero-point radial modes,

$$a \approx \frac{n}{4\pi(R_{max})^2 \sqrt{\pi}\rho(R_{max})}$$

and from it the mode energy $\omega_0 = \hbar^2/(m_{He}a^2)$ and the shell radius R^*, using the relation $R_{max} \simeq R^* - a^2/R^*$. Analyzing the data of Dalfovo[9] in this way, we obtain $a = 0.85$ Å, $\omega_0 = 17$ K, and $R^* = 4.37$ Å, and then, on geometric arguments (11) we obtain $d = 3.54$ Å for the distance between helium atoms in the shell.

From the dependence of the binding energy of the Xe atom with a cluster He$_n$ one can estimate the total energy of a XeHe$_n$ cluster by using the fact that for $n \cong 20$ the energy of He$_n$ is $-n1.6$ K.[23] This estimate gives $E \cong -230$ K for $n = 21$. All of the values found are presented in Table III. We see from this table that the cluster structure calculated using formulas (12) and (14) is close to that obtained in the density-functional approach. However the degree of localization of the helium shell (and, accordingly, the characteristic frequency ω_0) turned out to be too high in comparison with that found in Ref. 9.

The real energy spectrum of the vibrational excitations of the helium shell can be calculated by the approach described above, and the reason for the overestimates of the total energy of the radial modes is clear: we have assumed for purposes of estimation that all n radial modes have an energy equal to the energy of the highest completely symmetric mode. However the problem of calculating the specific form of the spectrum is a problem of independent interest. If one is concerned solely (for purposes of comparison with the density-functional method) with correctly taking

TABLE III. Structure and characteristics of an isolated XeHe$_n$ cluster in different approximations.

Approach	n	R^*, Å	d, Å	R_{max}, Å	E, K	a, Å	ω, cm^{-1}
Eq. (12)	20	4.121	3.419	4.04	-208.4	0.585	35
Eq. (14)	19	4.099	3.484	4.02	-180.5	0.583	36
Eq. (21)	19	4.603	3.913	4.41	-239.2	0.778	20
						0.786 (b)	
Density functional[9]	21	4.37	3.54	4.2	-230	0.85	17

into account the total energy of the zero-point vibrations of the helium shell, then it can be done in our model through the introduction of a radial delocalization of the helium shell, which is uniquely related to the kinetic energy.

To take the delocalization of each helium atom in the shell explicitly into account, we choose a density distribution of the atom in the form

$$\rho_A(r) = \frac{1}{\sqrt{\pi^3}(a_\perp)^2 a_\parallel} \exp[-(x/a_\perp)^2 - (y/a_\perp)^2 - (z/a_\parallel)^2],$$

in which the anisotropy of the effect of the impurity center is taken into account by introducing different degrees of delocalization of the helium atoms in the radial ($a_\parallel$) and lateral ($a_\perp$) directions. Essentially, at the instantaneous positions of the helium atoms the potential energy of the system is described to good accuracy by a sum of pair potentials, and it is therefore necessary only to correctly average the pair interaction over the delocalization of the interacting centers A and B as specified by their distribution functions. This averaging must be done with allowance for the pair correlation function $g(\mathbf{r}_1, \mathbf{r}_2)$:

$$\bar{U}(R) = \int \rho_A(r_1) U(R+r_1-r_2) \rho_B(r_2) g(r_1,r_2) dv_1, dv_2. \tag{17}$$

For a simplified calculation of this integral we use the following technique.[6] In integrating over the distribution functions of the helium atoms we take into account that the main contribution to the integral comes from the regions near the centers of the distribution ($r_1 \sim 0$ and $r_2 \sim 0$), while the region of intersection of the distribution functions of the helium atoms ($|\mathbf{r}_1 - \mathbf{r}_2| \sim R$) actually gives a small contribution when correlation effects are taken into account. Thus in view of the smallness of the localization region compared to the internuclear distance, we can approximate the averaged potential by several leading terms of the expansion

$$U(\mathbf{R}+\mathbf{r}_1-\mathbf{r}_2) \cong U(R) + U'(R)$$

$$\times \left[\frac{\mathbf{R}(\mathbf{r}_1-\mathbf{r}_2)^2}{R} + \frac{1}{2}\frac{(\mathbf{r}_1-\mathbf{r}_2)^2}{R} \right]$$

$$+ \frac{1}{2}U''(R)\left[\frac{\mathbf{R}(\mathbf{r}_1-\mathbf{r}_2)}{R} \right]^2 \tag{18}$$

and simultaneously set $g(\mathbf{r}_1, \mathbf{r}_2) = 1$. In the case of a Lennard–Jones potential with equilibrium distance R_e and potential well depth U, the averaged potential (17) can then be found in analytical form:

$$U_{AB}(R) = U\left\{ \left(\frac{R_e}{R} \right)^{12} \right.$$

$$\times \left[1 + \frac{21(\langle z^2 \rangle_A + \langle z^2 \rangle_B) - 3(\hat{a} + \hat{b}^2)}{R^2} \right] - \left(\frac{R_e}{R} \right)^6$$

$$\left. \times \left[2 + \frac{24(\langle z^2 \rangle_A + \langle z^2 \rangle_B) - 3(\hat{a}^2 + \hat{b}^2)}{R^2} \right] \right\} \tag{19}$$
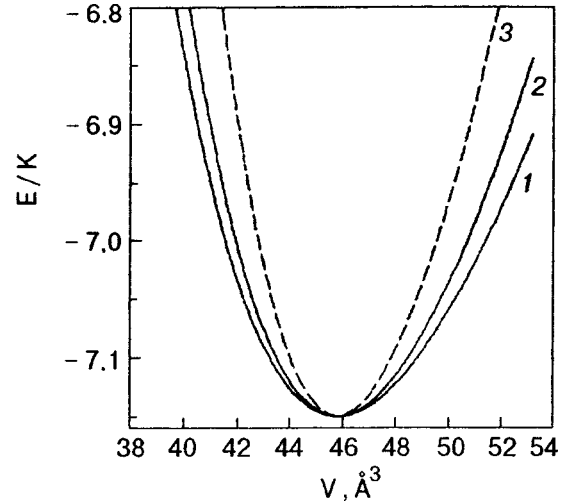
where

FIG. 7. Energy of liquid helium per atom versus the atomic volume: 1—experimental data of Ref. 16; 2—variational calculation based on Eq. (20); 3—approximation of the function in Eq. (1) by the Lennard–Jones potential (3).

$$\langle z^2 \rangle_A = a_\parallel^2 \cos^2 \varphi_a + a_\perp^2 \sin^2 \varphi_a,$$

$$\langle z^2 \rangle_B = b_\parallel^2 \cos^2 \varphi_b + b_\perp^2 \sin^2 \varphi_b,$$

$\hat{a}^2 = (a_\parallel)^2 + 2(a_\perp)^2$, $\hat{b}^2 = (b_\parallel)^2 + 2(b_\perp)^2$, and φ_a and φ_b are the angles made by the radius vector $\mathbf{R}$, directed from B to A, and the local z axis for the centers A and B.

When Eq. (19) is applied to liquid helium, the distribution function is isotropic and is described by a single parameter a. Then the total energy of a helium atom (kinetic plus potential) in the liquid in the presence of Z neighbors (we take $Z=12$ on considerations of close packing) located at a distance R can be written

$$E(R) = \frac{3\hbar^2}{4m_{He}a^2} + \frac{Z}{2}U_{He}\left\{ \frac{R_e^{1/2}(R^2+66a^2)(1-x)}{(R^2-66a^2x/7)^7} \right.$$

$$\left. -2\frac{R_e^6(R^2+15a^2)(1-y)}{(R^2-15a^2x/4)^4} \right\}, \tag{20}$$

where the parameters of the He–He pair potential (HFD–B3–FCI1) have the values $U_{He}=10.956$ K, $R_e=2.968$ Å.[24] The additional parameters x and y in expression (20) have been introduced according to the principle of constructing a Padé approximant, and the correct choice of these parameters can improve the accuracy of the description of the averaged potential by the leading terms of the expansion. The chosen values $x=0.4828$ and $y=0.5072$ were obtained from the condition that the calculated values of the atomic volume and energies for liquid helium at $T=0$ agree with the known values in the literature.[20] The correct choice of the parametric form for (20) was made so as to obtain a satisfactory description of the equation of state of liquid helium over a wide range of densities (see Fig. 7). For example, the compressibility of liquid helium was underestimated by 20% from the known value, an accuracy higher than that achieved when the effective He–He potential in the liquid is described by a Lennard–Jones potential. The calculated kinetic energy

$3\hbar^2/(4m_{\text{He}}a^2)$ as a function of the atomic volume is also in good agreement with the results of exact variational calculations.[25] At the equilibrium density the respective calculations give 14.20 and 14.77 K, at a density of 90% of the equilibrium density they give 11.97 and 12.26 K, and at a density of 120% of the equilibrium density they give 19.32 and 20.34 K. This is because the dependence of the parameter a on the distance is practically linear, and the formula $3\hbar^2/(4m_{\text{He}}a^2)$ and Eq. (13) for the kinetic energy take on the same functional form. By changing the mass at fixed values of the parameters x and y one can also calculate the equation of state of ^{3}He. The agreement of the calculated values of the energy per atom, -3.3 K, and the atomic volume, 58 Å^3, with the experimental values -2.5 K and 61 Å^3 for $T=0$ (Ref. 22) should be adjudged satisfactory for such a simple model.[5)] The value found for the delocalization parameter $a=0.8$ Å at $P=0$ and $z=12$ implies that the height

of the first maximum in the radial distribution function for liquid helium should be 1.48 and 1.99, in units of $1/V_{\text{He}}$, for a finite and an infinite mass of the central atom, respectively, in fair agreement with the results of quantum calculations[26] for these cases: 1.30 and 1.80.

Let us take this approach to the description of the helium shell around an impurity center—a xenon atom. To a first approximation one can take the parameters x and y for the averaged interatomic potentials Im–He and He–He so as to obtain the best description of the equation of state of liquid helium. The delocalization amplitudes of the He atoms, which are in general different in the radial (a) and lateral (b) directions, are the parameters of the variational function. In view of the large mass of the Xe atom, it can be regarded as immobile, which simplifies the problem.

For a heavy impurity center the total energy of the ImHe system becomes

$$E(R,a,b)=n\frac{\hbar^2}{4m_{\text{He}}}\left(\frac{1}{a^2}+\frac{2}{b^2}\right)+nU_{\text{ImHe}}(R)|_{a_\perp=a_\parallel=0,b_\parallel=a,b_\perp=b,\varphi=0}+(3n-6)U_{\text{HeHe}}(d_n(R))|_{a_\parallel=b_\parallel=a,a_\perp=b_\perp=b,\ \sin\varphi_a=\sin\varphi_b=\frac{d_n(R)}{2R}}, \quad (21)$$

where the potential terms are given by expression (19) with parameters x and y introduced in it as in Eq. (20). The total energy of the system and the radius of the helium shell are found as a result of the optimization:

$$\frac{\partial E}{\partial a}=0,\ \frac{\partial E}{\partial b}=0,\ \frac{\partial E}{\partial R}=0,$$

and the additional condition $\partial E/\partial n=0$ yields the optimum value of n.

The solid curves in Figs. 4 and 5 show the results for a XeHe$_n$ cluster in comparison with those obtained previously. It can be seen from Fig. 4 that the XeHe$_n$ cluster as before has the structure with attraction ($R^*>R_e$, $d^*<r_e$). However, allowance for delocalization increases both the Im–He and He–He distances, without changing the character of the environmental structure. This is because, in addition to the potential forces shown in Fig. 1, there is a quantum ''kinetic pressure'' present in the system on account of the large zero-point kinetic energy $\approx 3\hbar^2/(4m_{\text{He}}a^2)$, which depends strongly on R.

The energy calculation is based on a quantum-mechanical description of the system. Therefore the existing agreement of the calculated energy of XeHe$_n$ with $n\sim20$ (see Table III and Fig. 5) and the density of the radial displacement of He (Fig. 6) with the results obtained by the density-functional method, which is also a quantum-mechanical model, is not surprising. However, we also see that the dependence of the energy on n in the approximate approaches of Eqs. (12) and (14) is in rather good agreement with the results of the quantum-mechanical description. This justifies the proposed simplification of the method of calculating the radial modes of the shell and provides a way of obtaining its vibrational spectrum.

The radial a and lateral b delocalization parameters of the He atoms, as can be seen in Fig. 8, have the same behavior as functions of n as do the Im–He and He–He distances.[6)] Here the parameter b is in good agreement with the delocalization amplitude in liquid helium of the corresponding density. This confirms the correctness of using the equation of state of liquid helium for describing the delocalization of helium in the shell around an impurity center.

Returning to Fig. 6, where the calculated radial distribution of the density in a XeHe$_{19}$ cluster is compared with the distribution around a Xe atom in liquid helium as calculated by the density-functional method,[9] we notice the following.

1. The peak density of the shell is a strong function of the degree of radial localization of the helium shell and at the same time does not reflect the real density of the shell (the number of helium atoms in a shell of radius R). Although the maximum of the distribution function can exceed the bulk density of helium severalfold, this does not mean that there is such a strong increase in the density, as is stated in Ref. 3, for example. In our case the threefold increase in the density of the distribution is equivalent to an increase of 30% in the number of atoms found inside the geometric dimensions of the shell.

2. The true form of the peak of the radial distribution function is asymmetric on account of the fact that the repulsive branch of the Im–He potential is very steep, and this is not taken into account in the harmonic approximation. Therefore the effective value of the radial delocalization of helium, as judged from the half-width of the peak, is intermediate between the values calculated in the two models. This, in turn, affects the distances between helium atoms in the shell, which also turn out to be intermediate. Thus the extremely simple potential model (12) has entirely satisfactory accuracy if it is supplemented by the energy contribu-
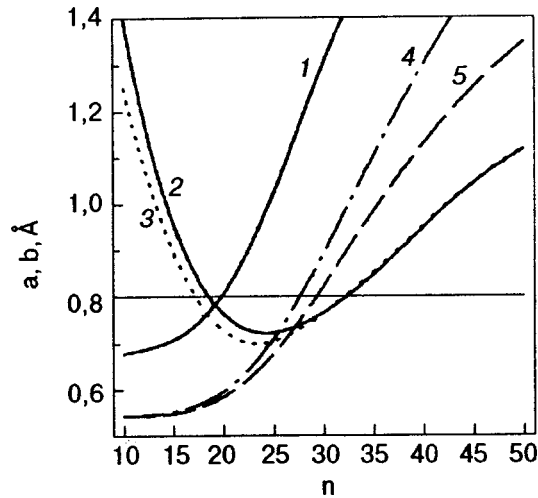
FIG. 8. Dependence of the radial delocalization parameter a (*1*) and and the lateral delocalization parameter b (*2*) on n for a $XeHe_n$ cluster. For comparison, the delocalization parameter in liquid helium (*3*) is shown for the same value of the interatomic distance as the value of d for the given n. Also shown are the radial delocalization amplitudes (*4*) and (*5*), found in the approaches based on Eqs. (12) and (14), respectively. The horizontal straight line corresponds to the delocalization in liquid helium at $P=0$.

FIG. 9. Analytical model. The dependence of the energy of an impurity–helium cluster on the the parameter γ for $m=5$ in the absence (*1*) and presence (*2,3*) of the contribution of the energy of zero-point radial modes for $R_e=r_e$ (*2*) and $R_e=0.9r_e$ (*3*).

tion of the zero-point radial modes calculated in the harmonic approximation, $\frac{1}{2}n\omega_0(n)$, where

$$\omega_0(n)=\hbar\left(\frac{1}{nm_{He}}\frac{\partial^2 E(R,n)}{\partial R^2}\right)^2.$$

We note in conclusion that the above analysis suggests a simple way of estimating the characteristics of the helium environment of impurity atoms in liquid helium. Using the analytical solution for the energy (7), which is based on the approximations (3) and (4) for the potentials, one can then add to it the energy of the radial modes calculated in the harmonic approximation:

$$E=E^*+\frac{1}{2}n^*\omega^*,$$

where $\omega^*=(\hbar/R^*)[72|E^*|/(n^*m_{He})]^{1/2}$. With this contribution taken into account (see the result in Fig. 9), one can predict the cluster energy for any center, which is characterized by the parameter γ. Here the parameters of the structure remain practically unchanged and, as before, are determined by the curves in Figs. 2 and 3. One notices that at small values of the parameters γ (from γ_{cr} to $\gamma\approx3$), taking the vibrational energy into account alters the sign of the total energy of a cluster, and the system acquires a metastable character.

IMPURITY CENTER IN LIQUID HELIUM

As we have said, atoms that interact strongly with helium acquire shells having the structure with attraction, and the structure should not change much when the cluster is immersed in liquid helium. Nevertheless, the solution of this problem is of definite interest in connection with the existence of effects of an external pressure. It also becomes pos-
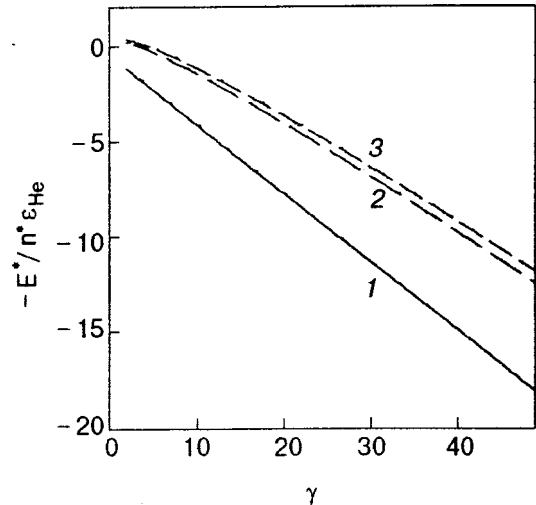
sible to treat another limiting case of shells with repulsion, which, as we have said, can exist only in the presence of a surrounding liquid.

The continuum description of liquid helium as a quantum liquid, based on its known equation of state, in principle enables one to formulate and solve the problem of the behavior of an isolated atom in liquid helium. However, the density distribution thus obtained is more a description of liquid helium perturbed by the presence of an impurity in it rather than the desired description of an impurity atom whose state is perturbed by a helium environment. From this standpoint the main shortcoming of the continuum approach and, foremost, of the density-functional method is that, even through the kinetic energy is taken into account, it still cannot give the energy spectrum of the shell in explicit form. At the same time, it is perfectly obvious that, for example, at optical transitions in an impurity center surrounded by a rather stiff helium shell, what will be primarily excited are not the states of bulk helium (phonons, rotons, etc.) but rather various vibrations and rotations of this shell. Attempts to describe these vibrational motions in terms of mechanical vibrations of a ''bubble''[13,27] for shells having the structure with attraction can scarcely be fruitful, if only because of the aforementioned negativity of the ''coefficient of surface tension.'' In this case we will therefore use an approach based on an explicit analysis of the interatomic interactions. Such an approach is justified simply by the fact that the number of He atoms in the layer nearest to the impurity is not very large. It is therefore of interest to analyze whether there can exist effects associated with the discrete nature of the environment, when the average number of helium atoms in the shell jumps rather than changing continuously as the external conditions vary.[7]

In this regard the continuum approach has, in principle, another important shortcoming, particularly for describing atoms that interact strongly with helium—both on account of the larger localization of the He atoms surrounding them and

also on account of their smaller number. In the continuum approach one essentially assumes that the quantum delocalization of helium is so large that a spherically symmetric helium environment is always maintained around an impurity center. However, the correlations of the relative positions of the helium atoms in the shell with a definite and not very large radius, which do not allow the atoms to approach to arbitrarily small distances from each other, means that there are certain geometric limitations. In other words, for a given number of helium atoms in the shell, it is in general impossible to cover the sphere in such a way that every helium atom would have the optimum number of neighbors at the optimum distances. An exception are the magic numbers corresponding to regular or semiregular polygons. Therefore, in the general case a spherically symmetric helium distribution arises in the shell around a spherically symmetric center only on average, on account of the rotation of the energetically preferred spherically asymmetric configuration. In an approach based on analysis of atom–atom interactions, this important circumstance can in principle be taken into account. Nevertheless, in the present paper we have for simplicity taken into account the He–He interaction in the shell on average, i.e., we have limited consideration to the spherically dominant case. This means that we are neglecting the influence of magic occupation numbers on the stability of the shell and also the geometric factors of the ''instantaneous'' deviation of its shape from spherical, the inclusion of which can lead to changes in both the effective numbers m of helium atoms in the shell and also degree of radial delocalization.

Therefore the results obtained in the continuum approaches and by the method used in the present paper should be regarded as qualitative.

Keeping this in mind, let us consider the interaction energy of an impurity center with liquid helium (including the presence of an external pressure P) in the following approximation. We separate out the layer of the n nearest helium atoms and treat them in the same manner as for an isolated cluster of $ImHe_n$. The interaction of the $ImHe_n$ cluster with the surrounding helium is governed by pair interactions of atoms of the shell with the next-nearest layer, which consist of n_v helium atoms, and also by the residual van der Waals interaction of this second layer with the impurity center. At the same time, because of the small influence of the impurity center on this helium layer and the next, one can neglect the difference of the properties of the helium in this region from those of liquid helium. The total energy of a cluster can be written as

$$E_{Im}(R,n) = E(R,n) - n\mu(P) + \Sigma(R,n) + PV, \qquad (22)$$

where the first term describes the energy (12) of an isolated cluster, the second takes into account the change of the chemical potential of the system when n atoms of the liquid are incorporated in the first shell of the cluster, the third is the interaction of the cluster with the liquid helium layer surrounding it (which is analogous to a surface energy), and the last term is the work done by the pressure forces. The

quantity $\mu(P) = \varepsilon(V(P))$ is specified by the equation of state (10) of liquid helium, where $V(P)$ is implicitly determined by the equation $-P = \partial\varepsilon/\partial V$.

The number of atoms in the second layer is determined by its thickness and the outer radius of the helium shell. The thickness of the spherical layer, in view of its large radius, will be taken to be the same as for a plane layer: $2r_s(P) = V(P)/S(P)$, where $S(P)$ is the area per helium atom in the surface layer. For the six neighbors in close-packed structures one has $S(P) = (\sqrt{3}/2)[V(P)\sqrt{2}]^{2/3}$. In this case for $P = 0$ the value of $2r_s$, which is equal to 3.2 Å, is close to the distance between the positions of the first and second maxima for the radial distribution function of liquid helium,[26] and also for the radial distribution function of helium around an impurity center (see Fig. 6).

The change in the radius of the inner shell with pressure is taken into account implicitly in the process of optimization of the energy of the system, and we therefore have $R + r_s(0)$ for the outer radius of the shell. Then

$$n_v = \frac{4}{3}\pi \frac{[R + r_s(0) + r_s(P)]^3 - [R + r_s(0)]^3}{V(P)},$$

and the contribution to χ corresponding to the interaction with the impurity center is

$$n_v E_{ImHe}(R + r_s(0) + r_s(P)). \qquad (23)$$

The interaction energy between the helium atoms of the first and second layers is determined by the average number M_s of van der Waals bonds that arise and is equal to $\varepsilon_{He}M_s$. The number of bonds is proportional to the number of atoms in the adjacent layers. The coefficient of proportionality is equal to 3 for $R \to \infty$ on considerations of close packing. For finite R the condition that the number of bonds be independent of the method of counting them (whether by proceeding from the number of atoms in the inner or outer layer) implies

$$M_s = n\left(3 + \frac{6}{R + r_s(0)}\right)$$

or

$$M_s = n_v\left(3 - \frac{6}{R + r_s(0)}\right).$$

The energy expended on the formation of the surface of a cavity of radius $R + r_s(0)$ (accommodating an impurity–helium cluster $ImHe_n$) in liquid helium is equal to $\sigma 4\pi[R + r_s(P)]^2$. Taking this energy into account, we get

$$\Sigma(R,n,P) = n_v(P)E_{ImHe}(R = r_s(0) + r_s(P))$$
$$+ n\left(3 + \frac{6}{R + r_s(0)}\right)\tilde{E}_{He}\left[r_e\frac{2r_s(0)}{r_s(0) + r_s(P)}\right]$$
$$+ \sigma 4\pi[R + r_s(P)]^2, \qquad (24)$$

where the coefficient of surface tension was taken as 0.272 K/Å^2, which is the theoretical value at $T = 0$,[11] and we have assumed that the change in distance between interacting helium atoms of the first and second layers is proportional to the distance between layers, $r_s(0) + r_s(P)$.

The last term in Eq. (22) can be written as

$$\frac{4\pi}{3}\left(R+\frac{r_e}{\sqrt{6}}\right)^3 P. \tag{25}$$

Thus the problem of finding the energy of an impurity immersed in liquid helium and the structure of its helium shell reduces to one of minimizing the energy described by Eq. (22) together with (12), (24), and (25):

$$\frac{\partial E_{\mathrm{Im}}}{\partial R}=0; \quad \frac{\partial E_{\mathrm{Im}}}{\partial n}=0.$$

Now it is also possible to describe the change in the properties of the helium shell around an impurity center under the influence of the external pressure. This change is determined not only by the contribution of the work performed by the pressure forces but also by the pressure dependence of the properties of liquid helium itself, $\mu(P)$ and $S(P)$. Since this problem can be solved only numerically, let us give the results for two typical examples: Cs, which is the atom that interacts most weakly with helium, and N, which interacts most strongly with helium (among those listed in Table I).

It should be noted, however, that in the simplified approach taken here, the kinetic energy of the helium environment is taken into account effectively through a parametrization of the He–He interaction according to the equation of state of liquid helium. Therefore, for the structures with repulsion this approximation does not lead to serious error. For the structures with attraction, however, the appreciable radial localization makes it necessary to introduce a correction for the increase in energy of the zero-point radial modes. However, the formal procedure of adding up the total energy of the zero-point radial modes, which gives a fair result for a XeHe$_n$ cluster, has a lower accuracy in the case of an atom in liquid helium on account of the influence of the helium environment on the frequency of the radial modes.[8]

Since for structures with attraction the correction for the vibrational energy does not alter the geometry of the shell, we will omit it entirely for the examples considered below.

Nitrogen atom in liquid helium. The calculations whose results are shown in Figs. 10–14 were done on the basis of expression (22) for the energy for the He–N pair potential, which is specified in the form of a generalized Morse potential:

$$U_{\mathrm{NHe}}=D_{\mathrm{NHe}}M\left(Q,\frac{R-R_e}{R_e-R_0}\right),$$

$$M(Q,x)=Q\left(\frac{Q}{Q+1}\right)^{(Q+1)x}-(Q+1)\left(\frac{Q}{Q+1}\right)^{Qx},$$

where $D=33.2$ K, $Q=0.7453$, $R_e=3.441$ Å; $R_0=3.083$ Å, which was obtained using a specially developed extrapolation procedure with the use of the known potentials for He–Ne, He–F, and He–0.[28-30]

It is seen in Fig. 10 that a nitrogen atom in liquid helium forms around itself a structure with attraction. As expected, the structure of the cluster does not change greatly when it is immersed in liquid helium. For comparison, let us give the characteristics we calculated for the optimum shell of a ni-
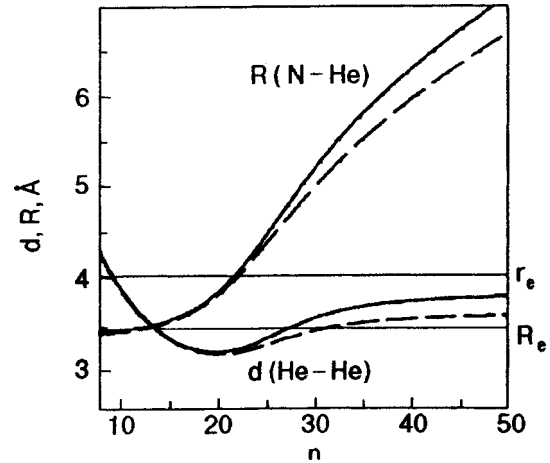

FIG. 10. Radius R of the shell and distance d between helium atoms in it versus the number n of He atoms in the nearest-neighbor environment of a nitrogen atom immersed in liquid helium ($T=0$). The solid curves are for $P=0$, and the dashed curves for $P=25$ bar. The horizontal straight lines correspond to equilibrium distances R_e and r_e for the N–He and He–He pair potentials, respectively.

trogen atom in an isolated cluster: $R^*=3.54$ Å, $d^*=3.36$ Å, and $n^*=15$. For a nitrogen atom in liquid helium Figs. 10 and 12 yield $R^*=3.52$ Å, $d^*=3.35$ Å, and $n^*=15$. It is natural to expect that the differences will also be small for other impurity atoms which interact strongly ($\gamma\gg1$) with helium. In this case the distances between helium atoms in the shell are shortened in comparison with the distances between He atoms in liquid helium (3.8 Å) at the solidification pressure. This raises the question of whether an analog of a phase transition exists in the shell (corresponding to a liquid–solid phase transition in the bulk), where the lateral delocalization of the helium atoms decreases abruptly, so that an additional number of helium atoms can fit in the shell. This transition could also occur for $P\neq0$, and then instead of the slight shortening of d with increasing P (Fig. 10) there would be a downward jump in d. However, this question requires a special analysis beyond the scope of the present paper.
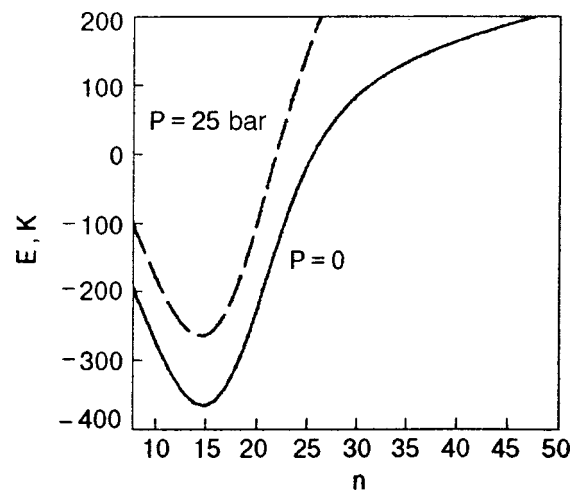

FIG. 11. Energy of a nitrogen atom in liquid helium versus the number n of He atoms in the nearest layer.
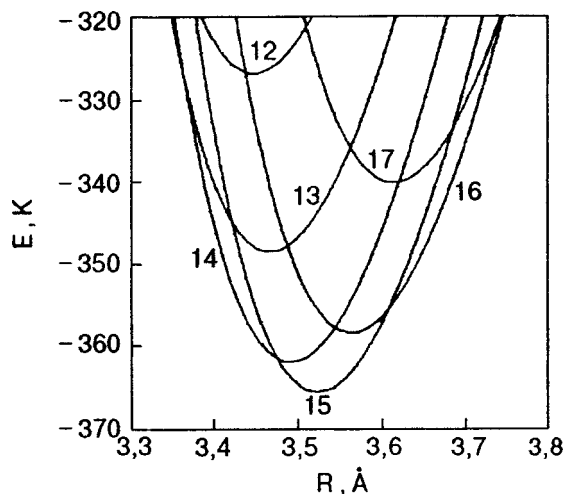
FIG. 12. Nitrogen atom in liquid helium. Effective potentials for shells with different n at $P=0$.

FIG. 14. Pressire dependence of the different contributions to the total energy E_{tot} of a nitrogen atom in liquid helium; P is the external pressure.

It follows from Fig. 12 that for atoms that bond strongly with helium the difference in energies for shells with different numbers of helium atoms, as a rule, is substantially greater than the typical temperatures at which experiments are done. However, for the particular case of the N atom there are two shells, containing 15 and 14 He atoms, which are close in energy (3 K). Since they nevertheless differ in terms of the N–He distance, this should give rise to a double structure in the optical spectra; the relative intensity of the components of this doublet should be a strong function of the temperature and (as can be deduced from Fig. 13) pressure. Moreover, it is seen from the same figure that for the particular case of N atoms a change in pressure over the range 0–25 bar does not lead to a change in the number of He atoms in the shell, although from the $E(P)$ curves for different n one can discern a tendency for the number of atoms in the shell to decrease as the external pressure increases.
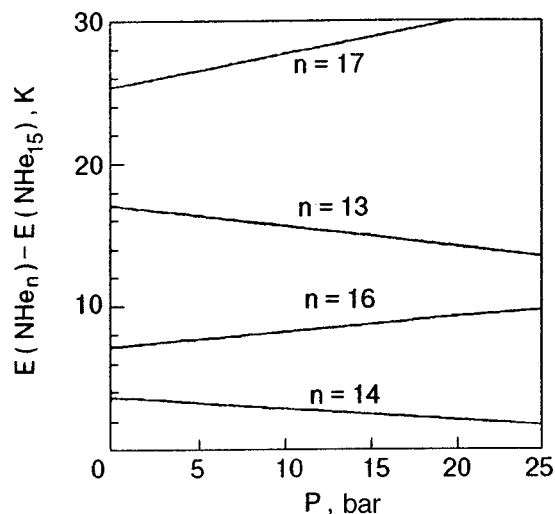

FIG. 13. Pressure dependence of the relative energy of a nitrogen atom in liquid helium (as compared to the energy of a system of optimum composition $n^*=15$) for different occupation numbers n of the He shell; P is the external pressure.
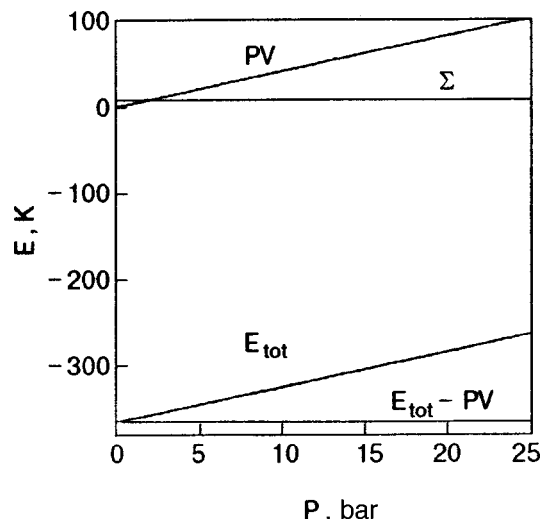
As can be seen in Fig. 14, the contribution of the energy Σ to the total energy is extremely small. Furthermore, the only contribution to the energy that actually depends on pressure (linearly!) is the work of the change in volume, which even at high pressures is small compared to the total energy. From an energy standpoint the structure under discussion is thus a practically incompressible ball. The strong binding of the helium atoms in the shell to the central atom justifies the neglect of the exchange interaction with the environment, but at the same time and for the same reason, one expects a larger manifestation of ''magic number'' effects in the occupation number.

A cesium atom in liquid helium. The calculation was done using a Cs–He pair interaction potential in the form of a Lennard–Jones potential with the parameters indicated in Table I. Unlike the case of an isolated CsHe$_n$ cluster, a stationary spherical helium shell does exist around a Cs atom in liquid helium, since the radius R of the shell cannot increase without bound even at zero pressure. However, the total energy of the shell in this case is positive (see Fig. 15), reflecting the fact that cesium is unwettable by helium. As we see from Fig. 16, the structure of the environment corresponds to the case of repulsion, and therefore, counterintuitively, its radius is smaller than the equilibrium radius for the Cs–He pair potential.

The distances d between helium atoms in the shell are found to be in the neighborhood of r_e over a wide range of values of n, including the very gradual minimum on the curve of E versus n (Fig. 15). To draw more definite qualitative conclusions about d in the case of atoms lying on a curvilinear surface and in view of the systematic errors of the model, we will compare these distances to the distances between helium atoms in the shell for Im–He at $P=0$. For structures with attraction, for which the distances d are strongly shortened in comparison with r_e, these refinements do not alter the qualitative conclusions. The approach used here gives an optimum value of $n=12$ for the helium environment, in complete agreement with the basic assumptions,
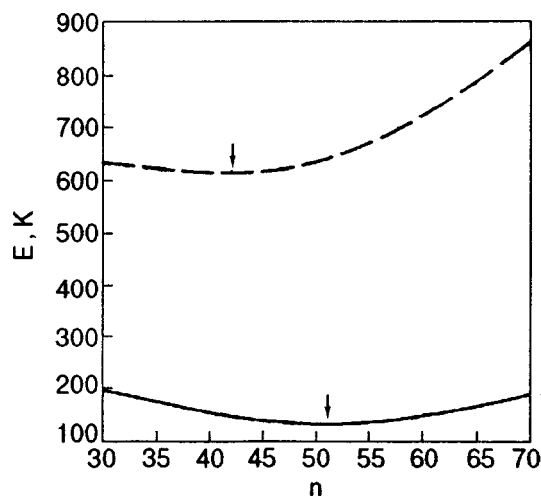
FIG. 15. Energy of a Cs atom in liquid helium versus the number of atoms in the helium shell surrounding it ($T=0$). The solid curve is for $P=0$; the dashed curve for $P=25$ bar. The arrows indicate the positions of the minima.

FIG. 17. Cs atom in liquid helium. The effective potentials for shells with different n at $P=0$.

and a value $d=3.84$ Å, which turns out to be smaller than d(He–He) for the optimum $n=51$ (see Fig. 16). At the same time, the area per helium atom in the shell (14.0 Å^2) is almost exactly the same as $S(0)=13.99$ Å^2, and the average volume per He atom in He$_{12}$, which is equal to 47 Å^3, comes out greater than $V(0)$.[9]

A distinctive feature of the system under study is the small (~ 0.1 K) energy difference of shells containing different numbers of helium atoms (see Fig. 17). Here, as can be seen from Fig. 18, the radius of the shell varies noticeably as n changes: indeed, the data of Ref. 12 suggest that the change in the Cs–He distance from 7.2 to 6.6 Å under the influence of an external pressure leads to a shift of the spectral absorption band by 400 cm^{-1}. This means that for $\Delta R \cong 0.02$ Å one can expect an experimentally measured line shift of 10 cm^{-1}. The results, $R^* = 7.36$ Å and a value of 132

K for the energy of a Cs atom in liquid helium, are in good agreement with the data of a more complicated calculation in the ''bubble'' model,[12] which gives 7.19 Å and 130 K. However, these binding energies differ from the result of a calculation by the density-functional method, which gives 84 K.[9]

It is extremely remarkable that, in spite of the significant decrease in the radius of the shell with increasing pressure, the number of helium atoms in it decreases so strongly in the process that the distance between helium atoms even increases somewhat (see Fig. 19). Thus the density of helium in the shell even falls off somewhat with pressure; this is a striking and fundamental difference from the case of atoms that interact strongly with helium (cf. Fig. 10): for Cs atoms the shell is ''liquid'' and it only becomes more ''liquid'' as the pressure is increased! This result is a qualitative consequence of the fact that as the pressure increases, the helium approaches closer and closer to the center of the Cs atom, where there is ever-increasing repulsion. Therefore in this region the average potential energy of the helium increases
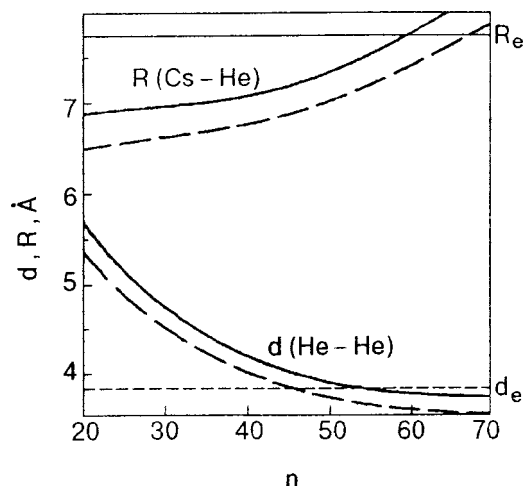

FIG. 16. Cs atom in liquid helium. The radius R of the shell and the distance d between helium atoms in it as functions of the number of atoms in the shell. The solid curves are for $P=0$; the dashed curves are for $P=25$ bar. The horizontal lines are the equilibrium distances R_e for a Cs–He pair potential and the distance d_e between He atoms in the shell for He–He.
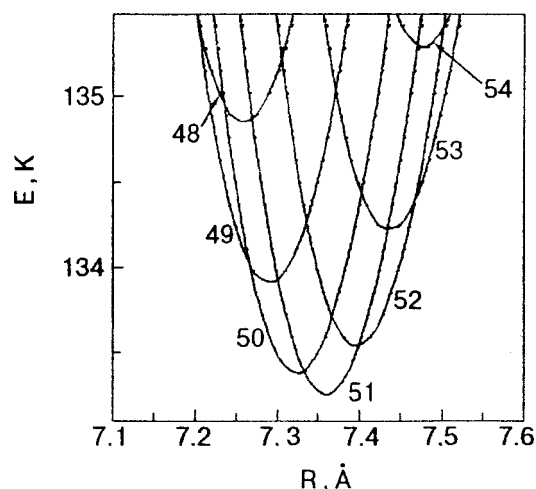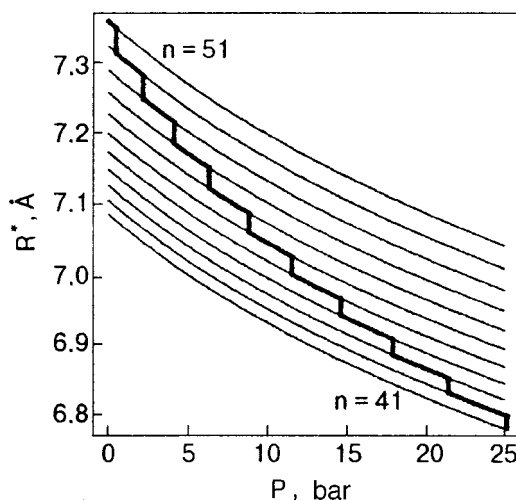

FIG. 18. Cs atom in liquid helium. The radius R of the shell as a function of the external pressure. The vertical segments denote the pressures at which the energy of the states of shells with adjacent n become equal ($T=0$).
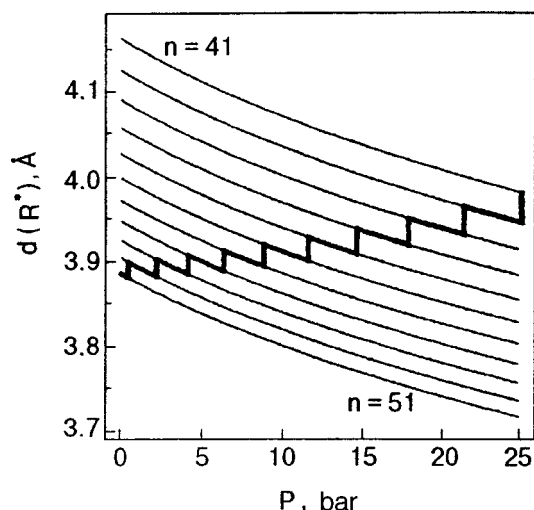
FIG. 19. Cs atom in liquid helium. The He–He distance in the shell as a function of the external pressure. The vertical segments denote the pressures at which the energies of states of shells with adjacent n become equal ($T=0$).

with increasing pressure at a rather high rate, higher than the growth rate of the chemical potential of liquid helium.

The pressure dependence of the different contributions to the binding energy of a Cs atom with the surrounding helium (Fig. 20) has practically the same functional form as for a nitrogen atom in liquid helium (cf. Fig. 14), but here, in view of the larger volume of the shell, the term corresponding to the work of creating the cavity is predominant. This means that even a structure with repulsion is only slightly compressible (although in this case one can already notice a deviation from linearity on the curve of PV versus P).[10]

This is a fundamental and important difference in the behavior of the helium environment of impurity atoms in liquid helium as compared to an easily compressible electronic ''bubble.'' In the latter case the volume changes by a factor of seven as the pressure is raised from 0 to 25 bar,
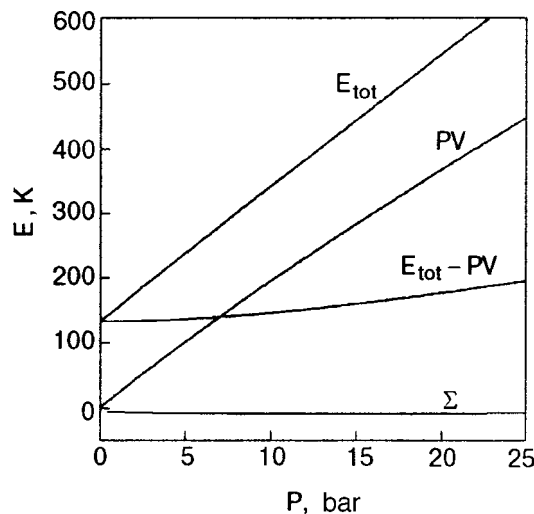

FIG. 20. Pressure dependence of the different contributions to the total energy E_{tot} of a Cs atom in liquid helium; P is the external pressure.

whereas for Cs the change is only 25%. The low compressibility of the ''bubble'' was noted back in Ref. 12.

Finally, while correctly describing the interaction on the whole, the chosen model may be inaccurate in the description of the details. For example, because of exchange with the environment the occupation numbers of the shell may not be good quantum numbers describing the individual quantum states, as illustrated in Fig. 17, and the true state of lowest energy will be a superposition of states with definite n, coupled with the He volume. However the conclusion that at temperatures of the order of 1 K there are several energetically accessible states characterized by different average numbers of helium atoms in the shell, and the conclusion that these numbers decrease with increasing pressure, are undoubtedly valid. The details of the energy spectrum of these states, in view of the possibility of more significant effects of asphericity of the shell and the existence of ''magic'' occupation numbers, cannot be calculated anyway without constructing suitable models.

In conclusion it should be noted that the two types of structures of the helium environment of impurity atoms in condensed helium, which can be classified as structures with repulsion (''bubbles'') and structures with attraction (''snowballs''), should behave in fundamentally different ways when ^{4}He is replaced by ^{3}He. Indeed, while the structure with attraction should swell substantially when such a substitution is made, and its energy should increase, the structure with repulsion, on the contrary, should decrease in energy. Since there is no doubt that in any case the optical spectra of atoms in condensed helium should be different for ^{4}He and ^{3}He, this effect can be used for an experimental determination of which type of structure is formed in helium by a given impurity, and what the characteristics of that structure are. Suppose we do an experiment in liquid ^{3}He with a small (less than 1%) admixture of ^{4}He. Then in the case of a structure with attraction the optical spectrum will be that which is characteristic for ^{4}He (since those atoms at sufficiently low temperature displace the ^{3}He atoms from a single-layer shell around an impurity), while for a structure with repulsion the admixture will have no effect on the spectrum. Conversely, the optical spectra of a structure with repulsion, unlike those for a structure with attraction, will be sensitive to small admixtures of ^{3}He in ^{4}He, since in them the ^{3}He atoms will displace ^{4}He atoms from the shell. Moreover, by studying how the spectrum is transformed as a function of the amount of the admixture of whichever isotope of helium at different temperatures, one can determine the equilibrium constant of a process of the type

$$\text{Im}^4\text{He}_n + n\,^3He \rightleftarrows \text{Im}^3\text{He}_n + n\,^4\text{He}$$
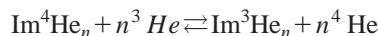
and, hence, the change in enthalpy and entropy of the structure in the case of total (or partial) isotopic substitution.

We should point out that such a study has already been published. For example, in experiments[31] with fine droplets of helium doped with Cs, the identical nature of the optical spectra in ^{4}He and ^{3}He drops with 60 atoms of ^{4}He added to a drop containing around 10^4 atoms of ^{3}He was explained by a ^{4}He ''screening'' of the impurity molecules from the ^{3}He. On the other hand, theoretical calculations[32] show that alkali

metal atoms have larger binding energies with ^{3}He than with ^{4}He. This result is obvious from the standpoint of our model, since, because of the lower effective energy in ^{3}He in comparison with ^{4}He the parameter γ will be noticeably larger for the light isotope of He at the same value of U. Thus for impurity centers that interact weakly with helium, the replacement of ^{4}He by ^{3}He can lead to a transition from the region $\gamma < \gamma_{cr}$ to the region $\gamma > \gamma_{cr}$.

Experiments with single-layer clusters of a single isotope of helium immersed in a liquid of the other isotope are also attractive from the standpoint of simplicity of their theoretical interpretation: for them one can reliably neglect the effect of exchange of helium atoms between the shell and the bulk of the liquid.

Using the results obtained in this study, let us analyze the published experimental data and try to predict some effects due to the specific combination of continuous and discrete properties of the helium environment of impurities in liquid and solid helium.

The structure and energy spectrum of the helium environment of impurities in liquid and solid helium determine such properties as the optical, ESR, and NMR spectra of the impurity, the reaction to changes in the external parameters (which may be of the nature of a phase transition), the specific heat and thermal conductivity of the shell, and its magnetic polarizability (in the case of ^{3}He). Finally, they play a decisive role in the description of an impurity–helium solid phase (IHSP),[6] the very existence of which is due w the localization of the helium around a heavy impurity introduced in it. On the other hand, in the ''dry'' state practically all the helium in the IHSP is partially localized, and therefore the properties listed above, which are characteristic of the ensemble of He atoms adjacent to the impurity, are in this case macroscopic properties of the sample. In particular, for an IHSP one expects anomalously large values of the thermal conductivity and magnetic polarizability (in the case of ^{3}He).

OPTICAL SPECTRA

The optical spectra of impurity particles in condensed helium have been studied the most. Here we do not intend to present a complete analysis of the results that have been obtained (for this we recommend the recent reviews),[1–3] but we will briefly summarize the main conclusions.

As a rule, the observed optical transitions of alkali and alkaline-earth metals are rather wide (1–10 nm) and practically structureless bands which are strongly blue-shifted in the absorption spectra relative to the fundamental transition. The emission lines are shifted considerably less (one can observe a blue rather than red shift), have a more symmetric shape, and are substantially narrower. This behavior has been successfully explained by a combination of a vertical phototransition and large changes in the size of the cavity surrounding impurity atom upon its electronic excitation. After the absorption of a photon the radius of the cavity is smaller than the equilibrium radius, i.e., the system of atom plus surrounding helium has more than the equilibrium energy. During emission the system undergoes a vertical transition
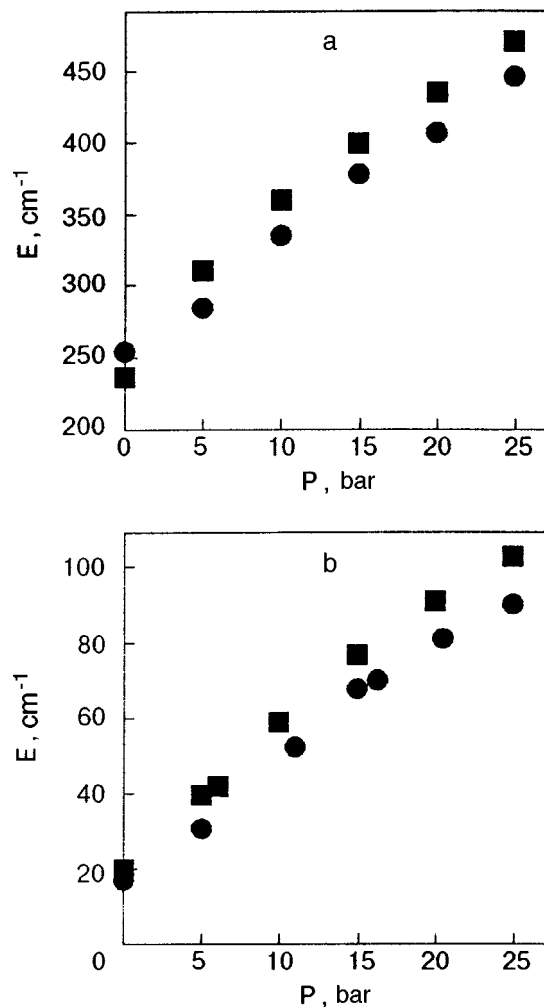

FIG. 21. Experimental plots[12] of the energy of the resonance transition relative to the energy of the transition in vacuum in the emission (a) and absorption (b) spectra of Cs (■) and Rb (●) atoms in liquid helium versus the external pressure.

from the equilibrium state for the excited atom to a state with a cavity radius larger than the equilibrium radius of the unexcited atom, and it is therefore characterized by a smaller perturbation of the electronic state of the central atom[1] in view of the difference in the steepness of the repulsive and attractive branches of the Im–He potential. Broad, structureless lines in a spectrum are not very informative, and the most noteworthy fact is a strong pressure dependence of the spectral shift of the absorption and emission lines. In both cases the lines are blue-shifted, the shift being considerably stronger for the absorption band than for the emission band. The pressure dependence of the bandwidths is small and is approximately the same for the absorption and emission bands. The experimental results[12] for Cs and Rb are shown in Fig. 21.

For atomic transitions involving the participation of electrons from the inner shells, such as in Eu (Ref. 33) and Tm (Ref. 34), which are characterized by small changes in the van der Waals dimensions of the atom, the corresponding shifts and broadening of the spectral lines are substantially smaller, as one would expect. In addition, besides the structureless band the spectra have a rather narrow line (on the

red side in absorption), which the authors call the zero-phonon line, by analogy with the spectra of matrix-isolated particles, in contradistinction with the wide (and sometimes quite remote) band which is designated as the phonon wing.

A similar structure is possessed by the individual electronic–vibrational lines in the optical spectra of molecules implanted in liquid helium.[35,36] Moreover, the so-called phonon wings exhibit a certain structure which corresponds in energy to the collective excitations in the bulk of liquid helium (maxons, rotons) and, for the experiments on small droplets of helium, ripplons.[34–38]

For an electronic ''bubble,'' in view of its large radius, the short-range dispersion forces of attraction do not play an important role, and the interaction with the surroundings during an optical transition can be can be reduced to high-frequency ''breathing'' oscillations of the bubble.[1] To a certain degree the alkali-metal atoms during an optical transition can be regarded as coupled with the volume of liquid helium surrounding them. However, as is clear from what we have said, atoms that interact more strongly with helium are surrounded by a stiff elastic shell, the characteristic frequencies of which are substantially higher than the frequencies of excitations in liquid helium. Therefore, these atoms are more naturally considered as a comparatively soft (in the sense of the intermode vibrational interaction and the anharmonicity of the potential) van der Waals molecule ''dissolved'' in liquid helium. Consequently, for bound–bound optical transitions the shape of the spectral band should be determined primarily by the vibrational–rotational spectrum of the quasimolecule $ImHe_n$. Then, of course, the shape of the individual components will be affected by both the softness of the core of the molecule and exchange of the atoms in the molecule with the surroundings and by the weaker interaction with the modes of liquid helium.

It should be kept in mind, however, that the characteristic frequencies of the vibrations of stiff helium shells have values of approximately $10–30$ cm^{-1}, whereas the total binding energy of an impurity center with liquid helium is $100–300$ cm^{-1}. Since these shells are also very incompressible, only a small change in the equilibrium radius of the shell upon electronic excitation of the central atom is needed in order for the corresponding electronic transition to become bound–free, the final state of which being determined mainly by the bulk properties of liquid helium. Unlike the case of diatomic molecules,[39] in polyatomic molecules the boundary between bound–bound and bound–free transitions is smeared, since the ''dissociation energy'' is different for different types of vibrations. Nevertheless, it cannot be much smaller than the energy of total decomposition of the the cluster into atoms, since vibrations in which less than half of all the atoms actively participate should have low Franck–Condon factors. Of course, the structure and mechanical properties of the nearest-neighbor environment should have some influence on the shape of the spectrum of bound–free transitions, but the general features of the spectra of these transitions should be similar to those for transitions in alkali-metal atoms.

For systems with a stiff helium shell the number of He atoms in the shell is fixed. Since the energies of excitations

of the shell are $\gg kT$, we can assume without restricting the generality that the system is initially found in the vibrational ground state $|i,0,0,\ldots,0\rangle$. Then, neglecting the difference of the vibrational frequencies ω_j of the lower and upper terms, we have the following expression for the transition amplitude $A_{if}=\langle f,k_1,k_2,k_3,\ldots,k_n|D|i,0,0,0,\ldots 0\rangle$:

$$A_{if}=D_{if}\prod_{j=1}^{n}\langle k_j|0\rangle,$$

where D_{if} is the electronic matrix element, and the Franck–Condon factors are completely determined by the displacements of the minimum of the upper term relative to the minimum of the lower term along the jth vibrational coordinates ΔR_j (in units of the amplitude of the corresponding zero-point vibrations):

$$\langle k_j|0\rangle^2=e^{-(\Delta R_j)^2}\frac{(\Delta R_j)^{2k_j}}{k_j!}.$$

In the harmonic model, only the even modes (approximately one-half of all modes) have nonzero displacements. Then, with allowance for the widths γ_j of the vibrational states, we have the following form of the spectrum:

$$I_{if}(\omega)=D_{if}^2\exp\left[-\sum_j(\Delta R_j)^2\right]\left[S(\omega+\omega_e,\gamma_0)\right.$$
$$\left.+\sum_j S(\omega+\omega_e\pm\omega_j,\gamma_j)(\Delta R_j)^2+\cdots\right], \quad (26)$$

where ω_e is the energy of the electronic 0–0 transition, the plus and minus signs denote absorption and emission, respectively, and the function

$$S(\omega,\gamma)=\frac{1}{\gamma\sqrt{\pi}}\exp\left(-\frac{\omega^2}{\gamma^2}\right)$$

describes the Gaussian shape of an individual component of the spectrum. In view of what we have said, $\gamma_0\ll\gamma_j$, and the 0–0 transition is therefore distinguished among the bound–bound transitions by its narrow linewidth, and it can therefore be detected against the background of the wide spectral line even in cases when it has a small fraction of the intensity of the transition.

For impurity atoms that interact strongly with helium, as a rule (inert-gas atoms are a special case), the optical transitions do not change the principal quantum number of the outer electrons. Therefore the possible changes in the radius of the helium shell upon excitation are small, and in view of the rather appreciable amplitude of the zero-point vibrations of the He atoms (~ 0.8 Å), the parameters ΔR_j turn out to be small, and the shape of the spectrum can be adequately described by just the leading terms in formula (26).

In this case the structure of the spectrum qualitatively comprises the narrow line of the 0–0 transition and an extended structure in the form a long shoulder on the blue side for absorption and on the red side for emission. The extent of the shoulder is equal to the maximum vibrational frequency of the helium shell, which lies in the interval 20–40 K, as can be estimated from the calculated frequencies of the radial

zero-point modes. The possible errors due to the influence of the interaction of the radial modes and anharmonicity effects have different signs, and this improves the accuracy of the estimate. The lateral vibrations of the helium shell cannot be found in the framework of the models used here. It can be assumed, however, that their average energy is less than the energy of the radial modes and that their interaction is greater than the interaction of the radial modes. In the limiting case this makes the energy of the individual modes close to zero (as, e.g., the unhindered pseudorotations of certain groups of atoms in the helium shell).[6] Thus the lower boundary of the spectral structure can lie quite close to the line of the 0–0 transition, and in the limit it can even coincide with it. The number of lateral modes is twice the number of radial modes, and the effect of energy transfer to the medium for them is expected on geometric grounds to be lower. Therefore, in the general case one expects that the shoulder will deviate appreciably from the main line. We have observed just such a structure of the line for the $^2D-^4S)$ transition in atomic nitrogen.[40,41]

The spectra obtained for Eu (Ref. 33) and Tm (Ref. 34) atoms immobilized in liquid helium qualitatively confirms the arguments presented above. Here the finite (and temperature-dependent) width of the narrow line interpreted as the 0–0 transition is explained by the finite time for exchange between a helium atom belonging to the shell and the surrounding helium. The wide component can be interpreted as a pseudomolecular band (with a possible contribution of bound–free transitions for excitations of optical electrons; these can be interpreted provisionally as a phonon wing).

Unfortunately, there are no published data on the spectra of heavy inert-gas atoms immersed in liquid helium. Meanwhile, in view of the fact that the size of such atoms changes strongly upon transition from the ground state to the first excited state, all the vibronic transitions should be bound–free.

As we have said, for alkali-metal atoms, which form repulsion structures in helium, the observation of quasimolecular structures in the spectrum is very improbable, and one expects that the spectrum will reflect only processes of energy dissipation into the medium. Apparently the most probable process is an optical transition with several He atoms being ejected from the shell into the medium or combining with the shell. In this case one expects more or less symmetric and strongly broadened spectral lines. Another probable energy dissipation process is the excitation of vibrations of the surface of the helium layer adjacent to the impurity. The energy of such vibrations can be estimated using the following model. We assign to each atom of the surface layer a radial Gaussian smearing function

$$\frac{1}{a\sqrt{\pi}}\exp\left[-\frac{(r-R)^2}{a^2}\right]$$

(the delocalization of the helium atoms in the lateral direction varies only slightly with the radius R, by virtue of of the large value of R for centers that interact weakly with helium) and the corresponding kinetic energy $\hbar^2/(4m_{He}a^2)$. Then,

taking into account the dependence of the average area of the surface layer on the smearing, we find the total energy per atom for the system:

$$E(a)=\frac{\hbar^2}{4m_{He}a^2}+\frac{4\pi\sigma}{n}\left(R^2+\frac{a^2}{2}\right),$$

where R is the given radius of the shell, ω is its surface tension, and n is the number of atoms in it. Optimization of the energy gives the optimum value a $=[\hbar^2\sigma n/(8\pi m_{He})]^{1/4}$. Assuming that it is related to the vibrational energy by the same law as for a harmonic oscillator, we obtain the following characteristic frequency:

$$\omega=\hbar\left(\frac{8\pi\sigma}{m_{He}n}\right)^{1/2}\approx\left(\frac{100}{n}\right)^{1/2}\text{K}.$$

Thus the frequencies of the surface modes are quite low, and if this kind of energy dissipation is predominant, the absorption spectrum will be an asymmetric broad line with a more or less noticeable peak of the adiabatic transition on its red wing (especially in the case of large displacements of the maximum relative to the energy of the adiabatic transition). For the emission spectra the peak of the adiabatic transition will be observed on the blue wing.

In general, the spectra of alkali-metal atoms should be extremely smeared and structureless on account of inhomogeneous line broadening, since at room temperature there is occupation of a large number of states having nearly equal energies but different numbers of He atoms in the nearest-neighbor environment and, hence, different structures.

Both types of structures behave as relatively incompressible objects in a readily compressible liquid (see the energy diagrams in Figs. 14 and 17), but for the structure with repulsion the object is the atom itself, while for the structure with attraction it is a stiff helium shell. Therefore the measurements of the shifts of the absorption and emission bands can be given a simple physical interpretation without requiring special calculations. For such systems the following expressions can be written, to the leading quadratic term in the expansion of the energy of the poorly compressible center in powers of its volume, for the two states participating in the optical transition:

$$E_1=E_1^0+\frac{k_1(P)}{2}[V-V_1^0(P)]^2+VP,$$

$$\tag{27}$$

$$E_2=E_2^0+\frac{k_2}{2}[V-V_2^0(P)]^2+VP,$$

where E_1^0 and E_2^0 are the changes in energy of the atom in states 1 and 2 when it is put into helium. By minimizing the energy and neglecting the terms quadratic in the pressure and the pressure dependence of all the parameters (since the experimental curves are, to good accuracy, linear in P), we can write the energies of the absorbed (transition $1\to2$) and emitted (transition $2\to1$) photons,

$$h\nu_{abs}\equiv\Delta E_{12}=E_2|_{V=V_1(P)}-E_1(P),$$

$$h\nu_{em}\equiv\Delta E_{21}=E_2(P)-E_1|_{V=V_2(P)}$$

in the form

$$\Delta E_{12} = \Delta E_{12}^0 + \frac{k_2}{2}(V_2^0 - V_1^0)^2 + \frac{k_2}{k_1}(V_2^0 - V_1^0)P,$$

$$\Delta E_{21} = \Delta E_{12}^0 - \frac{k_1}{2}(V_2^0 - V_1^0)^2 + \frac{k_1}{k_2}(V_2^0 - V_1^0)P,$$

where $\Delta E_{12}^0 = E_2^0 - E_1^0$ is the difference of the transition energy for the equilibrium state of the system relative the vacuum, and $V_i^0 \equiv V_i^0(0)$, $k_i \equiv k_i(0)$. Writing the experimental dependences in the form

$$\Delta E_{12}^{obs} = a_{12} + b_{12}P, \quad \Delta E_{21}^{obs} = a_{21} + b_{21}P, \tag{28}$$

we can use Eqs. (27) to relate the experimentally observable quantities with the characteristics of the system:

$$|V_2^0 - V_1^0| = \sqrt{b_{12}b_{21}}, \quad \frac{k_2(0)}{k_1(0)} = \sqrt{b_{12}/b_{21}},$$

$$k_1(0) = \frac{2(a_{12} - a_{21})}{(\sqrt{b_{12}} + \sqrt{b_{21}})b_{12}\sqrt{b_{21}}}, \tag{29}$$

$$\Delta E_{12}^0 = \frac{a_{12}\sqrt{b_{21}} + a_{21}\sqrt{b_{12}}}{\sqrt{b_{12}} + \sqrt{b_{21}}}.$$

Analysis of expressions (29) shows that the shift of the absorption and emission frequencies with increasing pressure is always toward the blue if the volume of the excited system is greater than that of the unexcited system, $V_2^0 > V_1^0$, and toward the red in the contrary case. If the system has a greater stiffness in the excited state than in the ground state ($k_2 > k_1$), then the pressure dependence of the absorption frequency has a larger slope than does the emission frequency ($b_{12} > b_{21}$), and vice versa. Finally, if for $P = 0$ the absorption and emission frequencies are blue-shifted relative to the transition frequency in vacuum, then the energy of the optical adiabatic transition ΔE_{12} is greater than in the vacuum, while if both frequencies are red-shifted, then ΔE_{12} is lower than in the vacuum.

This last statement is extremely important, since upon excitation of an atom both its polarizability and its size usually increase simultaneously. Therefore the depth of the potential well is determined by the competition of these two antagonistic factors, and the sign of the change of energy of the adiabatic transition in a medium is not obvious.

Our analysis of the available experimental data did not reveal any inconsistencies with our proposed treatment. Moreover, when for the Cs atom the experimental values characterizing the dependence of the transition frequency shifts on the external pressure from Ref. 12 are put into (29), the resulting values of the parameters are close to those calculated by those same authors using a complicated quantum-mechanical modeling: $\Delta E_0 = 90$ cm^{-1}, $\Delta V = 1400$ Å^3 (Ref. 12), and $E_0 = 110$ cm^{-1}, $\Delta V = 1000$ Å^3, respectively. In addition, the stiffness of Cs in the ground state is close to the value that we calculated here.

For shells surrounding atoms that interact strongly with helium the simple method of analysis proposed here [relations (28) and (29)] can still be applied, provided that the observed frequency shifts under external pressure are comparable to the shift arising when the atoms are immersed in

liquid helium at $P = 0$ and that they are linear in P. Here the noticeable overestimate of the volumes calculated from the frequency shifts as compared to the known van der Waals volumes of the atoms can serve as proof of the formation of a stiff helium shell around the impurity.

As we have said, the energy difference between helium clusters containing different numbers of helium atoms and therefore having different sizes is extremely small for Cs atoms. This means that at the typical experimental temperatures, 1.3–1.7 K, there is appreciable inhomogeneous broadening of the spectral lines. In addition, there is also a large homogeneous broadening due to the exchange of helium atoms between the shell and the next layer. Each type of broadening should have a specific and strong dependence on temperature.

The most important conclusion of a general nature is that when atoms are isolated by condensed (liquid or solid) helium, one would never expect to see very narrow spectral lines, even if the transition involves a change in the state of an inner electron and/or is a forbidden transition. Therein lies the main difference of a helium matrix from the formally less inert matrices of heavy rare gases (Rg), where there are no broadening mechanisms due to exchange between the atoms of the matrix or to the presence of a rotational structure, and the Im–Rg vibrations have frequencies which are too high to be manifested in the optical spectra.

For this reason, in our experiments[40,41] with an impurity–helium phase containing nitrogen atoms in the ^4S ground and ^2D metastable states, we did not observe absorption at the $^4S - ^2D$ transition nor emission from N(^2D) atoms in the absence of a heavy neighbor in a single helium shell. From this we can estimate the width of the 0–0 transition as $\Delta\nu > 10^{-1}$ cm^{-1}. We are also inclined to regard the specific two-humped shape of the experimentally observed emission spectrum of metastable atoms N(^2D) (the $^2D - ^4S$ transition) immobilized in an impurity–helium phase[40,41] (see Fig. 22) to be a manifestation of these features. Indeed, as can be seen in Fig. 12, near $n = n^*$ the energy difference between states adjacent in n is always less than in the case when n is far from n^*. This feature, of course, exists not only for the ground state but also for the excited electronic state. In the
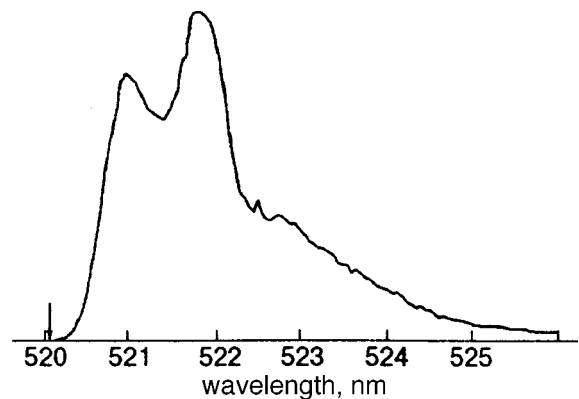

FIG. 22. Experimental emission spectrum of the $^2D - ^4S$ transition of nitrogen atoms stabilized in solidified helium. The arrow indicates the position of the line of the transition N($^2D - ^4S$) in vacuum.

general case the optimum values of n^* are different for the helium shell of an atom in the ground state (n_g^*) and excited state (n_e^*). Therefore, when the conservation of the value of n in optical transitions, which is a consequence of the Franck–Condon principle, is taken into account in the case of ImHe$_n$ clusters immersed in liquid helium, one would expect that there should be two transitions in the spectrum (from the the lowest-energy states n_e^* and n_e^*+1 or $n_e^* -1$), the difference in the energies of which is mainly due to the different positions of the levels of the system with $n_g = n_e^*$, n_e^*+1, n_e^*-1. Thus it is only in the case of coincidence $n_e^*=n_g^*$ that one would expect the presence of a narrow line of the 0–0 transition in the optical spectra; otherwise, even for atoms that interact strongly with helium, all the spectral transitions acquire significant broadening on account of the coupling of the excited states of the He shell with the medium.

A particular case is that of molecules immersed in liquid helium. Here the good quantum numbers are those which describe the molecule itself, while the influence of the medium can mainly affect the shape of the individual rotational components.[2] Two types of effects can be observed here. The first of these is due to rotation of the tightly bound helium shell together with the molecule and should be manifested in a decrease of the corresponding rotational constant. The second is due to the direct coupling of the vibrations which alter the geometry of the molecule, with excitations in the bulk of the surrounding liquid helium. These vibrations are so powerful that they can interact not only with phonons but also with rotons and maxons. Both of these effects have been observed experimentally.[37,38]

MAGNETIC RESONANCE SPECTRA

The most interesting feature of the magnetic resonance spectra of alkali-metal atoms implanted in solid helium and observed by the optical pumping method,[31,42] in our view, is the long relaxation times T_1 and T_2, which attest to a weak perturbation of the magnetic moments by the matrix. It is particularly noteworthy that the pressure-induced transition of solid helium from the hcp to the fcc phase causes an abrupt increase in T_1 and T_2 by more than two orders of magnitude, while only small changes occur in the hyperfine splitting and g factor. The authors of Ref. 42 attribute this surprising effect to the higher isotropicity of the fcc phase.

It must be kept in mind, however, that the helium shell around a Cs atom, for example, has an outer diameter of more than 18 Å and is substantially bigger than the lattice constant of solid helium. Therefore, since the occupation of the first shell is determined by the close-packing condition on a sphere and there is appreciable exchange between the helium atoms belonging to the shell and the atoms of the adjacent layer, it is hard to believe that the order in this adjacent layer would be the same as in the bulk of solid helium. At the same time, it is these first two layers closest to the impurity atom that determine the values of the relaxation times. It therefore seems to us that the effect obtained in Ref. 42 is more likely described by the following treatment. As we have said, for the Cs atom the shell is always (and more
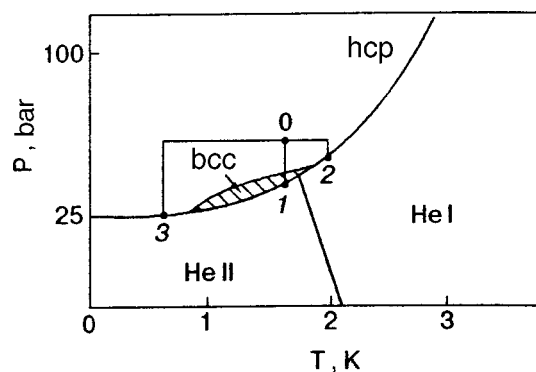

FIG. 23. Phase diagram of ^{4}He. The point 0 corresponds to the conditions of growth of the solid sample, point *1* to the conditions of observation of magnetic resonance in the bcc phase,[42] and Figs. *2* and *3* to conditions proposed in the present paper.

so at high pressures) found in a delocalized liquid state, which lends it a high isotropicity. The layer of helium atoms adjacent to the shell is subject to homogenizing van der Waals and exchange interactions with the shell, and it therefore "melts" a little earlier than the helium in the bulk. In other words, we are inclined to view the cause of the effect in question not as a phase transition of solid helium but in the proximity of the system to the melting curve (in the experiments described in Ref. 42 the distance along the pressure axis to the melting point (see Fig. 23) was only about 0.2 bar). This hypothesis can be checked experimentally; as can be seen from Fig. 23, it is sufficient to move along path *2* or, better, *3*, skirting the bcc phase.

While quite long, the times T_1 and T_2 are nevertheless bounded from above by processes of transition of the helium atoms from the shell into the adjacent layer: T_2 by the quantum-mechanical exchange, and T_1 by the temperature-dependent process of changing the number of helium atoms in the shell.

PHASE TRANSITIONS IN THE SHELL

The regular distribution of helium atoms in the shell makes it possible to treat it as a unified ensemble. In this ensemble two types of phase transitions can, in principle, occur: a transition from the delocalized to the localized state, which is analogous to a liquid–solid transition in the three-dimensional case, and an abrupt change in the number of He atoms in the shell, accompanied by a coherent restructuring of the entire ensemble.

The number of helium atoms in the shell (12–60) is large enough that the phase transition, if there is one, will be quite pronounced, while small enough that the discreteness of the number of particle participating in it will be clearly manifested. It is the smallness of the ensemble and the fact that the radius of the shell is comparable to an interatomic distance that make the effects in question fundamentally different from the now actively studied[43,44] phase transitions in two-dimensional helium ensembles.

For the case of alkali-metal atoms, when the shell has the structure with repulsion, only transitions involving a change in the coordination number n can occur. In view of
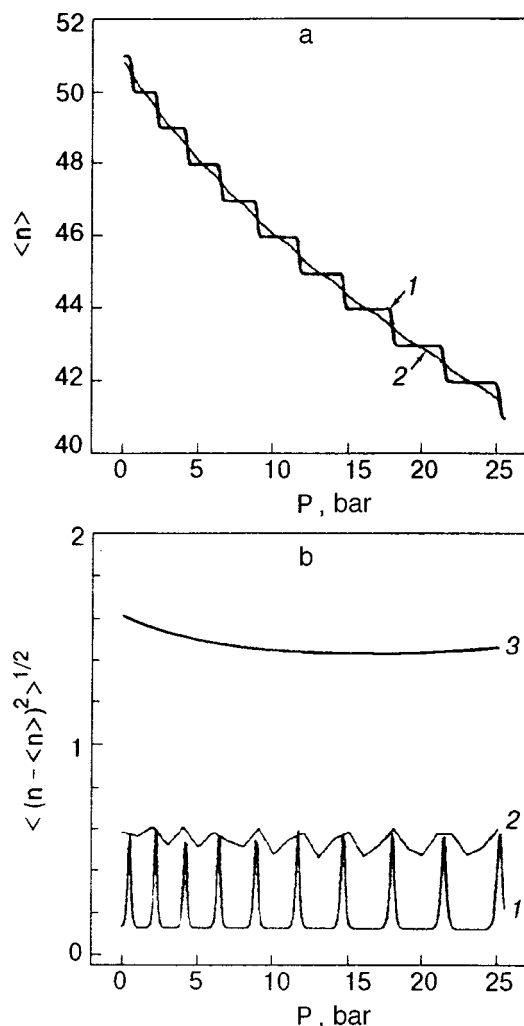
FIG. 24. Effect of pressure on the mean (a) and variance (b) of the number of atoms in the helium shell surrounding a Cs atom in liquid helium at different temperatures T, K: 0.01 (*1*), 0.1 (*2*), and 1 (*3*).

the small energy difference between states with different n, only at temperatures of the order of 10 mK can one expect a predominant occupation of one of the states (see Fig. 24). In addition, the intensity of the exchange of atoms between the shell and the surroundings fundamentally ''smears'' the difference between the different states of the shell. Such phase transitions can occur for Im^3He_n clusters suspended in liquid helium ^4He. Since alkali-metal atoms should draw ^3He atoms toward them from the bulk of the liquid helium, such objects can be created experimentally.

For atoms around which a structure with attraction forms, on the contrary, a transition of the liquid–solid type should be more the rule than the exception: as the external pressure increases, localization of the helium atoms in the shell should be occur considerably sooner than the solidification of helium in the bulk. As regards the transitions involving a change in the number of atoms in the shell, the atoms studied in this paper are not very good choices: the interaction of N and Xe with helium is too strong, and the transition $n \rightarrow n-1$ occurs at very high pressures (see Fig. 16). Therefore, a special analysis must be undertaken in order to choose a suitable system for observing this effect.

It should be stressed that the calculations reported here cannot in any way serve as a quantitative basis for predicting the characteristics of phase transitions or even to prove their existence in any particular case. It is sufficient to recall that we have always proceeded from the assumption that any number of atoms can be uniformly close-packed on a sphere; in other words, we have neglected the ''magic number'' effect and the deviation of the shape of the shell from spherical. Our goal was only to show that phase transitions can in principle occur and to elucidate which systems are most promising for carrying out the corresponding experiments. In this connection it is of interest to analyze how the coherent changes in the structure of the helium shells surrounding impurity centers might be manifested in experiment.

First, such transitions should be visible on the curves of the external pressure dependence of the characteristics of the optical spectra of impurity atoms. As experiments show, the spectra are transformed substantially as the pressure is changed from 0 to 25 bar, and here the shift of the spectral line is sensitive to both the radius of the shell and the number of helium atoms in it. For the typical example of europium atoms[33] the maximum ratio of the width of the 0–0 transition to its frequency shift is around 2%. This means that a ''step'' of height 0.1 cm^{-1} on the curve of the pressure dependence of the frequency shift of the line would be fully detectable, and estimates show that the size of the step would be at least an order of magnitude larger than that. The phase transitions should also affect the line shape of the spectral bands.

The relaxation times in the magnetic resonance of paramagnetic atoms are sensitive mainly to the homogeneity of the environment, i.e., to the degree of localization of the atoms in the shell and the deviations of the shape of the latter from spherical; therefore transitions of the liquid–solid type, at least, should be reflected in the ESR spectra.

IMPURITY–HELIUM PHASE

The strongest effects due to localization of helium atoms around impurities should be expected for an impurity–helium solid phase, which owes its very existence to this localization[6] and which consists entirely of localized helium shells. For this case one should be able to reliably observe not only the effects discussed above, but also such specific properties of localized shells as the specific heat, thermal conductivity, and magnetic nuclear polarizability of ^3He at low temperatures,[45,46] which would be manifested as macroscopic properties of the whole sample. Experimentally an impurity–helium solid phase has been obtained for impurity particles such as nitrogen atoms and molecules and for atoms of heavy inert gases—neon, argon, krypton, and xenon. The analysis in the present paper confirms the high stability of the helium shells around these particles and an appreciable increase in the degree of localization of the atoms making them up. However, the possibility of stabilizing conglomerated shells requires a special analysis which we are preparing to do in the near future. Of particular interest is the question of whether an impurity–helium phase can exist in ^3He. As the analysis presented in this paper shows, the shells surrounding atoms that interact weakly with helium are even

more stable in ^{3}He than in ^{4}He, and metastability with respect to the formation of metallic clusters may be provided by the application of high magnetic fields.

The idea of this paper came up as a result of fruitful discussions of the problem with specialists active in the field—J. P. Toennies and A. F. Vilesov (Göttingen), S. I. Kanorsky and A. Weis (Bonn), M. Takami and Q. Hui (Tokyo), T. Yabuzaki (Kyoto), G. Scoles (Princeton), and G. zu Putlitz (Heidelberg). This study was supported by the Russian Fund for Fundamental Research, Grants Nos. 98-03-32283 and 99-03-33261.

occupied by the Na atom; this is comparable to the volume, 1100 Å^3, of a sphere having a radius equal to the equilibrium distance for the Na–He pair potential.

----

[1])For example, for an electron in a $1s$ state the introduction of a positively charged core of an alkali metal atom causes the pair interaction of the neutral system with the He atom to decrease, while in the case of a $1p$ state it increases.[7] The situation is different in the case of excited states of the atom near the dissociation limit; these are populated in photoabsorption processes. For them the ''free'' state of the electron, i.e., an electron confined within the volume of a ''bubble,'' is a reasonable zeroth approximation, and because of the strong perturbation of weakly bound and very delocalized states of an optical electron the solution of the problem of the perturbation of an electron ''bubble'' by a positively charged atomic core is quite justified.

[2])In this regard neutral atoms are fundamentally different from ions, for which the interaction with helium is of a polarizational character and decays much more slowly with distance ($\propto R^{-4}$).

[3])A direct estimate of the pressure inside the helium shell on the basis of the forces of repulsion between helium atoms is difficult to make because of the indeterminacy of the thickness of the shell.

[4])For incompletely symmetric modes of the shell the harmonic approximation holds better, since for them there are antiphase radial motions of the He atoms. Therefore the potential energy increases without bound for both positive and negative displacements of the normal coordinate from the equilibrium position. For completely symmetric modes, taking the anharmonicity into account in the approximation of the potential curve by a Morse potential leads only to a small correction, viz., to the zero-point energy $\omega_0(n)/16|E(R^*,n)|$, since their frequency $\omega_0(n)$ is much less than the potential well depth $|E(R^*,n)|$.

[5])Strictly speaking, one would not expect exact agreement in view of the different statistics of the two quantum liquids, which is not explicitly included in the model.

[6])Interestingly, for XeHe$_n$ clusters of optimum composition the delocalization parameters, while being close to those calculated by the density-functional method (see Table III), have about the same value ($a \cong b$) and are close to the delocalization parameter of liquid helium.

[7])The presence of bends has now been observed on the curve of the fall in the density of helium near its free surface.[11,15] In addition, there are oscillatory deviations of the binding energy of the helium atom in large clusters from the energy calculated for the model of a homogeneous droplet.

[8])In particular, for the binding energy of a Xe atom with liquid helium it gives a value of 490 K, as compared to the value 313 K obtained by the density-functional method.[9]

[9])Thus a more correct assessment of the properties of He in the shell can be made only from the character of the change of its delocalization, which reflects the shape and height of the first peak of the radial distribution function.

[10])A similar conclusion can be reached on the basis of the results of a density-functional calculation for Na in liquid helium,[9] according to which the chemical potential of Na in liquid helium increases by 25 K as the pressure is raised from 0 to 5 atm. If this is interpreted as a change in energy due solely to the PV term, we obtain 700 Å^3 for the volume

[1]B. Tabbert, H. Gunther, and G. zu Putlitz, J. Low Temp. Phys. **103**, 653 (1997).

[2]J. P. Toennies and A. F. Vilesov, Annu. Rev. Phys. Chem. **49**, 1 (1998).

[3]S. I. Kanorsky and A. Weis, Adv. At., Mol., Opt. Phys. **38**, 87 (1997).

[4]J. P. Hernández, Rev. Mod. Phys. **63**, 675 (1991).

[5]P. B. Lerner, M. B. Chadwick, and I. M. Sokolov, J. Low Temp. Phys. **90**, 319 (1993).

[6]E. B. Gordon, A. A. Pel'menev, E. A. Popov, O. F. Pugachev, V. V. Khmelenko, and A. F. Shestakov, Fiz. Nizk. Temp. **18**, 1365 (1992) [J. Low Temp. Phys. **18**, 952 (1992)].

[7]S. Bililign, M. Gutowski, J. Simons, and W. H. Breckenridge, J. Chem. Phys. **100**, 8212 (1994).

[8]G. DeToffol, F. Ancilotto, and F. Toigo, J. Low Temp. Phys. **102**, 381 (1996).

[9]F. Dalfovo, Z. Phys. D **39**, 61 (1994).

[10]S. Stringari and J. Treiner, J. Chem. Phys. **87**, 5021 (1987).

[11]F. Dalfovo, A. Lastri, L. Pricaupenko, S. Stringari, and J. Treiner, Phys. Rev. B **52**, 1193 (1995).

[12]T. Kinoshita, K. Fukuda, Y. Takahashi, and T. Yabuzaki, Phys. Rev. A **52**, 2707 (1995).

[13]S. I. Kanorsky, S. Lang, T. Eichler, K. Winkler, and A. Weis, Phys. Rev. Lett. **81**, 401 (1998).

[14]E. Cheng, M. W. Cole, W. F. Saam, and J. Treiner, Phys. Rev. Lett. **67**, 1007 (1991).

[15]M. A. McMahon, R. N. Barnett, and K. B. Whaley, J. Chem. Phys. **104**, 5080 (1996).

[16]J. Dehmer and L. Wharton, J. Chem. Phys. **57**, 4821 (1972).

[17]R. Cambi, D. Cappelletti, G. Liuti, and E. Pirani, J. Chem. Phys. **95**, 1852 (1991).

[18]S. H. Patil, J. Chem. Phys. **94**, 8089 (1991).

[19]D. S. Greywall, Phys. Rev. B **27**, 27247 (1983).

[20]R. De Bruyn Ouboter and C. N. Yang, Physica B **44**, 127 (1987).

[21]J. A. Hodgdon and F. H. Stillinger, J. Chem. Phys. **102**, 457 (1995).

[22]A. M. Duygaev, J. Low Temp. Phys. **78**, 79 (1990).

[23]V. R. Pandharipande, J. G. Zabolitzky, S. C. Pieper, R. L. Wiringa, and U. Helmbrecht, Phys. Rev. Lett. **50**, 1676 (1993).

[24]A. R. Janzen and R. A. Aziz, J. Chem. Phys. **103**, 9626 (1995).

[25]Q. N. Usmani, S. Fanton, and V. R. Pandharipande, Phys. Rev. B **26**, 6123 (1982).

[26]J. Dupont-Roc, M. Himbert, M. Pavloff, and J. Treiner, J. Low Temp. Phys. **81**, 131 (1990).

[27]T. Kinoshita, K. Fukuda, and T. Yabuzaki, Phys. Rev. B **54**, 6600 (1996).

[28]M. Keil, L. J. Danielson, U. Buck, J. Schleusener, F. Huisken, and T. W. Dingle, J. Chem. Phys. **89**, 2866 (1988).

[29]V. Aquilanti, R. Candori, and F. Pirani, J. Chem. Phys. **89**, 6157 (1988).

[30]V. Aquilanti, E. Luzzatti, F. Pirani, and G. G. Volpi, J. Chem. Phys. **89**, 6165 (1988).

[31]S. Grebenev, J. P. Toennies, and A. F. Vilesov, Science **279**, 2083 (1989).

[32]F. Ancilotto, E. Cheng, M. W. Cole, and F. Toigo, Z. Phys. D **29**, 61 (1994).

[33]A. Bartelt, J. D. Close, F. Federmann, K. Hoffmann, N. Qaas, and J. P. Toennies, Z. Phys. D**39**, 1 (1997).

[34]K. Ishikawa, A. Katakeyama, K. Gosyono-o, S. Wada, Y. Takahashi, and T. Yabuzaki, Phys. Rev. B **56**, 780 (1997).

[35]M. Hartmann, R. E. Miller, J. P. Toennies, and A. F. Vilesov, Science **272**, 1631 (1996).

[36]D. Blume, M. Lewerenz, F. Huisken, and M. Kaloudis, J. Chem. Phys. **105**, 8666 (1996).

[37]M. Hartmann, F. Mielke, J. P. Toennies, and A. F. Vilesov, Phys. Rev. Lett. **76**, 4560 (1996).

[38]J. Higgins, C. Callegari, J. Reho, F. Stienkemeier, M. Gutowski, W. E. Ernst, and G. Scoles, J. Phys. Chem. A **102**, 4952 (1998).

[39]E. B. Gordon and O. S. Rzhevskiĭ, Opt. Spektrosk. **78**, 360 (1995) [Opt. Spectrosc. **78**, 320 (1995)].

[40]R. E. Boltnev, E. B. Gordon, V. V. Khmelenko, N. Krushinsaya, M. V. Martynenko, A. A. Pelmenev, E. A. Popov, and A. F. Shestakov, Chem. Phys. **189**, 367 (1994).

[41] R. E. Boltnev, E. B. Gordon, V. V. Khmelenko, M. V. Martyneno, A. A. Pelmenev, E. A. Popov, and A. F. Shestakov, J. Chem. Phys. **92**, 362 (1994).

[42] S. Lang, M. Arndt, T. W. Hansch, S. I. Kanorsky, S. Lucke, S. B. Ross, and A. Weis, J. Low Temp. Phys. **22**, 1292 (1996).

[43] D. S. Greywall, Physica B **197**, 1 (1994).

[44] K. Ishida, M. Morishita, K. Yawata, and H. Fukuyama, Phys. Rev. Lett. **79**, 3451 (1997).

[45] M. Castaing and P. Nozieres, J. Phys. (France) **40**, 257 (1979).

[46] M. Chapellier, G. Frossati, and F. B. Rasmusssen, Phys. Rev. Lett. **57**, 1231 (1979).

Translated by Steve Torstveit

LOW-TEMPERATURE MAGNETISM

Influence of Mn concentration on the physical phenomena in the semimagnetic semiconductor Hg$_{1-x-y}$Cr$_x$Mn$_y$Se

V. D. Prozorovskiĭ,* I. Yu. Reshidova, and A. I. Puzynya

*A. A. Galkin Donetsk Physicomechanical Institute, National Academy of Sciences of Ukraine,
72 R. Luxemburg St., 340114 Donetsk, Ukraine*

Yu. S. Paranchich

Yu. Fed'kovich Chernivtsi State University, 2 Kotsyubinsky 2, 274012 Chernovtsy, Ukraine

Results are presented from a study of the magnetic susceptibility and electron spin resonance (ESR) on Cr^{3+} and Mn^{2+} ions in a series of samples of the semimagnetic semiconductor Hg$_{1-x-y}$Cr$_x$Mn$_y$Se with $x=0.02$ and $0.01 \leqslant y \leqslant 0.08$. The experimental results show that the structure of the ESR spectrum and the character of its shift with respect to magnetic field as the temperature changes depend on the ratio of the concentrations of chromium and manganese ions, which form two interacting substructures. The observed transition of Hg$_{1-x-y}$Cr$_x$Mn$_y$Se to a spin glass phase is not related to the distortion of the symmetry of the crystal lattice. The shared and distinctive properties of the systems Hg$_{1-x}$Cr$_x$Se and Hg$_{1-x-y}$Cr$_x$Mn$_y$Se are determined. © *2000 American Institute of Physics.*
[S1063-777X(00)00201-2]

Among the representatives of the semimagnetic semiconductor (SMSC) class, the broadest spectrum of new physical effects have been observed experimentally in the solid solutions Hg$_{1-x}$Cr$_x$Se (Refs. 1–3). For example, at liquid-nitrogen temperatures the the Landau energy levels in Hg$_{1-x}$Cr$_x$Se can exhibit a rather large spin splitting, induced by $sp-d$ exchange,[2] and at certain values of the composition x and temperature T a phase transition to a spin glass phase occurs in this system. This makes Hg$_{1-x}$Cr$_x$Se a promising material for the creation of infrared sources and detectors that can be tuned by a magnetic field over a wide spectral range, modulators, magnetometers for measuring magnetic fields of the order of megaoerstads, and other devices capable of operating at liquid-nitrogen temperatures. This has enormous practical significance, since similar devices made from Hg$_{1-x}$Mn$_x$Te, Hg$_{1-x-y}$Cd$_x$Mn$_y$Te, and Hg$_{1-x}$Mn$_x$Se operate at liquid-helium temperatures. In this respect the Hg$_{1-x}$Cr$_x$Se system has some advantages over the known narrow-gap SMSCs.

According to Ref. 4, the admixture of Mn atoms to Hg$_{1-x}$Cr$_x$Se in concentrations small compared to that of the Cr atoms improves the magnetic and electrophysical characteristics substantially and changes the defect structure of Hg$_{1-x}$Cr$_x$Se. We have not been able to observe the electron spin resonance (ESR) spectrum of Mn^{2+} ions in the quaternary system Hg$_{1-x-y}$Cr$_x$Mn$_y$Se at manganese concentrations N_{Mn} much smaller than the chromium atom concentration N_{Cr}, and no studies of this system have been done for $N_{Cr} \leqslant N_{Mn}$. It is therefore of interest to investigate a series of Hg$_{1-x-y}$Cr$_x$Mn$_y$Se samples with different concentrations of manganese atoms at a fixed concentration of chromium atoms.

To establish the influence of the manganese concentration on certain physical properties of Hg$_{1-x-y}$Cr$_x$Mn$_y$Se, we have carried out a comprehensive investigation of ESR and the magnetic susceptibility χ in a series of samples of this material.

ELECTRON SPIN RESONANCE

According to Refs. 1, 3, and 5, the ESR spectrum of Cr^{3+} ions in Hg$_{1-x}$Cr$_x$Se has been observed and studied at temperatures ranging from liquid-helium to room temperature, and the characteristic shape of the spectrum was found to depend on N_{Cr} and T. ESR and magnetic susceptibility studies have established that when the crystal is cooled below a certain temperature T_f the cubic symmetry of the lattice begins to break down, and at a certain temperature $T_g < T_f$ a phenomenon occurs which we have interpreted as a transition of Hg$_{1-x}$Cr$_x$Se to a spin glass phase. In Ref. 4 it was shown experimentally that at equal concentrations of chromium atoms in the systems Hg$_{1-x-y}$Cr$_x$Mn$_y$Se and Hg$_{1-x}$Cr$_x$Se, their physical characteristics are qualitatively similar and differ mainly in a quantitative sense.

The ESR spectrum was studied on a radio spectrometer with a working frequency of 36.04 GHz. During the measurements the temperature of the samples was stabilized and measured to an accuracy of ± 0.1 K by means of an electronic device.[6]
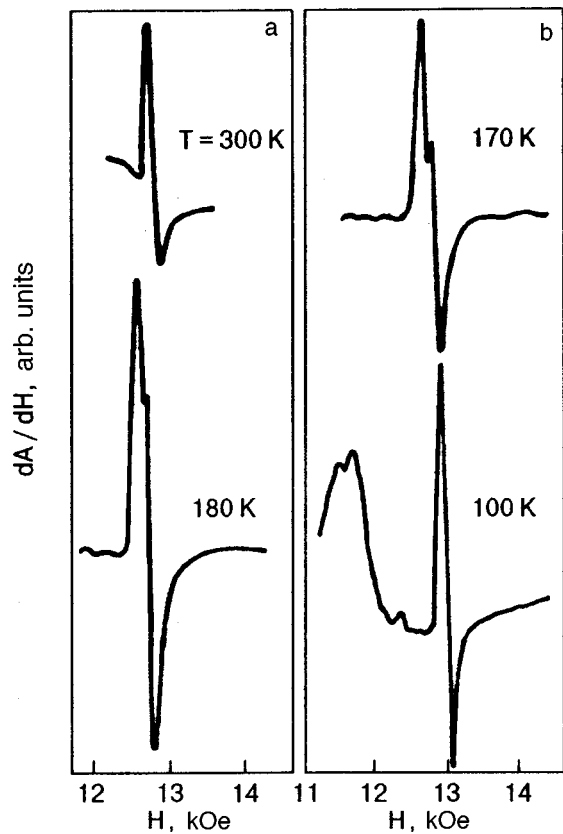
FIG. 1. Change in the structure of the ESR spectrum as the temperature is lowered in a $Hg_{1-x-y}Cr_xMn_ySe$ sample with $x=0.02$ and $y=0.01$ (in part b the gain was a factor of 2 lower than in part a).
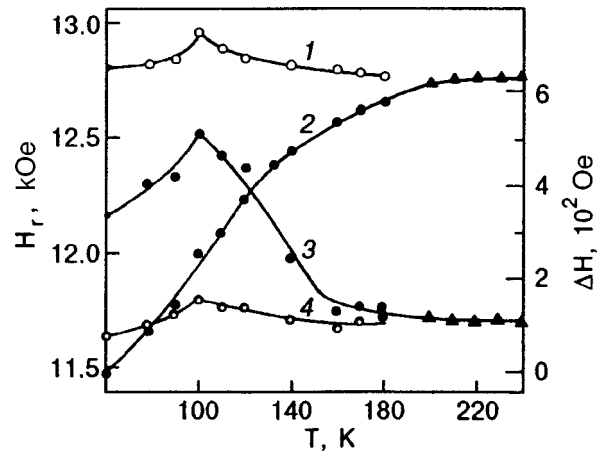

FIG. 2. Temperature dependence of the resonant magnetic field H_r (*1,2*) and the linewidth ΔH (*3,4*) of the absorption lines observed on Cr^{3+} (●) (the transition $-1/2 \leftrightarrow 1/2$) and Mn^{2+} (○) at $T \leqslant 180$ K and the unresolved absorption spectrum (▲) for $T > 180$ K in a $Hg_{1-x-y}Cr_xMn_ySe$ sample with $x=0.02$ and $y=0.01$.

susceptibility and studied its variation with temperature. The measurements of χ were made by an induction method on an apparatus consisting of a modified differential magnetometer with modulation by a low-frequency field.[7] The apparatus was calibrated using a superconducting lead replica of the sample to be studied. The amplitude and frequency of the alternating magnetic field inducing the emf in the measuring coils of the apparatus could be varied smoothly over the intervals 0–5 Oe and 60–1100 Hz, respectively.

The results of the $\chi(T)$ measurements are shown in Figs. 3 and 4. Figure 3 shows the temperature dependence of χ measured for the sample with $y=0.01$ at frequencies of 63
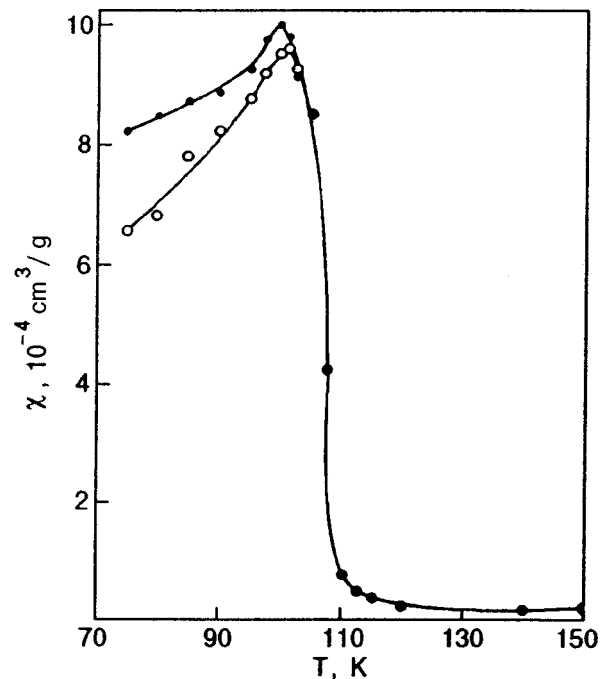
Samples of $Hg_{1-x-y}Cr_xMn_ySe$ with $x=0.02$ and $y=0.01$, 0.02, 0.04, 0.06, and 0.08 were investigated in the temperature interval 58–300 K. In this entire interval the character of the temperature dependence of the observed ESR spectrum was found to depend on x and y. Figure 1 shows the dynamics of the change in the ESR spectrum with temperature for the sample with $y=0.01$. As the sample was cooled to 180 K the spectrum consisted of a single isotropic line. At $T=180$ K the line begins to split into two lines, one of which is axially anisotropic and the other isotropic. As the temperature is lowered further, a fine structure appears against the background of the anisotropic line, the distance between the lines of the fine structure increases, and the whole anisotropic spectrum is shifted strongly to lower fields, as can be seen in Fig. 2 (curve *2*). Figure 2 shows the temperature dependences of the resonant magnetic field H_r and the linewidths ΔH of these absorption lines. Curves *2* and *3* show H_r and ΔH for the central absorption line of the anisotropic spectrum, while curves *1* and *4* are the analogous curves for the isotropic spectrum. For samples with $y \geqslant 0.02$ a single isotropic line is observed over the entire range of temperatures investigated, and the resonant field for this line is independent of T within the experimental error.

MAGNETIC SUSCEPTIBILITY

In the same samples of $Hg_{1-x-y}Cr_xMn_ySe$ on which the ESR spectrum was investigated, we measured the magnetic

FIG. 3. Temperature dependence of the magnetic susceptibility of $Hg_{0.97}Cr_{0.02}Mn_{0.01}Se$, measured at frequencies of 63 Hz (●) and 330 Hz (○).

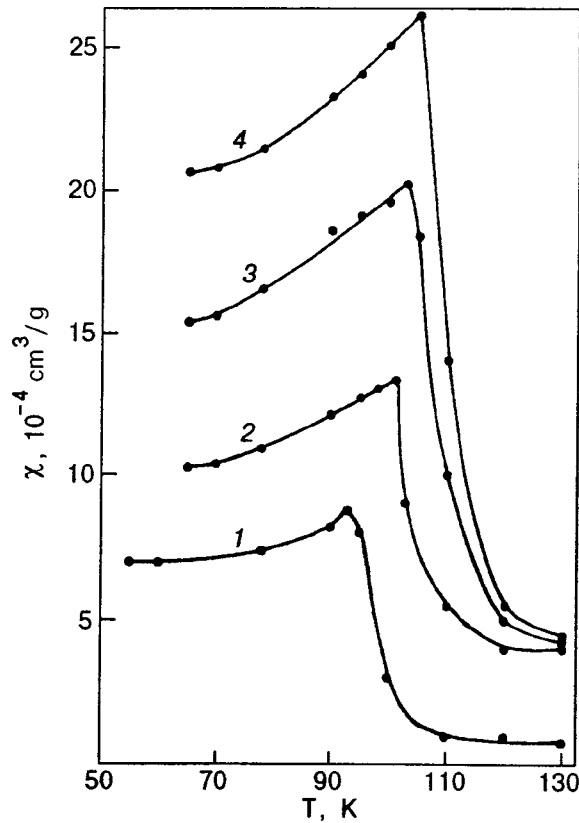FIG. 4. Temperature dependence of the magnetic susceptibility of a $Hg_{1-x}Cr_xSe$ sample with $x=0.02$ (*1*) and of $Hg_{1-x-y}Cr_xMn_ySe$ samples with $x=0.02$ for different values of y: 0.04 (*2*), 0.06 (*3*), 0.08 (*4*).

and 330 Hz. It is seen that as the frequency increases, the extremum of $\chi(T)$ shifts to higher temperatures. Similar behavior of $\chi(T)$ with increasing frequency was also observed for the samples with $y \geq 0.02$. The $\chi(T)$ curves for these samples are shown by curves *2–4* in Fig. 4. Also shown in that figure for comparison is the $\chi(T)$ curve for $Hg_{1-x}Cr_xSe$ with $x=0.02$ (curve *1*). A comparison of curves *2–4* with curve *1* shows that these materials differ in having substantially different absolute values of χ in the temperature region around and below the maximum of the $\chi(T)$ curve and also in the values of the temperatures at which the maximum of the magnetic susceptibility occurs, while the character of the change of the $\chi(T)$ curve remains the same. These experimental observations and the shift of the extremum of $\chi(T)$ to higher temperatures as the measurement frequency increases attest to the presence of a transition to a spin glass phase in the $Hg_{1-x-y}Cr_xMn_ySe$ system at the temperature $T=T_g$ where $\chi(T)$ reaches its maximum value.[3–5,8,9]

DISCUSSION AND CONCLUSIONS

A comparative analysis of the experimental results for the $Hg_{1-x-y}Cr_xMn_ySe$ sample with $y-0.01$ and the data of Ref. 3 suggests that the ESR spectrum of this sample at $T > 180$ K consists of two unresolved spectra of the ions Cr^{3+} and Mn^{2+}, a situation which arises because the g factors of Cr^{3+} and Mn^{2+} in this cubic crystal are close in value, and the linewidths are comparatively large. At $T=180$ K these spectra are resolved. As the temperature is lowered further,

the anisotropic spectrum is shifted to lower magnetic fields, and at a certain temperature a fine structure of the spectrum begins to appear. According to Ref. 3, this spectrum is due to the Cr^{3+} ions. The isotropic spectrum, which has a monotonic and less pronounced temperature dependence than does the spectrum of Cr^{3+} (Fig. 2), is attributed by the authors to the Mn^{2+} ion. These results and the data obtained from ESR studies for samples with $y \geq 0.02$, along with the analogous results of Ref. 4, are evidence that when the concentration N_{Cr} in $Hg_{1-x-y}Cr_xMn_ySe$ is much larger than N_{Mn}, or when N_{Cr} and N_{Mn} are of the same order of magnitude but $N_{Mn} \geq N_{Cr}$, the spectra of the Cr^{3+} and Mn^{2+} ions are not resolved. In this case the structure and temperature dependence of the whole spectrum is determined by those ions having the higher concentration. If $N_{Mn} < N_{Cr}$ (e.g., in the sample with $y=0.01$), then at a certain temperature the spectrum is resolved into the two spectra of the Cr^{3+} and Mn^{2+} ions, and these spectra differ in their structure and in the character of their temperature dependence (Figs. 1 and 2). This behavior of the spectra can be explained as follows. According to Ref. 3, in the ternary system $Hg_{1-x}Cr_xSe$ at $T \leq T_f$ a displacement of the Cr^{3+} ions along the axial axis of the crystal occurs as the temperature is lowered. This displacement induces a shift of the spectra of these ions with respect to the magnetic field. One expects that analogous displacements of the Cr^{3+} ions occurs in the system $Hg_{1-x-y}Cr_xMn_ySe$ as well, and this is confirmed by the results of Ref. 4 and the present study. It follows that under certain conditions, which will be set forth below, an analogous displacement of the Cr^{3+} ions can occur in the $Hg_{1-x-y}Cr_xMn_ySe$ system and will induce a shift of the spectrum. The indicated experimental results show that for $Hg_{1-x-y}Cr_xMn_ySe$ the character of the shift of the spectrum with respect to the magnetic field as the temperature decreases depends on the relative values of the concentrations of chromium and manganese atoms. For example, for $N_{Cr} \gg N_{Mn}$ the spectrum shifts but does not split, while for $N_{Cr} > N_{Mn}$ (the sample with $y=0.01$) the spectrum is resolved, and as the temperature is lowered there is a shift of the spectrum due to the Cr^{3+} ions to lower magnetic fields, while for the spectrum due to the Mn^{2+} ions there is a slight nonmonotonic variation of H_r (Fig. 2). We attribute the experimental results obtained for $Hg_{1-x-y}Cr_xMn_ySe$ to the Coulomb interaction between the subsystems of Cr and Mn ions. This interaction causes the system $Hg_{1-x-y}Cr_xMn_ySe$ to behave either like a system consisting of one kind of spin center or like a system consisting of two kinds of spin centers, depending on the relative concentrations of chromium and manganese. This is indicated by the structure of the ESR spectra and the character of their shift with respect to magnetic field as a function of T. For example, for $N_{Cr} \gg N_{Mn}$ the ESR spectrum in $Hg_{1-x-y}Cr_xMn_ySe$ is determined mainly by the Cr^{3+} ions, while for $N_{Cr} \leq N_{Mn}$ it is determined mainly by the Mn^{2+} ions. In the first case both the Cr^{3+} and the Mn^{2+} ions are displaced along the axial axis of the crystal as the temperature changes, while in the second case these ions are fixed. The different relationship between N_{Cr} and N_{Mn} for the first and second cases is attributed by the authors to the difference in the ionic radii of Cr^{3+} and Mn^{2+}. Since the ionic radius of Mn^{2+} is much greater than that of Cr^{3+},

for displacement of the Mn^{2+} ions under the influence of the Cr^{3+} ions it is clearly necessary to satisfy the condition $N_{Cr} \gg N_{Mn}$, while for fixation of the Cr^{3+} ions the condition $N_{Mn} \gg N_{Cr}$ must be satisfied. It should be noted that the approximately equal contribution of the Cr and Mn subsystems to the Coulomb interaction arising between these subsystems in $Hg_{1-x-y}Cr_xMn_ySe$ leads to different temperature dependences of these spin centers, as is attested to by the ESR spectrum of the sample with $y = 0.01$.

Thus from investigations of the ESR spectrum on Cr^{3+} and Mn^{2+} ions and measurements of χ in $Hg_{1-x-y}Cr_xMn_ySe$ it follows that in this system the temperature T_f at which the distortion of the symmetry of the crystal lattice begins (if this occurs), the temperature T_g of the phase transition to the spin glass, and the value of χ in the phase transition region and at $T < T_g$ are larger in magnitude than in $Hg_{1-x}Cr_xSe$ for samples with the same value of N_{Cr}. In $Hg_{1-x-y}Cr_xMn_ySe$ the nonmonotonic character of the $\chi(T)$ curve is more pronounced and the exchange interaction increases, as is indicated by the rise in the phase transition temperature. These phenomena were explained in Ref. 4 on the basis of a cluster model of the spin glass. The fact that the distortion of the symmetry of the crystal lattice does not occur for certain values of x and y (this is confirmed by the isotropicity of the spectrum over the entire range of temperatures investigated) indicates that the observed transi-

tion of $Hg_{1-x-y}Cr_xMn_ySe$ to the spin glass phase[8] is not related to the a distortion of the lattice symmetry. The presence of chromium and manganese ions forming two interacting subsystems in $Hg_{1-x-y}Cr_xMn_ySe$ gives rise to various physical effects in this material.

[*]E-mail: prohorov@host.dipt.donetsk.ua

[1] V. D. Prozorovskiĭ, I. Yu. Reshidova, and Yu. S. Paranchich, Fiz. Tverd. Tela (Leningrad) **34**, 882 (1992) [Sov. Phys. Solid State **34**, 472 (1992)].

[2] V. D. Prozorovskiĭ, I. Yu. Reshidova, and S. Yu. Paranchich, Ukr. Fiz. Zh. **40**, 1005 (1995).

[3] V. D. Prozorovskiĭ, I. Yu. Reshidova, A. I. Puzynya, and Yu. S. Paranchich, Fiz. Nizk. Temp. **21**, 1057 (1995) [Low Temp. Phys. **21**, 813 (1995)].

[4] V. D. Prozorovskiĭ, I. Yu. Reshidova, A. I. Puzynya, and S. Yu. Paranchich, Fiz. Nizk. Temp. **24**, 851 (1998) [Low Temp. Phys. **24**, 639 (1998)].

[5] V. D. Prozorovskiĭ, I. Yu. Reshidova, A. I. Puzynya, and Yu. S. Paranchich, Fiz. Nizk. Temp. **22**, 1396 (1996) [Low Temp. Phys. **22**, 1058 (1996)].

[6] V. D. Prozorovskiĭ and Yu. M. Nikolaenko, Inventor's Certificate 1319000 (USSR); publ. Byull. Izeobret., No. 23 (1987).

[7] A. Goldstein, S. J. Williamson, and S. Foner, Rev. Sci. Instrum. **36**, 1356 (1965).

[8] S. L. Ginzburg, *Irreversible Phenomena in Spin Glasses* [in Russian], Nauka, Moscow (1989).

[9] J. K. Furdyna, J. Appl. Phys. **64**, R29 (1988).

Translated by Steve Torstveit

Magnetic phase transition and magnetoresistive effect in $Nd_{0.6}Ca_{0.4}(Mn_{1-x}Me_x)O_3$ (Me=Cr, Al, Ti, Nb)

I. O. Troyanchuk and D. A. Efimov

*Instiute of Solid State and Semiconductor Physics, National Academy of Sciences of Belarus,
ul. P. Brovki 17, 220072 Minsk, Belarus*

V. V. Eremenko and V. A. Sirenko*

*B. Verkin Institute for Low Temperature Physics and Engineering, National Academy of Sciences
of Ukraine, pr. Lenina 47, 310164 Kharkov, Ukraine*

G. Shimchak and A. Nabyalek

Institute of Physics, Polish Academy of Sciences, 02-668, Al. Lotnikov, 32/46, Warsaw, Poland

The properties of $Nd_{0.6}Ca_{0.4}(Mn_{1-x}Me_x)O_3$ (Me = Cr^{3+}, Al^{3+}, Ti^{4+}, Nb^{5+}) are investigated. It is shown that the indicated substitutions destroy the long-range order in the positions of the Mn^{3+} and Mn^{4+} ions, but the properties depend sharply on the type of substituent ion. The replacement of a small fraction of the Mn^{3+} ions by Cr^{3+} ($0.04 \leqslant x \leqslant 0.1$) leads to antiferromagnet–ferromagnet and insulator–metal transitions. At chromium concentrations $x \geqslant 0.1$ the solid solutions again become nonconducting and exhibit the properties of inhomogeneous ferrimagnets in which the magnetic moments of the chromium and manganese ions are directed opposite to each other. For $T < 30$ K there is a phase transition in which the magnetic moments of the Nd^{3+} ions order antiparallel to the moments of the Mn ions. All of the samples containing chromium have a large magnetoresistive effect at temperatures below the Curie point. The replacement of manganese by Al^{3+}, Ti^{4+}, or Nb^{5+} ions leads to a transition from the antiferromagnetic state to a spin glass state with no change in conductivity. The data obtained indicate that the superexchange interactions between the chromium and manganese ions is of an antiferromagnetic character. © *2000 American Institute of Physics.*
[S1063-777X(00)00301-7]

INTRODUCTION

It is known that the manganites $RE_{1-y}Ca_yMnO_3$ (RE = Pr, Nd) in the concentration interval $0.3 < y < 0.7$ are antiferromagnetic insulators on account of the charge-ordering effect.[1–3] In Ref. 4 it was found that replacing a small fraction of the manganese ions by chromium ions in $Pr_{0.5}Ca_{0.5}MnO_3$ leads to destruction of the antiferromagnetic charge-ordered state: $Pr_{0.5}Ca_{0.5}(Mn_{0.95}Cr_{0.05})O_3$ is a ferromagnet which undergoes a metal–insulator transition near the Curie point $T_C = 160$ K.[4] It has been established by neutron diffraction studies that upon ferromagnetic ordering in $Pr_{0.5}Ca_{0.5}(Mn_{0.95}Cr_{0.05})O_3$ the distortions of the crystal structure decrease. It was conjectured that the trivalent chromium ions, having electronic configuration d^3, the same as the tetravalent manganese ions, take part in ''double exchange,'' as a result of which a ferromagnetic ordering occurs in manganites.[1] In the double exchange model the electrotransport between $3d$ ions with different valences and the ferromagnetism are intimately related: the higher the electrical conductivity, the more stable the ferromagnetic state. There is information in the literature about doping the charge-ordered phases of manganites (mainly $Pr_{0.5}Ca_{0.5}MnO_3$) with small amounts of chromium, nickel, cobalt, iron, and titanium.[4–6] To establish the mechanism of the phase transitions upon substitution of other ions for manganese, we did a study of the properties of the solid solutions $Nd_{0.6}Ca_{0.4}(Mn_{1-x}Me_x)O_3$ (Me=Al, Nb, Ti, Cr) over a wide range of Me concentrations, all the way up to $x = 0.4$.

EXPERIMENT

Polycrystalline samples were obtained from simple oxides and carbonates of especially high purity (grade OSCh), mixed in stoichiometric proportions. The final synthesis was done in air at 1450 °C. The samples were cooled slowly at a rate of 100 °C/h in order to ensure stoichiometry in respect to oxygen. Magnetic measurements were made on a Foner vibrating magnetometer, and the electrical conductivity was measured by the standard four-probe method. Contacts were formed by the ultrasonic deposition of indium.

RESULTS AND DISCUSSION

For $Nd_{0.6}Ca_{0.4}MnO_3$ samples the curves of the temperature dependence of the magnetization have a maximum at 260 K and a slight anomaly near 180 K. According to Ref. 7, the maximum at 260 K is due to charge ordering (long-range order in the positions of the Mn^{3+} and Mn^{4+} ions), whereas
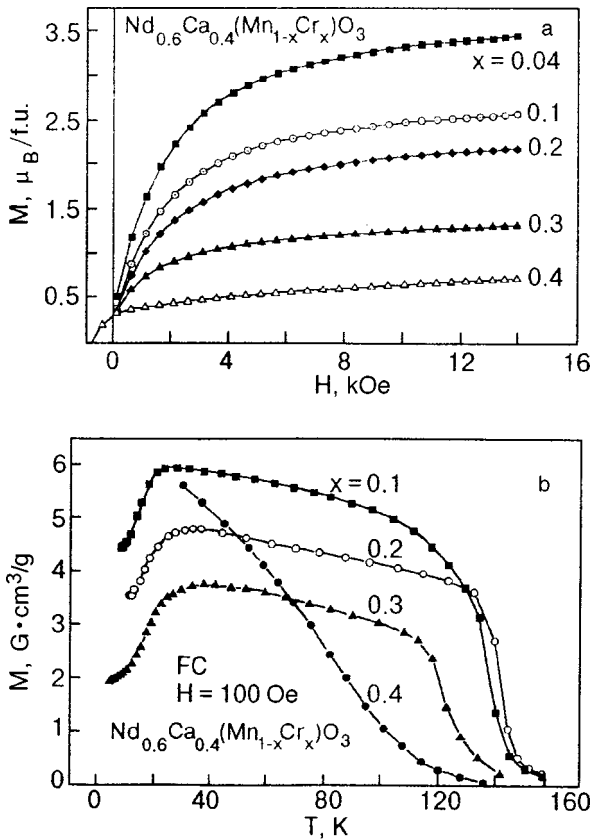
FIG. 1. Magnetic-field dependence of the magnetization of $Nd_{0.6}Ca_{0.4}(Mn_{1-x}Cr_x)O_3$ samples at $T=6$ K in a decreasing field (a) and the temperature dependence during heating after cooling in a field of 100 Oe (FC) (b).

FIG. 2. Temperature dependence of the magnetization in $Nd_{0.6}Ca_{0.4}Mn_{0.7}Cr_{0.3}O_3$ measured in fields $H=5$ kOe and 100 Oe in different regimes: ZFC — zero-field cooled; FC — field cooled (curves *1* and *2* were measured on heating; curve *3* on cooling).

the anomalous behavior at 180 K entails the establishment of long-range antiferromagnetic order. Figure 1a shows the magnetic field dependence of the magnetization of $Nd_{0.6}Ca_{0.4}(Mn_{1-x}Cr_x)O_3$ samples on the magnetic field strength, measured at 6 K in a decreasing field. The magnetic moment increases abruptly to $3.5\,\mu_B$ per formula unit $(x=0.04)$ and decreases smoothly to $0.7\,\mu_B$ as the chromium content is increased further $(x=0.4)$. All of the samples with chromium concentrations up to $x=0.3$ are magnetically soft materials. In the sample with $x=0.4$ the coercive field increases sharply, reaching a value of 600 Oe.

Figure 1b shows the temperature dependence measured in a low field (100 Oe) after cooling in this same field. It is seen that the temperature of the transition to the paramagnetic state $(T\cong150$ K) for the samples with chromium concentrations up to $x=0.2$ depends weakly on the chromium concentration. The sample with $x=0.4$ undergoes a transition to the paramagnetic state over a wide range of temperatures, a fact which is indicative of a nonuniform magnetic state. At low temperatures the magnetization increases sharply with increasing temperature; this may be due to the contribution from the neodymium sublattice. This hypothesis is supported by the fact that the anomalous behavior of the magnetization in the low-temperature region becomes significantly less pronounced as the magnetic field is increased. Such a situation can arise in the presence of two different magnetic sublattices weakly coupled to each other. In the
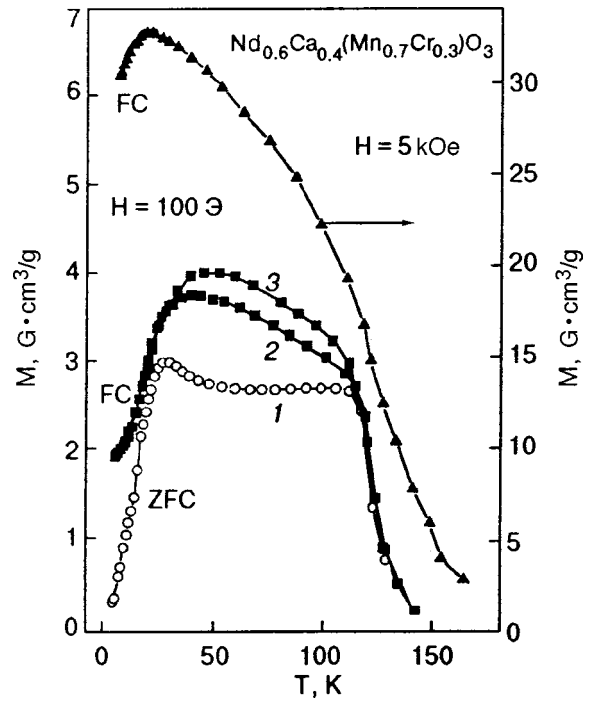
case of antiferromagnetic ordering in the manganese sublattice the magnetic fields inducing the transition to the ferromagnetic state are quite large, as a rule.[7] To elucidate the causes of the anomalous behavior of the magnetization at low temperatures, we investigated the magnetization of the sample with $x=0.3$ as a function of its prehistory and the magnitude of the field (Fig. 2). We found that after cooling in the absence of field (zero-field cooling), the $M(T)$ curve has a maximum in the region of the low-temperature anomaly of the magnetization. At temperatures above 30 K the magnetization is larger during cooling than during heating. This indicates that the domain structure changes below 30 K. We observed considerably sharper anomalies of the magnetization in the low-temperature region for the $Nd(Mn_{0.9}Cr_{0.1})O_3$ sample. This sample satisfies approximately the same magnetic ordering temperature as $NdMnO_3$, in which $T_N=86$ K.[8] However, the magnetic properties of these two compounds differ markedly. In $NdMnO_3$ the magnetization increases strongly as the temperature is lowered (from $T=20$ K), whereas in the sample containing chromium the magnetization falls off sharply. During heating after zero-field cooling a very pronounced maximum of the magnetization appears at low temperatures (Fig. 3). The large hysteresis in temperature (6 K) corresponds to a first-order phase transition.

The electrical conductivity of the solid solutions $Nd_{0.6}Ca_{0.4}(Mn_{1-x}Cr_x)O_3$ depends strongly on the chromium concentration. In the sample with $x=0.04$ the conductivity peak is observed below the Curie temperature T_C (Fig. 4). Samples with a large chromium content remain semiconduct-
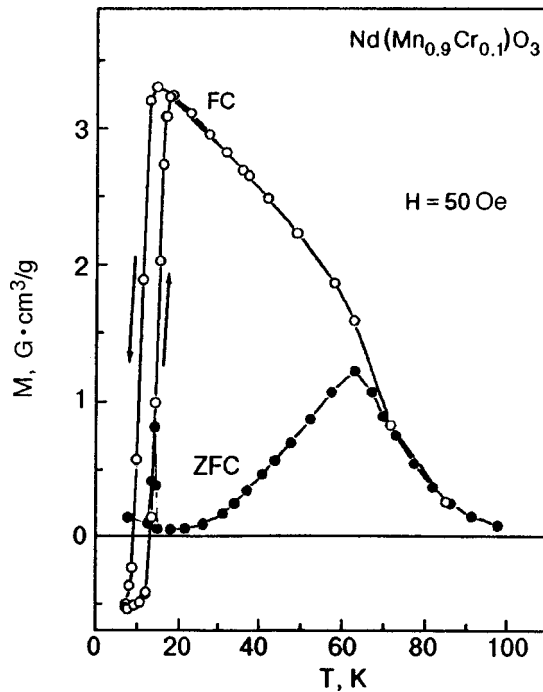
FIG. 3. Temperature dependence of the magnetization of the NdMn$_{0.9}$Cr$_{0.1}$O$_3$ sample (in zero field and at $H = 50$ Oe) in different measurement regimes.

FIG. 5. Magnetoresistance MR defined as $\{[\rho(H=9 \text{ kOe}) - \rho(H=0)]/\rho(H=0)\}100\%$, as a function of temperature in Nd$_{0.6}$Ca$_{0.4}$(Mn$_{1-x}$Cr$_x$)O$_3$ samples.

ing over the entire temperature interval investigated, 77–300 K.

The magnetoresistive effect is most pronounced in the sample with $x = 0.04$ (Fig. 5). That sample has a peak of the magnetoresistive effect near $T = 100$ K. The magnetoresistive effect in the sample with $x = 0.1$ increases smoothly as
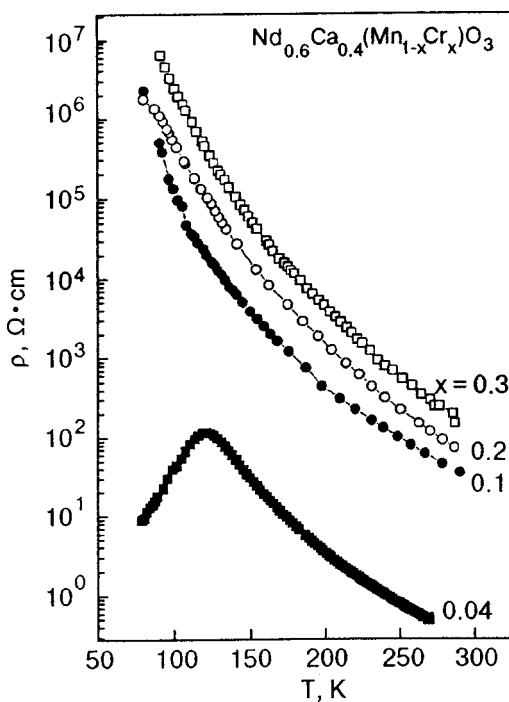
the temperature is lowered. Similar behavior is observed for $x = 0.2$, where the effect is even somewhat larger than for $x = 0.1$.

All of the compounds doped with the nonmagnetic ions Al, Ti, or Nb possess a spontaneous magnetization at low temperatures ($T < 40$ K). However, the magnetization is not saturated in fields up to 15 kOe (Fig. 6). The $M(H)$ curves measured after cooling in a field and in zero field diverge smoothly near $T_f = 40$ K, the temperature at which the maximum of the magnetization is observed during heating after zero-field cooling. Behavior of this sort is would be expected for cluster magnetic systems in which the long-range magnetic order is destroyed through a competition of exchange interactions of different sign.

FIG. 4. Electrical conductivity versus temperature in Nd$_{0.6}$Ca$_{0.4}$(Mn$_{1-x}$Cr$_x$)O$_3$ samples.

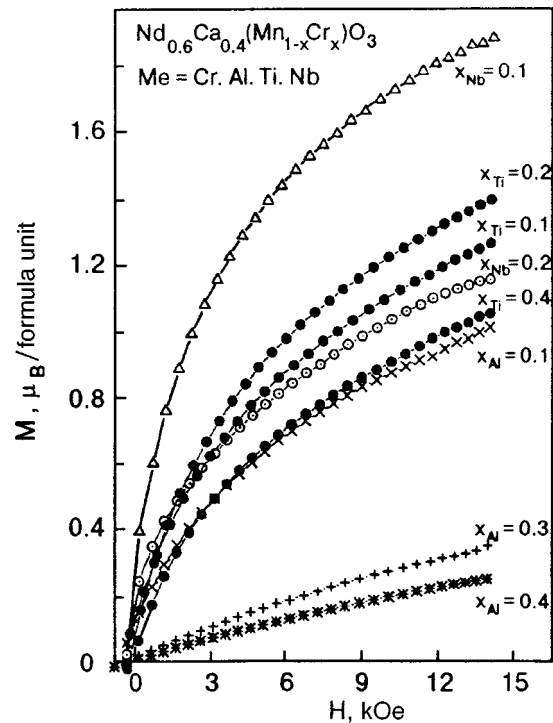FIG. 6. Magnetization as a function of field for $T = 7$ K in Nd$_{0.6}$Ca$_{0.4}$(Mn$_{1-x}$Cr$_x$)O$_3$ samples, where (Me = Nb, Ti, Al).

As in Ref. 4, we assume that the chromium ions enter the manganite mainly in the trivalent state. This is indicated by the extremely small magnetic anisotropy of samples with chromium concentrations up to 30%. In the case of Cr^{4+} ions the magnetic anisotropy is ordinarily rather large. On the basis of the existing data, however, it cannot be ruled out that a small number of chromium ions are in the tetravalent state. Ions of aluminum, titanium, and niobium enter the manganite with valences of three, four, and five, respectively, since the synthesis is done under oxidizing conditions, which are incompatible with the stability of Ti^{3+} and Nb^{4+} ions.

The sharp drop in magnetization and the growth of the resistivity as the chromium concentration is increased indicate that the exchange interactions between chromium and manganese ions are of a different nature than double exchange. As we have said, the Cr^{3+} ions, like the Mn^{4+} ions, have a d^3 electronic configuration. Therefore, according to the Goodenough–Kanamora rules, the 180° superexchange interaction $Mn^{3+}-O-Cr^{3+}$ should be positive. The results of a study of $La(Mn_{1-x}Cr_x)O_3$ are consistent with this assumption.[9] In the $Eu(Mn_{1-x}Cr_x)O_3$ system, however, the ferromagnetic state was not observed.[10] In order to understand the behavior of manganites containing Cr ions, we also studied the system $La_{0.7}Sr_{0.3}(Mn_{1-x}Cr_x)O_3$. In that system the compound not containing chromium is a metallic ferromagnet with $T_C = 370$ K. It turned out that the substitution of chromium for magnesium leads to a gradual decrease in the spontaneous magnetization and in the temperature of the transition to the paramagnetic state to $M_S = 1.2\mu_B$ and $T_N = 180$ K at $x = 0.4$.

The decrease of the magnetization may be due to the circumstance that the magnetic moments of the chromium ions are oriented antiparallel to the magnetic moments of the manganese or that fractions of the spin-glass type form, the percentage of these increasing in proportion to the chromium concentration. However, in the compounds $Nd_{0.6}Ca_{0.4}(Mn_{1-x}Cr_x)O_3$ with $0.04 < x < 0.3$ there is a well-defined transition to the paramagnetic state. The magnetic anisotropy of these compounds is small, as is indicated by the weak role of frustration of the exchange interactions in comparison with the compound with $x = 0.4$. We therefore assume that in the Cr-containing manganite the magnetic moments of the chromium and manganese ions are oriented antiparallel on account of the rather strong negative superexchange interaction $Cr^{3+}-O-Mn^{3+}(Mn^{4+})$. All in all, we conclude that the exchange interaction is very close in magnitude to the exchange interaction between manganese ions. The replacement of the manganese ions by the nonmagnetic ions Al, Ti, and Nb for $x \geq 0.1$ brings about a spin glass state. The substitution of Nb^{5+} ions increases the Mn^{3+} fraction, whereas the substitution of Al^{3+} ions increases the Mn^{4+}

fraction. At a concentration of the diamagnetic ions $x = 0.1$ the magnetization is largest for the niobium-containing compound and smallest for the aluminum-containing compound. This fact supports the assumption that the $Mn^{3+}-O-Mn^{3+}$ exchange interactions in the system $Nd_{0.6}Ca_{0.4}(Mn_{1-x}Cr_x)O_3$ are ferromagnetic.

It follows from the results of the resistivity measurements that the chromium ions do not promote electrotransport processes. The most intimate connection between the magnetic state and the electrical conductivity is observed in the compound with $x = 0.04$, in which the chromium content is minimal, a circumstance which favors electrotransport between manganese ions. In ferrimagnetic states ($0.1 \leq x \leq 0.3$) the magnetoresistance is apparently of a different nature than in the compound with $x = 0.04$, since the magnetoresistance peak is absent. It can be assumed that the magnetoresistance of these compounds is due to intergranule electrotransport of spin-polarized charge carriers, as is often observed in ferromagnetic oxides with a semimetallic character of the conduction.[11] It may be that in the ceramics investigated here there are microregions with rather high conductivity, owing to which the conductivity is of the percolation type.

In our view, the phase transition leading to magnetic ordering of the neodymium ions is of significant interest. In the high-temperature phase the $f-d$ exchange interaction is unimportant, while in the low-temperature phase the $f-d$ exchange increases sharply. Apparently the ground state of the Nd^{3+} ions changes at the phase transition.

*E-mail: sirenko@ilt.kharkov.ua

[1] Z. Jirak, S. Krupicka, Z. Simsa, M. Dlouha, and S. Vratislav, J. Magn. Magn. Mater. **53**, 153 (1985).
[2] P. G. Radaelli, D. E. Cox, M. Marezio, and S.-W. Cheong, Phys. Rev. B **55**, 3015 (1997).
[3] C. H. Chen and S.-W. Cheong, Phys. Rev. Lett. **76**, 4042 (1996).
[4] F. Damay, C. Martin, A. Maignan, M. Hervieu, and B. Raveau, Appl. Phys. Lett. **73**, 25, 3772 (1998).
[5] A. Barnabe, A. Maignan, M. Hervieu, F. Damay, C. Martin, and B. Raveau, Appl. Phys. Lett. **71**, 3907 (1998).
[6] P. V. Vatintha, R. S. Singh, S. Natarajan, and C. N. R. Rao, Solid State Commun. **109**, 135 (1999).
[7] M. Tokunaga, N. Miura, Y. Tomioka, and Y. Tokura, Phys. Rev. B **57**, 5259 (1998).
[8] I. O. Troyanchuk, N. V. Kasper, G. Shimchak, and A. Nabyalek, Fiz. Nizk. Temp. **23**, 409 (1997) [Low Temp. Phys. **23**, 300 (1997)].
[9] G. H. Jonker, Physica **22**, 707 (1956).
[10] I. O. Troyanchuk, N. V. Samsonenko, N. V. Kasper, H. Szymczak, and A. Nabialek, Phys. Status Solidi A **160**, 195 (1997).
[11] S. Sundar Manoharan, D. Elefant, G. Reiss, and J. B. Goodenough, Appl. Phys. Lett. **72**, 984 (1998).

Translated by Steve Torstveit

ELECTRONIC PROPERTIES OF METALS AND ALLOYS

Magnetic breakdown and the Fisher–Kao effect in zinc

L. T. Tsymbal* and A. N. Cherkasov

A. A. Galkin Donetsk Physics and Technology Institute, National Academy of Sciences of Ukraine, 72 R. Luxemburg St., 340114 Donetsk, Ukraine

A study is made of the decompensation effect in zinc due to magnetic breakdown between the electron and hole orbits near the K point of the Brillouin zone. It is shown that, in contrast to the general case for compensated metals, zinc exhibits the Fisher–Kao effect in a magnetic field which is tilted with respect to the hexagonal axis. The regularities of the changes in the shift of the Fisher–Kao peak in a magnetic field upon changes in the frequency and surface quality are established. It is shown that the field-induced shift is related to the appearance of a subsurface damaged layer. An explanation is proposed for the effect wherein the square-root frequency dependence of the position of the maximum with respect to the field is transformed to a linear function when the state of the surface of the slab is modified. © *2000 American Institute of Physics.* [S1063-777X(00)00401-1]

INTRODUCTION

The normal metals can be divided into two groups: uncompensated $(n_e - n_h \neq 0)$ and compensated $(n_e - n_h = 0)$, where n_e and n_h are the total numbers of electron and holes in the primitive cell. The difference of the electron and hole concentrations is given by the relation

$$n_e - n_h = sz - 2(F + J), \tag{1}$$

where s is the number of atoms in the primitive cell, z is the number of electrons given up by each atom to the conduction band, F is the number of filled bands, and J is the number of bands containing holes.

In high magnetic fields the carrier concentration N in a metal requires a more detailed analysis.

The research reported here was done at relatively low ω frequencies and in high fields H, subject to the restriction

$$\omega \ll \nu \ll \omega_c, \tag{2}$$

where ν is the carrier relaxation frequency and $\omega_c = eH/(mc)$ is the cyclotron frequency.

Under these conditions the concentration difference $N_e - N_h$ that is manifested in an experiment is equal to $(n_e - n_h)/V$ only for closed isoenergetic surfaces, which can be unambiguously classified as electronic or hole. Here V is the volume of the primitive cell, and N_e and N_h are the concentrations of carriers enclosed in the closed regions formed by the electron and hole orbits in the magnetic field. On multiply connected Fermi surfaces (FSs) of the ''monster'' type in an external magnetic field both electron and hole orbits are observed. Such surfaces on the whole cannot be classified as being of the electron or hole type, and for them $N_e - N_h$ need not be equal to $(n_e - n_h)/V$, and it may even turn out to be nonzero for $n_e = n_h$. Consequently, a metal which is compensated according to Eq. (1) may actually behave in an experiment as an uncompensated metal, and vice versa. In this paper we shall use the terms ''compensation'' and ''decompensation'' as pertaining to the relationship between N_e and N_h.

The spectra of collective excitations of a magnetized electron plasma for compensated and uncompensated metals are fundamentally different. For example, an Alfvén wave can exist only in a compensated metal and a helicon only in an uncompensated metal, while a doppleron can exist in either. These spectra are completely determined by the conductivity of the metal. However, as we have said, in high magnetic fields (2) the contribution to the conductivity (more precisely, the sign of this contribution) is determined not by whether the carriers belong to one sheet of the Fermi surface or another but by the type of orbit (electron or hole) on which these carriers are found. In a magnetic field an electron may be found on a hole orbit (and vice versa), and compensation and decompensation effects arise; consequently, the structure of the spectra of collective excitations can change in a fundamental way as the external parameters (field, temperature, geometry of the experiment) are varied.

Let us consider the most characteristic features of the spectra of electromagnetic modes in uncompensated and compensated metals.

The spectrum of transverse electromagnetic modes in normal metals with a FS that is axially symmetric about the $\hat{z}$ axis in the geometry $\mathbf{k} \| \mathbf{H} \| \hat{\mathbf{z}}$ is described by the dispersion relation

$$k^2 = \frac{4\pi i \omega}{c^2} \sigma_\pm \quad (\pm \text{ polarization}). \tag{3}$$

Here $\mathbf{k}$ is the wave vector of the wave, and $\sigma_\pm = \sigma_{xx} \pm i \sigma_{yx}$ is the conductivity for the circularly polarized components of the field: $E_\pm = E_x \pm iE_y$. The main details of interest in the
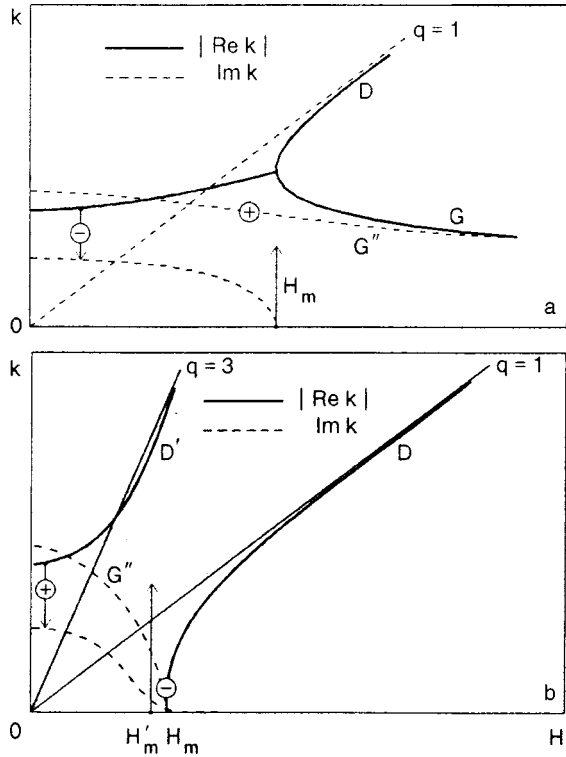
FIG. 1. Electromagnetic mode spectra obtained in the limit $\gamma \to 0$: uncompensated metal—solution (2), (3) for $\beta=0$ (a); compensated metal—solution (2), (3) for $\beta=1$ and $\alpha=1/3$ (b). Solutions G and G' are the helicon and damped helicon, and D and D' are doppleron solutions. The signs of the circular polarization are indicated in circles. The scales along the coordinate axes can be determined by using the relations for H_m (see text), the position of the straight lines $q=1$, and the values of the parameters of the metal.

FIG. 2. Qualitative character of the electromagnetic mode spectrum in a compensated metal, obtained with collisions taken into account, $\nu \gg \omega$ (the D' branch of the spectrum is omitted; cf. Fig. 1b). For clarity the spectrum has been divided into two fragments. It is seen that in the ''−'' polarization the Alfvén branch of the spectrum, which lies at fields $H<H_m$ ($|\mathrm{Re}\,k| \simeq \mathrm{Im}\,k$), is associated with the D branch (fragment a), while that lying at fields $H>H_m$ is associated with the G'' branch (fragment b) of the electromagnetic mode spectrum. Since in the ''+'' polarization $\mathrm{Re}\,k \simeq \mathrm{Im}\,k$ [see Eq. (5)] for the Alfvén mode throughout the entire field interval, only the $\mathrm{Im}\,k(H)$ curve is shown for this mode in the two fragments. The signs of the circular polarization are indicated in the circles.

electromagnetic mode spectra of uncompensated and compensated metals can be analyzed using a model FS of the ''corrugated cylinder'' type, for which the type of orbit (electron or hole) always corresponds to the type of carrier (electrons or holes, respectively), i.e., the relation $(n_e - h_h)/V = N_e - N_h$ holds. If the FS consists of two cylinders, i.e., an electron cylinder and a hole cylinder, then[1,2]

$$\sigma_{\pm} = \sigma_{\pm}^e + \sigma_{\pm}^h = \pm i \frac{N_e e c}{H} \{ [(1 \pm i\gamma)^2 - q^2]^{-1/2}$$

$$- \beta [(1 \mp i\gamma)^2 - \alpha^2 q^2]^{-1/2} \}, \qquad (4)$$

where

$$q = k v_e / \omega_c; \quad \gamma = (\nu - i\omega)/\omega_c. \qquad (5)$$

In Eqs. (4) and (5) the indices e and h denote the electron and hole parameters, respectively; $\beta = N_h / N_e$ ($\beta=1$ for a compensated metal and $\beta \neq 1$ for an uncompensated metal); $\alpha = v_h / v_e$ (v is the maximum velocity of the carriers along **H**). We assume that ω_c and $\nu = \mathrm{const}$ for all carriers, with $\omega_c > 0$ for both electrons and holes. Figure 1 shows the spectra of electromagnetic modes in uncompensated (a) and compensated (b) metals in the limit $\gamma \to 0$. For specificity we have set $\beta=0$ in the uncompensated metal and $\gamma=1/3$ in the compensated metal. We see that for $H > H_m$ the dispersion relation in the uncompensated metal has three solutions: heli-
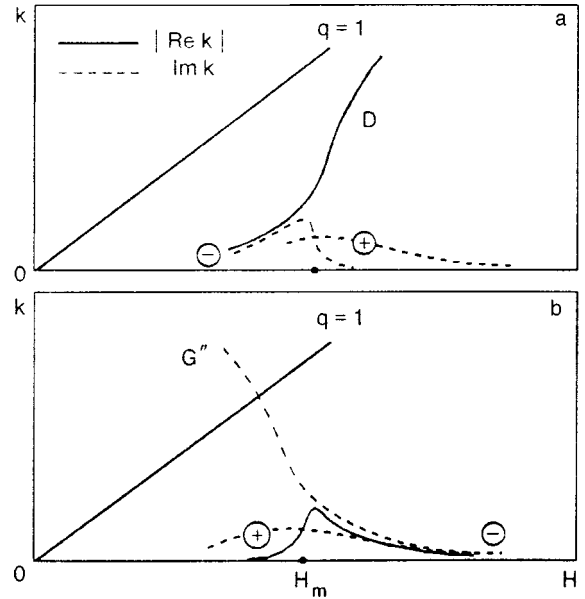
con (G), doppleron (D), and damped helicon (G'); the value of the threshold field H_m is determined by the relation $\xi^3 = (27/4)^{1/2}$, where $\xi^3 = \omega_c^3 c^2/(\omega_p^2 \omega v_e^2)$, $\omega_p^2 = 4\pi N_e d^2/m$ (Refs. 1 and 2). In fields below H_m all three solutions describe an anomalous skin effect in an external static magnetic field.[3] The introduction of a hole group of carriers ($N_h = N_e$) in an uncompensated metal in the ''−'' polarization causes the helicon branch of the spectrum to vanish and modifies the spectrum of the doppleron D, and for $H < H_m$ [the value of H_m is determined by the relation $\xi^3 = (1 - \alpha^2)/2$] the solution of the dispersion relation becomes purely imaginary (branch G'' of the spectrum). In the ''+'' polarization the branch G' vanishes and a solution D'—a ''hole'' doppleron—appears. In fields below the threshold field of the doppleron D' ($H < H'_m$) all the solutions, as in the uncompensated metal, describe an anomalous skin effect. Actually, the solutions G and G' do not vanish but degenerate to zero as $\gamma \to 0$ and $N_h \to N_e$. For $\gamma \neq 0$ the degeneracy is lifted, and in the local limit ($|q^2| \ll |1 \pm i\gamma|^2$) these solutions can be written in the form

$$k^2 \cong 8\pi i N_e m \frac{(\nu - i\omega)\omega}{H^2 \pm H_m^2} (\pm \text{ polarization}). \qquad (6)$$

In the high-frequency region ($\omega \gg \nu$) in fields $H > H_m$ the solutions (6) are almost real-valued and describe the well-known propagating mode called the Alfvén wave.[4] In our case, however, by virtue of inequality (2), the solutions are importantly complex (see Fig. 2). Despite the appreciable
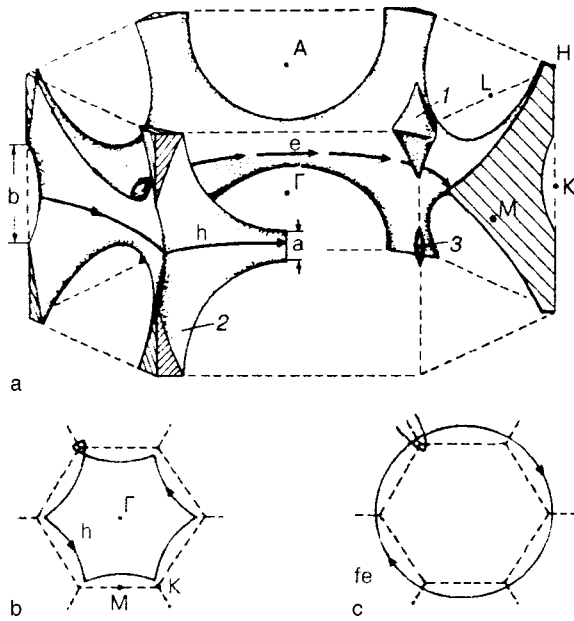
FIG. 3. Fragment of the Fermi surface of zinc. a: *1* (First zone)—hole ''pyramids'' at the *H* points; *2* (second zone)—the hole ''monster;'' *3* (third zone)—electron ''needles'' at the *K* points. b: *h*—Hole orbits lying on the ''monster'' surface near the basal plane ($\mathbf{H} \| [0001]$). c: *fe*—Magnetic-breakdown electron orbits of nearly-free electrons ($\mathbf{H} \| [0001]$).

damping, however, in sufficiently high magnetic fields the field components corresponding to these solutions become dominant in amplitude. Then $\delta = 1/\mathrm{Im}\, k$ can exceed the thickness of a typical sample. The passage of mode (6) through a metal slab is manifested experimentally as a ''strong'' anomaly of the surface resistance $\mathrm{Re}\, Z$ of the metal (the Fisher–Kao effect;[5] see also Refs. 6 and 7). As the field is increased under conditions of almost total transparency of the sample, the value of $\mathrm{Re}\, Z$ reaches a maximum at $\mathrm{Im}(kd/2) \approx 1$ (*d* is the sample thickness), and then decreases on account of the growing compensation of the high-frequency electrical currents on opposite sides of the slab. In typical samples one ordinarily has $H_{\max}^2 > H_m^2$, where $H_{\max}$ is the field corresponding to the maximum of $\mathrm{Re}\, Z$, and, hence, from Eq. (6) we have

$$H_{\max} \propto d(\omega \nu)^{1/2}. \tag{7}$$

It should be emphasized that the Fisher–Kao effect cannot exist in an uncompensated metal.

In the present study we investigate the Fisher–Kao effect in zinc. The choice of metal was mainly based on the features of the electronic structure of Zn. Zinc is a compensated metal [with $s = 2$, $z = 2$, $F = 0$, and $J = 2$ in Eq. (1)], the FS of which has been thoroughly investigated and is well known.[8,9] Figure 3a shows the region of interest on the FS of zinc: the ''hole monster'' in the second zone and the ''electron needles'' at the *K* points of the third Brillouin zone. Because the ''monster'' is a multiply connected surface, in the geometry $\mathbf{H} \| [0001]$ a layer of electron orbits *e* with a thickness *a* exists on its surface. However, since $b > a$ [Ref. 10; see Fig. 3a], the layer of hole orbits *h* has the same thickness, and the ''geometric'' decompensation of the electron and hole volumes does not arise. Nevertheless decompensation in zinc

can occur by a different mechanism. The reason is that the energy gap between the second and third zones near the *K* point is small. As a result, even in fields $H \gtrsim 1.3$ kOe[11] the hole orbits *h* [Fig. 3b] begin to vanish, and magnetic-breakdown orbits *fe* appear [Fig. 3c], these in fact being orbits lying on the nearly-free-electron sphere. A decompensation arises which, in the geometry $\mathbf{H} \| [0001]$, reaches a value

$$N_e - N_h \cong \frac{2}{(2\pi\hbar)^3} 2S_0 a \cong 0.82 \times 10^{22}\, \mathrm{cm}^{-3}. \tag{8}$$

In Eq. (8) S_0 is the cross-sectional area of the Brillouin zone on the [0001] plane. Measurements of the Hall coefficient in fields up to 18 kOe give approximately the same value.[11] When the magnetic field direction deviates from the [0001] axis by an angle $\theta \gtrsim 1.5°$ the orbits *fe* vanish, and hence so does the magnetic-breakdown decompensation.

We have previously[9] calculated the spectra of the electromagnetic modes in both ''compensated'' and ''decompensated'' zinc in the geometry $\mathbf{k} \| \mathbf{H} \| [0001]$. In the details of interest to us, the spectra obtained are qualitatively similar to those shown in Fig. 1. The doppleron solution D comes about because of the Doppler-shifted cyclotron resonance of the electrons of the resting point of the ''lens.'' At a frequency $\omega/2\pi = 3.5$ MHz a value $H_m \cong 22$ kOe was obtained for the threshold field for the helicon [Fig. 1a], while the threshold field of the doppleron [Fig. 1b] had the value $H_m \cong 12.5$ kOe ($\theta_m \propto \omega^{1/3}$).

EXPERIMENT

We studied the surface resistance $\mathrm{Re}\, Z$ of a plane-parallel zinc slab. The samples were prepared by cleaving a 99.9999% pure Zn single crystal along the (0001) plane. The surface quality of the samples was varied by rubbing with a corundum abrasive and by chemical etching in an aqueous solution of CrO_3.

An rf spectrometer of the autodyne NMR type was used in the experiment. The samples were placed in a flat coil of the oscillator. The exciting field was parallel to the plane of the sample. The measurements were made in the frequency range 4–900 kHz at temperatures of 1.8–4.2 K in fields reaching as high as 60 kOe. Rotation of the sample in the magnetic field was done with an accuracy of $\sim 0.1°$. The angle θ between the normal to the sample, $\mathbf{n} \| [0001]$, and the $\mathbf{H}$ direction was varied in the range 0–40°.

Comparative measurements were made on samples of tungsten ($\mathbf{n} \| [001]$), indium ($\mathbf{n} \| [001]$), and cadmium ($\mathbf{n} \| [0001]$). The cadmium and indium samples were grown from metals of 99.9999% purity in knock-down forms of polished quartz. The tungsten samples were cut by electro-erosion from massive perfect single crystals with a ratio of room-temperature to liquid-helium-temperature resistivity $\rho_{300\,K}/\rho_{4.2\,K} \approx 10^5$, ground, and then electrically or chemically polished. Tungsten and cadmium are compensated metals, while indium is an uncompensated metal.
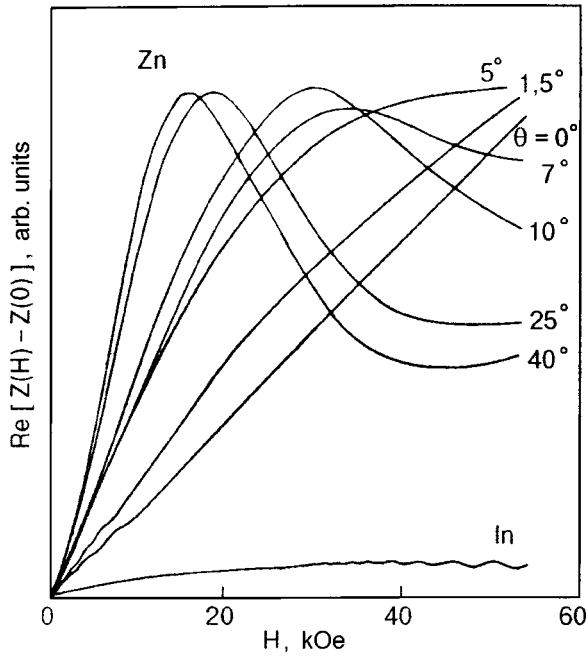
FIG. 4. Magnetic-field dependence of the surface resistance of zinc ($\omega/2\pi = 378$ kHz, $d = 0.31$ mm, θ is the angle between the directions of **H** and **n**∥[0001]) and indium ($\omega/2\pi = 860$ kHz, $d = 2.55$ mm, **H**∥**n**∥[100]). Temperature 4.2 K.

EXPERIMENTAL RESULTS AND DISCUSSION

Magnetic-breakdown decompensation in zinc. Figure 4 shows examples of the experimental curves of the surface resistance of zinc versus the external static magnetic field for various angles θ. It is seen that for $\theta \approx 0$ the value of Re Z increases monotonically with increasing field, all the way up to the maximum fields attainable in the experiment. The absence of a maximum indicates that the damped Alfvén ($\omega \ll \gamma$ modes (6) are not excited. Consequently, for small θ zinc appears more like an uncompensated metal. Here, however, the strong and monotonic increase of Re Z is unexpected. In fact, it has been shown[12,13] that in low magnetic fields ($H \ll H_m$) the surface resistance of alkali metals (the nearly-free-electron model) is relatively small and does not depend significantly on the magnetic field. As H increases, the value of Re Z increases smoothly, and in the particular case of specular reflection of electrons by the surface of the sample, a peak forms near the helicon threshold.[13] This peak is due to the fact that near H_m the group velocities of the helicon and doppleron change sharply (they vanish in the limit $\nu \sim 0$). As the field increases further, the value of the nonoscillatory contribution to Re Z approaches the asymptotic value in the helicon propagation region. A similar result has been obtained[1] for the "corrugated cylinder" model. To a certain degree the experiment agrees with the theory developed for simple metallic systems. For example, we see from Fig. 4 that as the field increases, the surface resistance of indium increases slowly and reaches a certain limiting value in the helicon propagation region (the observed oscillations are helicons). However, there is no peak of Re Z in the neighborhood of the helicon threshold. This fact requires explanation. First, this maximum is "smeared"

by collisions and cannot exceed the helicon oscillations in amplitude. Second, in the limit of purely diffuse boundary conditions the maximum of Re Z near H_m does not arise at all. This was shown in Ref. 13 for free electrons and in Ref. 1 for a "parabolic lens" model of the FS.

In accordance with the calculation for zinc, at $\theta = 0$ the threshold field for the helicon at a frequency of $\omega/2\pi = 378$ kHz is $H_m = 10$ kOe. We see that there are no anomalies on the curve in Fig. 4 (for $\theta = 0$) in going from the anomalous skin effect regime to the propagating mode regime. The surface resistance increases monotonically, and the value of Re Z is relatively large even in absolute value in comparison with the value of Re Z in indium, for example. Nevertheless, the fact that a helicon is excited in zinc cannot be doubted. In Ref. 14 a helicon resonance was observed in the low-frequency magnetic susceptibility of zinc, but because of an incorrect interpretation of the experimental results, the value of $N_e = N_h$ obtained in that experiment is four times larger than the calculated value (8). In our experiment the amplitude of the helicon oscillations was too small, and in Fig. 4 they can not be differentiated against the overall trend of the Re Z curve (the oscillations observed in weak fields have a period equal to the period of quantum oscillations caused by the extremal cross sections of the electron "needles").

Thus the experiment provides evidence that zinc, a metal decompensated under conditions of magnetic breakdown, is fundamentally distinct from the common class of actually uncompensated metals. What could cause such a strong growth of Re Z with magnetic field? A quite realistic and justified explanation can be formulated as follows. In relatively high fields the most probable orbits are the nearly-free-electron magnetic-breakdown orbits [*fe*; Fig. 3c]. Nevertheless there also exist other magnetic-breakdown orbits of different configurations. Of course, the conductivity tensor will differ fundamentally from that in the regime of "ideal" decompensation,[9] when only the orbits *fe* arise in place of the orbits *h*. The magnetic-breakdown orbits, which are rather extended in the direction perpendicular to **H**, are to a certain degree open orbits. The existence of these orbits leads to growth of the surface resistance. By nature this growth is analogous to the growth of the transverse magnetoresistance in metals with open orbits in the plane perpendicular to **H**.

Compensated zinc. We see from Fig. 4 that when the magnetic field **H** is tilted from the [0001] axis the Re $Z(H)$ curve is distorted, and a peak appears on it which is initially weak but becomes quite pronounced. This peak is undoubtedly due to the Fisher–Kao effect. A rough estimate of ν gives the completely acceptable value $\nu \sim 10^9$ s^{-1}. Consequently, as the angle θ increases, the magnetic-breakdown decompensation vanishes, and zinc appears to be a compensated metal, in complete agreement with Eq. (1). The magnetic-breakdown orbits *fe* vanish for $\theta \geq 1.5°$. However, magnetic-breakdown orbits of various configurations will exist even for large angles θ. It is because of this that a pronounced component that increases monotonically with H appears on the surface resistance Re $Z(H)$ in a certain interval of angles. It is only for $\theta \geq 5°$, when the transverse dimensions of the magnetic-breakdown orbits become relatively small and the thicknesses of these orbits decrease that a pro-
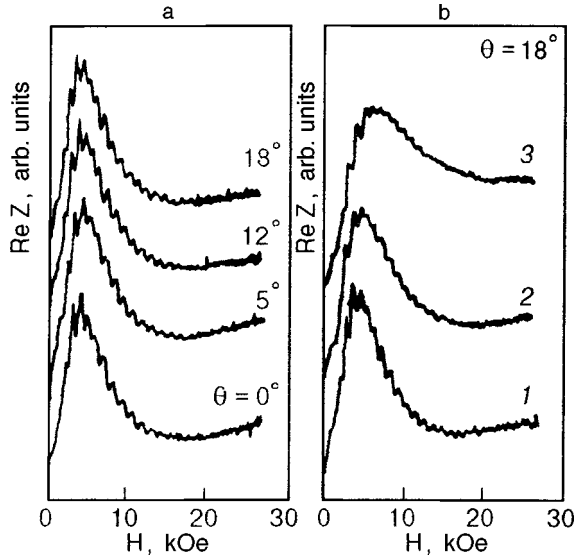
FIG. 5. Surface resistance of tungsten as a function of magnetic field: $\omega/2\pi = 147$ kHz, $d = 0.185$ mm, $T = 4.2$ K, θ is the angle between the directions of **H** and **n**∥[100]. a: Both surfaces of the sample are chemically polished. b: $\tau = 18°$; curve *1*—both surface of the sample are chemically polished; *2*—one surface was subjected to an abrasive with a grain size of 30 μm; *3*—both surface were subjected to the abrasive. The curves exhibit oscillations due to the excitation of a hole *A* doppleron.[17]

FIG. 6. Surface resistance of zinc as a function of magnetic field: $\omega/2\pi = 175$ kHz, $d = 0.33$ mm, $T = 4.2$ K; $\theta = 15°$ is the angle between the directions of **H** and **n**∥[0001]. Curve *1*—cleaved surface; *2*—both surface of the sample were treated with an abrasive having a grain size of 10 μm.

nounced Fisher–Kao peak on the $\mathrm{Re}\,Z(H)$ curve.

The Fisher–Kao effect is a dimensional effect. Indeed, the dependence $H_{max} \propto d$ in (7) is confirmed by experiment both in zinc and in tungsten and cadmium. The frequency dependence $\theta_{max} \propto \omega^{1/2}$ is also described quite well by formula (7) for all $\theta \leqslant 30°$, although the validity of this formula is problematical for the oblique propagation of electromagnetic modes. In particular, this is caused by the fact that for $\theta \neq 0$ a dissipative term appears in the conductivity as a result of the Landau magnetic damping.[15] The wave vector of the damped Alfvén wave will, of course, no longer be determined by the simple relation (6). Analysis of the oblique propagation of electromagnetic waves is, in principle, a clear problem, but in our case it is extremely difficult to solve. First, because of the complexity of the surface of the ''monster.'' Second, because of the presence of magnetic-breakdown orbits whose layer thicknesses are unknown, particularly since there exists another system of magnetic-breakdown orbits that arises as a result of the magnetic breakdown between the ''pyramid'' and ''monster.''[16] Therefore, without analyzing this aspect of the problem, let us just give the experimental results. In tungsten the position of the $\mathrm{Re}\,Z$ peak is practically independent of the angle θ [Fig. 5a], while in cadmium this peak is initially shifted to higher fields (by about 3% at $\theta = 8°$) and then to lower fields (by about 6% at $\theta = 18°$). In zinc, on the other hand, the maximum of $\mathrm{Re}\,Z$ shifts, and quite considerably (Fig. 4), to lower fields as θ increases. We see that the $\mathrm{Re}\,Z(\theta)$ curves obtained do not have even a qualitative generality. This is not surprising, since the collisionless damping is due to non-local effects, which are sensitive to features of the zone structure of each particular metal. Also understandable is the special role of magnetic breakdown, which fundamentally
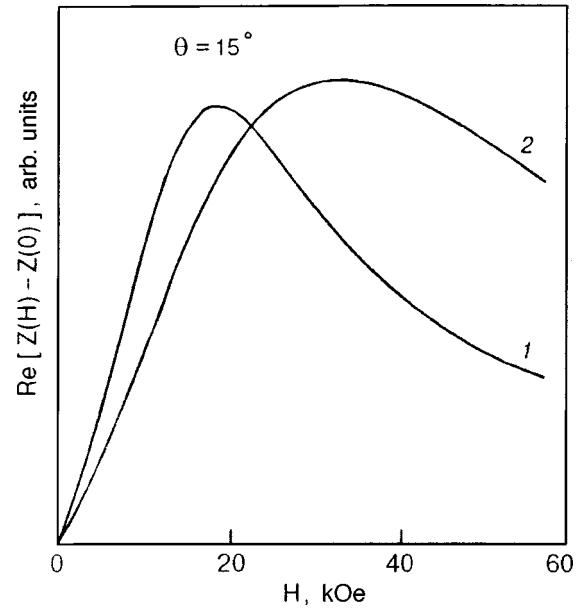
alters the character of the free-carrier dynamics in zinc.

Influence of the surface quality of the sample. Up until now we have been analyzing experimental results obtained on samples with rather high-quality surfaces. For zinc we studied cleaved surfaces, for cadmium and indium we studied samples grown in polished quartz forms, and for tungsten the surfaces were electropolished. By changing the state of the surface, or, more precisely, the state of a subsurface layer of the samples, one can qualitatively alter the character of $\mathrm{Re}(H)$ and $H_{max}(\omega)$. Figure 6 shows the experimental curves of $\mathrm{Re}\,Z(H)$ obtained in zinc for different states of the surface. We see that after the surface is subjected to an abrasive treatment the maximum of $\mathrm{Re}\,Z$ is noticeably shifted to higher fields. The change in H_{max} is $\sim 70\%$. Similar results for tungsten, where H_{max} increased by a factor of approximately one and a half, are shown in Fig. 5b.

We recall that in Refs. 6 and 18 the surface impedance of tungsten was also investigated in the geometry **H**∥**n**∥[001]. Here the surface was not subjected to mechanical treatment. The state of the surface of the samples was varied by cyclic oxidation followed by annealing in vacuum. The significant (like ours) shift of the $\mathrm{Re}\,Z$ peak was attributed to a change in the specularity coefficient of the scattering. Indeed, for diffuse scattering a surface current arises near the oxidized surface due to the static skin effect.[19,20] The impedance of the slab can be written in the form[21]

$$Z_s^{-1} = Z^{-1} + S, \qquad (9)$$

where Z_s is the impedance with allowance for the surface currents, Z is the impedance in the case of specular reflection of electrons from the surface of the sample, and $S \sim \sigma_0(r/l)r$ is the same as the resistance of a thin slab to a direct current in the case of diffuse boundaries.[21] Here $\sigma - = ne^2/\nu m$, $r \propto H^{-1}$ is the Larmor radius, and $\lambda \propto \nu^{-1}$ is

the effective mean free path. Since $S=0$ for specular reflection, the change of the specularity coefficient p leads to a shift of the Re Z peak. Formula (9) convincingly describes the experiment on the assumption that p varies in the range from zero to 0.5. This assumption is reasonable for vacuum annealing. In our case, however, this explanation is unsuitable. After polishing, the samples were held in air. For tungsten samples of this type, measurements of the specularity coefficient give a value of p not more than $\sim 0.1-0.15$ (Ref. 22). This value is clearly insufficient for explaining the observed shift of the Re Z peak in tungsten after abrasive treatment. The situation is more subtle in a tilted magnetic field, when the initial coefficient of specularity can vary in a complicated way as a result of interzone umklapp processes on the FS. Such a picture has been observed, in particular, in zinc[23] and should have led to substantial changes in respect to the shift of the Fisher–Kao peak for different angles $(\mathbf{H},[0001])$. No such angular effects have been observed in zinc or tungsten.

From what we have said, the following simple and physically clear explanation for this effect seems a reasonable alternative. The abrasive surface treatment not only changes the coefficient of specularity of the reflection but also creates a subsurface layer of defects. As a result, the electron relaxation frequency increases substantially near the surface. Actually, a defect concentration gradient arises near the surface of the sample. However, we shall assume that the sample consists of three layers: an internal layer with a relaxation frequency ν, and two subsurface layers of thickness d' and relaxation frequency ν'. This assumption is suggested by the experimental fact that when the damaged layer (~ 0.02 mm) is chemically removed, the experimental curve 2 in Fig. 6 again practically coincides with curve 1 (a similar thing happens for tungsten as well). Now, by analogy with optics, the shift of the Re Z peak can be described by using the resonance condition ($\text{Im}(kd/2)\approx 1$), which we write in the form

$$k(H_{max},\nu)d=k(H'_{max},\nu)(d-2d')+k(H'_{max},\nu')2d'. \tag{10}$$

Here H_{max} and H'_{max} are the fields corresponding to the maximum of Re Z before and after the surface treatment, respectively. Assuming that H^2_{max} and $H'^2_{max} \gg H^2_m$, we obtain from (6) and (10) the relation

$$H'_{max}/H_{max}=1+2(d'/d)(\sqrt{\nu'/\nu}-1). \tag{11}$$

Relation (11) satisfactorily describes the shift of the Re Z peak in zinc (Fig. 6) for $d'\approx 10$ μm (the average grain size of the abrasive) and $\nu'/\nu \sim 10^2$. The measured ratio of the relaxation frequencies is completely real-valued. However, this ratio is an averaged quantity. Therefore, if the defect concentration gradient is taken into account, the high-field condition ($\omega_c \gg \nu$) may be violated in a narrow subsurface layer. As a result, the regime of the "classical" normal skin effect ($k\propto(\omega/\nu)^{1/2}$) obtains in this layer, and relation (10) becomes incorrect there. Nevertheless, the proposed "optical" model can be used for a purely qualitative description of the shift of the Re Z peak.
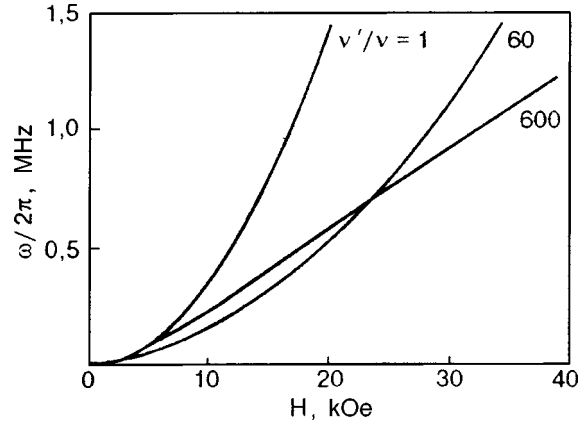

FIG. 7. Frequency–field curves of the Fisher–Kao effect, obtained for different values of ν'/ν (three-layer sample model; see text).

The frequency dependences obtained for the Fisher–Kao effect indicative that the state of the sample surface is of fundamental importance. In all our samples of uncompensated metals with high-quality surfaces we obtained $H_{max} \propto \omega^{1/2}$, in agreement with Eq. (7). After the abrasive treatment of the surfaces of zinc and tungsten the square-root frequency dependence was transformed to a linear dependence: $H_{max} \propto \omega$. In Ref. 6 a more subtle method was used to alter the state of the surface. As we have said, oxidation of atomically clean annealed tungsten surfaces also led to a strong shift of the peak of Re $Z(H)$. However, $H_{max}(\omega)$ remained a square-root dependence, as before. It is therefore obvious that when the results obtained on samples with abrasive-treated surfaces, one must take into account not so much the change of the state of the surface itself but the presence of a subsurface layer with a nonuniform distribution of defects over its thickness. Formula (11) does not describe the transformation of the frequency dependence $H_{max}(\omega)$, since it was obtained under the high-field assumption: $\nu,\nu' \ll \omega_c$. However, as we have said, near an abrasive-treated surface a damaged layer can arise in which the high-field condition does not hold. We again use the "optical" model, assuming that the sample consists of three layers, with $\nu' \gg \omega_c$ in the subsurface layers. Then the wave vector in Eq. (10) obeys the relation

$$k(\nu')\cong[2i\omega_p^2\omega\nu'/c^2(\nu'^2+\omega_c^2)]^{1/2}. \tag{12}$$

As a result, on the right-hand side of Eq. (11), a factor $1+\nu'^2/\omega_c^2$ appears in the denominator of the expression under the radical, with the result that the function $H_{max}(\omega)$ is distorted at large values of ν'. Figure 7 shows the frequency-field curves for the Fisher–Kao effect, obtained for different values of ν'/ν ($\nu=2\times 10^9$ s^{-1}, $N=0.6\times 10^{22}$ cm^{-3}, $d=0.33$ mm, $d'=15$ μm). We see that as ν' increases, the peak shifts to higher fields, but that $H_{max}(\omega)$ remains a square-root dependence as long as the high-field condition is satisfied ($\omega_c \gg \nu'$). As ν' is increased further, this dependence is distorted, transforming to a practically linear dependence at high enough frequencies. Consequently, the shift of the Re Z peak and the transformation of the frequency dependence $\theta_{max}(\omega)$ can be described qualitatively within the

proposed simplified model, which assumes the creation of subsurface damaged layers with a nonuniform distribution of defects.

CONCLUSION

We have investigated the consequences of the decompensation of the electron and hole volumes in zinc due to interzone magnetic breakdown and have investigated the influence of the state of the surface of the samples on the character of the frequency-field curves for the Fisher–Kao effect. The results can be stated as follows.

1. In zinc at small angles between the direction of **H** and the axis $[0001]\|\mathbf{n}$ the value of Re Z increases monotonically with H all the way up to the maximum attainable fields, whereas in other compensated metals, e.g., in tungsten and cadmium, the Re $Z(H)$ curve exhibits a maximum due to the Fisher–Kao effect. This suggests that at small θ zinc does not behave as a typical compensated metal. The decompensation of charge carriers arises as a result of the magnetic breakdown between the second and third Brillouin zones in the neighborhood of the K points (Fig. 3). However, the monotonically increasing function Re $Z(H)$ obtained distinguishes zinc from the common class of uncompensated metals as well. The form of Re $Z(H)$ in zinc is most likely due to the fact that, along with the magnetic-breakdown orbits fe (Fig. 3) there also exist other magnetic-breakdown orbits of different configurations—in particular, open ones.

2. As the angle θ is increased, the Re $Z(H)$ curve for Zn deforms, and for $\theta > 5°$ it exhibits a peak that indicates that a damped Alfvén wave, which propagates through the sample, is excited in zinc. Consequently, when the direction of **H** deviates from the [0001] axis, the magnetic-breakdown decompensation vanishes, and zinc, in accordance with formula (1), behaves as a compensated metal.

3. When the surface of the sample is subjected to an abrasive treatment the peak on the Re $Z(H)$ curve is shifted substantially to higher fields, and the standard frequency dependence for the Fisher–Kao effect, $H_{max} \propto \omega^{1/2}$ (7) is transformed to a linear dependence: $H_{max} \propto \omega$. This result cannot be described in a theory which takes into account only the change in the specular reflection coefficient of electrons from the surface of the sample. The proposed model gives a satisfactory description of the frequency–field dependence of the Fisher–Kao maximum.

*E-mail: tsymbalhost.dipt.donetsk.ua

[1] D. S. Falk, B. Gerson, and J. F. Carolan, Phys. Rev. B **1**, 406 (1970).
[2] L. T. Tsymbal and A. N. Cherkasov, Fiz. Nizk. Temp. **24**, 250 (1998) [Sov. Low Temp. Phys. **24**, 189 (1998)].
[3] L. T. Tsymbal, A. N. Cherkasov, and O. F. Panchenko, Fiz. Nizk. Temp. **24**, 1157 (1998) [Sov. Low Temp. Phys. **24**, 868 (1998)].
[4] S. J. Buchsbaum and R. Bowers, in *Plasma Effects in Solids (7th International Conference on the Physics of Semiconductors, Paris, 1964)*, Dunod, Paris (1965), p. 215.
[5] H. Fischer and Y. Kao, Solid State Commun. **7**, 275 (1969).
[6] Yu. S. Ostroukhov, O. A. Panchenko, and A. A. Kharlamov, Zh. Éksp. Teor. Fiz. **70**, 1838 (1976) [Sov. Phys. JETP **43**, 957 (1976)].
[7] D. É. Zherebchevskiĭ, V. P. Naberezhnykh, and V. V. Chabanenko, Fiz. Nizk. Temp. **12**, 434 (1978) [Sov. J. Low Temp. Phys. **12**, 229 (1978)].
[8] R. W. Stark and L. M. Falicov, Phys. Rev. Lett. **19**, 795 (1967).
[9] A. A. Galkin, V. A. Mishin, L. T. Tsymbal, and A. N. Cherkasov, Zh. Éksp. Teor. Fiz. **80**, 1861 (1981) [Sov. Phys. JETP **53**, 1030 (1981)].
[10] O. L. Steenhaut and R. G. Goodrich, Phys. Rev. B **1**, 4511 (1970).
[11] W. A. Reed and G. F. Brennert, Phys. Rev. **130**, 565 (1963).
[12] M. Ya. Azbel' and M. I. Kaganov, Dokl. Akad. Nauk SSSR **95**, 41 (1954).
[13] R. Alig, Phys. Rev. **165**, 833 (1968).
[14] M. Yamamoto, Phys. Lett. A **107**, 337 (1985).
[15] É. A. Kaner and V. G. Skobov, Usp. Fiz. Nauk **89**, 367 (1966) [Sov. Phys. Usp. **9**, 480 (1967)].
[16] L. V. Volkova, L. T. Tsymbal, and A. N. Cherkasov, Fiz. Nizk. Temp. **9**, 1262 (1983) [Sov. J. Low Temp. Phys. **9**, 649 (1983)].
[17] T. F. Butenko, V. T. Vitchinkin, A. A. Galkin, A. M. Grishin, V. A. Mishin, L. T. Tsymbal, and A. N. Cherkasov, Zh. Éksp. Teor. Fiz. **78**, 1811 (1980) [Sov. Phys. JETP **51**, 909 (1980)].
[18] A. A. Mitryaev and O. A. Panchenko, Fiz. Nizk. Temp. **3**, 850 (1977) [Sov. J. Low Temp. Phys. **3**, 411 (1977)].
[19] V. G. Peschanskiĭ and M. Ya. Azbel', Zh. Éksp. Teor. Fiz. **55**, 1980 (1968) [Sov. Phys. JETP **28**, 1045 (1969)].
[20] M. Ya. Azbel' and S. Ya. Rakhmanov, Zh. Éksp. Teor. Fiz. **57**, 295 (1969) [Sov. Phys. JETP **30**, 163 (1970)].
[21] M. Ya. Azbel' and V. G. Peschanskiĭ, Zh. Éksp. Teor. Fiz. **49**, 572 (1965) [Sov. Phys. JETP **22**, 399 (1966)].
[22] V. S. Tsoĭ and I. I. Razgonov, JETP Lett. **25**, 26 (1977).
[23] V. A. Mishin, L. T. Tsymbal, and A. N. Cherkasov, Fiz. Nizk. Temp. **10**, 1285 (1984) [Sov. J. Low Temp. Phys. **10**, 675 (1984)].

Translated by Steve Torstveit

Field, temperature, and concentration dependences of the magnetic susceptibility of bismuth–antimony alloys

G. P. Mikitik*⁾ and Yu. V. Sharlaĭ

B. Verkin Institute for Low Temperatures Physics and Engineering, National Academy of Sciences of Ukraine, pr. Lenina 47, 310164 Kharkov, Ukraine
(Submitted April 9, 1999; revised August 11, 1999)
Fiz. Nizk. Temp. **26**, 54–64 (January 2000)

In the framework of the McClure model, which describes the electronic energy spectrum of bismuth and its alloys in the neighborhood of the L point of the Brillouin zone, an expression is obtained for the electron energy levels in a magnetic field. This expression is used to calculate the magnetic susceptibility of bismuth alloys at arbitrary magnetic fields. It is shown that the theoretical results are in good agreement with the entire set of published experimental data on the field, temperature, and concentration dependences of the magnetic susceptibility of bismuth–antimony alloys. © *2000 American Institute of Physics.*
[S1063-777X(00)00501-6]

INTRODUCTION

The electronic band structure of bismuth and its alloys with antimony has been the subject of many papers (see, e.g., Refs. 1 and 2 and the references cited therein). It has been established that the Fermi surface of bismuth and its alloys (at low concentrations of antimony) consists of one hole ellipsoid, located at the T point, and three closed electron surfaces of nearly ellipsoidal shape, centered at the L points of the Brillouin zone. Another circumstance that is extremely important for understanding many of the properties of bismuth is that in the neighborhood of the L point the conduction band is separated by only a small energy gap from another, filled band. The detailed study of the energy spectra of the charge carriers near the L and T points is done mainly by methods based on oscillation and resonance effects. By now the values of the main parameters characterizing the band structure of bismuth and its alloys with antimony have been determined by these methods.[2]

The smooth (nonoscillatory with respect to the magnetic field H) part of the magnetic susceptibility of the solid solutions $Bi_{1-x}Sb_x$ exhibits noticeable (and often nonmonotonic) changes upon variations of H, the temperature T, the antimony concentration x, and the admixture of dopants that shift the level of the chemical potential ζ of the alloy.[3–7] These changes in the susceptibility are due to electronic states located near the L points and belonging to two bands separated by a small energy gap.[8–10] The rest of the electronic states all give a contribution to the magnetic susceptibility that is practically independent of T, ζ, H, and x and represents a constant background. The study of the ''variable'' contribution to the magnetic susceptibility (i.e., its dependences on T, ζ, H, and x) will make it possible to check and refine the data on the electronic band structure in the neighborhood of the L point as obtained from investigations of oscillation and resonance effects.

Calculations of the special (or ''variable'') contribution to the magnetic susceptibility of bismuth and its alloys in the

limit $H \to 0$ were done in Ref. 8–10. The models of the electronic band structure[11,12] used in Refs. 8 and 9 would later be found to give a poor description of the spectrum of bismuth alloys in the neighborhood of the L point. In Ref. 10 the magnetic susceptibility was calculated using a spectrum which is intermediate in accuracy between those proposed in Ref. 13 and in Refs. 14 and 15; both of these last provide a good description of the entire set of experimental data on oscillation and resonance effects in bismuth alloys. However, in Ref. 10 the theoretical and experimental results were compared only for the dependences of the magnetic susceptibility χ on ζ and x, and the comparison was done using values[16] of the spectrum parameters that were later revised considerably.[2] In Ref. 17 the same model of the spectrum as in Ref. 10 was used to calculate the field dependence of the magnetic susceptibility, but only in low magnetic fields. For high magnetic fields a calculation of χ was done in Refs. 6 and 9, but with the use of unrealistic, oversimplified models of the spectrum.[11,12] Thus, at the present time there is no complete quantitative description of the experimental curves of the magnetic susceptibility of bismuth alloys as a function of H, T, ζ, and x.

It was shown in Ref. 18 that under conditions of degeneracy of the electronic energy bands of the crystal in a weak magnetic field ($H \to 0$) there can be giant anomalies of the magnetic susceptibility, and the types of degeneracy of the bands which can lead to such anomalies were listed. In Ref. 19 the problem of the electron energy levels in a magnetic field was solved exactly for two of these types (those most often encountered in crystals), and the special contribution to the magnetic susceptibility was calculated for arbitrary values of H. As expected, this contribution depends strongly on H, ζ, and T. The spectrum of bismuth–antimony alloys in the neighborhood of the L point of the Brillouin zone is close to degenerate and is characterized by the circumstance that for a nonzero gap in the spectrum, the type of degeneracy is intermediate between those considered in Ref. 18. This is what accounts for the strong field, temperature, and concen-

tration dependences of χ in these alloys. However, a detailed comparison of the theoretical and experimental results must be done with allowance for the aforementioned feature of the spectrum of bismuth alloys. Therefore, generalizing the results of Ref. 19, in Sec. 1 of the present paper we give a solution to the problem of the energy levels of an electron in a magnetic field for the McClure spectrum,[13] and in Sec. 2 we obtain the corresponding expressions for the magnetic susceptibility, valid for arbitrary H. In Sec. 3 we use these expressions to compare the theoretical and published experimental results for the field, temperature, and concentration dependences of χ in $Bi_{1-x}Sb_x$ alloys. We conclude with a summary of our findings.

1. SPECTRUM

As we said in the Introduction, the dependences of the magnetic susceptibility on the field and on temperature, impurity concentration, and other external parameters are governed mainly by the electronic states located in the neighborhoods of the L points of the Brillouin zone and belonging to two bands which lie close to each other and to the level of the chemical potential. These electronic states are described using several models of the energy spectrum which have different degrees of accuracy in terms of the parameter

$$\delta = \frac{\varepsilon_0}{E_0} \ll 1,$$

where ε_0 is the characteristic energy scale for the two nearby bands, and E_0 is the energy distance from these bands to the nearest of the remaining bands. The most complete models[10,14,15] have an accuracy of order δ. However, at present the values of the parameters of the spectrum have all been determined for the simpler McClure model,[13] which describes the spectrum with an accuracy of order $\delta^{1/2}$. We will use the McClure model here. In it the Hamiltonian of the electrons in the neighborhood of an L point has the form

$$\mathcal{H} = \begin{pmatrix} \Delta + K_c & 0 & t & u \\ 0 & \Delta + K_c & -u^* & t^* \\ t^* & -u & -\Delta - K_v & 0 \\ u^* & t & 0 & -\Delta - K_v \end{pmatrix}. \quad (1)$$

Here and below the energy and chemical potential ζ are reckoned from the center of the energy gap 2Δ (here $\varepsilon_0 \sim 2\Delta, |\zeta|$) which separates the two bands, denoted c and v, which are nearly twofold degenerate at this point. The quantities t, u, K_c, and K_v are given by the formulas

$$t = q_1 k_1, \quad u = q_2 k_2 + q_3 k_3, \quad K_{c,v} = \frac{\alpha_{22}^{c;v}}{2} k_2^2, \quad (2)$$

in which q_1, q_3, and $\alpha_{22}^{c;v}$ are real parameters of the model, and q_2 is a complex number. The origin of coordinates for the wave vector $\mathbf{k}$ is at the L point. The axis 1 is along the binary axis, and axis 2 is along the length of the Fermi surface of pure bismuth at the L point, i.e., at an angle $\varphi \approx 6°$ to the bisector direction. For pure bismuth $Re(q_2) = 0$. In

$Bi_{1-x}Sb_x$ alloys the dependences of the parameters q_i, $\alpha_{22}^{c,v}$, and Δ on the antimony concentration x are well described by the linear functions[2]

$$q_1 = 0.457 - 0.188x; \quad \alpha_{22}^c = 0.615 + 0.4x;$$

$$Im(q_2) = 0.03 - 0.04x; \quad \alpha_{22}^v = 1.1 + 0.7x; \quad (3)$$

$$q_3 = 0.344; \quad 2\Delta = (10 - 242x) \text{ meV}$$

(q_i and $\alpha_{22}^{c;v}$ are given in atomic units, a.u.). In addition, as x increases, the parameter $q_2(x)$ generally acquires a real part.[10] A nonzero $Re(q_2)$ causes the long direction of the electronic isoenergy surfaces to deviate from the axis 2 by an angle $\delta\varphi \sim (Re(q_2)/q_3)$. Such a deviation was actually observed in Ref. 16, and it follows from the data of that study that

$$Re(q_2) \sim 0.05x.$$

The band energies $\varepsilon_c(\mathbf{k})$ and $\varepsilon_v(\mathbf{k})$ are found from the equations

$$\left[\varepsilon - \frac{1}{4} (\alpha_{22}^c - \alpha_{22}^v) k_2^2 \right]^2 = E^2, \quad (4)$$

where

$$E^2 = \left[\Delta + \frac{1}{4} (\alpha_{22}^c + \alpha_{22}^v) k_2^2 \right]^2 + q_1^2 k_1^2 + |q_2|^2 k_2^2$$
$$+ q_3^2 k_3^2 + 2 q_3 Re(q_2) k_2 k_3. \quad (5)$$

The relative position of these bands as a function of the antimony concentration x is shown in Fig. 1.
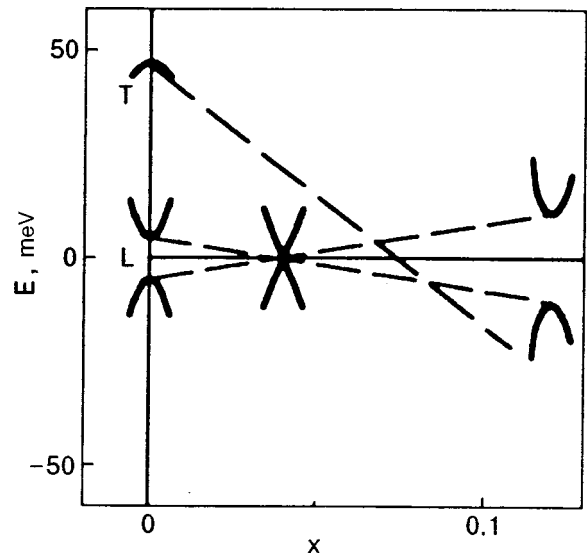
FIG. 1. Diagram of the changes in the electronic energy spectrum of $Bi_{1-x}Sb_x$ alloys at the L and T points of the Brillouin zone. The dashed lines indicate the path of the band edges $\varepsilon_c(0)$ and $\varepsilon_v(0)$ at the L points and $\varepsilon_T(0)$ at the T point as x is changed. The lines were constructed using formulas (3) and (10). At $x \approx 0.04$ the gap in the spectrum at the L point goes to zero, and for $x > 0.07$ the alloy undergoes a transition to a semiconducting state. The solid curves show a schematic illustration of $\varepsilon_c(\mathbf{k})$, $\varepsilon_v(\mathbf{k})$, and $\varepsilon_T(\mathbf{k})$ at the respective points.

The spectrum of electrons in a magnetic field **H** directed along the k_2 axis can be obtained from the general expression[19]

$$S(\varepsilon_n, k_2) = \frac{2\pi e H}{c\hbar} n, \tag{6}$$

where e is the absolute value of the electron charge, $S(\varepsilon_n, k_2)$ is the cross-sectional area of the isoenergy surface on a plane $k_2 = \text{const}$, and n is a nonnegative integer. Here it should be kept in mind that the energy levels ε_n with $n > 0$ are twofold degenerate. In the derivation of (6) we neglected the direct interaction of the electron spin with the magnetic field, since the purely spin contribution to the magnetic susceptibility is of order δ (but the spin–orbit interaction is taken into account in all the formulas given above). We note that, although the quantization condition (6) has the quasi-classical form, in this case it gives the exact eigenvalues for the energy of an electron with the Hamiltonian (1), (2). From Eqs. (4)–(6) we obtain

$$\varepsilon_n^{c,v}(k_2, H) = \left(\frac{\alpha_{22}^2 - \alpha_{22}^v}{4}\right)k_2^2 \pm \left[\alpha H n + \left(\Delta + \frac{\alpha_{22}^c + \alpha_{22}^v}{4}k_2^2\right)^2 \right.$$
$$\left. + (\text{Im}(q_2))^2 k_2^2\right]^{1/2}, \tag{7}$$

where $\alpha = 2e|q_1 q_3|/c\hbar$. If the magnetic field is directed at an angle θ to the k_2 axis, then, as was shown in Ref. 19, to an accuracy of $\delta \tan^2\theta$ the eigenvalues $\varepsilon_n^{c,v}(k_2, H)$ are described, as before, by formula (7) but with $H\cos\theta$ substituted for H.

Besides the electronic states in the neighborhoods of the L points of the Brillouin zone, bismuth also has hole states in the neighborhood of the T point. These states have the energy spectrum[1]

$$\varepsilon_T(\mathbf{k}) = E_T - \frac{\hbar^2}{2m_1^h}(k_1^2 + k_2^2) - \frac{\hbar^2}{2m_3^h}k_3^2. \tag{8}$$

Here the values of the effective masses m_1^h and m_3^h are

$$m_1^h = 0.212 \text{ a.u.}, \quad m_3^h = 0.0639 \text{ a.u.}, \tag{9}$$

k is reckoned from the T point, the axes 1 and 2 coincide with the binary and bisector axes, respectively, and E_T is the energy of the band edge, which in $Bi_{1-x}Sb_x$ alloys falls off linearly with increasing x (see Fig. 1):

$$E_T = (46.9 - 601.26x) \text{ meV}. \tag{10}$$

The contribution to χ from the hole states at the T point is small compared to the contribution from the electronic states near the L points and is of order δ. This is because of the relatively large masses $m_{1,3}^h$ and, accordingly, the small distances between energy levels ε_n^T in a magnetic field:

$$\varepsilon_n^T(k_2) = E_T - \frac{\hbar e H}{c\sqrt{m_1^h m_3^h}}\left(n + \frac{1}{2}\right) - \frac{\hbar^2 k_2^2}{2m_1^h}. \tag{11}$$

However, while neglecting the contribution of these states to the susceptibility, one must take into account their influence on the position of the chemical potential of the electrons in bismuth–antimony alloys.

2. CALCULATION OF THE MAGNETIC SUSCEPTIBILITY

The magnetic susceptibility of bismuth and its alloys can be written as the sum of a special contribution due to the electronic states near the three L points and a background term due to all the remaining states. The background term is practically independent of the magnetic field and temperature and even remains constant upon variations of the chemical potential $|\delta\zeta| \sim |\Delta|$. The special contribution to the magnetic susceptibility consists of a sum of three terms due to the states near the respective L points. Each of this terms can be obtained from the following expression for the Ω potential (per unit volume):

$$\Omega(H_\theta) = -\frac{e H_\theta T}{4\pi^2 c\hbar}\sum_{c,v}\sum_{n=0}^{\prime}\int_{-\infty}^{+\infty}dk_2$$
$$\times \ln\left\{1 + \exp\left(\frac{\zeta - \varepsilon_n^{c,v}(k_2, H_\theta)}{T}\right)\right\}, \tag{12}$$

where the prime on the summation sign means that in taking the sum over n the terms with $n > 0$ must be doubled; H_θ is the projection of the magnetic field on the k_2 axis at the given L point. In an experiment one measures the quantity

$$\chi = h_i h_j \chi^{ij},$$

where $\mathbf{h} = \mathbf{H}/H$ is a unit vector in the magnetic field direction, and the differential magnetic susceptibility χ^{ij} is given by the expression

$$\chi^{ij} = -\frac{\partial^2 \Omega}{\partial H_i \partial H_j}.$$

Since the Ω potential (12) depends on H only through H_θ, in our approximation (to accuracy $\delta^{1/2}$) we have

$$\chi = \sum_{i=1}^{3} \cos^2\theta_l \chi^{22}(H\cos\theta_l),$$

where θ_l are the angles between the magnetic field **H** and the k_2 axis for the three L points.

In the case of weak magnetic fields, for which the characteristic distance between energy levels in the magnetic field obeys $\delta\varepsilon_H \ll T$, we integrate (12) by parts, use the Euler–Maclaurin summation formula, and differentiate with respect to the magnetic field to obtain for the susceptibility an expression of the form $\chi = \chi_0 + \chi_1 H^2$, where the expressions for the H-independent terms χ_0 and χ_1 are the same as those obtained previously in Refs. 10 and 17.

Let us now analyze χ^{22} in the case of high magnetic fields, $\delta\varepsilon_H \gg T$. The contribution of the electrons in the conduction band to the magnetic susceptibility can be calculated directly using formula (12), since the number of filled levels ε_n^c is finite. To calculate the contribution of the filled band v to χ^{22}, we once again integrate (12) by parts as many times as necessary, use the Poisson summation formula, and set $T = 0$ ($\delta\varepsilon_H \gg T$). The resulting formula includes one summation and integrations over n and k_2. If the quantity $(d\varepsilon_n^v/dn)$ in this formula [where ε_n^v is defined in Eq. (7)] is written as

$$\left|\frac{d\varepsilon_n^v}{dn}\right| = \frac{2}{\sqrt{\pi}} \int_0^\infty dt\, \exp\left\{-\left(\frac{d\varepsilon_n^v}{dn}\right)^{-2} t^2\right\},$$

then the summation and integration over n and k_2 can be done in explicit form. As a result, we obtain for $|\zeta| < |\Delta|$

$$\chi^{22}(H) = -\frac{1}{4\pi^2}\left(\frac{e}{c\hbar}\right)\alpha\left(\frac{|Q|}{\pi|\Delta(\alpha_{22}^c + \alpha_{22}^v)|}\right)^{1/2}$$

$$\times \int_0^\infty dt\, f\left(\frac{H}{H_\Delta} t^2\right) e^{(Q^2-2)t^2} K_{1/4}(Q^2 t^2), \quad (13)$$

where Q is the following dimensionless combination of parameters:

$$Q = \operatorname{sgn}[\Delta(\alpha_{22}^c + \alpha_{22}^v)]\left(1 + \frac{2(\operatorname{Im}(q_2))^2}{\Delta(\alpha_{22}^c + \alpha_{22}^v)}\right); \quad (14)$$

H_Δ is the characteristic magnetic field, at which $\delta\varepsilon_H \sim |\Delta|$, i.e., $H_\Delta = \Delta^2/\alpha$; $K_{1/4}(x)$ is a modified Bessel function, and

$$f(x) = 2\left(\frac{x\coth x - 1}{\sinh^2 x}\right).$$

In the derivation of expression (13) we have assumed that the parameter

$$\gamma = \left|\frac{\alpha_{22}^c + \alpha_{22}^v}{\alpha_{22}^c - \alpha_{22}^v}\right| \geq 1. \quad (15)$$

We note that this condition is satisfied for $Bi_{1-x}Sb_x$ alloys for any antimony concentrations x.

If the magnetic fields are such that $H \ll H_\Delta$, then the magnetic susceptibility (13) is independent of the field, and it is described by the same expression as that given in Ref. 10 for $T \to 0$. On the other hand, if $H \gg Q^2 H_\Delta$ (for bismuth–antimony alloys $Q \gg 1$ for $x \sim 0.04$, while for other antimony concentrations $Q \gtrsim 1$ in the region $x < 0.2$), then

$$\chi^{22}(H) \approx -A\frac{e}{c\hbar}\frac{\alpha^{3/4}}{|\alpha_{22}^c + \alpha_{22}^v|^{1/2}} H^{-1/4}, \quad (16)$$

where

$$A = \frac{21}{32}\frac{\zeta(7/4)\cos(\pi/8)\Gamma(1/4)}{2^{3/4}\pi^{13/4}} \approx 6.21\times 10^{-2}; \quad (17)$$

$\zeta(x)$ is the Riemann zeta function, and $\Gamma(x)$ is the gamma function. Formulas (16) and (17) agree with those obtained in Ref. 9.

In Ref. 19 the field dependence of the magnetic susceptibility of electrons was investigated for two of the three types of degeneracy of the energy bands of crystals leading to strong field dependence. According to Eqs. (3)–(5), in $Bi_{0.96}Sb_{0.04}$ alloys there is band degeneracy of the first type according to the classification of Ref. 18, i.e., a band splitting that is linear in the wave vector **k** in the neighborhood of the degeneracy point L. However, bismuth alloys are characterized by relatively small values of the matrix element q_2 responsible for this linear splitting along the k_2 axis. That is why we took terms quadratic in k_2 into account in the Hamiltonian (1)–(3). According to Eqs. (3)–(5), as the point **k** moves away from the L point along the k_2 axis, the splitting

of the bands rapidly deviates from linearity and approaches a quadratic law. This leads to a more complicated dependence of $\chi(H)$ than in Ref. 19 [see Eq. (13)]. The limiting expression (16) corresponds to the case when the initial (linear in k_2) part of the band splitting can be neglected, and one can assume that $|\varepsilon_c(k_2) - \varepsilon_v(k_2)| \propto k_2^2$ (we note that this approximation is justified even for $\Delta \neq 0$). Thus formula (16) actually describes the behavior of $\chi(H)$ for the third type of band degeneracy,[18] for which a giant anomaly of the magnetic susceptibility can occur and which was not considered in Ref. 19. Here Eq. (15) corresponds to the condition when $\varepsilon_c(k_2)$ and $\varepsilon_v(k_2)$ have different signs. If $\varepsilon_c(k_2)$ and $\varepsilon_v(k_2)$ had the same sign, i.e., if $\gamma < 1$, then, as one can show, for $H \gg H_\Delta Q^2 \gamma^2/(1-\gamma^2)$ the magnetic susceptibility is described as before by formula (16) but with a different constant A:

$$A = \frac{21}{16}\frac{\zeta(7/4)\cos(\pi/8)}{2^{1/4}\pi^{11/4}\Gamma(1/4)}\gamma^{1/2}F\left(\frac{1}{4}, -\frac{1}{4}, \frac{5}{4}, \gamma^2\right), \quad (18)$$

where F is the hypergeometric function. In the limiting case $\gamma = 0$ (and $|q_2| = 0$) we would arrive at a line of degeneracy of the bands, i.e., at the second case according to the classification of Ref. 18. Then expression (16) with the factor A from (18) agrees with the expression obtained in Ref. 19. Finally, we note that in the case of band degeneracy at an L point or for small Δ the parameter $Q \gg 1$, and there is a region of magnetic fields $H_\Delta \ll H \ll Q^2 H_\Delta$ in which the part of the band splitting that is linear in k_2 plays the governing role in $\chi(H)$. Then it follows from Eq. (13) that

$$\chi^{22}(H) = -\frac{1}{6\pi^2}\frac{e}{c\hbar}\frac{\alpha}{2|\operatorname{Im}(q_2)|}\ln\left(\frac{H_\Delta}{H}\right)^{1/2}.$$

With an accuracy up to the background constant, this result agrees with that obtained in Ref. 19 for the first type of band degeneracy. Thus the strong field dependence of the magnetic susceptibility of bismuth alloys is a manifestation of the fact that the spectrum of these alloys is close to those cases of band degeneracy which lead to a giant anomaly of the magnetic susceptibility.[18]

The chemical potential ζ of the electrons in the crystal, generally speaking, itself depends on the magnetic field. This dependence is determined from the condition that the total electron density is constant:

$$\nu \equiv -\frac{\partial\Omega}{\partial\zeta} = \text{const.} \quad (19)$$

To evaluate the magnetic susceptibility at constant ν, it is necessary to go over from the Ω potential to the free energy. As a result, for $\chi^{ij}(H,\nu)$ we have[19]

$$\chi^{ij}(H,\nu) = \left[\chi^{ij}(H,\zeta) - \frac{\partial\nu}{\partial H_i}\frac{\partial\nu}{\partial H_j}\left(\frac{\partial\nu}{\partial\zeta}\right)^{-1}\right]_{\zeta=\zeta(H,\nu)}. \quad (20)$$

When obtaining the function $\zeta(H,\nu)$ using formula (19) it is necessary to take into account the contributions to the Ω potential not only from the electronic states near the L points but also the states near the T point, and also the influence of donor and acceptor impurities. The states at the T point give

a term in the Ω potential which is determined by formula (12) with the energy levels from (11). Impurities, first, cause scattering of the charge carriers and, second, give an additional impurity contribution to the Ω potential in semiconducting alloys. The scattering of charge carriers can be taken into account in a simple way by the introduction of a Dingle temperature T_D, i.e., by replacing T by $T+T_D$ in all the formulas. In semiconducting alloys of $Bi_{1-x}Sb_x$ ($x>0.07$) we consider the impurity contribution to the Ω potential, Ω_{imp}, in the limiting case of lightly and heavily doped n-type semiconductors. The case of light doping is characterized by the presence of carrier–impurity bound states, the energies of which form a narrow impurity band lying in the gap of the spectrum. In bismuth–antimony alloys these energies ε_i practically coincide with the band edge, i.e., $\varepsilon_i \approx |\Delta|$. We then have

$$\Omega_{imp} = -T\nu_{imp}\ln\left(1+\exp\left(\frac{\zeta-\varepsilon_i}{T}\right)\right), \quad \nu=\nu_{imp}, \quad (21)$$

where ν_{imp} is the density of doping impurities. As we know,[20] the main condition for the existence of impurity levels is that the average size d of the carrier–impurity bound state be small compared to the distance between impurities, i.e., the condition $d\nu_{imp}^{1/3}\ll 1$. The dimension d is of the order of the ''Bohr'' radius $d\sim a_B^* = \kappa\hbar^2/e^2 m^*$, where κ is the dielectric constant of the crystal and m^* is the effective mass of a charge carrier. For a heavily doped semiconductor $d\nu_{imp}^{1/3}\geqslant 1$, and carrier–impurity bound states do not arise. In this case we have

$$\Omega_{imp}=0, \quad \nu=\nu_{imp}, \quad (22)$$

i.e., the semiconductor is transformed into a ''poor'' metal with an intrinsic electron density ν_{imp}. If the semiconductor is in a magnetic field H, then we must take into account the dependence on H of the average size d of a localized state. In a weak magnetic field we have $d\sim a_B^*$, as before. However, when the magnetic length $\lambda\cong(\hbar c/eH)^{1/2}$ becomes smaller than a_B^*, the size of the localized state in the directions perpendicular to $\mathbf{H}$ is determined by the value of λ, and the average size $d\sim(\lambda^2 a_B^*)^{1/3}$ falls off with increasing H. Therefore, in sufficiently high fields $H\geqslant H_{cr} \sim(\hbar c/e)\nu_{imp}a_B^*$ there occurs a magnetic ''freeze-out'' of the electrons,[21] and the heavily doped semiconductor is transformed into a lightly doped one.

3. COMPARISON OF THE RESULTS OF THE CALCULATION OF χ WITH EXPERIMENTAL DATA

In Refs. 3–7 significant changes in χ were observed in bismuth–antimony alloys upon variations in the magnetic field, temperature, antimony concentration, or chemical potential, the level of the last being regulated by the introduction of doping impurities in the alloy. Our theoretical analysis of the dependence of the susceptibility on H, T, x, and ζ will be done on the basis of the formulas obtained in Sec. 2, using the values in (3), (9), and (10) for the parameters of the spectrum.

Let us first consider the dependence of $\chi(H\to 0)$ on the antimony concentration x in $Bi_{1-x}Sb_x$ alloys (Fig. 2). Ex-
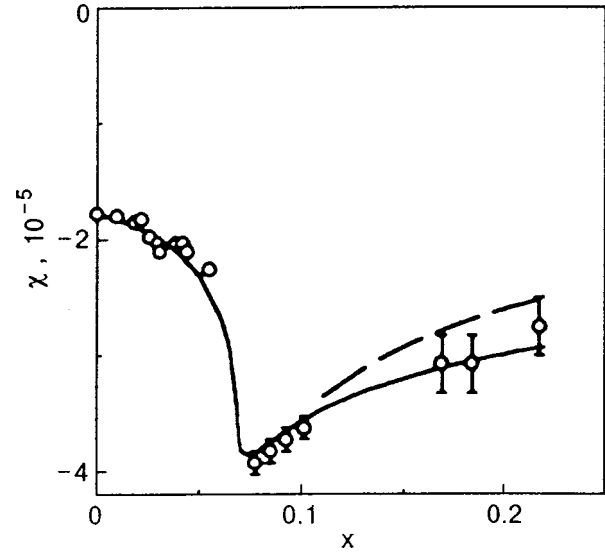

FIG. 2. Low-field magnetic susceptibility χ as a function of the antimony concentration x in $Bi_{1-x}Sb_x$ alloys. The magnetic field is applied in the basal plane of the crystal. $T=4.2$ K. χ is normalized to a unit volume; $\bigcirc$—experimental data of Ref. 7; solid curve—calculation according to the formulas of Ref. 10 with the use of the parameter values given in Eqs. (3), (9), (10); dashed curve—calculation done in Ref. 10 using the spectrum parameters given in Ref. 16.

pressions for the magnetic susceptibility in low fields were obtained previously.[10] In the present paper, however, the calculations using these expressions were done with the new values of the parameters (3), (9), (10). In comparing the theoretical and experimental results we chose the constant background in the susceptibility so as to obtain coincidence with the corresponding values for pure bismuth. In the calculation it is necessary to find the dependence of the chemical potential ζ on x for the semimetallic alloys $Bi_{1-x}Sb_x$ ($x<0.07$) from the condition that there be equal numbers of electrons and holes at the L and T points, respectively. In the region of semiconducting alloys ($x>0.07$) the chemical potential is assumed to lie in the gap of the spectrum between the valence band and conduction band, and the impurity concentration ν_{imp} is taken equal to zero. From the results presented in Fig. 2 it follows that the use of the parameter set (3), (9), (10) provides a better description of the experimental data for the semiconducting alloys than does the set from Ref. 16. In addition, we have calculated the dependence of χ in a weak field H on the level of the chemical potential ζ for the alloys $Bi_{0.92}Sb_{0.08}$ and $Bi_{0.97}Sb_{0.03}$. The results of the calculation with the new parameter values agreed with the results of Ref. 10 to within the limits of experimental error.

Figure 3 shows the field dependence of the magnetization M of pure bismuth in magnetic fields so high that the only the lowest Landau level in the conduction band remains occupied, and there are no de Haas–van Alphen oscillations. In accordance with Eqs. (13) and (16), this curve is nonlinear in H. Here for a detailed comparison of the results of the calculation with the experimental data of Ref. 6, we took into consideration that $\zeta>\Delta$ in bismuth, and we added to Eq. (13) the contribution due to the conduction electrons. The expression for this contribution was obtained directly from
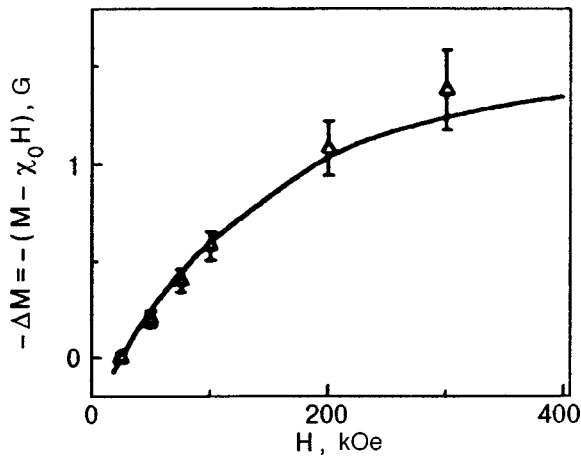
FIG. 3. Magnetization M of pure bismuth as a function of the magnetic field H, directed along the binary axis, for $T=20$ K and $H \geqslant 20$ kOe; △—the experimental data of Ref. 6; solid curve—the calculation of the present paper.

FIG. 5. Magnetic susceptibility χ as a function of magnetic field H for fields greater than 3 kOe, for the same alloy as in Fig. 4. The calculation was done using formula (13) for two orientations of the magnetic field—along the binary axis and along the bisector direction. The results of the calculation for the two cases practically coincide (solid curve); △, ○—the experimental data of Ref. 7 for the first and second of the indicated directions of **H**, respectively. The values of x, ν_{imp}, T, and T_D are the same as in Fig. 4.

Eq. (12). We see that the agreement of the theoretical and experimental results is quite good, and it is achieved without the use of any adjustable parameters.

The results of the calculations of the field dependence of the magnetic susceptibility of the semiconducting alloys $Bi_{0.92}Sb_{0.08}$ with a concentration of donor impurities $\nu_{\text{imp}} = 10^{15}$ cm^{-3} are presented in Fig. 4. The two $\chi(H)$ curves shown differ in that they correspond to the dependence of ζ on H obtained for heavily and lightly doped semiconductors. For the given value of ν_{imp} an estimate of the field H_{cr} gives $H_{\text{cr}} \sim 1$ kOe. In accordance with the arguments set forth in Sec. 2, at fields much smaller than H_{cr} the theoretical curve corresponding to the case of heavy doping gives a good description of the experiment. For magnetic fields that are so
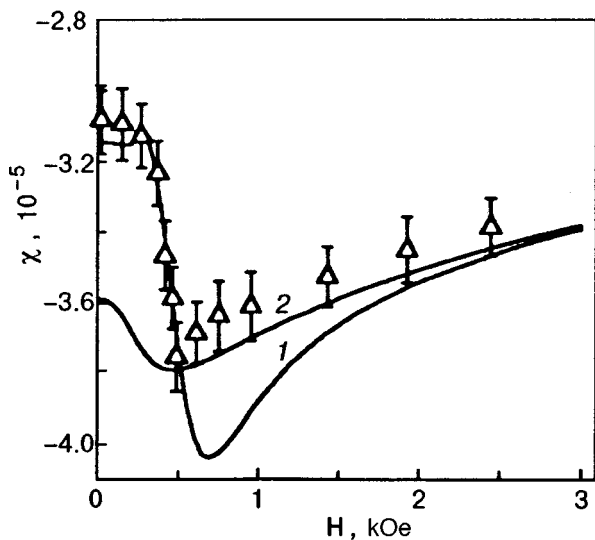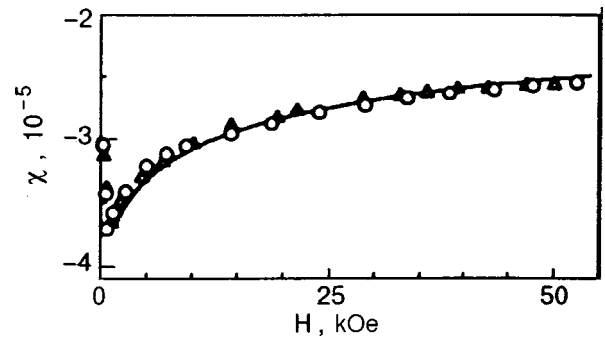

FIG. 4. Magnetic susceptibility χ as a function of the magnetic field H for the semiconducting alloy $Bi_{0.92}Sb_{0.08}$ with a concentration of donor impurities $\nu_{\text{imp}} = 10^{15}$ cm^{-3}. The magnetic field is directed along the binary axis; $T=4.2$ K, $T_D = 3.5$ K; χ is the susceptibility per unit volume. The curves *1* and *2* correspond to the cases of heavily doped [Eq. (22)] and lightly doped [Eq. (21)] semiconductors, respectively; △—the experimental data[7] for an alloy $Bi_{1-x}Sb_x$ with $x=0.076 \pm 0.005$.

weak ($H < 50$ Oe) that the characteristic distance between electronic energy levels at the L points is much less than the temperature ($T=4.2$ K), the aforementioned curve is approximated by the expression $\chi(H) = \chi_0 + \chi_1 H^2$, and the values of χ_0 and χ_1 agree with those calculated using the formulas in Refs. 10 and 17. As the magnetic field is increased a transition to the case of light doping occurs on account of the magnetic freeze-out of the electrons, and, accordingly, in the region $H > H_{\text{cr}}$ the agreement with experiment is better for the other curve. As the magnetic field is increased further, the chemical potential of the electrons comes to lie in the gap of the spectrum, and the field dependence of $\zeta(H)$ ceases to influence the magnetic susceptibility; then the theoretical curves in Fig. 4 practically coincide. Here one can find $\chi(H)$ directly using formula (13). The results of this calculation are shown in Fig. 5. We see that, in complete agreement with experiment, the magnetic susceptibility is practically independent of the direction of the magnetic field **H** in the basal plane.

Figure 6 shows the results of calculations of $\chi(H)$ for the alloy $Bi_{0.92}Sb_{0.08}$ with admixtures of the dopant telluride at concentrations $\nu_{\text{imp}} \approx 3 \times 10^{16}$ but 4×10^{17} cm^{-3}. For the first of these concentrations $H_{\text{cr}} \sim 30$ kOe, and in fields lower than this, the difference in χ for the heavily and lightly doped semiconductor practically vanishes. For the second of these concentrations $H_{\text{cr}} \sim 400$ kOe, and the alloy remains heavily doped throughout the magnetic field region considered. Thus for an analysis of the $\chi(H)$ curves it suffices to use the formulas corresponding to a heavily doped semiconductor. The introduction of the donor impurity Te raises the level of ζ significantly, and the first few de Haas–van Alphen oscillations appear; these, however, cannot be described by the quasiclassical formulas. We see that, although the magnetic susceptibility is a nonmonotonic function of H, the theoretical curves rather accurately describe both the positions of the extrema of χ and the overall trend of the function $\chi(H)$. We note one final circumstance. In constructing the theoretical curves in Figs. 4–6 the Dingle temperatures T_D were chosen so as to give the best fit of these curves with the experimental data. In agreement with the existing ideas about
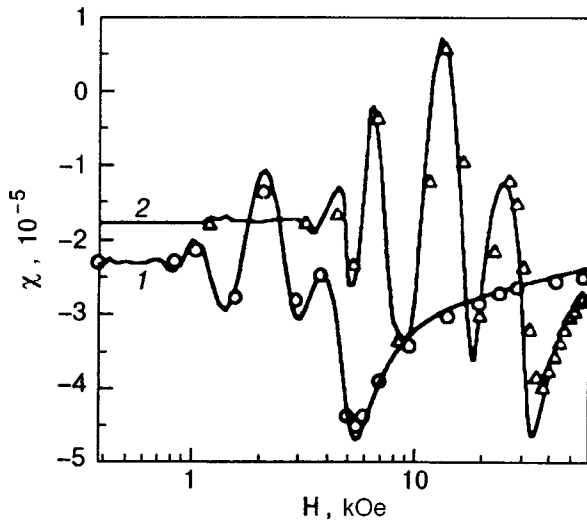
FIG. 6. Magnetic susceptibility χ as a function of magnetic field H for a field directed along the bisector direction, for the alloy $Bi_{0.92}Sb_{0.08}$ with two different concentrations of the donor impurity tellurium: $\nu_{imp} = 3 \times 10^{16}$ cm^{-3} (curve 1) and $\nu_{imp} = 4 \times 10^{17}$ cm^{-3} (curve 2). The calculation was done using formula (22); $T = 4.2$ K, $T_D = 7$ K and 11 K for curves 1 and 2, respectively; $\bigcirc, \triangle$—the experimental data of Ref. 7 for $Bi_{1-x}Sb_xTe_{0.000001}$ and $Bi_{1-x}Sb_xTe_{0.00001}$, respectively, where $x = 0.076 \pm 0.005$.

the scattering of charge carriers in heavily doped semiconductors,[20] the values obtained for T_D are of the order of order of the characteristic Bohr energies $E_B = m^*e^4/2\hbar^2\kappa^2$ and depend approximately logarithmically on ν_{imp}.

The temperature dependence of the magnetic susceptibility of bismuth–antimony alloys is shown in Fig. 7 and 8. The nonmonotonic behavior of $\chi(T)$ (Fig. 8b) is easily explained on the basis of qualitative arguments. For the alloy
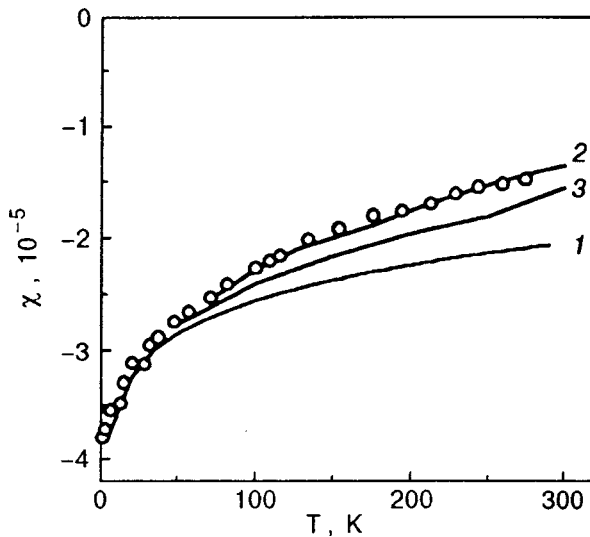

FIG. 7. Magnetic susceptibility χ as a function of temperature T in a constant magnetic field $H = 500$ Oe applied along the bisector direction, for the same alloy as in Fig. 4. Curve 1 is for temperature-independent parameters of the spectrum; curve 2 is for parameters having temperature dependences described by formulas (23) and (24); curve 3 is obtained for parameters q_1, q_3, and Δ depending on T according to Eq. (23) but for $q_2(T) = q_2(0)$; $\bigcirc$—experimental data of Ref. 7 for $Bi_{1-x}Sb_x$ with $x = 0.076 \pm 0.005$.
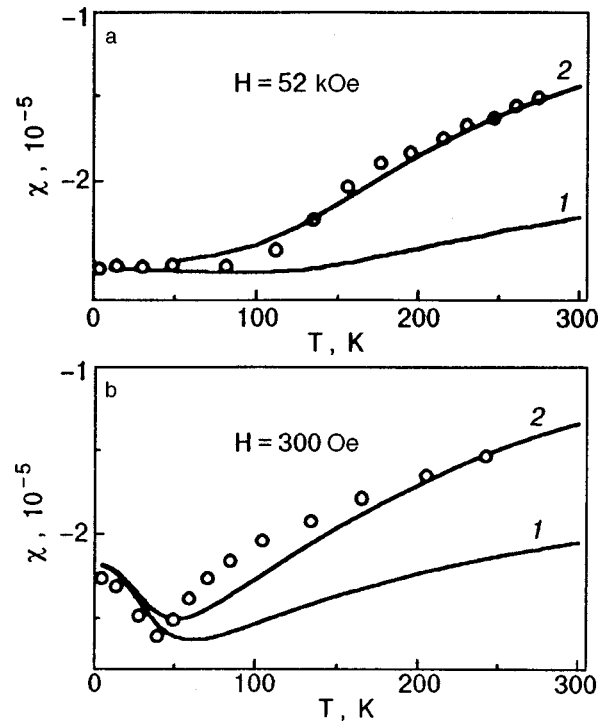

FIG. 8. Temperature dependence of χ in constant magnetic fields applied along the bisector direction, with a value of 52 kOe for the alloy $Bi_{0.92}Sb_{0.08}$ (a) and a value of 300 Oe for the alloy $Bi_{0.92}Sb_{0.08}$ with a concentration of the the donor impurity tellurium $\nu_{imp} = 3 \times 10^{16}$ cm^{-3} (b); curves 1 are for temperature-independent spectrum parameters; curves 2 are for spectrum parameters with temperature dependences described by formulas (23) and (24); $\bigcirc$—experimental data of Ref. 7 for $Bi_{1-x}Sb_x$ (a) and $Bi_{1-x}Sb_xTe_{0.000001}$ (b) with $x = 0.076 \pm 0.005$.

$Bi_{0.92}Sb_{0.08}$ at $H \lesssim 500$ Oe the characteristic distance between electron energy levels in the magnetic field $\delta\varepsilon_H$ is less than or of the order of 10 K, and the $\chi(T)$ curves in Fig. 7 and 8b actually correspond to the low-field case, when $\delta\varepsilon_H < T$. Here, as follows from the results of Ref. 18, $|\chi|$ falls off monotonically with increasing temperature if ζ lies in the gap of the spectrum or if $\zeta - |\Delta| \lesssim T$. It is just such a situation that is observed in the case with $\nu_{imp} = 10^{15}$ cm^{-3} (Fig. 7), since $\zeta - |\Delta| \lesssim 20$ K in that case. For the alloy with $\nu_{imp} = 3 \times 10^{16}$ cm^{-3} (Fig. 8b) one has $\zeta - |\Delta| \approx 120$ K at $T = 0$.

As the temperature is raised, the chemical potential of the degenerate electron gas decreases, $\zeta(0) - \zeta(T) \sim T^2/(\zeta(0) - |\Delta|)$, approaching the bottom of the conduction band. As long as $\zeta(T) - |\Delta| > T$, the behavior of χ can be explained by using the results of Ref. 18 for the function $\chi(\zeta, T = 0)$. According to those results, $|\chi|$ increases with decreasing ζ. Finally, when T becomes greater than $\zeta(T) - |\Delta|$ (i.e., for $T \gtrsim 70$ K), $|\chi|$, as we have said, begins to fall off with increasing T. This explains the appearance of an extremum of $\chi(T)$ in Fig. 8b. As to the data presented in Fig. 8a, they correspond to $\delta\varepsilon_H \sim 600$ K. As long as $T \ll \delta\varepsilon_H$ one can assume $T = 0$ in all the formulas presented in this paper, and χ is practically independent of temperature. It is only for $T \gtrsim \delta\varepsilon_H$, when a transition to the low-field case occurs, that one should expect to see an appreciable decrease of $|\chi|$ with increasing T. If it is assumed that the parameters of the spectrum do not change as the temperature increases, then the

calculated functions $\chi(T)$ give a good quantitative description of all the experimental data only for $T < 50$ K. In Ref. 22 the temperature dependences of some of the parameters of the spectrum for pure bismuth were determined from magnetooptical measurements:

$$q_1(T)q_3(T) = q_1(0)q_3(0) - 1.35 \times 10^{-4}\, T - 3.8$$
$$\times 10^{-7}\, T^2\,[\text{a.u.}], \tag{23}$$

$$\Delta(T) = \Delta(0) + 2.1 \times 10^{-3}\, T + 2.5 \times 10^{-4}\, T^2\,[\text{meV}].$$

These parameters indeed vary hardly at all for $T \leqslant 50$ K. The results of a calculation of the magnetic susceptibility with allowance for formulas (23) are presented in Fig. 7. It is seen that taking the temperature dependences (23) into account noticeably improves the agreement with the experimental data. Moreover, from the function $\chi(H)$ one can determine the temperature dependence of those parameters of the spectrum which cannot be found from magnetooptical measurements. In particular, by fitting the theoretical curve to the experimental data presented in Fig. 7, we obtain the temperature dependence $q_2(T)$:

$$q_2(T) = q_2(0) + 8.9 \times 10^{-7}\, T^2\,[\text{meV}]. \tag{24}$$

Interestingly, the use of this temperature dependence together with (23) for calculating $\chi(T)$ at another value of the magnetic field (Fig. 8a) or impurity concentration (Fig. 8b) yields a satisfactory description of the other experimental results as well.

CONCLUSION

The strong field, temperature, and concentration dependences of the magnetic susceptibility of bismuth–antimony alloys is explained by the fact that the electronic energy spectrum of these alloys is nearly degenerate. The magnetic susceptibility χ calculated in this paper for $Bi_{1-x}Sb_x$ solid solutions with the use of the McClure model gives a good quantitative description of all the aforementioned dependences, provided that one uses for the parameters of the spectrum the values reported in Ref. 2, which were obtained from oscillation and resonance effects. Here, in analyzing the field dependence of χ for the semiconducting Bi–Sb alloys, one must take into account that these alloys are heavily doped even at relatively low concentrations of donor or acceptor impurities. In particular, a comparison of the theoretical and experimental results for the alloy $Bi_{0.92}Sb_{0.08}$ shows that the Dingle temperature is a nonlinear function of the

dopant concentration ν_{imp}, and for $\nu_{\text{imp}} \sim 10^{15}\,\text{cm}^{-3}$ a magnetic freeze-out of the electrons occurs. The temperature dependence of χ appears to give evidence of an appreciable influence of the electron–phonon interaction on the magnetic susceptibility of semiconducting alloys of bismuth at $T > 50$ K. The existing experimental data can be described in the framework of an extremely simple approach in which this interaction affects only the temperature dependence of the parameters of the spectrum.

*)E-mail: mikitik@ilt.kharkov.ua

[1] V. S. Édel'man, Usp. Fiz. Nauk **123**, 257 (1977) [Sov. Phys. Usp. **20**, 819 (1977)].

[2] S. Sh. Akhmedov, R. Herrmann, K. N. Kashirin, A. Krapf, V. Kraak, Ya. G. Ponomarev, and M. V. Sudakova, Zh. Éksp. Teor. Fiz. **97**, 663 (1990) [Sov. Phys. JETP **70**, 370 (1990)].

[3] B. I. Verkin, L. B. Kuz'micheva, and I. V. Sverchkarev, JETP Lett. **6**, 225 (1967).

[4] L. Wehrli, Phys. Kondens. Mater. **8**, 87 (1968).

[5] N. B. Brandt and M. V. Semenov, Zh. Éksp. Teor. Fiz. **69**, 1072 (1975) [Sov. Phys. JETP **42**, 546 (1975)].

[6] J. W. McClure and D. Shoenberg, J. Low Temp. Phys. **22**, 233 (1976).

[7] N. B. Brandt, M. V. Semenov, and L. A. Falkovsky, J. Low Temp. Phys. **28**, 85 (1977).

[8] F. A. Buot and J. W. McClure, Phys. Rev. B **6**, 4225 (1972).

[9] S. D. Beneslavskiĭ and L. A. Fal'kovskiĭ, Zh. Éksp. Teor. Fiz. **69**, 1063 (1975) [Sov. Phys. JETP **42**, 541 (1975)].

[10] G. P. Mikitik, Fiz. Nizk. Temp. **12**, 272 (1986) [J. Low Temp. Phys. **12**, 153 (1986)].

[11] B. Lax, J. G. Mavroides, H. J. Zeiger, and R. J. Keyes, Phys. Rev. Lett. **5**, 241 (1960).

[12] A. A. Abrikosov, J. Low Temp. Phys. **8**, 315 (1972).

[13] J. W. McClure, J. Low Temp. Phys. **25**, 527 (1976).

[14] J. W. McClure and K. H. Choi, Solid State Commun. **21**, 1015 (1977).

[15] E. A. Dorofeev and L. A. Fal'kovskiĭ, Zh. Éksp. Teor. Fiz. **87**, 2202 (1984) [Sov. Phys. JETP **60**, 1273 (1984)].

[16] N. B. Brandt, R. Hermann, G. I. Golysheva, L. I. Devyatkova, D. Kusnik, V. Kraak, and Ya. G. Ponomarev, Zh. Éksp. Teor. Fiz. **83**, 2151 (1982) [Sov. Phys. JETP **56**, 1247 (1982)].

[17] G. P. Mikitik, Fiz. Nizk. Temp. **12**, 955 (1986) [Sov. J. Low Temp. Phys. **12**, 541 (1986)].

[18] G. P. Mikitik and I. V. Sverchkarev, Fiz. Nizk. Temp. **15**, 295 (1989) [Sov. J. Low Temp. Phys. **15**, 165 (1989)].

[19] G. P. Mikitik and Yu. V. Sharlaĭ, Fiz. Nizk. Temp. **22**, 762 (1996) [Low Temp. Phys. **22**, 585 (1996)].

[20] V. L. Bonch-Bruevich and S. G. Kalashnikov, *Physics of Semiconductors* [in Russian], Nauka, Moscow (1990).

[21] M. I. Dyakonov, A. L. Efros, and D. L. Mitchell, Physica A **180**, 813 (1969).

[22] M. P. Vecchi and M. S. Dresselhaus, Phys. Rev. B **10**, 771 (1974).

Low-temperature nonlinear lattices in ferroelectrics with protonic conductivity

M. B. Belonenko and E. Yu. Koleganova

*Volgograd State University, ul. 2-ya Prodol'naya 30, 400062 Volgograd, Russia**
(Submitted April 20, 1999; revised July 12, 1999)
Fiz. Nizk. Temp. **26**, 65–69 (January 2000)

An $S=1$ pseudospin formalism is constructed for ferroelectrics with protonic conductivity, the change carriers in which are protons moving along a network of hydrogen bonds. The Hamiltonian is written in the pseudospin form and in the second-quantization operator representation. A system of equations describing the state of the ferroelectric cell is obtained. A numerical analysis of this system reveals the presence of traveling nonlinear lattices that can affect the dynamical properties of the ferroelectric. © *2000 American Institute of Physics.* [S1063-777X(00)00601-0]

Hydrogen-bonded ferroelectrics, which have a phase transition of the order–disorder type, are of interest in connection with the problem of the structural and ferroelectric phase transitions caused by the ordering (disordering) of the protons on the hydrogen bonds.[1] Ordinarily the motion of a proton is treated as occurring only between two positions in the O..H–O bond, and because of the bounded nature of this motion the response of the proton subsystem to an external electric field is purely dielectric. It has been established experimentally, however, that hydrogen-bonded ferroelectrics can exhibit structural phase transitions with a fundamentally different type of ordering of the proton subsystem: the travel of the protons is not confined to the unit cell. They can undergo translational motion, with a low activation energy, over the whole crystal. The protonic conductivity in different crystals varies over a range of 10–13 orders of magnitude,[2] and it can become comparable to the conductivity of a fused sample. The construction of a consistent theory of the properties of crystals with protonic conductivity is therefore a topical problem.

We note that the substances having high protonic conductivity are compounds in which the number of protons is less than the number of hydrogen bonds. In such substances the hydrogen bond can be either occupied or unoccupied by a proton. A consistent theory of ferroelectric crystals with protonic conductivity should take into account the temperature-induced phase transition, proton (deuteron) tunneling in the hydrogen bond, and proton (deuteron) hopping from an occupied to an unoccupied hydrogen bond. Consequently, three states of the hydrogen bond must be considered: with a proton at one end of it, with a proton at the other end, and unoccupied.

If the hydrogen bond has a proton on it, the proton can be found in one of two equilibrium positions in the hydrogen-bond potential.[3,4] Assuming, as is customary, that the potential wells in which the proton moves are rather steep, neglecting the motion of the proton within each well, and assuming that the quantum-mechanical tunneling of the proton through the potential barrier between these two well lifts the degeneracy, we treat the proton on the hydrogen bond in the framework of a two-level system.[1,3,4] To each distribution of protons on the hydrogen bond we uniquely associate a displacement of the heavy ions responsible for the polarization. Thus the jth hydrogen bond can be found in three states: ''0'' — the absence of a proton on the hydrogen bond, ''+'' — the proton on the hydrogen bond is described by a symmetric wave function Ψ_+ ; ''−'' — the proton on the hydrogen bond is described by an antisymmetric wave function Ψ_- . It will be convenient to go over from the wave functions Ψ_+ and Ψ_- to a linear combination of wave functions localized in the left (Φ_L) and right (Φ_R) equilibrium positions:

$$\Psi_+ = \frac{1}{\sqrt{2}}(\Phi_L + \Phi_R); \quad \Psi_- = \frac{1}{\sqrt{2}}(\Phi_L - \Phi_R).$$

Then the jth hydrogen bond can be described with the aid of the wave function

$$\Psi_j = \begin{pmatrix} \Phi_{Lj} \\ \Phi_{oj} \\ \Phi_{Rj} \end{pmatrix},$$

where Φ_{0j} characterizes the probability that a bond will be unoccupied by a proton.[5–7]

We introduce the operators $\chi_j^{\alpha\beta} = |\Phi_{\alpha j}\rangle\langle\Phi_{\beta j}|$, which are analogs of the Hubbard operators;[8] the expectation value of the operator X_j^{00} will correspond to the number of vacancies on the hydrogen bonds, the expectation value of the operator $X_j^{LL} - X_j^{RR}$ will correspond to the polarization of the jth ferroelectric cell, and the operator $X_j^{LR} + X_j^{RL}$ will be the tunneling operator for the proton in the jth hydrogen bond. We write the Hamiltonian H of our ferroelectric in the form $H = H_0 + H_1$, where H_0 describes the effects of the interaction of the protons on the occupied hydrogen bonds and H_1 describes the effects due to the absence of protons on the unoccupied bonds. Then

$$H_0 = -\Omega \sum_j (X_j^{LR} + X_j^{RL}) - \frac{1}{2}\sum_j J_{ij}(X_i^{LL} - X_i^{RR})$$

$$\times (X_j^{LL} - X_j^{RR}) - 2\mu_0 \sum_j E_{0j}(X_j^{LL} - X_j^{RR}), \quad (1)$$

where Ω is the tunneling integral, J_{ij} is the exchange integral between the ith and jth cells, and E_{0j} is the external static electric field in the jth cell.

We write the Hamiltonian H_1 in the form

$$H_1 = H_p + H_v,$$

where H_p is responsible for the hops of the protons along the network of hydrogen bonds, and H_v describes the change in energy of the sample on account of the vacancies on the hydrogen bonds,

$$H_p = \sum_j t_\Delta \{ (X_{j+\Delta}^{0L} + X_{j+\Delta}^{0R}) X_j^{L0} + (X_{j+\Delta}^{0L} + X_{j+\Delta}^{0R}) X_j^{R0} \} + \text{h.c.},$$

$$H_v = \mu \sum_j X_j^{00} + \frac{1}{2} \sum_{ij} U_{ij} X_i^{00} X_j^{00} + \frac{1}{2} \sum_{ij} \bar{U}_{ij} X_i^{00} (X_j^{LL} + X_j^{RR}), \quad (2)$$

t_Δ is the hopping integral from the jth hydrogen bond to the bond $j+\Delta$, μ has the meaning of a chemical potential, $\bar{U}_{ij}$ corresponds to the interaction energy of a cell j containing a proton with a cell i containing a proton vacancy; U_{ij} describes the interaction energy of the ith and jth hydrogen bonds in the absence of protons, Δ is a vector in the direction of a possible proton hop.

We now go over from the operators $X_j^{\alpha\beta}$ to the operators S_j^z, S_j^+, S_j^- (spin $S=1$), choosing a diagonal representation for the operator S_j^x and taking into account that $[S_i^z, S_j^\pm] = \pm S_j^\pm \delta_{ij}$, $[S_i^+, S_j^-] = 2S_j^z \delta_{ij}$.

In this case we have

$$H_0 = -\frac{\Omega}{2} \sum_j (S_j^{+2} + S_j^{-2}) - \frac{1}{2} \sum_j J_{ij} S_i^z S_j^z - 2\mu_0 \sum_j E_{0j} S_j^z,$$

$$H_p = -\sum_j \frac{t_\Delta}{2} \{ (S_{j+\Delta}^+ - S_{j+\Delta}^-) S_{j+\Delta}^z + S_j^z (S_j^+ - S_j^-) \} + \text{h.c.},$$

$$H_v = \tilde{\mu} \sum_j S_j^{z2} + \frac{1}{2} \sum_{ij} k_{ij} S_j^{z2} S_i^{z2}, \quad (3)$$

$$\tilde{\mu} = -\mu + \frac{1}{2} \sum_j \bar{U}_{ij} - \sum_j U_{ij},$$

$$K_{ij} = U_{ij} - \bar{U}_{ij}.$$

The Hamiltonian obtained is the pseudospin Hamiltonian for a ferroelectric with protonic conductivity.

Using the Holstein–Primakoff transformation[9]

$$S_j^+ = \sqrt{2} \left(1 - \frac{1}{4} a_j^+ a_j \right) a_j;$$

$$S_j^- = \sqrt{2} \left(1 - \frac{1}{4} a_j^+ a_j \right) a_j^+; \quad S_j^z = (1 - a_j^+ a_j),$$

which is done in an approximate way, to an accuracy which includes the main low-temperature nonlinear effects, we write our Hamiltonian in terms of creation and annihilation operators:

$$\hat{H} = -\Omega \sum_j \left(a_j a_j - \frac{1}{2} a_j^+ a_j a_j a_j + a_j^+ a_j^+ - \frac{1}{2} a_j^+ a_j^+ a_j^+ a_j \right)$$

$$- 2\mu_0 \sum_j E_{inj} (1 - a_j^+ a_j) - \frac{1}{2} \sum_{ij} J_{ij} (1 - a_i^+ a_i - a_j^+ a_j$$

$$+ a_i^+ a_i a_j^+ a_j) - \sum_{j\Delta} t_\Delta \left(\frac{5}{4} a_{j+\Delta}^+ a_{j+\Delta}^+ a_{j+\Delta} a_j \right.$$

$$- \frac{5}{4} a_{j+\Delta}^+ a_{j+\Delta} a_{j+\Delta} a_j - \frac{5}{4} a_{j+\Delta}^+ a_j^+ a_j^+ a_j$$

$$+ \frac{5}{4} a_{j+\Delta}^+ a_j^+ a_j a_j - a_{j+\Delta}^+ a_j + \frac{5}{4} a_j^+ a_j^+ a_j a_{j+\Delta}$$

$$- \frac{5}{4} a_j^+ a_j a_j a_{j+\Delta} - \frac{5}{4} a_j^+ a_{j+\Delta}^+ a_{j+\Delta}^+ a_{j+\Delta}$$

$$+ \frac{5}{4} a_j^+ a_{j+\Delta}^+ a_{j+\Delta} a_{j+\Delta} - a_j^+ a_{j+\Delta} \right)$$

$$+ \bar{\mu} \sum_j (1 - 2a_j^+ a_j + a_j^+ a_j a_j^+ a_j)$$

$$+ \frac{1}{2} \sum_{ij} K_{ij} (1 - 2a_j^+ a_j - 2a_i^+ a_i + a_j^+ a_j a_j^+ a_j$$

$$+ a_i^+ a_i a_i^+ a_i + 4a_i^+ a_i a_j^+ a_j). \quad (4)$$

The equation of motion for the operators a_j and a_j^+ are $(a_j^- \equiv a_j)$

$$\dot{a}_j^\pm = i \left\{ \mp \Omega \sum_j \left(-\frac{1}{2} a_j^\mp a_j^\mp a_j^\mp + 2a_j^\mp - \frac{3}{2} a_j^\mp a_j^+ a_j^- \right) \right.$$

$$\pm 2\mu_0 E_{in} a_j^\pm \mp \frac{1}{2} \sum_i J_{ij} (-a_j^\pm + a_i^+ a_i a_j^\pm)$$

$$+ \sum_\Delta t_\Delta \left(\mp \frac{5}{2} a_{j+\Delta}^+ a_j^\pm a_j^- \pm \frac{5}{4} a_{j+\Delta}^+ a_j^+ a_j^\pm \right.$$

$$+ \frac{5}{2} a_j^+ a_j^- a_{j+\Delta} - \frac{5}{4} a_j^\pm a_j^\pm a_{j+\Delta}^- - \frac{5}{4} a_{j+\Delta}^+ a_{j+\Delta}^+ a_{j+\Delta}^-$$

$$+ \frac{5}{4} a_{j+\Delta}^+ a_{j+\Delta}^- a_{j+\Delta}^- \pm a_{j+\Delta}^\pm \right) \mp \tilde{\mu} (2a_j^\pm - a_j^\pm a_j^+ a_j^-$$

$$- a_j^+ a_j^- a_j^\pm) \mp \frac{1}{2} \sum_j K_{ij} (2a_j^\pm - a_j^\mp a_j^+ a_j^-$$

$$- a_j^+ a_j^- a_j^\pm - 4a_i^+ a_i a_j^\pm) \right\}. \quad (5)$$

Multiplying the right and left sides of Eq. (5) by the basis functions of the generalized coherent states for Bose operators, $|\Psi\rangle = \Pi_j |\alpha_j\rangle$ (Ref. 10):

$$|\alpha_j\rangle = \exp(-|\alpha_j|^2/2) \exp(\alpha_j a_j^+) |0\rangle,$$

we perform a decoupling of the equations of motion[11]

$$\langle \Psi | \hat{A}\hat{B} | \Psi \rangle = \langle \Psi | \hat{A} | \Psi \rangle \langle \Psi | \hat{B} | \Psi \rangle$$

and the operation of passing to the continuum limit:

$$\langle \Psi | \alpha_{j+1} | \Psi \rangle = \alpha_{j+1} \approx a_j \pm \Delta \frac{\partial \alpha_j}{\partial X} + \frac{\Delta^2}{2} \frac{\partial^2 \alpha_j}{\partial X^2}.$$

We obtain

$$\begin{cases} \dot{\alpha} = -i[A\alpha(\alpha^2 + 3\alpha^{+2}) + B\alpha^2\alpha^+ + C\alpha - 2\Omega\alpha^+ + \Delta^2 t\alpha''], \\ \dot{\alpha}^+ = -i[A\alpha^+(\alpha^{+2} + 3\alpha^2) + B\alpha^{+2}\alpha - C\alpha + 2\Omega\alpha - \Delta^2 t(\alpha^+)''], \end{cases}$$
$$(6)$$

where for the extremely simple case of a square lattice $K_0 = 4K$, $J_0 = 4J$, $A = \frac{1}{2}(\Omega + 5t)$; $B = -J - 10t + 2\tilde{\mu} + 8K$; $C = 2\mu_0 E_{in} + 2J + 2t - 2\tilde{\mu} - 4K$; $\alpha'' = \partial^2\alpha/\partial x^2$; x is the direction of propagation of the wave.

For the present purposes we concentrate on traveling-wave solutions of equation (6). Traveling nonlinear waves are analogous to the widely studied soliton lattices, which largely determine the dynamical and kinetic properties of ferroelectrics; for this reason an examination of the possibility that such structures exist is indeed a topical problem.

We seek a solution of the form

$$\alpha = be^{i\varphi}; \quad \alpha^+ = be^{-i\varphi}; \quad \dot{\alpha} = -V\alpha';$$

$$\dot{\alpha}^+ = -V(\alpha^+)', \quad b = b(x - Vt); \quad \varphi = \varphi(x - Vt),$$

and, as a result, we obtain a new system for the amplitude b and phase φ of traveling waves:

$$\begin{cases} \Delta^2 tb\varphi'' + 2\Delta^2 tb'\varphi' + Vb' + 2b(Ab^2 - \Omega)\sin(2\varphi) = 0, \\ \Delta^2 tb'' - \Delta^2 t(\varphi')^2 - Vb\varphi' + 2b(2Ab^2 - \Omega) \\ \quad \times \cos(2\varphi) + b(Bb^2 + C) = 0. \end{cases}$$
$$(7)$$

Besides the solutions with zero b, there exist nonzero stationary solutions of the system of equations (7):

$$b_0 = \left[\frac{C + 2\Omega}{4A - B} \right]^{1/2}; \quad \varphi_0 = \frac{\pi}{2}.$$

The solution obtained can be interpreted as a state with proton hops over the network of hydrogen bonds. This state corresponds to a nonzero expectation value of the operators $S^\pm$ and, consequently, describes states with a change in the number of protons in a given ferroelectric cell.

The stability of the stationary solutions obtained is determined from an analysis of the localized system of equations (7):

$$\begin{cases} V\Delta b' = 4\Delta\varphi(Ab_0^3 - \Omega b_0), \\ Vb_0\Delta\varphi' = -2\Delta b(2\Omega + C)' \end{cases}$$
$$(8)$$

$$\Delta b \sim e^{ikx}; \quad \Delta\varphi - e^{ikx}.$$

The roots of the characteristic equation have a negative imaginary part under the conditions:

$$\begin{cases} 2\Omega + 2\mu_0 E_{in} + 2J + 2t - 2\tilde{\mu} - 4K < 0, \\ 2\Omega + 20t + J - 2\tilde{\mu} - 5K < 0 \end{cases}.$$
$$(9)$$

Since it is not possible to solve the resulting equations in analytical form, for subsequent study we performed a numerical analysis of the above system, the main results of which are presented in Fig. 1. We see that there exist traveling nonlinear lattices for a wide range of variation of the parameters describing ferroelectrics with protonic conductivity. The existence of these lattices may be due to the balance of nonlinear and dispersion processes of the $S = 1$ pseudospin system of the ferroelectric. The period and amplitude of the nonlinear lattices are determined by the proton tunneling integral in the hydrogen bond (see Figs. 1a and 1b. This behavior can be linked with the known fact that the nonlinear properties of ferroelectrics with protonic conductivity depend strongly on the tunneling integral.[12] Changes in the

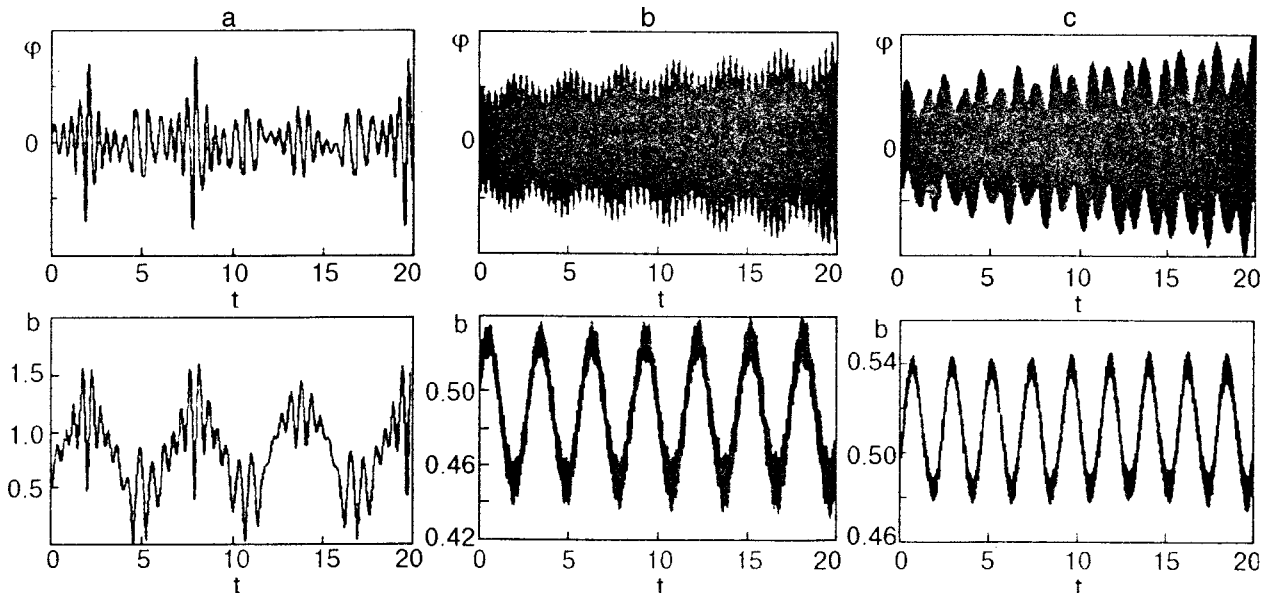FIG. 1. Dependence of the phase φ and amplitude b of traveling waves on the time t for $\Delta = 1$, $J = 10^{14}$ s^{-1}, $\tilde{\mu} = 10^{12}$ s^{-1}; a: $\Omega = 10^{14}$ s^{-1}, $t = 10^{13}$ s^{-1}, $K = 10^{14}$ s^{-1}; b: $\Omega = 10^{13}$ s^{-1}, $t = 10^{12}$ s^{-1}, $K = 10^{14}$ s^{-1}; c: $\Omega = 10^{13}$ s^{-1}, $t = 10^{12}$ s^{-1}, $K = 10^{13}$ s^{-1}.

chemical potential do not have a substantial effect on the shape of the lattices. At the same time, changes in the parameters characterizing the interaction of unoccupied hydrogen bonds give rise to a high-frequency component in the form of a soliton lattice (see Figs. 1b and 1c. This circumstance can be linked to the fact that the given parameters strongly affect the effective nonlinearity constant of our system and, hence, give rise to a high-frequency component.

In summary, we have proposed a microscopic approach to the theory of ferroelectrics with protonic conductivity. Our analysis allows one to consider in a unified way the properties of ferroelectrics with protonic conductivity and the properties of other ferroelectrics in the framework of a microscopic $S = 1$ pseudospin formalism for ferroelectrics with protonic conductivity. Because of the strong anharmonicity of the pseudospin Hamiltonian for ferroelectrics with protonic conductivity, these substances can support traveling nonlinear lattices which can have an appreciable influence on the dynamical properties of the ferroelectric. The existence of such lattices is largely determined by the contribution of the unoccupied hydrogen bonds to the energy of the sample.

[*]E-mail: poplar@sprint-v.com.ru

[1] M. E. Lines and A. M. Glass, *Principles and Applications of Ferroelectrics and Related Materials* [Clarendon Press, Oxford (1977); Mir, Moscow (1981)].

[2] A. I. Baranov, Izv. Akad. Nauk SSSR, Ser. Fiz. **51**, 2146 (1987).

[3] V. G. Vaks, *Introduction to the Microscopic Theory of Ferroelectrics* [in Russian], Nauka, Moscow (1973).

[4] A. R. Kessel', *Nuclear Acoustic Resonance* [in Russian], Nauka, Moscow (1969).

[5] M. B. Belonenko, Author's Abstract of Doctoral Dissertation [in Russian], Saratov State University, Saratov (1998).

[6] V. V. Nemesh, Author's Abstract of Candidate's Dissertation [in Russian], Volgograd State University, Volgograd (1998).

[7] M. B. Belonenko and V. V. Nemesh, Preprint [in Russian], Volgograd State University, Izd. VolGU, Volgograd (1998).

[8] Yu. A. Izyumov and Yu. N. Skryabin, *Statistical Mechanics of Magnetically Ordered Systems*, Nauka, Moscow (1987).

[9] S. V. Tyablikov, *Methods of the Quantum Theory of Magnetism*, Nauka, Moscow (1975).

[10] A. M. Perelomov, *Generalized Coherent States and Their Applications* [in Russian], Nauka, Moscow (1987).

[11] V. K. Fedyanin and V. Yu. Yushankhaĭ, OIYaI Preprint R17-12896 [in Russian], Joint Institute for Nuclear Research, Dubna (1979).

[12] M. B. Belonenko and V. V. Kabakov, Izv. Akad. Nauk SSSR, Ser. Fiz. **62**, 1497 (1998).

Translated by Steve Torstveit

LOW-DIMENSIONAL AND DISORDERED SYSTEMS

Low-temperature thermopower in quasiamorphous carbons

L. Yu. Matsuĭ, L. L. Vovchenko, and I. V. Ovsienko

Faculty of Physics, Taras Shevchenko Kiev University, ul. Vladimirskaya 64, 252017 Kiev-17, Ukraine
(Submitted March 9, 1999)
Fiz. Nizk. Temp. **26**, 70–75 (January 2000)

Results are presented from a study of the thermopower of quasiamorphous carbons in the
temperature interval from 20 to 200 K. It is shown that the thermopower of quasiamorphous
carbons is described satisfactorily in a model based on the series connection of regions
with metallic conductivity, hopping conductivity with a variable hopping length, and hopping
conductivity with a constant hopping length. It is found that when considering the
thermopower of the regions with the metallic conductivity, it is necessary to take into account
the temperature dependence of the main mechanisms of carrier scattering. The parameters
of the electronic structure of quasiamorphous carbon are calculated using experimental data on
the temperature dependence of the electrical resistivity and thermopower. © *2000*
American Institute of Physics. [S1063-777X(00)00701-5]

Quasiamorphous carbons comprise a wide class of carbon–graphite materials obtained by annealing raw carbon at temperatures up to 2000 °C. The structure of the amorphous carbon is a packet of two-dimensional ribbon-shaped crystallites oriented arbitrarily relative to one another in space and deformed by various defects of the layers. However, the graphite layer has two-dimensional symmetry. The dimensions L of the crystallites in quasiamorphous carbon do not exceed 100 Å, and the distance d_{002} between layers is ~ 3.44 Å. This structure of quasiamorphous carbon is substantially different from the structure of the highly oriented pyrolytic graphite, and therefore the electrophysical properties of amorphous carbon are substantially different from those of other carbon–graphite materials.

In the study reported here we investigate the mechanism of formation of the thermopower in quasiamorphous carbons in the temperature interval 20–200 K by the method described in Ref. 1.

Figure 1 shows the typical curves of the temperature dependence of the thermopower of carbonaceous materials with quasiamorphous structure. The materials were based on polyacrylnitrile, carbon fibers of types VPR-1 and VPR-2, with fiber diameters $\sim 10\,\mu$m and crystallite sizes $L \sim 100$ Å, ungraphitized carbon fiber of type VMN, with a fiber diameter of $\sim 7\,\mu$m and crystallite dimensions $L \sim 50$ Å, and quasiamorphous carbons AV1 and AV2, annealed at temperatures of 2100 and 2300 °C, respectively. One can see from the figures that all these materials have a similar temperature dependence of the thermopower: at low temperatures there is a minimum (at a temperature $T \sim 40$ K in the VMN fiber and in the amorphous carbon), and the thermopower in the quasiamorphous AV2 carbon is equal to zero, in the VMN fiber $S \sim -0.4\,\mu$V/K, and in the quasiamorphous carbon AV1 $S \sim -0.5\,\mu$V/K. The lowest temperature at which the minimum of the thermopower occurs

and the lowest value of the thermopower at the minimum were observed in the VPR-2 fiber ($T \sim 25$ K, $S \sim -1\,\mu$V/K). The highest temperature of the thermopower minimum was registered for the VPR-1 fiber ($T \sim 50$ K, $S \sim -0.5\,\mu$V/K). As the temperature is raised, the thermopower of all the samples increases, but at different rates. The lowest value of S at 200 K was observed in the AV1 samples
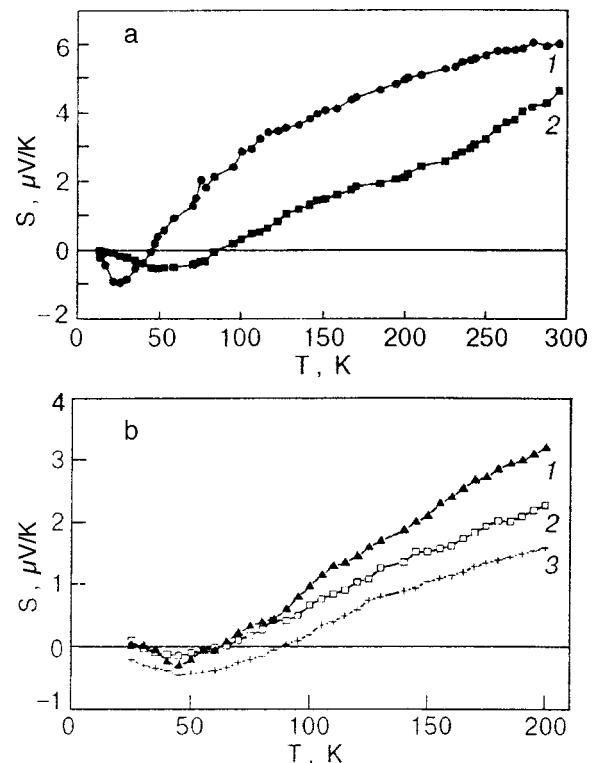

FIG. 1. $S(T)$ curves for carbon fibers: VPR-2 (*1*), VPR-1 (*2*) (a), and for quasiamorphous carbons and fibers: VMN (*1*), AV2 (*2*), AV1 (*3*) (b).

($S\sim 1.5\,\mu$V/K), AV2 ($S\sim 2.0\,\mu$V/K), and in the VMN carbon fiber ($S\sim 3.5\,\mu$V/K). High values of the thermopower at 200 K were observed in the VPR-1 and VPR-2 carbon fiber samples, with $S\sim 2.7\,\mu$V/K and $\sim 5\,\mu$V/K, respectively.

According to the model proposed in Refs. 2 and 3, quasiamorphous carbon consists of a set of regions with metallic conductivity and regions with variable-length hopping conductivity. These regions can be connected in series or in parallel.[3] We denote the thermopower and conductivity of the regions with metallic and hopping conductivity by S_1, σ_1 and S_2, σ_2, respectively. Then the total thermopower S_{I} for series-connected regions with the different types of conductivity can be written as

$$S_{\mathrm{I}} = S_1 - S_2, \tag{1}$$

and the total thermopower S_{II} for parallel-connected islands with different types of conductivity is

$$S_{\mathrm{II}} = \frac{S_1}{1+(\sigma_2/\sigma_1)} + \frac{S_2}{1+(\sigma_1/\sigma_2)}. \tag{2}$$

For the regions with metallic conductivity, S_1 depends linearly on temperature:[4]

$$S_1 = \frac{k_B}{e}\,\frac{\pi^2}{3}\,\frac{k_B T}{\Delta}(1+p), \tag{3}$$

where k_B is Boltzmann's constant, e is the charge of an electron, Δ is the shift of the Fermi level, p is a parameter which depends on the predominant mechanism of carrier scattering; the electrical conductivity of these regions, according to the two-dimensional Wallace model,[5] is given by

$$\sigma_1 = \frac{\Delta e^2 L}{\pi\sqrt{3}\,\gamma_0 a_0 d_{002}\hbar}, \tag{4}$$

where γ_0 is the overlap of the electron wave vectors in the graphite layer, a_0 is the lattice constant of graphite, d_{002} is the distance between graphite layers, $\hbar$ is Planck's constant, and the mean free path L is approximately equal to the dimensions of the crystallites. The thermopower S_1 is positive, since the regions with metallic conductivity consist of a degenerate hole conductor.

The conductivity of the regions with variable-length hopping conductivity is given by the expression[6]

$$\sigma_2 = \sigma_0 \exp[-(T_0/T)^{1/4}], \tag{5}$$

where σ_0 and T_0 are constants. The thermopower of the regions with variable-length hopping conductivity has the form[6]

$$S_2 = \frac{k_B^2}{2e}(T_0 T)^{1/2}\left.\frac{d\ln N(E_F)}{dE}\right|_{E=E_F}, \tag{6}$$

where $N(E_F)$ is the density of states at the Fermi level.

A feature of the two-dimensional Wallace model is a point of tangency of the valence band and the conduction band and a linear relation between the energy and the electronic density of states near the point of tangency of the bands:[7]
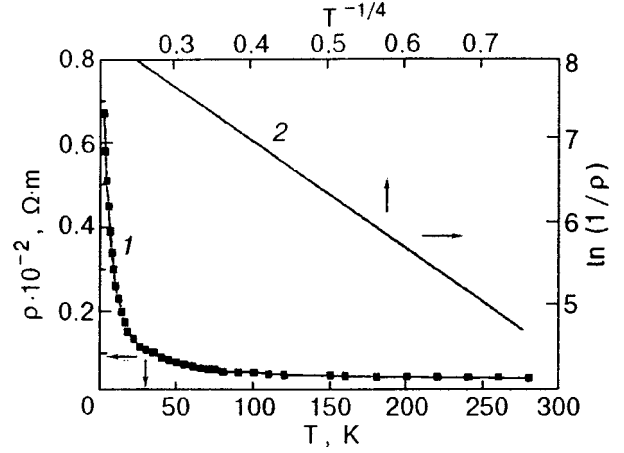
$$N(E) = B|E|, \tag{7}$$

FIG. 2. Temperature dependence of the resistivity of quasiamorphous carbon AV1 (curve *1*) and the same function plotted in the coordinates $\ln(1/\rho)=f(T^{-1/4})$ (curve *2*).

where B is a coefficient of proportionality, and E is the energy reckoned from the point of tangency of the bands. Using expression (7), we write relation (6) in the form

$$S_2 = \frac{k_B^2}{2e}(T_0 T)^{1/2}\frac{1}{E_F(T)}, \tag{8}$$

where E_F is temperature-dependent. It is known, however, that quasiamorphous carbon has excess holes on account of the acceptor effect of the structural defects, and $E_F \gg k_B T$ in this material; therefore the temperature dependence of E_F can be neglected in the temperature region investigated here.

Figure 2 shows the temperature dependence of the resistivity of the AV1 sample in both a $\rho(T)$ plot and in the coordinates $\ln(1/\rho)=f(T^{-1/4})$. We see that the latter is a linear plot of the type $y=b-ax$, where $b=\ln\sigma_0$ and $a=T_0^{1/4}$, over a wide temperature interval, which means that a hopping mechanism of conductivity with a variable hopping length is indeed present in this sample over the given temperature range. From the plot of $\ln(1/\rho)=f(T^{-1/4})$ we determined the values of the constants σ_0 and T_0; the results are tabulated with the analogous results for the AV2 sample in Table I.

The thermopower calculated in the model with a parallel connection of regions with different types of conductivity according to expression (2) has a linear trend (Fig. 3), but it does not agree with the experimentally measured $S(T)$ in the investigated materials. Consequently, the thermopower of quasiamorphous carbon cannot be described in a model of parallel-connected islands with different types of conductivity.

To elucidate the mechanisms giving rise to the thermopower in quasiamorphous carbons we considered a model

TABLE I. Calculated parameters of the electronic structure of amorphous carbons AV1 and AV2.

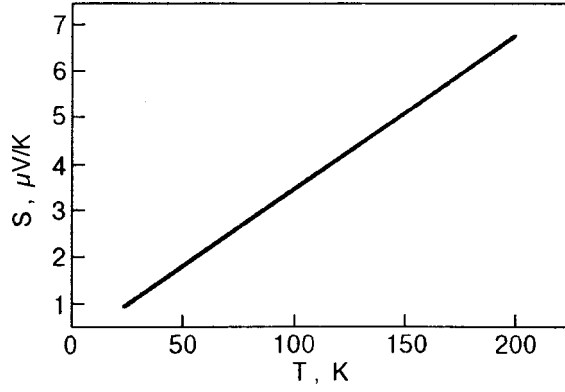| Sample	σ_0, S/m	T_0, K	E_F, eV	Δ, eV	ε, eV	C
AV1	169	1967	0.4	0.45	3.8×10^{-5}	0.001
AV2	436	552	0.22	0.35	$4.4\times10^{-}$	0.012

FIG. 3. Calculated temperature dependence of the thermopower in a model with the regions of different conductivity connected in parallel.

in which regions of metallic conductivity are connected in series with regions of hopping conductivity with a variable hopping length. Analysis of the experimental data in the framework of this model with the use of Eq. (1) showed that in order to describe the temperature dependence of the thermopower it is necessary to include one more term, S_3 in Eq. (1); this term is responsible for the positive ''tail'' of the thermopower in the low-temperature region. An obvious assumption is that S_3 is due to hopping conductivity with a constant hopping length. For this mechanism the conductivity and thermopower can be described by the expressions

$$\sigma_3 = \sigma_0 e^{-(\varepsilon/k_B T)},$$

$$S_3 = \frac{k_B}{2e}\left(\frac{\varepsilon}{k_B T} + C\right), \qquad (9)$$

$$\varepsilon = E_C - E_F,$$

where E_C is the mobility edge, $\varepsilon > 0$, and C is a constant that can be positive or negative.[8]

From the experimental data on the temperature dependence of the thermopower of the AV1 and AV2 samples at low temperatures we calculated the following parameters: the shift Δ of the Fermi level in the regions with metallic conductivity, the values of the Fermi energy E_F in the regions with variable-length hopping conductivity, and the differences ε between the mobility edge and Fermi level, and the constants C (for the regions with constant-length hopping conductivity). The results of the calculations are presented in Table I. We see that the values of the parameters Δ, E_F, ε, and C are completely real-valued: for example, for the regions with metallic conductivity the shift of the Fermi level into the valence band is in good agreement with the value of this parameter in disordered isotropic graphite,[9] which, as was shown in Ref. 9, is a single-band hole conductor, with the parameter $\varepsilon > 0$, which corresponds to hopping conductivity with a constant hopping length. Using the values obtained for the parameters Δ, E_F, ε, and C, we calculated the temperature dependence of the thermopower in the AV1 sample at temperatures up to 200 K (Fig. 4a). An analysis of this plot implies that the calculated thermopower gives a fair description of the temperature dependence at low temperatures, while at high temperatures there is a significant dis-
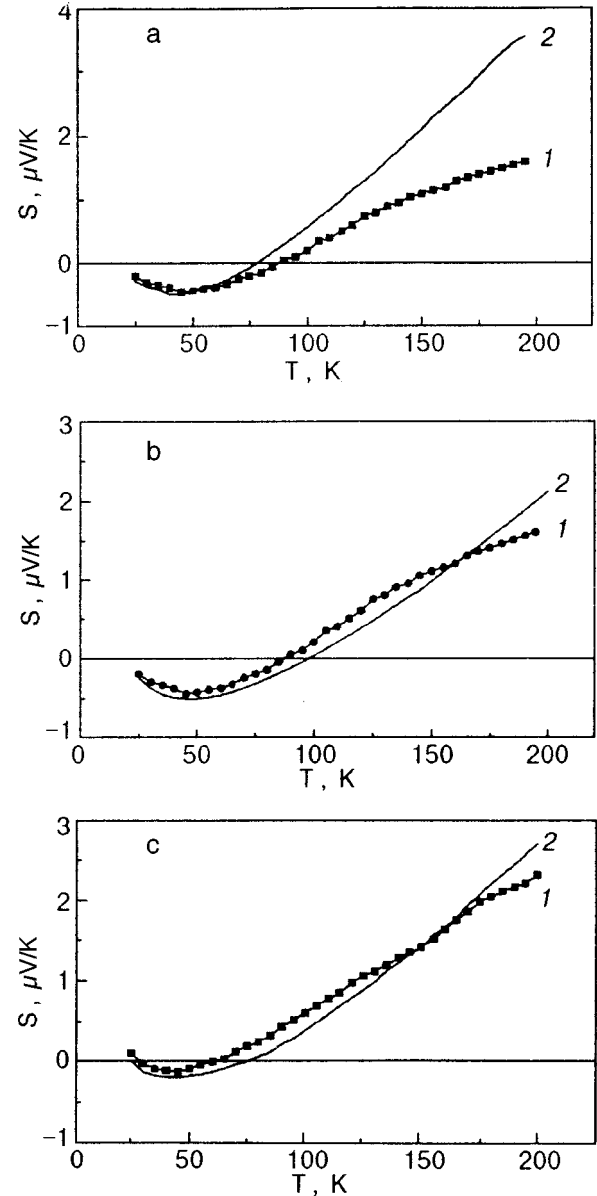

FIG. 4. $S(T)$ curves for quasiamorphous carbons: experimental (curves *1*), calculation in the model with a series connection of the regions with different types of conductivity (curves *2*) in the AV1 samples, in which $S(T)$ is linear in the regions with metallic conductivity; in samples of AV1 (b) and AV2 (c) with allowance for the temperature dependence of the carrier scattering mechanisms in the regions with metallic conductivity.

agreement (by about a factor of two). The reason for this is that in a rigorous treatment one cannot assume that the thermopower in the regions with metallic conductivity is a linear function of temperature (it is of a diffusional nature). It was shown by Sugihara[10,11] that for describing the thermopower over a wide interval interval, the parameter p in Eq. (3) should be determined not by a single predominant mechanism of carrier scattering in the material but with allowance for all the main mechanisms of carrier scattering; this leads to a complicated temperature dependence of p:

$$p = \frac{\Gamma^{(DH)} + \Gamma^{(lo)}(1 + p^{(lo)}) + \Gamma^{(ph)}(1 + p^{(ph)})\Gamma^2}{(1 + \delta/E_F)\Gamma}, \qquad (10)$$

$$\Gamma = \sum_i \Gamma^{(i)}, \quad \delta = \frac{\gamma_1}{2},$$

where γ_1 is the overlap of the wave functions of the electrons of adjacent atoms in equivalent layers.

The parameters $\Gamma^{(i)}$ are related to the relaxation times $\tau^{(i)}$ in the plane of the layer as

$$\Gamma^{(i)}(E) = \frac{\hbar}{2\tau^{(i)}} \propto E^{-p^{(i)}}, \tag{11}$$

where $p^{(i)}$ takes on different values, depending on the scattering mechanism: $\Gamma^{(DH)}$ for scattering at the boundaries of the crystallites, $p^{(DH)} = 0$; $\Gamma^{(Io)}$ for scattering on charged impurities, $p^{(Io)} = 1 + 2\delta/E_F$; $\Gamma^{(ph)}$ for scattering on phonons in the plane of the graphite layer, $p^{(ph)} = 0$ at low temperatures and $p^{(ph)} = -1$ at high temperatures.

The parameter $\Gamma^{(ph)}$ is a complicated function of temperature:

$$\Gamma^{(ph)} = \frac{\hbar D^2}{4\pi v_s d_{002}} \frac{E + \Delta}{p_0^2 k}$$

$$\times \int_0^{2k} dq \frac{q}{[1 - (q/2k)^2]^{1/2}} \frac{1}{\exp(\hbar\omega_q/k_B T) - 1}, \tag{12}$$

$$p^{(ph)} = -\left[E \frac{(d\Gamma^{(ph)}/dE)}{\Gamma^{(ph)}} \right]_{E=E_F}, \quad p_0 = \frac{\sqrt{3}}{2}\gamma_0 a_0.$$

where D is the pairing constant of the charge carriers and phonons in the plane of the layer; v_s is the speed of sound, k and q are the electron and phonon wave vectors, respectively.

The calculated temperature dependence of the thermopower with the temperature dependence of the carrier scattering mechanisms taken into account is shown in Fig. 4b and 4c. It is seen that the theory gives a good description of the experimental dependence over the entire temperature interval.

Figure 5 shows the calculated temperature dependence of the thermopower with allowance for the fractions of the sample made up of regions with the different types of conductivity. Curve *1* is for equal parts with each type of conductivity, curve *2* is for a greater fraction (0.7) with metallic conductivity, and curve *3* is for the greater fraction (0.7) with hopping conductivity. We see that as the fraction with metallic conductivity increases and the fraction with hopping conductivity decreases (as occurs with increasing annealing temperature of the raw carbon), the value of the thermopower at equal temperatures increases, as does the rate of increase of the thermopower, while the location of the minimum of the thermopower (curve *2*) decreases to lower temperatures. This tendency is in fact observed experimentally in the samples studied: for example, sample AV2, annealed at 2300 °C, has larger values of the thermopower at the same temperatures than does sample AV1, annealed at 2100 °C, and the fibers VPR-1 and VPR-2, having a higher heat-treatment temperature, have even higher values of the thermopower at the same temperatures. As the heat-treatment
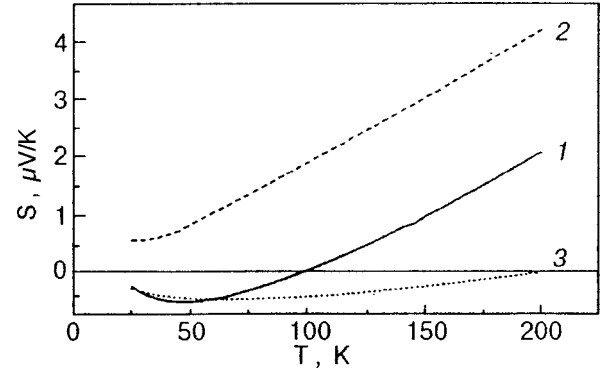

FIG. 5. Calculated $S(T)$ curves with allowance for the fraction of the sample consisting of regions with different types of conductivity: curve *1*—with equal fractions of regions with each type of conductivity; curve *2*—with a larger fraction (0.7) made up of regions with metallic conductivity, curve *3*–with the larger fraction (0.7) made up of regions with hopping conductivity.

temperature is increased further the regions with hopping conductivity vanish, and the materials consist of a single-band hole conductor.[9] Increasing the fraction consisting of regions with hopping conductivity, i.e., increasing the amorphous-phase fraction, results in S becoming negligibly small (curve *3*).

In summary, these studies have shown that the thermopower of quasiamorphous carbons can be described using a model in which regions of metallic conductivity and regions of hopping conductivity with variable and constant hopping lengths are connected in series. As the heat-treatment temperature is raised and the crystal structure of the quasiamorphous carbons is perfected, the regions of hopping conductivity vanish, and a transition to metallic conductivity throughout the volume of the sample occurs (disordered graphite with crystallite dimensions $L \sim 200$ Å).[9] When the heat-treatment temperature is increased further to ~ 2600–3000 °C the dimensions of the crystallites increase, and a three-dimensional crystal structure is formed with overlapping valence and conduction bands; this leads to two-band conductivity (holes and electrons) and to a complicated dependence of S on T, since an additional thermopower arises on account of the phonon dragging of electrons.

The results presented here on the thermopower of quasiamorphous materials indicate that the trend of the function $S(T)$ and the value of S are very sensitive to the parameters of the crystal structure of carbon materials, which is determined by the methods and conditions of their synthesis.

[1] L. L. Vovchenko, I. V. Dvorkina, and L. Yu. Matsuĭ, Fiz. Nizk. Temp. **20**, 463 (1994) [Low Temp. Phys. **20**, 386 (1994)].

[2] Y. Kaburagi, Y. Hishiyama, and A. Y. Hoshida, *Abstracts of the 4th International Carbon Conference (Carbon-86)*, Baden Baden (1986), p. 219.

[3] Y. Hishiyama and Y. Kaburagi, *Abstracts of the 4th International Carbon Conference (Carbon-86)*, Baden Baden (1986), p. 222.

[4] C. Klein, J. Appl. Phys. **35**, 2947 (1964).

[5] P. R. Wallace, Phys. Rev. **71**, 622 (1947).

[6] I. P. Zvyagin, *Kinetic Phenomena in Disordered Semiconductors* [in Russian], Izd. MGU, Moscow (1984).

[7] A. S. Kotosonov, Konstr. Mater. Osn. Ugleroda, No. 14, 55 (1979).

[8] N. F. Mott and E. A. Davis, *Electronic Processes in Non-Crystalline Materials* [Clarendon Press, Oxford (1971); Mir, Moscow (1982)].

[9] L. Yu. Matsuĭ, I. V. Ovsienko, and L. L. Vovchenko, Visn. Kiiv. Univ. Ser. Fiz.-Mat. Nauki, No. 2, 216 (1996).

[10] K. Kobayahi, K. Sugihara, H. Oshima, and T. Tsuzuku, J. Phys. Soc. Jpn. **63**, 4451 (1994).

[11] K. Kobayashi, K. Sugihara, and H. Oshima, J. Phys. Chem. Solids **57**, 931 (1996).

Translated by Steve Torstveit

Behavior of the layered crystals TlInS$_2$ and TlGaSe$_2$ near phase transitions in a static electric field

K. R. Allakhverdiev

Department of Physics, TUB/TAK Marmara Research Centre, Gebze, Kocaeli, Turkey

N. D. Akhmed-zade, T. G. Mamedov, T. S. Mamedov, and Mir-Gasan Yu. Seidov*[)]

G. M. Abdullaev Institute of Physics, Academy of Sciences of Azerbaijan, pr. G. Dzhavida 33, 370143 Baku, Azerbaijan
(Submitted April 22, 1999; revised July 27, 1999)
Fiz. Nizk. Temp. **26**, 76–83 (January 2000)

The effect of an orienting electric field on the anomalies of the temperature dependence of the dielectric constant ε of the crystals TlInS$_2$ and TlGaSe$_2$ and of the pyroelectric current i in TlInS$_2$ near phase transitions is investigated. It is found that the $\varepsilon(T)$ profile of both crystals undergoes the same transformation at the point of the phase transition to the incommensurate phase under the influence of a static electric field applied in the plane of the layer. It is established that the maximum of $\varepsilon(T)$ in TlGaSe$_2$ and of $i(T)$ in TlInS$_2$ at the point of the phase transition to the commensurate polar phase is shifted in a certain range of orienting electric fields and that the sign of the temperature shift depends on the value of the external electric field. An interpretation is offered for the experimental results. © *2000 American Institute of Physics.* [S1063-777X(00)00801-X]

INTRODUCTION

The ternary thallium compounds thallium–gallium diselenide (TlGaSe$_2$) and thallium–indium disulfide (TlInS$_2$) belong to the class of chalcogenide semiconductor compounds with a layered structure. The x-ray diffraction data for these compounds are identical, indicating that their crystal structures in the high-temperature paraphase are topologically similar and are characterized by symmetry space group C_{2h}^6 (see, e.g., Refs. 1–6 and references cited therein). On cooling, both crystals undergo sequences of structural phase transitions, including transitions to an incommensurate (IC) phase and a commensurate polar phase. According to the data of structural studies, the phase transition to the IC phase (at $T_i = 216$ K for TlInS$_2$ and $T_i = 115$ K for TlGaSe$_2$) is due to the condensation of a soft mode at the point of the Brillouin zone corresponding to the wave vector $\mathbf{k}_i = \delta \times (\mathbf{a}^* + \mathbf{b}^*) + 0.25\mathbf{c}^*$, where $\mathbf{a}^*$, $\mathbf{b}^*$, and $\mathbf{c}^*$ are reciprocal lattice vectors, and δ is the incommensurability parameter: $\delta = 0.012$ for TlInS$_2$ and 0.02 for TlGaSe$_2$. For $T_C = 201$ K for TlInS$_2$ and $T_C \sim 110$ K for TlGaSe$_2$ the parameter δ vanishes discontinuously, and both compounds undergo a transition to an improper commensurate polar modulated phase with a spontaneous polarization vector lying in the plane of the layer. The symmetry of the low-temperature polar phase of the two crystals has not been determined experimentally.

The temperature dependence of the dielectric constant ε (Fig. 1) and of the other thermodynamic parameters of TlInS$_2$ (Refs. 1–4 and 6) are characterized by significant anomalies at other temperatures as well: $\sim$206 K, 204 K, and in the interval 190–195 K, and these are in no way distinguished by structural studies. Two equally well-founded approaches to explaining these anomalies have been advanced.[6,8,9] One of them is based on the conjecture that

intracrystalline weak perturbations (structural defects, uncontrolled impurities) can give rise to a spontaneous splitting of the transition to the the commensurate phase in TlInS$_2$ into two phase transitions lying close together. In this model the anomaly at 206 K should be regarded as the point in temperature at which a change of incommensurabilities occurs, each of which is related to one of the commensurate phases realized at 201 K and 204 K, while the temperature region 190–195 K is interpreted as the coexistence interval of the polar regions of the phases arising at 201 and 204 K and having symmetry space groups C_2^3 and S_2^1, respectively, according to a group-theoretic analysis.[7]

The other approach[8,9] postulates the existence of an incommensurate–incommensurate (IC–IC) phase transition in TlInS$_2$ in the vicinity of 204 K. According to this model, the basic experimentally observed features in the behavior of $\varepsilon(T)$ and the elastic characteristics[2–4,10,11] of TlInS$_2$ can be explained and described quantitatively in the framework of the following nontrivial scheme for the sequences of the phases and phase transitions in this crystal: at $T_i = 216$ K a transition from the high-temperature paraphase to an IC phase which is stable in the interval 204–216 K (we denote it as IC-1), at $T_{ii} = 204$ K there is an IC–IC phase transition, the newly arising incommensurability (we denote it by IC-2) exists in the interval 201–204 K, and, finally, at $T_c = 201$ K there is a phase transition to a commensurately modulated ferrophase.

In this paper we present the results of investigations into the effect of an applied static electric field in the plane of the layer on the phase-transition-related anomalies of $\varepsilon(T)$ and the pyroelectric current $i(T)$ in the crystals TlInS$_2$ and TlGaSe$_2$. Such studies are of interest, in particular, in view of the theoretical indications[12,13] that applying a static elec-
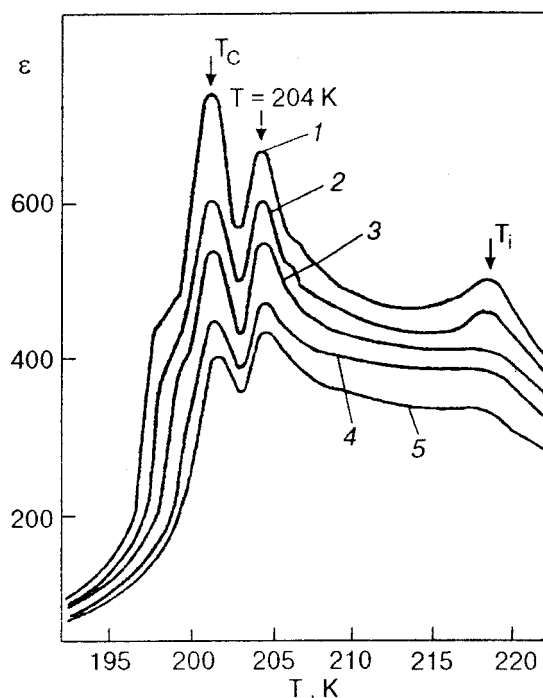
FIG. 1. Temperature dependence of the dielectric constant of TlInS$_2$ (frequency 55 kHz) near the phase transition when the crystal is subjected to static electric fields of various intensities, kV/cm: 0 (*1*), 4 (*2*), 6 (*3*), 9 (*4*), and 11 (*5*).

tric field along the polar axis in these crystals is equivalent to applying the corresponding components of a shear stress in respect to their effect on the temperature behavior of the various physical quantities near the IC phase transition. This is because the invariants of the interaction of the order parameter components and of the generalized coordinates in the expansion of the free energy density have analogous form. The effect of a uniaxial stress on the transformation of the shape of $\varepsilon(T)$ near the IC phase transition in TlGaSe$_2$ and TlInS$_2$ was investigated in Refs. 5 and 14.

SAMPLES AND TECHNIQUES

The samples were slabs ~ 2 mm thick, with plane-parallel ends ~ 12 mm^2 in area, cut from TlInS$_2$ and TlGaSe$_2$ single crystals perpendicular to the polarization axis, which coincides with the crystallographic axis $\mathbf{b} \| C_2$, where C_2 is the twofold symmetry axis. The surfaces perpendicular to the polar axis were carefully ground and mechanically polished to a mirror finish. Electrical contact was provided by applying a silver paste to the working surfaces of the crystals. The samples were mounted on the copper cold stage of a nitrogen cryostat.

Measurements of $\varepsilon(T)$ in the presence of a biasing electric field applied to the crystal were made by a bridge method based on a balancing scheme. The temperature of the sample was scanned at a rate of 0.1 K/min; the range of working frequencies was 50–60 kHz; the instrumental threshold sensitivity was ~ 0.1 pF, the error tolerance was $\sim 2\%$.

Measurements of the pyroelectric current in TlInS$_2$ were made by a quasistatic method[15,16] with a rate of temperature scanning ~ 3 K/min.

To decrease the influence of the poling of these compounds by the static electric field, it was applied to the samples at liquid-nitrogen temperature.

EXPERIMENTAL RESULTS AND DISCUSSION

The effect of electric field on the IC phase transition in TlInS$_2$ and TlGaSe$_2$ crystals

Figure 1 shows the temperature dependence of the dielectric constant of TlInS$_2$ for various intensities of the static electric field. It is seen that the orienting effect of the electric field leads to a transformation of the profile of the anomalies on the $\varepsilon(T)$ curve which is qualitatively similar to those observed when a mechanical stress $\sigma_\perp$ is applied perpendicular to the layers.[5,16] It should be noted that the variation of the intensity of the external electric field has a decisive influence on the profile of the dielectric anomaly corresponding to the IC phase transition. It is seen in Fig. 1 that an increase in the intensity of the external electric field is accompanied by a decrease in the amplitudes of the dielectric anomalies observed at the phase transition point ~ 204 K and at the point of the transition to the ferrophase $T_C = 201$ K; meanwhile, the position of these anomalies on the temperature scale is practically independent of the intensity of the external bias field. The structure observed on the curve of the temperature dependence of ε at certain values of the electric field is most likely not of a physical nature but rather the result of errors in the experimental technique. We note that for TlInS$_2$ the breakdown electric field is ~ 12 kV/cm.

Everything we have said about the relationships pertaining to the transformation of the anomalies of $\varepsilon(T)$ observed near the phase transition in a static electric field in the layered crystal TlInS$_2$ can be repeated almost verbatim for TlGaSe$_2$, the corresponding $\varepsilon(T)$ curves of which for electric fields of various intensities are shown in Fig. 2a. We note also that TlGaSe$_2$ has a higher breakdown field, ~ 22 kV/cm, than its isostructural counterpart TlInS$_2$.

It was shown in Ref. 7 that the single mixed invariant, which can be composed of components of the order parameter and polarization vector P_y (in the axes of the paraphase $x = a$, $y = b$, $z = c$), has the form $\sim \text{const} \, P_y \rho 4 \sin^4 \varphi$, where ρ and φ are the amplitude and phase of the two-component order parameter in a polar coordinate system. From a physical standpoint the experimentally observed effect of the generalized coordinate P_y of the external biasing electric field on the profile of the dielectric constant for $T = T_i$ in TlInS$_2$ and TlGaSe$_2$ can be explained only by the interaction of the polarization component P_y with the phase of the two-component parameter of the phase transition (in the constant-amplitude approximation),[12,13] which can result in a change in the spatial distribution law for the phase along the modulation axis. Thus the anomalous nature of the behavior of the transformation of the anomalies on the $\varepsilon(T)$ curve kv at the point of the IC phase transition when the crystal is acted on by external fields of different natures is explained by the circumstance that the application of an electric field and the application of a mechanical stress similarly cause a change in the topology of the incommensurate wave of modulation but do not eliminate it (we recall that in Refs. 5 and 16 the
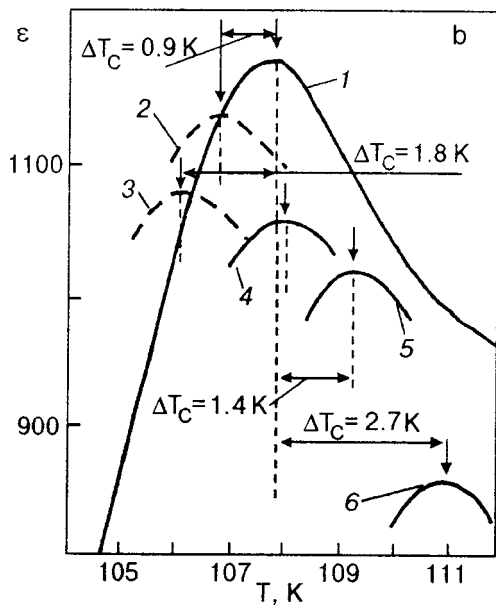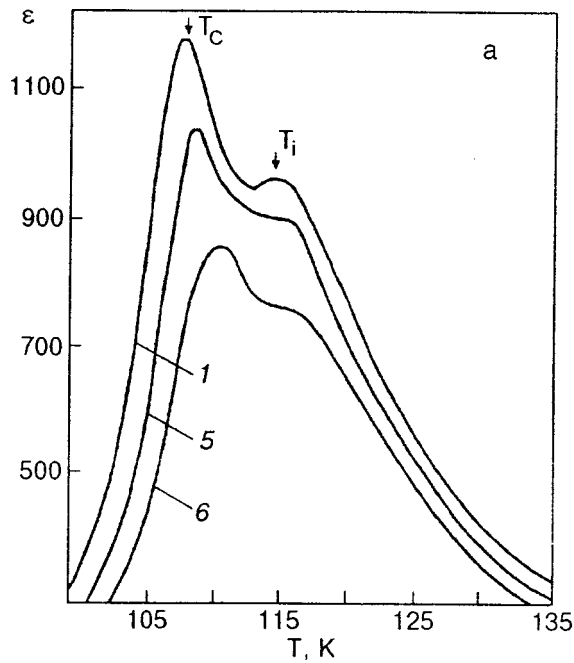
FIG. 2. Temperature dependence of the dielectric constant of TlGaSe$_2$ (frequency 57 kHz) near the phase transition when the crystal is subjected to a static electric field E (a), and the temperature behavior of the maximum of ε at $T=T_C$ for various intensities of the electric field, kV/cm: 2 (*1*), 4 (*2*), 6 (*3*), 8 (*4*), 10 (*5*), and 22 (*6*).

analogous modification of the profile of the curve at the point $T=T_i$ when a stress $\sigma_\perp$ was applied to TlInS$_2$ and TlGaSe$_2$ crystals was interpreted on the basis of the invariant $\sim$const $U_{yz}\rho^4\cos 4\varphi$, which is of a similar character to that discussed here).

Influence of external field on the transition to the commensurate phase in TlInS$_2$ and TlGaSe$_2$

Let us consider the results of an investigation of the effect of a static electric field on the anomalies of $\varepsilon(T)$ and $i(T)$ near the transition to the commensurate polar phase in
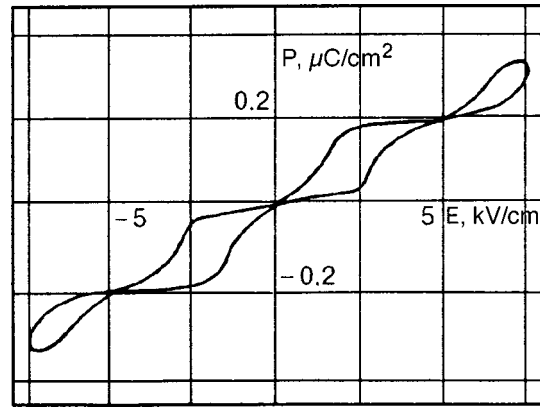

FIG. 3. Dielectric hysteresis loop for TlGaSe$_2$ in the temperature region $T<T_C$.

TlInS$_2$ and TlGaSe$_2$. The experiments demonstrate that a common feature of the orienting effect of an electric field on the anomaly at the Curie point in TlInS$_2$ and TlGaSe$_2$ is due the a change in the sign of the temperature shifts of these anomalies as a function of the intensity of the external field E applied to the sample. This is evidenced most clearly by the data shown in Fig. 2b, which reflect the temperature dynamics of the maximum on the $\varepsilon(T)$ curve of TlGaSe$_2$ at $T=T_C$ as E is varied. It is seen from Fig. 2b that at electric fields smaller than a certain threshold value $E_{cr}=7$ kV/cm, the maximum of the $\varepsilon(T)$ curve is shifted by 2K to lower temperatures from the position of this anomaly in zero electric field. In the region $E>E_{cr}$ the maximum on the $\varepsilon(T)$ curve is shifted to higher temperatures; the size of this shift from the position of this maximum in zero electric field is $\sim$3 K for fields in the prebreakdown region. We note that the application of an electric field leads only to a shift of the maximum of $\varepsilon(T)$ as a whole, without leading to a Leningrad or appreciable broadening of this maximum. We emphasize that the observed feature cannot be set aside as being instrumental, since the apparatus is capable of a practically identical rate of temperature scanning over the whole mm cycle, and the values of the temperature shifts are too large to be the result of methodological errors in the detection system.

If we take into account the known fact[17] that a uniform electric field shifts the peak in ε corresponding to the Curie point of classical or ''lattice'' antiferroelectrics to lower temperatures from its position in zero field, then, at first glance, the data presented above for TlGaSe$_2$ can be regarded as the result of the induction of a ferroelectric state from the antiferroelectric state of that crystal by an external field $E>E_{cr}$. We note that this is an extremely general indicator which permits us to reliably classify the low-temperature polar phase of TlGaSe$_2$ as antiordered. An illustration of the fact that the low-temperature polar phase of TlGaSe$_2$ is distinguished by a rather complicated dipole configuration is the nontrivial dielectric hysteresis loop, with four different regions of spontaneous polarization, which we observed by the Sawyer–Tower method (see Fig. 3).

In principle the possibility of antiferroelectric dipolar ordering of the low-temperature polar phase of TlGaSe$_2$ is ad-

mitted by the models proposed previously in the literature[18,19] for the structural phase transition in the compounds under study. For example, in Ref. 19 a model is discussed in which the layered crystal is considered as a system in which the phase transition to the commensurate polar phase occurs at different temperatures in different layers. The stable state of the crystal may be a structure of commensurate polar layers separated from one another by layers found in the incommensurate phase. It can be supposed that in the layered crystal TlGaSe$_2$ the state of the system in the neighborhood of the phase transition at $T = T_C$ is a system of dipolar ordering in which different layers have oppositely directed spontaneous polarization vectors, the magnitudes and directions of which vary in a random manner from one polar layer to another, and they average to zero on summation over the whole crystal. Increasing the external electric field above the threshold value E_{cr} enhances the influence of one of the directions of spontaneous polarization of the crystal and thereby leads to a ''transition'' of TlGaSe$_2$ to a uniform ferroelectric state by virtue of of the fact that the mutual influence of the counterdirected dipole moments of the different layers is relatively small.

It appears that another approach, based on the model concepts developed in Ref. 6, is also useful. The results of a group-theoretic analysis presented in that paper reduce to the following. The phase transition from the high-symmetry paraphase with space group C_{2h}^6, corresponding to a wave vector $\mathbf{k}_c = 0.25\mathbf{c}^*$, to the commensurate polar phase can be realized according to two symmetry schemes, depending on the sign of the coefficient γ in the anisotropic invariant $\sim \gamma\rho^8\cos 8\varphi$: for $\gamma > 0$ the stability condition is satisfied by a ferroelectric phase with space group C_2^3, while for $\gamma < 0$ the stable phase is one with space group S_2^1, which may be a centrosymmetric antiferroelectric. If it is assumed that in the absence of an external electric field the symmetry of the commensurate phase of TlGaSe$_2$ corresponds to S_2^1 and that $\gamma \sim f(E)$, with $\gamma < 0$ for $E < E_{cr}$ and $\gamma > 0$ for $E > E_{cr}$, then the role of the biasing electric field reduces to one of inducing a phase transition between the equitranslational polar phases, $S_2^1 \rightarrow C_2^3$.

Meanwhile, the results obtained from studying a large number of TlGaSe$_2$ samples picked from different technological batches clearly demonstrate substantially different properties of the low-temperature polar phase of TlGaSe$_2$ in the presence of an external electric field as compared to the analogous properties of ''lattice'' antiferroelectrics, and the nature and properties of the antiordered state of TlGaSe$_2$ in the low-temperature phase is found to be very sensitive to the structure. These results include the following.

1. The application of an electric field to the antipolar phase of TlGaSe$_2$ does not lead to saturation of ε, as would be expected for classical antiferroelectrics;[17] ε in the low-temperature phase of TlGaSe$_2$ decreases monotonically with increasing E, and the size of the temperature shift of the maximum of $\varepsilon(T)$ is not proportional to the square of the electric field.

2. Certain groups of samples exhibit a strong deviation of the temperature shifts of the $\varepsilon(T)$ peak and the values of
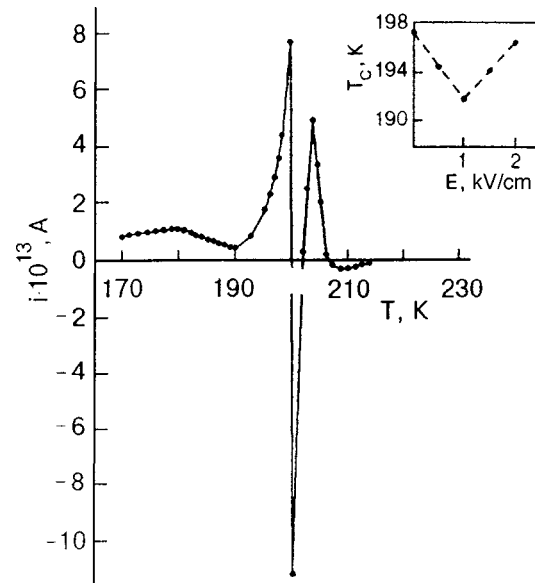

FIG. 4. Temperature depend of the pyroelectric current of TlInS$_2$ near the phase transition. The inset shows the shift of the maximum of the $i(T)$ curve at $T = T_C$ as a function of the applied external electric field.

E_{cr} from those described above (although the picture of the inversion of the sign of the temperature shift of $\varepsilon(T)$ with increasing E is qualitatively the same as described), and in other samples the temperature shift of the $\varepsilon(T)$ peak as a function of E is only partially present or absent entirely.

3. Chipping off part of a sample reduces both the interval of the temperature shift of $\varepsilon(T)$ and the value of the critical field E_{cr}; an analogous situation is observed when the polarity of the electric field applied to the sample is reversed.

4. Turning off the external field from values at which the position of the $\varepsilon(T)$ peak after the monotonic shifts is restored to the temperature position of the anomalies of ε in the absence of electric field leads only to growth of the absolute value of ε to its original value (for $E = 0$).

While the investigation of $\varepsilon(T)$ for TlInS$_2$ samples prepared from the same bar did not confirm an anomalous shift of the $\varepsilon(T)$ peak corresponding to the phase transition at $T = T_C$ over the whole range of applied electric fields, measurements of $i(T)$ in an external static electric field on samples of TlInS$_2$ from different technological batches registered an effect analogous to that observed for the $\varepsilon(T)$ measurements in TlGaSe$_2$.

The clearest of the experimental curves of the pyrocurrent of TlInS$_2$ in the absence of field is shown in Fig. 4. We see that the behavior of $i(T)$ is characterized by two anomalies in the form of sharp-tipped spikes, the temperature positions of which correspond to the phase transition points at ~ 204 K and $T_C = 200$ K, and the higher of the spikes in $i(T)$ in all the samples of TlInS$_2$ investigated is characterized by a sharp ''overshoot'' of the pyrocurrent at temperatures close to the point of the phase transition to the polar commensurate phase (~ 200.4–200.7 K for samples from different technological batches), and the direction of this ''overshoot'' of the pyrocurrent is always opposite to the $i(T)$ spikes at the other phase transition points.

Interestingly, the form of the $i(T)$ curves is essentially

reproducible for TlInS$_2$ samples from the same batch. At the same time, we identified certain samples of TlInS$_2$ for which the shape of the $i(T)$ curve differed substantially from that shown in Fig. 4: by the number of anomalies present (in some samples the $i(T)$ curve has only one spike, at $T=T_C$, with a sharp ''overshoot'' of the pyrocurrent preceding this anomaly), by the ratio of the amplitudes of the anomalies of $i(T)$ at the phase transition points (in one group of samples the higher spike is observed at 204 K), and by an unstable character of the $i(T)$ spike at $\sim$204 K (during measurements in a heating–cooling mode, in the course of a thermal hold of the sample at $\sim$204 K the amplitude of the $i(T)$ spike become significantly higher than the initial value and then relaxes to it over a time of several hours).

The application of a static electric field along the spontaneous polarization direction of a TlInS$_2$ sample noticeably transforms the values and contours of the $i(T)$ anomalies on account of additional contributions to the pyroresponse from other mechanisms occurring in ferroelectric semiconductors. Nevertheless, the position of the spikes on the $i(T)$ curve is in no way related to these mechanisms but is due solely to the contribution of bound charges induced on the corresponding faces of the crystal as a result of the phase transition. It is also important that reversing the direction of the external electric field does not affect the character of the $i(T)$ curve of TlInS$_2$ — the signs of the spike signals of the pyrocurrent at the phase transition points and the sharp ''overshoot'' change to the opposite.

In the diagram shown in the inset of Fig. 4 the series of points shows the temperature positions of the $i(T)$ spike corresponding to the phase transition to the commensurate ferrophase on increasing E. One observes a complete analogy with the results obtained in a study of $\varepsilon(T)$ in TlGaSe$_2$ in an applied field E; the value of the critical field for the given sample is $E_{cr}=1$ kV/cm, and for samples from different batches it fluctuates over the interval from 0.6 to 1 kV/cm. It also follows from the experimental data that the $i(T)$ spike corresponding to the point $\sim$204 K (like the $\varepsilon(T)$ peak at this temperature; see Fig. 1) does not suffer any temperature shift as the external field is increased. Furthermore, it was found that the $i(T)$ spike at $T=T_C$ did not shift with increasing E for the TlInS$_2$ samples, which have only a single anomaly of $i(T)$ at the given point in temperature. Thus it can be stated that the reversible shift of the $i(T)$ spike on variations of E occurs only for the case of the phase transition from IC-2 to the polar commensurate phase and is absent from the neighborhoods of the phase transitions from the paraphase to IC-1, from IC-1 to IC-2, and from IC-1 to the polar commensurate phase, by virtue of of the special configurational arrangement of the incommensurate modulation wave in the IC-2 phase. Another noteworthy result is that even in the absence of an external electric field, the $i(T)$ curve for TlInS$_2$ in the existence region of the IC phase is characterized by numerous sharp ''overshoots'' against the background of the monotonic growth of $i(T)$ as $T\rightarrow T_C$, as is illustrated in Fig. 5. This circumstance provides grounds for considering the IC-1 and IC-2 phases of TlInS$_2$ as ''labile'' systems which are extremely sensitive to processes of phase restructuring of the incommensurate modulation wave
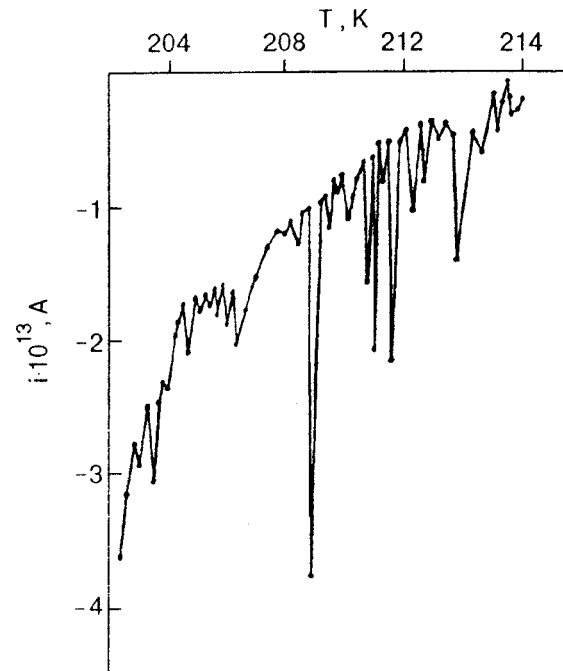

FIG. 5. Temperature dependence of the pyroelectric current of TlInS$_2$ in the stability region of the incommensurate phase.

to a structure consisting of topological phase solitons and regions of the commensurate polar phase.

The results presented above for synthesized TlInS$_2$ and TlGaSe$_2$ samples of different quality, having the same lattice resonance and a similar stacking of the layers in the real structures, prompted us to consider the change in sign of the temperature shift of the $\varepsilon(T)$ and $i(T)$ anomalies of TlGaSe$_2$ and TlInS$_2$, respectively, at the Curie point $T=T_C$ (i.e., at the ''exit'' from the IC phase) in an increasing electric field as resulting from the effect of the electric field on structural features of the IC modulation wave in a crystal containing defects, as a result of which one observes a broadening (for $E<E_{cr}$) or narrowing (for $E>E_{cr}$) of the temperature interval in which the IC phase is stable.

As we have said, the possibility of realizing an IC–IC phase transition in the sequence of structural phase transitions in TlInS$_2$ was demonstrated in Refs. 8 and 9; this phase transition gives rise to a new phase, IC-2, which is stable in the interval 200–204 K and is distinguished by the special topological arrangement of the IC-2 modulation wave, incomplete compensation of the local dipole moments of the regions of the sample occupied by phase solitons, and regions of the polar commensurate phase. The IC–IC phase transition is brought about through the introduction of an invariant $\lambda/2[d^2\varphi/dz^2]^2$ in the thermodynamic potential under the condition that the coefficient $k(T,P,n)$ (where P is the external pressure and n is the concentration of intrinsic structural defects or other distortions of the crystal lattice which are sources of internal static stresses) multiplying the invariant $k/2[d\varphi/dz]^2$, which is responsible for the stability of the IC-1 phase in a certain temperature interval, is close to zero. Then the IC-2 phase can be realized in a crystal containing defects, both from the IC-1 phase and from the C_{2h}^6 paraphase, if $k=0$ throughout the entire temperature range or

takes on negative values. Analysis shows[8,9] that the external electric field for $\varepsilon < E_{cr}$ can lead to a finer domain structure, i.e., to a substantial increase in the density of solitons in the IC-2 phase, owing to the pinning of the IC-2 modulation wave at intrinsic structural defects, microcracks, extended defects, or other mobile charged formations, which are concentrators of the intracrystalline electric fields, thereby enlarging the temperature interval in which the IC-2 phase is stable. For $E > E_{cr}$ the external field apparently destroys the IC-2 structure on account of the increase of polar commensurate regions built into the IC modulation wave, thereby shrinking the existence interval of the IC-2 phase (E_{cr} can probably be regarded as the threshold field for depinning).

By analogy with the above, we believe that it can be supposed that, depending on the defect density of the real structures of the TlGaSe$_2$ samples, there exist two extremely different schemes for the sequence of structural phase transitions in this compound: $C_{2h}^6 \rightarrow$ IC-1 $\rightarrow$ polar commensurate phase with modulation wave vector $\mathbf{k}_c = 0.25\mathbf{c}^*$, and $C_{2h}^6 \rightarrow$ IC-2 $\rightarrow$ polar commensurate phase with $\mathbf{k}_c = 0.25\mathbf{c}^*$. Here the reversible shift of the $\varepsilon(T)$ peak at $T = T_C$ with increasing E occurs only for those TlGaSe$_2$ samples in which the sequence of structural phase transitions is described by the second of the proposed schemes.

CONCLUSION

We have shown that an external static electric field affects the IC phases of TlInS$_2$ and TlGaSe$_2$ differently at T_i, where an IC superstructure arises in the crystal, and at T_C, where the structure of the IC phase is close to the polar commensurate phase.

Near T_i the phase of the IC wave is ''labile,'' and changing its spatial distribution law by means of an external electric field can lead to noticeable modification of the $\varepsilon(T)$ anomalies in the two crystals.

Near T_C the structure of the IC phase can be of two types: IC-1 or IC-2, depending on the defect density of the TlInS$_2$ and TlGaSe$_2$ crystals.

An external electric field can only shrink the temperature interval in which the IC-1 phase exists, since an electric field increases the regions of the polar commensurate phase in the IC wave on account of the involvement of regions occupied by phase solitons.

The IC-2 phase, because of the incomplete compensation of the local dipole moments of the regions occupied by phase solitons and the regions of the polar commensurate phase in the IC wave, is of an antiordering character. Therefore an external electric field up to a certain value E_{cr} can serve as a stabilizing factor for the IC-2 phase and can thereby increase the temperature interval in which this phase exists. Fields $E > E_{cr}$, on the other hand, destroy the regions occupied by phase solitons and thereby induce a transition to a uniform polar commensurate phase at higher temperatures.

*)E-mail: seidov@lan.ab.az

[1] K. R. Allakhverdiev, T. G. Mamedov, V. G. Akinoglu, S. S. Ellialtioglu, Turk. J. Phys. **18**, 1 (1994).
[2] K. R. Allakhverdiev, A. I. Baranov, T. G. Mamedov, V. A. Sandler, and Y. N. Sharifov, Ferroelectrics Lett. **8**, 125 (1988).
[3] Yu. V. Ilisavskii, V. M. Sternin, R. A. Suleĭmanov, F. M. Salaev, and M. Yu. Seidov, Fiz. Tverd. Tela (Leningrad) **33**, 104 (1991) [Sov. Phys. Solid State **33**, 57 (1991)].
[4] R. A. Suleĭmanov, M. Yu. Saidov, and F. M. Salaev, Fiz. Tverd. Tela (Leningrad) **33**, 1797 (1991) [Sov. Phys. Solid State **33**, 1010 (1991)].
[5] R. A. Suleĭmanov, M. Yu. Seidov, F. M. Salaev, and T. S. Mamedov, Fiz. Tverd. Tela (Leningrad) **34**, 1829 (1992) [Sov. Phys. Solid State **34**, 976 (1992)].
[6] R. A. Suleĭmanov, M. Yu. Seidov, F. M. Salaev, and F. A. Mikailov, Fiz. Tverd. Tela (St. Petersburg) **35**, 348 (1993) [Phys. Solid State **35**, 177 (1993)].
[7] F. M. Gashimzade and B. R. Gadzhiev, IFAN Azerb. Respubl. Preprint No. 199 [in Russian], Institute of Physics, Academy of Sciences of the Azerbaijan Republic, Baku (1986).
[8] B. R. Gadzhiev, M. Yu. Seidov, and V. R. Abdurakhmanov, Fiz. Tverd. Tela (St. Petersburg) **38**, 1 (1996) [Phys. Solid State **38**, 1 (1996)].
[9] B. R. Gadzhiev, M. Yu. Seidov, and V. R. Abdurakhmanov, Fiz. Nizk. Temp. **21**, 1241 (1995) [Low Temp. Phys. **21**, 950 (1995)].
[10] F. V. Salayev, K. R. Allakhverdiev, and F. A. Mikailov, Ferroelectrics **131**, 163 (1992).
[11] R. A. Aliev, K. R. Allakhverdiev, A. I. Baranov, N. R. Ivanov, and R. M. Sardarly, Fiz. Tverd. Tela (St. Petersburg) **26**, 1271 (1984) [Sov. Phys. Solid State **26**, 775 (1984)].
[12] D. G. Sannikov, Fiz. Tverd. Tela (Leningrad) **25**, 616 (1983) [Sov. Phys. Solid State **25**, 352 (1983)].
[13] V. A. Golovko and D. G. Sannikov, Fiz. Tverd. Tela (Leningrad) **25**, 3419 (1983) [Sov. Phys. Solid State **25**, 1968 (1983)].
[14] M. Yu. Seidov, Author's Abstract of Candidate's Dissertation [in Russian], Institute of Physics, Academy of Sciences of Azerbaijan, Baku (1992).
[15] É. Z. Aliev, A. E. Bakhyshov, N. A. Bakhyshov, T. G. Mamedov, and V. I. Tagirov, Kristallografiya **33**, 1038 (1988) [Sov. Phys. Crystallogr. **33**, 616 (1988)].
[16] E. Z. Aliev, E. E. Bakhyshov, and T. G. Mamedov, Ferroelectrics **83**, 161 (1988).
[17] G. A. Smolenskiĭ (ed.), *Physics of Ferroelectric Phenomena* [in Russian], Nauka, Moscow (1985).
[18] B. G. Gadzhiev, Fiz. Nizk. Temp. **17**, 889 (1991) [Sov. J. Low Temp. Phys. **17**, 465 (1991)].
[19] B. G. Gadzhiev, N. T. Mamedov, and F. B. Godzhaev, Fiz. Nizk. Temp. **20**, 59 (1994) [Low Temp. Phys. **20**, 50 (1994)].

Translated by Steve Torstveit

Rotational echo in amorphous ferromagnets

G. R. Kakabadze and L. L. Chotorlishvili

Tbilisi State University, ul. Chavchavadze 3, 380028 Tbilisi, Georgia
(Submitted May 18, 1999; revised July 12, 1999)
Fiz. Nizk. Temp. **26**, 84–85 (January 2000)

The rotational echo in amorphous ferromagnets is investigated. It is conjectured that amorphous ferromagnets contain a group of molecules having a dipole moment, and the change in the orientation of these molecules gives rise to oscillations of the echo signal. The transverse relaxation time associated with the interaction of two-level systems through spin waves is calculated. The time dependence of the echo signal is investigated. © *2000 American Institute of Physics.* [S1063-777X(00)00901-4]

There has recently been extensive research on amorphous systems, which are characterized by the presence of tunneling two-level systems (TLSs) (Ref. 1). The TLS model has been applied to crystalline materials, solid solutions such as $(KBr)_{1-x}(KCN)_x$, where the role of the TLS is played by the CN molecules, which have an electric dipole moment, and changing the orientation of these molecules leads to a change in the macroscopic polarization and to the experimental observation of a rotational echo.[2–4]

In this paper we make the conjecture that amorphous ferromagnets also have atoms that form a TLS. Clearly in an amorphous ferromagnet the tunneling transitions should be caused not only by phonons but also by spin waves.

The goal of this study was to investigate the rotational echo in amorphous ferromagnets.

In Ref. 5 the relaxation processes due to the interaction of the TLS with spin waves was investigated, and it was shown that under certain conditions this mechanism is predominant over the phononic relaxation mechanism.

When the expression obtained in Ref. 5 for the longitudinal relaxation time T_1 is averaged with the distribution function $p(\Delta_0 E)$ of the TLS, one obtains

$$\frac{1}{T_1} = \bar{p} \cdot \frac{\overline{D^2}}{8\sqrt{2}\alpha^{3/2}(4\pi\mu_0 M_0)^{1/2}} \frac{(2k_B T)^2}{\hbar}\left(\frac{E_{\max}}{2k_B T}\right)^2, \quad (1)$$

where $\bar{D}$ is the magnetic anisotropy constant, M_0 is the saturation magnetization, $E_{\max}$ is the maximum value of the energy splitting of the TLS, T is the temperature of the sample, and α is a quantity of the order of 10 K.

To calculate the transverse relaxation time T_2 we use the expression obtained in Ref. 5 for the interaction Hamiltonian of a TLS:

$$H_{\text{int}} = -\frac{1}{2}\sum_{a\neq b}\sum_{\mu\nu} J_{\mu\nu}^{ab}\sigma_\mu^{(a)}\sigma_\nu^{(b)}, \quad (2)$$

where $J_{\mu n}^{ab}$ is an interaction constant, the explicit form of the Hamiltonian for which is given in Ref. 5; $\sigma_\mu^{(a)}$ is the Pauli operator.

The transverse relaxation time of a TLS can be calculated from Eq. (2) in the same way as in the case of the interaction of a TLS via phonons:[6]

$$\frac{1}{T_2} = \frac{\pi}{2}\ln\frac{E_{\max}}{\Delta_0}\frac{\overline{D^2}}{\hbar\alpha}\frac{\overline{r^2}}{a^2}\exp\left(-\frac{q_0\bar{r}}{(\bar{p}k_B T)^{1/3}}\right)(\bar{p}k_B T)^{1/3}, \quad (3)$$

where $\bar{r}$ is the distance between TLSs, a is the interatomic distance, $\bar{p}$ is the density of states of the tunneling systems. Substituting into (1) and (3) the standard values

$$\bar{p}\sim 10^{19}\,J^{-1}, \quad T\sim 0.1\,K, \quad E_{\max}\sim 10\,K,$$

$$\bar{D}\sim 10^{-25}\,J, \quad \mu_0 M_0\sim 10^{-24}\,J, \quad \bar{r}\sim 10^{-8}\,m,$$

$$a\sim 10^{-10}\,m, \quad q_0\sim 5\times 10^6\,m,$$

and $\alpha\sim 10\,K$, we finally get

$$T_1\sim 10^{-5}\,s, \quad T_2\sim 3\times 10^{-6}\,s.$$

Following the procedure developed in Ref. 4, we obtain with the use of numerical methods the curve plotted in Fig. 1 for the time dependence of the amplitude of the echo for $T=0.1\,K$, $\omega=2\pi\times 10^9\,Hz$, $x=0.5$, and $t_r=10^{-6}\,s$.

Because of the lack of published experimental results on the rotational echo in amorphous ferromagnets, for an esti-
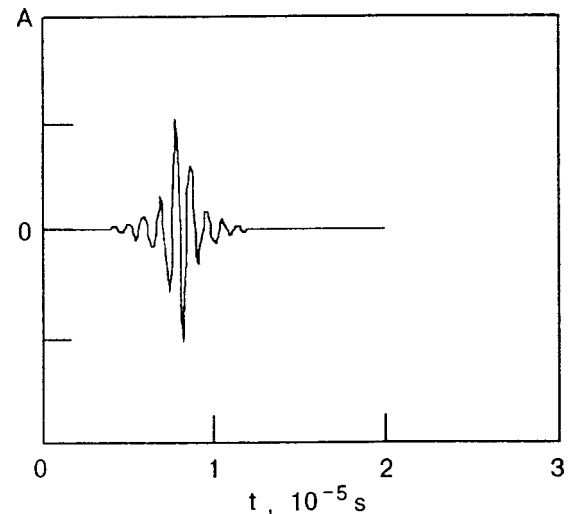

FIG. 1. Time dependence of the amplitude A of the rotational echo signal, as obtained by a numerical method.

mate of the dipole moment we used its value for solid solutions containing dipoles of the CN and OH type, $\bar{p}F_0 \sim 10^{-27}$ J.[3] We feel that this assumption is not of a fundamental nature, since it does not affect the shape of the echo signal. The results obtained here agree qualitatively with the data obtained for spin glasses,[4] and may stimulate interest in the experimental investigation of the rotational echo in amorphous ferromagnets.

[1] P. W. Anderson, B. J. Halperin, and C. M. Varma, Philos. Mag. **25**, 1 (1982); W. A. Phillips, J. Low Temp. Phys. **7**, 351 (1972).

[2] F. S. Vagapova and R. V. Saburova, Opt. Spektrosk. **43**, 474 (1977) [Opt. Spectrosc. **43**, 279 (1977)].

[3] F. S. Vagapova and R. V. Saburova, Izv. Vyssh. Uchebn. Zaved. Fiz. , No. 7, 49 (1993).

[4] C. Enss, R. Weis, S. Ludwig, and S. Hynklinger, Czech. J. Phys. **6**, 3287 (1996).

[5] S. V. Maleev and Yu. N. Skryabin, Zh. Éksp. Teor. Fiz. **83**, 380 (1982) [Sov. Phys. JETP **56**, 207 (1982)].

[6] L. L. Buishvili, L. Zh. Zakharov, and A. I. Tugushi, Teor. Mat. Fiz. **96**, 453 (1993).

Translated by Steve Torstveit

Nonlinear interaction of an electromagnetic wave and a dc current in a metallic film

S. A. Derev'anko

Kharkov State University, pl. Svobody 4, 310077 Kharkov, Ukraine

G. B. Tkachev* and B. A. Yampol'skiĭ

Institute of Radio Physics and Electronics, National Academy of Sciences of Ukraine, ul. Proskury 12, 310085 Kharkov, Ukraine
(Submitted May 20, 1999)
Fiz. Nizk. Temp. **26**, 86–95 (January 2000)

The nonlinear interaction of a dc current flowing in a thin metal film with an electromagnetic wave illuminating the sample in a symmetric manner with respect to the magnetic field is investigated theoretically. The nonlinearity is due to the most typical mechanism for pure metals at low temperatures — the magnetodynamic mechanism, involving the effect of the magnetic field of the current and wave field on the electron trajectories. It is shown that this interaction leads to sharp kinks in the time dependence of the electric field of the wave at the surface of the sample and to a peculiar electromagnetic signal amplification effect. © *2000 American Institute of Physics.* [S1063-777X(00)01001-X]

INTRODUCTION

It is known that metals have extremely peculiar nonlinear electrodynamical properties (see, e.g., the reviews).[1,2] In fact, the nonlinearity in the response of a plasma or semiconductor to an electromagnetic disturbance ordinarily arises as a result of a significant deviation of the electron system from its equilibrium position. In metals, on the other hand, because of the high concentration of charge carriers, the disequilibrium, as a rule, is weak. Nevertheless, it is comparatively easy to observe the nonlinear regime in metals. This is because the sources of disequilibrium and nonlinearity in metals are different. The disequilibrium is caused by a weak electric field, while the nonlinearity is caused by a strong magnetic field of electromagnetic excitation. The Lorentz force due to the magnetic field of the wave or the self-magnetic field of a dc current affects the dynamics of the charge carriers, and the conductivity of the sample therefore depends on the distribution of the magnetic field of the electromagnetic disturbance. This kind of magnetodynamic mechanism of nonlinearity is typical for pure metals at low temperatures, when the conduction electrons have a sufficiently long mean free path.

The magnetodynamic nonlinearity is the cause of a number of nontrivial electrodynamic effects. An example is the so-called ''current states'' [3,4]—an effect wherein a persistent magnetic moment is excited in the sample, with a hysteretic dependence on the external static magnetic field. Under conditions of ''current states'' one observes the hysteretic interaction of radio waves[5] and the formation of electromagnetic dissipative structures.[6] The specific mechanism of nonlinearity in metals leads to a decrease in the collisionless damping of helicons,[7] and helical waves of large amplitude can propagate under conditions such that there are no linear electromagnetic excitations.[8] Magnetoplasma shock waves[9] and excitations of the soliton type[10] have been predicted.

In the present paper we investigate a novel manifestation of magnetodynamic nonlinearity — the interaction of an external electromagnetic wave and a transport current in a thin metal film, an interaction which also comes about in a highly unusual way. The thickness d of the sample is assumed to be much smaller than the electron mean free path l, $d \ll l$, and the scattering of electrons on the surface of the metal is assumed to be diffuse. It is known[11] that in the static case (in the absence of an external alternating field) the self-magnetic field of the current can have a radical effect on the current-carrying capacity and current–voltage (I–V) characteristics of thin metallic samples. Here the value of the current I is such that the characteristic radius of curvature $R(I)$ of the electron trajectories in the magnetic field of the current is large compared to the thickness of the film:

$$d \ll R(I), \quad R(I) = c p_F / e H(I) \propto \Gamma^{-1}, \tag{1}$$

where $-e$ and p_F are the charge and Fermi momentum of the electron. It was shown in Ref. 11 that the features of the nonlinear response of a sample are due to the circumstance that the magnetic field of the current is distributed antisymmetrically over the thickness of the conductor: at the center of the film it is zero, and on opposite faces it takes on values which are equal in magnitude but opposite in sign: H and $-H$, where

$$H = 2\pi I / cD, \tag{2}$$

c is the speed of light in vacuum, and D is the width of the sample. The sign-alternating field of the current traps a portion of the electrons in a potential well. The trajectories of such particles are curves wound around the plane at which the magnetic field changes sign. The relative number of trapped electrons is equal in order of magnitude to the characteristic angle $(d/R)^{1/2} \ll 1$ at which the carriers approach this plane. Since the trapped carriers do not suffer collisions with the boundaries of the film and interact with the electric

field over the entire mean free path l, we obtain the following formula for estimating their conductivity σ_{tr}:

$$\sigma_{tr} \sim \sigma_0 (d/R(l))^{1/2} \propto I^{1/2}$$

(σ_0 is the electric conductivity of a massive sample).

At the same time, the electrons that do not suffer collisions before colliding with the boundaries of the metal have a conductivity of the order of $\sigma_0(d/l)$, as is well known.[12] We see that at high enough currents, when the following inequality holds,

$$[dR(I)]_{1/2} \ll l, \tag{3}$$

the conductivity of the film is determined by the group of trapped carriers. As a result, the I–V characteristic deviates from Ohm's law: the voltage U becomes proportional to the square root of the current,

$$U \propto I^{1/2}.$$

For a film of thickness $d = 10^{-3}$ cm and with an electron mean free path $l = 10^{-1}$ cm and a Fermi momentum $p_F = 10^{-19}$ g·cm/s the nonlinearity becomes appreciable $[(dR)^{1/2} \sim l]$ at values of the magnetic field of the current $H(I)$ of the order of 1 Oe. The theory of Ref. 11 is in good qualitative agreement with experiments (see, e.g., Ref. 13).

In an external magnetic field **h** parallel to the self-field of the current, the plane at which the magnetic field changes sign shifts toward one of the faces of the film (Fig. 1); this can lead to a significant decrease in the conductivity of the trapped particles. This should occur, in particular, when the film is uniformly illuminated by a large-amplitude electromagnetic wave at low frequencies, for which the external alternating magnetic field **h**(t) inside the conductor is practically uniform. In this situation the conductivity of the metal depends substantially on time and, consequently, strong nonlinear effects should appear in the response of the sample to an alternating electromagnetic disturbance. This topic, which is of interest from both the theoretical and experimental standpoints, has never been investigated before.

We have studied theoretically the time dependence of the electric field of a wave at the surface of a film along which flows a high dc current of a given value satisfying (1)

FIG. 1. Geometry of the problem. A diagram showing schematically the trajectories of the trapped (*1*), fly-through (*2*), and surface (*3*) electrons.

and (3). We show that as the amplitude h_m of the alternating magnetic field increases, this time dependence ceases to be quasiharmonic and is transformed into a series of sharp nonanalytic spikes. Of particular interest is the case of large amplitudes $h_m > H$, when during one part of the period of the wave the total magnetic field in the sample is sign-alternating while in the other it has a constant sign. In this situation the electric field has kinks as a function of time, due to the appearance and disappearance of groups of trapped carriers. An effect is predicted wherein an electrical signal is enhanced at the surface of the film. It turns out that on account of the presence of a strong transport current in the sample, the absolute value of the electric field of the wave is a factor of $l/(dR)^{1/2} \gg 1$ larger than the value in the absence of current.

FORMULATION AND GEOMETRY OF THE PROBLEM

We consider a metallic film of thickness d along which a dc current I is flowing. The sample is symmetrically illuminated from both sides by a monochromatic electromagnetic wave whose magnetic vector is collinear with the vector of the self-magnetic field of the current. We introduce a coordinate system with the x axis directed along the normal to the faces of the film. The plane $x = 0$ corresponds to the center of the sample (see Fig. 1). The y axis is chosen along the current, and the z axis is parallel to the vector of the magnetic field $\mathcal{H}(x,t)$, which is the sum of the magnetic field of the current $\mathbf{H}(x,t)$ and the magnetic field of the wave $\mathbf{h}(x,t)$:

$$\mathcal{H}(x,t) = \{0,0,H(x,t) + h(x,t)\}.$$

The length L (the dimension along the y axis) and width D (the dimension along the z axis) of the film are much greater than its thickness d. It is assumed that the scattering of electrons at the boundaries of the sample is diffuse.

In this geometry Maxwell's equations have the form

$$-\frac{\partial \mathcal{H}(x,t)}{\partial x} = \frac{4\pi}{c} j(x,t),$$

$$\frac{\partial E(x,t)}{\partial x} = -\frac{1}{c}\frac{\partial \mathcal{H}(x,t)}{\partial t}, \tag{4}$$

where $j(x,t)$ and $E(x,t)$ are the y components of the current density and electric field. The boundary conditions on Eqs. (4) are

$$\mathcal{H}(\pm d/2, t) = h_m \cos \omega t \mp H. \tag{5}$$

The symbol H denotes the absolute value of the magnetic field of the current at the surface of the metal, and h_m is the amplitude of the wave. The field H, according to Eq. (2), is determined by the total current I. The relationship between H and h_m is arbitrary.

We consider the quasistatic situation, when the wave frequency ω is much lower the the relaxation frequency ν of the charge carriers. Here we assume that the magnetic field of the wave inside the sample is quasiuniform and practically the same as its value at the surface: $h(x,t) \simeq h_m \cos \omega t$. In other words, the characteristic scale $\delta(\omega)$ for variations of the alternating magnetic field of the wave in the metal is
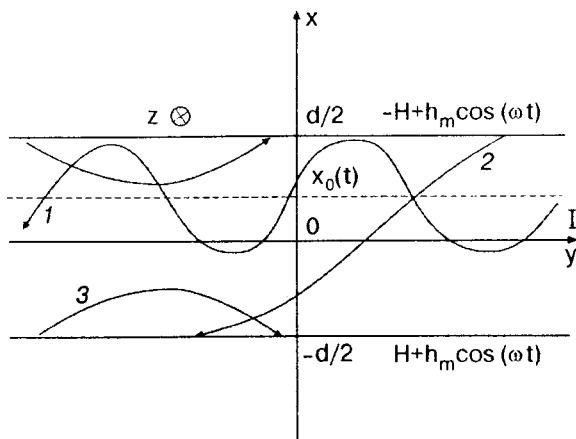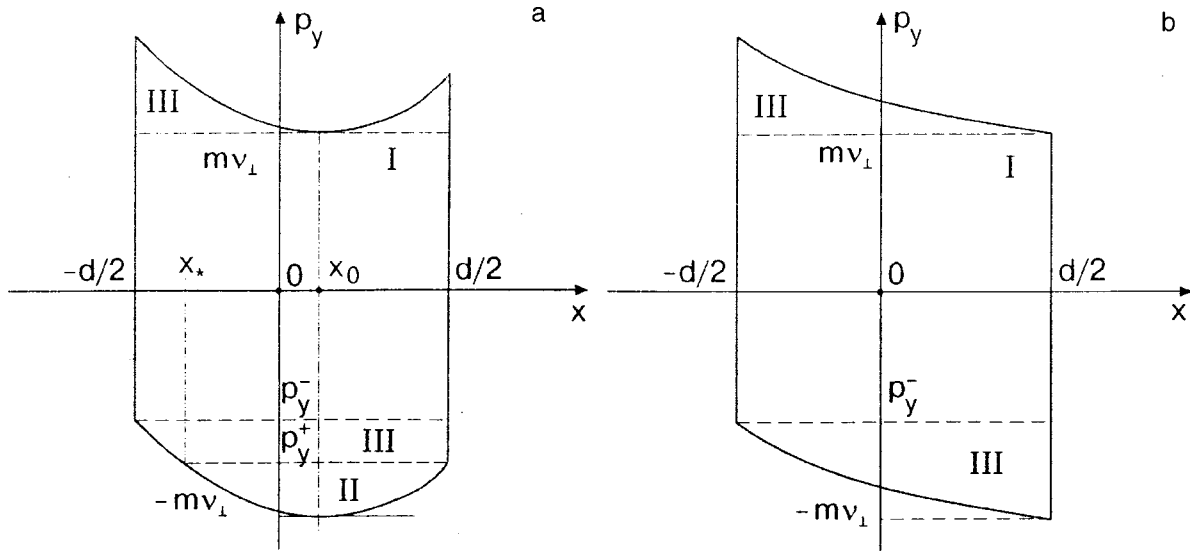
FIG. 2. Phase space (p_y, x). The existence regions of the fly-through (I), trapped (II), and surface (III) particles in alternating-sign (a) and constant-sign (b) total magnetic fields.

much larger than the film thickness d. In addition, we assume that the radius of curvature $R(x,t)$ of the electron trajectories in the total magnetic field $\mathcal{H}(x,t)$ is also considerably larger than d:

$$d \ll \delta(\omega), \quad d \ll R(x,t),$$

$$R(x,t) = cp_F/e|\mathcal{H}(x,t)|. \tag{6}$$

ELECTRON DYNAMICS, CURRENT DENSITY, AND I–V CHARACTERISTIC OF THE FILM

Let us consider the dynamics of the electrons in a non-uniform alternating magnetic field $\mathcal{H}(x,t)$. We choose the gauge of the vector potential in the form

$$A(x,t) = \{0, A(x,t), 0\}, \quad A(x,t) = \int^x dx' \mathcal{H}(x',t). \tag{7}$$

The lower limit of integration in (7) is conveniently chosen differently depending on whether or not at the given time there exists within the sample a plane $x = x_0(t)$ at which the magnetic field $\mathcal{H}(x,t)$ changes sign. For $h_m|\cos \omega t| < H$ such a plane does exist, since the values of the total magnetic field at the boundaries of the film, $h_m \cos \omega t - H$ and $h_m \cos \omega t + H$ [see Eq. (5)], are of opposite sign. In this case we will take $x_0(t)$ for the lower limit of the integral (7). Then the vector potential $A(x,t)$ is negative. At the point $x = x_0(t)$ it reaches a maximum, equal to zero. When the inequality $h_m|\cos \omega t| > H$ holds, the field $\mathcal{H}(x,t)$ is of a constant sign in space. In this situation the lower limit of integration is taken equal to sgn(cos ωt)$d/2$ (sgn(t) is the sign function). In this case the vector potential will also be negative, and it will vanish at the upper or lower boundary of the film.

The integrals of the motion of an electron in the field $\mathcal{H}(x,t)$ are the total energy (which we consider to be the Fermi energy) and the generalized momenta $p_z = mv_z$ and $p_y = mv_y - eA(x,t)/c$ (m is the mass of an electron). The trajectory of an electron in the plane perpendicular to the

magnetic field is determined by the velocities $v_x(x,t)$ and $v_y(x,t)$. For the Fermi sphere of radius $p_F = mv$ we have

$$|v_x(x,t)| = (v_\perp^2 - v_y^2)^{1/2}, \quad v_\perp = (v^2 - v_z^2)^{1/2},$$

$$v_y(x,t) = [p_y + eA(x,t)/c]/m. \tag{8}$$

The classically accessible regions of electron motion along the x axis are found from the inequalities

$$-p_y - mv_\perp \leqslant eA(x,t)/c \leqslant -p_y + mv_\perp .$$

These inequalities ensure positivity of the expression in the square root in formula (8) for $|v_x(x,t)|$.

Figure 2 shows a sketch of the regions of motion of an electron in the phase plane (x, p_y) in two cases: when there is a plane $(x = x_0(t))$ at which the field $\mathcal{H}(x,t)$ changes sign (Fig. 2a), and when there is no such plane (Fig. 2b). For the specificity we have chosen the point in time to be one for which the magnetic field of the wave is positive (cos $\omega t > 0$). The upper boundary on the phase plane is described by the curve $p_y = mv_\perp - eA(x,t)/c$, and the lower boundary by the curve $p_y = -mv_\perp - eA(x,t)/c$. We see that according to the nature of their motion it is natural to divide the electrons up into groups depending on the magnitude and sign of the integral of the motion p_y. Let us give the inequalities determining their existence regions at arbitrary times.

1. Fly-through electrons

For these electrons

$$p_y^- \equiv -mv_\perp - eA[-\text{sgn}(\cos \omega t)d/2, t]/c \leqslant p_y \leqslant mv_\perp ,$$

$$|x| \leqslant d/2$$

These particles collide with both boundaries of the film. Their trajectories are almost undistorted by the magnetic field, since $d \ll R(x,t)$. The fly-through electrons exist at all

times, independently of the presence of a plane $x=x_0(t)$ (i.e., independently of the relationship between $h_m \cos \omega t$ and H).

2. Trapped electrons

These electrons are manifested during periods of time, when $h_m \cos \omega t < H$ and the total magnetic field $\mathcal{H}(x,t)$ inside the sample passes through zero. The states of these electrons are bounded by the region (see Fig. 2a).

$$-m v_\perp \leq p_y \leq p_y^+ \equiv -m v_\perp - eA[\mathrm{sgn}(\cos \omega t)d/2,t]/c,$$

$$x_*(t)\mathrm{sgn}(\cos \omega t) < x \, \mathrm{sgn}(\cos \omega t) < d/2. \quad (9)$$

Here $x_*(t)$ is the farthest stopping point of a trapped electron from the boundary of the film. The coordinate $x_*(t)$ is found from the equation

$$A(x_*,t)=A[\mathrm{sgn}(\cos \omega t)d/2,t]. \quad (10)$$

According to Eq. (9), for $\cos \omega t > 0$ this electron group occupies the region $x_*(t) < x < d/2$, and for $\cos \omega t < 0$ it occupies the spatial interval $-d/2 < x < x_*(t)$. The trajectories of the trapped particles are nearly planar oscillating curves on account of the periodic motion in the direction of the x axis and the uniform motion along the y and z axes. The period of oscillation about the $x=x_0(t)$ plane is $2T$, where

$$T= \int_{x_1(t)}^{x_2(t)} \frac{dx}{|v_x(x,t)|}.$$

The turning points $x_1(t)$ and $x_2(t)$ ($x_1(t) < x_0(t) < x_2(t)$) are the roots of the equation

$$eA(x_{1,2},t)/c = -m v_\perp - p_y.$$

3. Surface electrons

The surface electrons collide only with one of the boundaries of the film. In the diffuse-reflection case considered here, the influence of the surface particles on the non-linear conductivity of the metal is unimportant.[11] Therefore, we shall henceforth disregard them.

The surface current of fly-through and trapped electrons is determined by the standard method of solving the Boltzmann transport equation. The transport equation is linearized with respect to the electric field $E(x,t)$, which is a sum of the uniform potential field $E_0(t)$ and the solenoidal wave field $\mathcal{E}(x,t)$:

$$E(x,t)=E_0+\mathcal{E}(x,t), \quad \mathcal{E}(x,t)=-\frac{1}{c}\frac{\partial A(x,t)}{\partial t}. \quad (11)$$

Here the nonlinearity is due entirely to the total magnetic field $\mathcal{H}(x,t)=H(x,t)+h(x,t)$ in the Lorentz force. In calculating the current density we restrict consideration to the leading approximation in the small parameter $d/\delta(\omega)$ [see Eq. (6)]. In such a case, as we have said, the magnetic field of the wave, $h(x,t)$, is spatially uniform and is equal to the value at the boundaries of the film, $h(x,t)=h_m \cos \omega t$. The electric field $E(x,t)$ in this approximation is also independent of the coordinates and is equal to the potential field $E_0(t)$. For uniform electric and external magnetic fields the

current density of the particles was obtained in Ref. 11. When conditions (1) and (3) are satisfied, the asymptotic behavior of the current of fly-through and trapped electrons are as follows:

$$j_\mathrm{fl}(t)=\sigma_\mathrm{fl}(t)E_0(t), \quad \sigma_\mathrm{fl}(t)=\frac{3}{8}\sigma_0\frac{d}{l}\ln\left(\frac{R_+(t)}{d}\right),$$

$$R_\pm(t)=\frac{cp_F}{e|h_m|\cos \omega t|\pm H|},$$

$$j_\mathrm{tr}(x,t)=\sigma_\mathrm{tr}(x,t)E_0(t),$$

$$\sigma_\mathrm{tr}(x,t)=\frac{36\pi^{1/2}}{5\Gamma^2(1/4)}$$

$$\times \sigma_0\left\{\frac{e}{cp_F}[A(x,t)-A(\mathrm{sgn}(\cos \omega t)d/2,t)]\right\}^{1/2},$$

$$x_*(t)\mathrm{sgn}(\cos \omega t) < x \, \mathrm{sgn}(\cos \omega t) < d/2. \quad (12)$$

In the limit $\omega \to 0$, expression (12) goes over to the formulas of Ref. 11.

Let us write the asymptotic formula for the current density (12) in the first of Maxwell's equations (4) and transform to a dimensionless coordinate and a dimensionless vector potential:

$$\xi=2x\,\mathrm{sgn}(\cos \omega t)/d, \quad (13)$$

$$a(\xi,t)=A(x,t)/A(\mathrm{sgn}(\cos \omega t)d/2,t).$$

The equation for $a(\xi,t)$ is

$$\frac{\partial^2 a(\xi,t)}{\partial \xi^2}=u\begin{cases} r[1-a(\xi,t)]^{1/2}+1, & \xi_*(t)\leq \xi \leq 1, \\ 1, & -1\leq \xi \leq \xi_*(t), \end{cases} \quad (14)$$

$$\xi_*(t)=2x_*(t)\mathrm{sgn}(\cos \omega t)/d. \quad (15)$$

This equation must be solved with the boundary conditions

$$\frac{\partial a(1,t)}{\partial \xi}=\frac{d}{2}\frac{h_m|\cos \omega t|-H}{A(\mathrm{sgn}(\cos \omega t)d/2,t)},$$

$$\frac{\partial a(-1,t)}{\partial \xi}=\frac{d}{2}\frac{h_m \cos \omega t|+H}{A(\mathrm{sgn}(\cos \omega t)d/2,t)}, \quad a(1,t)=1. \quad (16)$$

The first two of these boundary conditions are obtained by writing relations (5) in dimensionless form, and the third is a consequence of the normalization (13) for the vector potential. According to (10) and (13), the dimensionless coordinate $\xi_*(t)$ of the boundary of the existence region of the trapped particles satisfies the equation $a(\xi_*,t)=1$. The quantity r is the ratio of the maximum value of the conductivity of the trapped electrons $\sigma_\mathrm{tr}(\xi_0)$ to the conductivity of the fly-through particles:

$$r = \frac{\sigma_{\mathrm{tr}}(x_0)}{\sigma_{\mathrm{fl}}} = \frac{96\pi^{1/2}}{5\Gamma^2(1/4)}$$

$$\times \frac{1}{d}\left[\left|\frac{e}{cp_F}A(\mathrm{sgn}(\cos\omega t)d/2,t)\right|\right]^{1/2}\ln^{-1}(R_+/d),$$

$$(17)$$

and the dimensionless parameter u is related to the voltage across the sample, $U = E_0 L$:

$$u = \frac{U}{cL|A(\mathrm{sgn}(\cos\omega t)d/2,t)|/\pi\sigma_{\mathrm{fl}}d^2}. \tag{18}$$

In the interval $\xi_*(t) \le \xi \le 1$ the solution of equation (14) is symmetric with respect to the point $x_0(t) = \frac{1}{2}(1 + \xi_*(t))$ at which the dimensionless vector potential $a(\xi,t)$ has its minimum, equal to zero: $a(\xi_0,t) = \partial a(\xi_0,t)/\partial\xi = 0$. It is described by the formula

$$|\xi - \xi_0(t)| = (3/4ru)^{1/2}$$

$$\times \int_0^{a(\xi,t)} d\zeta[1 - (1-\zeta)^{3/2} + 3\zeta/2r]^{-1/2}. \tag{19}$$

The explicit form of the field and current density distributions in the existence region of the trapped particles cannot be found. However, Eq. (19) can be used to calculate the average value of the conductivity of the trapped carriers (12) over the interval (9):

$$\frac{\bar{\sigma}_{\mathrm{tr}}}{\sigma_{\mathrm{fl}}} = r\int_0^1 d\zeta(1-\zeta)^{1/2}[1-(1-\zeta)^{3/2}+3\zeta/2r]^{-1/2}$$

$$\times\left(\int_0^1 d\zeta[1-(1-\zeta)^{3/2}+3\zeta/2r]^{-1/2}\right)^{-1}. \tag{20}$$

The bar over σ_{tr} denotes the operation of averaging. In the rest of the sample, where only the fly-through electrons exist $(-1 \le \xi \le \xi_*(t))$, the solution of equation (14) is given by the expression

$$a(\xi,t) = 1 - (2u)^{1/2}(1+2r/3)^{1/2}(\xi - \xi_*(t))$$

$$+ \frac{1}{2}u(\xi - \xi_*(t))^2. \tag{21}$$

The functions (19) and (21) and their derivatives are matched at the point $\xi = \xi_*(t)$. Our solution (19), (21) contains three parameters, ξ_0, u, and r, which must be found from the boundary conditions (16). It should be kept in mind that the value $A(\mathrm{sgn}(\cos\omega t)d/2,t)$ of the vector potential appearing in Eq. (16) is not an independent parameter, since it is related to r by formula (17).

Adding up the first two boundary conditions (16) term by term and using Eqs. (18), (19), and (21), we arrive at the following expression for the displacement of the zero of the total magnetic field:

$$\xi_0 = \frac{2x_0\,\mathrm{sgn}(\cos\omega t)}{d} = \frac{cLh_m|\cos\omega t|}{2\pi U\sigma_{\mathrm{fl}}d},$$

$$h_m|\cos\omega t| \le H. \tag{22}$$

To determine the value of u (i.e., of the voltage U) we integrate the left and right sides of Eq. (14) from -1 to 1 with allowance for the boundary conditions (16) on the derivative $\partial a(\xi,t)/\partial\xi$. The integral of the function $[1-a(\xi,t)]^{1/2}$ that arises on the right-hand side can be reduced by using the condition $a(1,t) = 1$ to the product $2(1-\xi_0)\bar{\sigma}_{\mathrm{tr}}/r\sigma_{\mathrm{fl}}$. Taking this and the formulas for u (18) and ξ_0 (22) into account and performing some simple transformations, we obtain

$$U = \frac{cL}{2\pi d\sigma_{\mathrm{fl}(t)}}\frac{H(I)+(\bar{\sigma}_{\mathrm{tr}}/\sigma_{\mathrm{fl}})h_m\cos\omega t|}{1+\bar{\sigma}_{\mathrm{tr}}/\sigma_{\mathrm{fl}}},$$

$$h_m|\cos\omega t| \le H. \tag{23}$$

According to Eq. (20) the conductivity ratio $\bar{\sigma}_{\mathrm{tr}}/\sigma_{\mathrm{fl}}$ in (23) depends on the parameter r. Taking into consideration the expression for u (18) and the relation (17) between the quantities $a(\mathrm{sgn}(\cos\omega t)d/2,t)$ and r, from the first of conditions (16) with the use of (19) we obtain an algebraic equation for r:

$$r^2\left(1+\frac{2}{3}r\right) = \left(\frac{H-h_m|\cos\omega t|}{\tilde{H}}\right)^2\frac{\tilde{U}}{U\ln^3(R_+/d)},$$

$$h_m|\cos\omega t| \le H. \tag{24}$$

Here we have introduced the notation

$$\tilde{H} = \frac{25\Gamma^4(5/4)}{9\pi}\frac{cp_F d}{el^2}, \quad \tilde{U} = \frac{4clL\tilde{H}}{3\pi\sigma_0 d^2}. \tag{25}$$

The parameters $\tilde{H}$ and $\tilde{U}$ are the values of the magnetic field and voltage at which the characteristic arc of the electron trajectory $(Rd)^{1/2}$ is equal in order of magnitude to the mean free path l.

Expressions (20), (23), and (24) implicitly determine the dependence of the voltage U on the current I for $h_m|\cos\omega t| \le H$, when there is a plane on which the total magnetic field changes sign inside the sample. Under the opposite inequality, $h_m|\cos\omega t| \ge H$, trapped electrons are not present ($r = 0$, $\xi_* = 1$, $\sigma_{\mathrm{tr}} = 0$), and the I–V characteristic is described by the formula

$$U = \frac{cLH(I)}{2\pi d\sigma_{\mathrm{fl}}(t)}, \quad h_m|\cos\omega t| \ge H.$$

It follows from formula (23) that the voltage across the sample is a nonanalytic function of time: $U(t)$ has kinks at times where the magnetic field $h_m\cos\omega t$ of the wave goes to zero. This is an essentially nonlinear effect that is due to the contribution to the current from the large group of trapped electrons. Figure 3a shows the time dependence of the voltage (23) at not-too-large wave amplitudes $h_m < H$, when trapped particles exist in the sample throughout the entire period $2\pi/\omega$. Figure 3b shows $U(t)$ in the opposite case $h_m > H$, when the conductivity during part of the wave period ($h_m|\cos\omega t| \ge H$) is due solely to the fly-through particles.
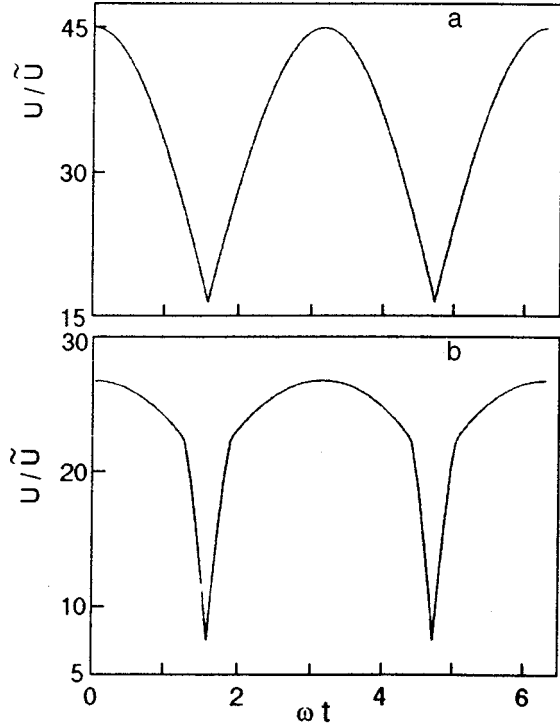
FIG. 3. Time dependence of the voltage U at relatively small $(h_m < H)$ (a) and large $(h_m > H)$ (b) wave amplitudes.

NONANALYTIC TIME DEPENDENCE OF THE ELECTRIC FIELD OF THE WAVE AT THE SURFACE OF THE FILM

Knowing the distribution of the vector potential $A(x,t)$, one can use formula (11) to calculate the solenoidal electric field $\mathcal{E}(x,t)$ as a correction to the potential component $E_0(t)$. This field goes to zero at the same point as the vector potential and reaches its largest absolute value at one of the boundaries of the film. We will be interested in the difference $\Delta\mathcal{E}(t)=\mathcal{E}(d/2,t)-\mathcal{E}(-d/2,t)$. This quantity is proportional to the rate of change of the magnetic flux through a cross section of the sample perpendicular to the vector of the total field $\mathcal{H}(x,t)$ and can be measured experimentally.

It follows from expressions (19) and (21) that the difference $a(1,t)-a(-1,t)$ of the values of the dimensionless vector potential is related to the derivatives $\partial a(1,t)/\partial\xi$ and $\partial a(-1,t)/\partial\xi$ by the relations

$$a(1,t)-a(-1,t)=-\xi_0(t)\left[\frac{\partial a(1,t)}{\partial\xi}-\frac{\partial a(-1,t)}{\partial\xi}\right],$$

$$h_m|\cos\omega t|\leqslant H, \tag{26}$$

$$a(1,t)-a(-1,t)=\frac{\partial a(1,t)}{\partial\xi}+\frac{\partial a(-1,t)}{\partial\xi},$$

$$h_m|\cos\omega t|\geqslant H. \tag{27}$$

Transforming in (26) and (27) to dimensionless variables, using the boundary conditions (16) and the relation (17) between the quantities $A(\mathrm{sgn}(\cos\omega t)d/2,t)$ and r, we obtain for the values of the vector potential at the boundaries of the film

$$A(\mathrm{sgn}(\cos\omega t)d/2,t)=-\tilde{H}d\ln^2(R_+/d)r^2/4,$$

$$A(-\mathrm{sgn}(\cos\omega t)d/2,t)=-\frac{1}{4}\tilde{H}d\ln^2(R_+/d)r^2-2H|x_0(t)| \tag{28}$$

for

$$h_m|\cos\omega t|\leqslant H$$

and

$$A(\mathrm{sgn}(\cos\omega t)d/2,t)=0, \tag{29}$$

$$A(-\mathrm{sgn}(\cos\omega t)d/2,t)=-dh_m|\cos\omega t|$$

for

$$h_m|\cos\omega t|\geqslant H.$$

Formulas (28) and (29) are matched at $h_m|\cos\omega t|=H$, when the parameter r (17) goes to zero, and the plane $x=x_0(t)$ coincides with one of the boundaries of the sample: $|x_0(t)|=d/2$. Using relations (11) and (28) and the formula (22) for $\xi_0(t)$, we obtain the following expression for the difference $\Delta\mathcal{E}(t)$ in the values of the electric field at the boundaries of the film:

$$\Delta\mathcal{E}(t)=-\frac{2H}{c}\frac{\partial x_0(t)}{\partial t}=-\frac{H(I)Lh_m}{2\pi}\frac{\partial}{\partial t}\left[\frac{\cos\omega t}{\sigma_{\mathrm{fl}}(t)U(t)}\right],$$

$$h_m|\cos\omega t|\leqslant H. \tag{30}$$

For $h_m\leqslant H$ this relation is valid over the entire period of the wave. If $h_m>H$, on the other hand, there exists a time interval during which the sample does not contain a plane $x=x_0(t)$ on which the total magnetic field changes sign. In that case formula (29) must be used to obtain the function $\Delta\mathcal{E}(t)$. The result is

$$\Delta\mathcal{E}(t)=\Delta\mathcal{E}_L\sin\omega t,\quad\Delta\mathcal{E}_L=dh_m\omega/c,$$

$$h_m|\cos\omega t|\geqslant H. \tag{31}$$

Of course, in the absence of a group of trapped electrons the difference in the values of the wave field $\Delta\mathcal{E}(t)$ is a harmonic function of time, i.e., the response of the film to the external electromagnetic excitation is linear. Clearly formula (31) also describes $\Delta\mathcal{E}(t)$ for small values of the current I $(H\ll\tilde{H})$, when the distribution of the trapped particle to the conductivity is unimportant throughout the entire wave period. Then $\Delta\mathcal{E}_L$ is the amplitude of the linear response.

Figure 4 shows the function $\Delta\mathcal{E}(t)$ over a wide range of values of the wave amplitude h_m at a large value of the magnetic field H of the current, when the condition $H\gg\tilde{H}$ [i.e., inequality (3)] holds. We see that the ratio of the oscillation amplitude $\Delta\mathcal{E}_m$ to the linear value $\Delta\mathcal{E}_L$ does not depend on h_m. From relations (30), (23), and (24) for $\cos\omega t=0$ we obtain the following expression for $\Delta\mathcal{E}_m$:

$$\frac{\Delta\mathcal{E}_m}{\Delta\mathcal{E}_L}=0.83\left(\frac{H}{\tilde{H}}\right)^{1/2}\frac{1}{\ln(R/d)},$$

$$\left(\frac{H}{\tilde{H}}\right)^{1/2}-\frac{l}{(Rd)^{1/2}}\gg 1. \tag{32}$$
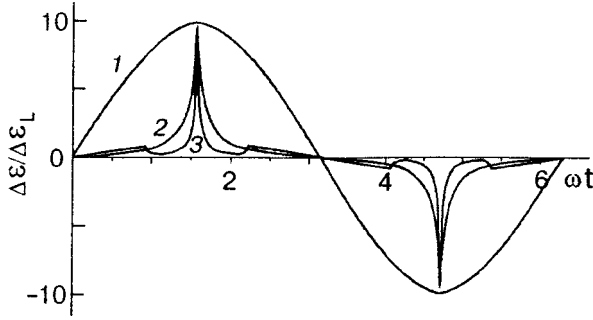
FIG. 4. Difference $\Delta\mathcal{E}$ in the values of the electric field of the wave at the boundaries of the film as a function of time at a fixed value of the current $(H=300\tilde{H})$ and different amplitudes $h_m/\tilde{H}$: 1 (*1*), 200 (*2*), 500 (*3*). The ratio of the mean free path l to the film thickness d is equal to 30. $\tilde{H}$ is the magnetic field at which the characteristic arc of the electron trajectory is of the order of the mean free path [Eq. (25)].

The ratio $\Delta\mathcal{E}_m/\Delta\mathcal{E}_L$ is determined by the value of the magnetic field H of the current and can be much greater than unity. In other words, there in an amplification of the electrical signal at the surface of the film. At small wave amplitudes (curve *1*, $h_m=H/300$) the signal is quasiharmonic. As h_m increases, however, kinks appear on the function $\Delta\mathcal{E}(t)$. Curve *2* ($h_m=2H/3$) has kinks at the extrema, i.e., at the time when the magnetic field $h_m\cos\omega t$ of the wave goes to zero. These features are due to the nonanalyticity of the I–V characteristic of the film (see Eq. (23) and Fig. 3). Curve *3* corresponds to the case $h_m=5H/3$, when there are no trapped electrons during a part of the wave period. In that case the function $\Delta\mathcal{E}(t)$ contains additional kinks arising at the times of the appearance and disappearance of the plane $x=x_0(t)$ on which the sign of the total magnetic field changes sign. On curve *3* these points are arranged symmetrically relative to the extrema. Using formulas (30), (31), (23), and (24), we find the derivatives of the function $\Delta\mathcal{E}(t)$ to the left and right of the point of the first kink $t_0=(1/\omega)\cos^{-1}(H/h_m)$:

$$\frac{\partial}{\partial t}\left.\frac{\Delta\mathcal{E}(t)}{\Delta\mathcal{E}_L}\right|_{t=t_0-0}=\frac{\omega H}{h_m},\tag{33}$$

$$\frac{\partial}{\partial t}\left.\frac{\Delta\mathcal{E}(t)}{\Delta\mathcal{E}_L}\right|_{t=t_0+0}=\frac{\omega H}{h_m}\left[1-\frac{\pi}{2\ln(R_+/d)}\left(\frac{H}{\tilde{H}}\right)^{1/2}\left(\frac{h_m^2}{H^2}-1\right)\right].\tag{34}$$

according to Eq. (34), when $[(h_m/H)^2-1]\geqslant 1$ the derivative on the right is already negative and large in absolute value.

CONCLUSION

In this paper we have investigated the nonlinear response of a thin metallic film carrying a high dc current to an external electromagnetic excitation that is symmetric with respect to the magnetic field. We have shown that as a result of the interaction of the wave and current the electric field of the wave at the surface of the metal is a nonanalytic function of

time, having a number of sharp kinks. Increasing the current leads to an increase in the amplitude of the oscillations of the electric field at the surface of the sample.

For observation of the effects predicted in this paper it will be necessary to have a sufficiently large electron mean free path [see inequality (3)]. This condition can be satisfied only at low temperatures and in rather pure samples. In addition, it is necessary that the magnetic field $h(x,t)$ of the wave in the film be quasiuniform $(h(x,t)\simeq h_m\cos\omega t)$, and the electric field $\mathcal{E}(x,t)$ of the wave be small compared to the potential field $E_0(t)$. Let us state an inequality under which this situation will be realized. On the basis of formulas (11), (28), and (29) one can conclude that the maximum (in absolute value) of the field $\mathcal{E}$ is of the order of $\Delta\mathcal{E}_m$ (32). Clearly, $\Delta\mathcal{E}_m$ should be much less than the minimum value of the function $E_0(t)$, i.e., the values of the potential field (23) at $\cos\omega t=0$. The corresponding inequality is written in the form

$$d^2\frac{h_m l}{Hr}\ll\delta_n^2(\omega),\quad\delta_n^2(\omega)=\frac{c^2}{4\pi\sigma_0\omega},\tag{35}$$

where $\delta_n(\omega)$ is the characteristic penetration depth of the alternating field into the metal in the normal skin effect. In addition to condition (35), it is necessary that the nonuniform component of the magnetic field of the wave inside the film be much less than h_m. The maximum value of the nonuniform correction can be estimated from the first of Maxwell's equations (4) as $(4\pi\sigma_{\text{tr}}\Delta\mathcal{E}_m d/c)\sim h_m(d/\delta)^2$, where the effective penetration depth $\delta(\omega)$ is equal to $\delta_n(\omega)(R/l)^{1/2}$. As a result, we arrive at the requirement (6) of quasiuniformity of the magnetic field of the wave:

$$d^2\frac{l}{R}\ll\delta_n^2(\omega).\tag{36}$$

From a comparison of inequalities (35) and (36) we see that at large wave amplitudes $h_m>H$ condition (35) is the stricter, while for a small-amplitude signal $h_m<H$ it is condition (36).

At a fixed temperature (fixed mean free path of the charge carriers) which ensures that the main condition (3) is satisfied, inequalities (35) and (36) are restrictions on the frequency of the wave. Let us estimate the values of the characteristic frequencies ω for which the kinks should be clearly observed on the time dependence of the electric field at the surface of the film. For a sample thickness $d=10^{-3}$ cm, an electron mean free path $l=10^{-1}$ cm, electron density $N=10^{23}$ cm^{-3}, and Fermi momentum $p_F=10^{-19}$ g·cm/s in magnetic fields $h_m=H=100$ Oe, inequalities (35) and (36) give $\omega<10^5$ s^{-1}. We note that at such values of the parameters of the problem the condition (3) that the mean free path of the particles be large is clearly satisfied.

*E-mail: tkachev@ire.kharkov.ua

[1] V. T. Dolgopolov, Usp. Fiz. Nauk **130**, 241 (1980) [Sov. Phys. Usp. **23**, 134 (1980)].

[2] H. M. Makarov and V. A. Yampol'skiĭ, Fiz. Nizk. Temp. **17**, 547 (1991) [Sov. J. Low Temp. Phys. **17**, 285 (1991)].

[3] G. I. Babkin and V. T. Dolgopolov, Solid State Commun. **18**, 814 (1976).

[4] N. M. Makarov and V. A. Yampol'skii, Zh. Éksp. Teor. Fiz. **85**, 614 (1983) [Sov. Phys. JETP **58**, 357 (1983)].

[5] L. M. Fisher, I. F. Voloshin, N. M. Makarov, and V. A. Yampol'skii, J. Phys.: Condens. Matter **5**, 8741 (1993).

[6] É. A. Kaner, N. M. Makarov, I. V. Yurkevich, and V. A. Yampol'skiĭ, Zh. Éksp. Teor. Fiz. **93**, 274 (1987) [Sov. Phys. JETP **66**, 158 (1987)].

[7] G. A. Vugal'ter and V. Ya. Demikhovskiĭ, Zh. Éksp. Teor. Fiz. **70**, 1419 (1976) [Sov. Phys. JETP **43**, 739 (1976)].

[8] V. G. Skobov and A. S. Chernov, Zh. Éksp. Teor. Fiz. **109**, 992 (1996) [JETP **82**, 535 (1996)].

[9] L. M. Fisher, N. M. Makarov, V. E. Vekslerchik, and V. A. Yampol'skii, J. Phys.: Condens. Matter **7**, 7549 (1994).

[10] N. M. Makarov, G. V. Tkachev, and V. E. Vekslerchik, J. Phys.: Condens. Matter **10**, 1033 (1989).

[11] É. A. Kaner, N. M. Makarov, I. B. Snapiro, and V. A. Yampol'skiĭ, Zh. Éksp. Teor. Fiz. **87**, 2166 (1984) [Sov. Phys. JETP **60**, 1275 (1984)].

[12] K. Fuchs, Proc. Cambridge Philos. Soc. **38**, 100 (1938).

[13] I. F. Voloshin, S. V. Kravchenko, N. A. Podlevskikh, and L. M. Fisher, Zh. Éksp. Teor. Fiz. **89**, 233 (1985) [Sov. Phys. JETP **62**, 132 (1985)].

Translated by Steve Torstveit

Sequence of structural phase transitions induced by an external magnetic field in the Jahn–Teller elastic KTm(MoO$_4$)$_2$

M. I. Kobets*

B. Verkin Institute for Low Temperature Physics and Engineering, National Academy of Sciences of Ukraine, pr. Lenina 47, 310164 Kharkov, Ukraine
(Submitted June 3, 1999; revised August 2, 1999)
Fiz. Nizk. Temp. **26**, 96–99 (January 2000)

Electron paramagnetic resonance and ac magnetic susceptibility studies in the compound KTm(MoO$_4$)$_2$ have revealed a number of features in the microwave absorption and magnetic susceptibility. It is conjectured that there is a sequence of magnetic-field-induced structural phase transitions involving the formation of a superstructure of the crystal lattice in KTm(MoO$_4$)$_2$. Experimental studies are carried out at a temperature of 1.7 K. © *2000 American Institute of Physics.* [S1063-777X(00)01101-4]

The compound KTm(MoO$_4$)$_2$ belongs to the family of isostructural binary alkaline–rare-earth molybdates of the type MRE(MoO$_4$)$_2$ (M=K, Cs, Li; RE=Er, Dy, Ho, Gd…), which have a layered crystal structure. A characteristic feature of this class of compounds is the presence of a correlation of the electronic subsystem of the rare earth with the phonon subsystem of the crystal lattice. Therefore, by acting on the electron subsystem with an external magnetic field, one can influence the structure of the crystal lattice of these compounds. This is manifested in the induction of structural phase transitions of the cooperative Jahn–Teller type.[1,2]

Previously it was reported[3] that a study of the angular dependence of the EPR spectrum of the Tm^{3+} ion in KTm(MoO$_4$)$_2$ revealed the presence of a low-temperature first-order structural phase transition induced by an external magnetic field. The external magnetic field was oriented along the small g factor, $g_a < 0.4$.

Further research on this phenomenon and a model description of the phase transition were published in Ref. 4. This description was based on the results of theoretical papers[5,6] which showed that structural phase transitions induced by external fields or temperature can occur not only in crystals containing ions with half-integer spin but also in paramagnets with a singlet ground state of the ions, where an external magnetic field can induce a structural phase transition that does not occur in the absence of field. Such a phase transition was observed by the authors of Ref. 7.

The present paper describes a study of the features of a structural phase transition induced by an external magnetic field. The microwave absorption spectra and the field dependence of the differential magnetic susceptibility were investigated.

EXPERIMENTAL RESULTS

The compound KTm(MoO$_4$)$_2$ at room temperature belongs to the orthorhombic system. Its symmetry is described by the space group D_{2h}^{14} with unit cell parameters $a = 5.05$ Å, $b = 18.31$ Å, $c = 7.89$ Å, and $Z = 4$.[8] The local

symmetry of the Tm^{3+} ions is C_2, and therefore the lowest electronic ground state of the Tm^{3+} ions ($^3H_6$) is split into nondegenerate states.

Experimental studies were carried out on a four-millimeter EPR spectrometer. The measurement cell was a high-Q cylindrical resonant cavity of the transmission type. The polarization of the microwave field at the sample was mixed relative to the direction of the magnetic field H. The angular dependence of the EPR spectrum was recorded at a fixed frequency. Two geometrically inequivalent centers were observed on the (ac) plane, rotated with respect to the a axis by $\pm 7.6°$. The measurements were made at a temperature of 1.7 K and a frequency of 80 GHz.

Figure 1 shows the form of the EPR absorption spectrum when the external magnetic field is oriented along the local magnetic axis a'. This direction corresponds to the minimum g factor of the Tm^{3+} ions ($g_a < 0.4$). It is seen that as the external magnetic field H is increased, at a field $H_c = 44.5$ kOe the absorption line is abruptly broken off at the high-field edge. In a decreasing external magnetic field one observes significant hysteresis with respect to the magnetic field, $\Delta H = 3.4$ kOe. The strong spin–orbit interaction, the presence of orbital quasidegeneracy in KTm(MoO$_4$)$_2$,

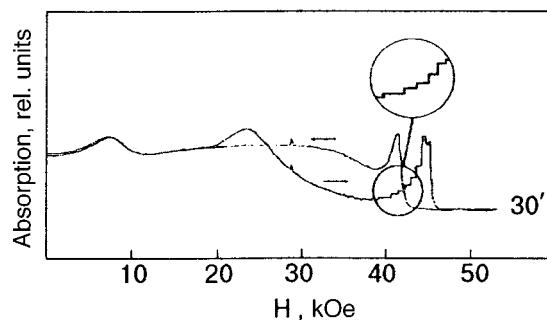FIG. 1. ESR absorption spectrum of the KTm(MoO$_4$)$_2$ crystal at a frequency of 80 GHz ($T = 1.7$ K; $H \| a'$). The narrow absorption line in a field $H = 28.5$ kOe is the signal of DPPH. Inset: Enlargement of the features on the absorption spectrum of the Tm^{3+} ion. The arrows indicate the direction of change of the external magnetic field.

and, as a consequence, the instability of the lattice suggest that we are observing the same kind of first-order structural phase transition of the Jahn–Teller type, induced by an external magnetic field, as those observed in $TmVo_4$ (Ref. 7) and $KEr(MoO_4)_2$ (Ref. 1).

This phase transition is accompanied by a feature in the absorption of microwave energy: the appearance of steps in magnetic fields lower than the transition field H_{c1}. The observation of steps and the value of the transition field depend strongly on the presence of defects in the crystal and the strength and rate of change (sweep rate) of the magnetic field. A decrease in the sweep rate of the field by a factor of approximately three causes the steplike feature to be ''saw-toothed.'' The stresses due to the mounting of the sample lead to the vanishing of the steps and to a shift of the phase transition field to higher values. In the region of the structural phase transition H_{c1} the absorption band is split into several features which are close in magnetic field, and a staircase dependence is preserved even at the line of the phase transition. When the temperature is raised to liquid-helium temperature there is an increase in the field of the structural phase transition, and the steps arising before the first-order phase transition are slightly smeared.

Reversing the sweep direction of the external magnetic field alters the form of the absorption spectrum (see Fig. 1): the steps acquire a different periodicity and height. If the field sweep is stopped at the steps before the onset of the main phase transition and the sweep direction is reversed, one observes hysteresis with respect to the magnetic field. One notices an additional absorption line at a field $H = 23.5$ kOe, which vanishes when the direction of the field sweep is reversed. We note that these results were obtained on new samples of very high quality, unlike the crystals used in Ref. 4. This led to some slight differences, both qualitative and quantitative, in the experimental results.

In addition to the resonance method we used the technique of measuring the magnetic susceptibility χ in an ac field at a frequency of 1 kHz. The experiment was carried out under conditions corresponding to the EPR measurements. Figure 2 shows the field dependence of the magnetic susceptibility of $KTm(MoO_4)_2$. One observes two jumplike

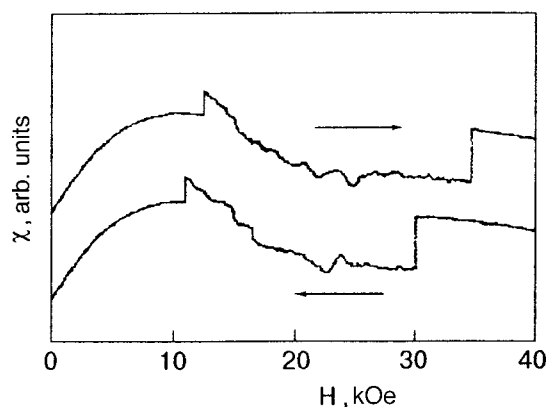changes in the field dependence of χ ($H_{c2} = 13.1$ kOe, $H_{c1} = 34.9$ kOe), with hysteresis in the position of the jumps with respect to the magnetic field. We attribute this behavior of χ to first-order structural phase transitions. The feature at $H_{c2} = 13.1$ kOe is not observed by the resonance technique. The steplike change in χ between the two phase transitions is less pronounced than at resonance. The value of H_{c1} is slightly different from the value determined previously for the field of the structural phase transition. We attribute all of the aforementioned disagrees of the experimental results to inaccuracy in the adjustment of the sample. It is seen from the measurements of χ that phase instability in the compound $KTm(MoO_4)_2$ begins in low magnetic fields H_{c2}.

DISCUSSION OF THE RESULTS AND CONCLUSIONS

An analysis of the experimental results presented above and their features, such as the steps, the regularity in their onset, and the dependence on the sweep rate of the field, the splitting of the maximum of the absorption band into several features lying close in magnetic field, and the memory effect, all indicate that in the field interval $H_{c2} - H_{c1}$ we apparently are observing a modulated superstructure of the lattice.

By now a rather large number of modulated superstructures in which the modulation period is not a multiple of the period of the initial lattice have been observed and investigated in detail; e.g., the family of crystals $[N(CH_3)_4]_2MeCl_4$ ($Me = Co, Fe, Cu, Zn$).

It is ordinarily assumed that the wave vector of the superstructure is a continuous function of temperature. However, as Dzyaloshinkiĭ has shown,[9] commensurability of the periods of the superstructure and lattice confers a finite energy advantage. Therefore, the change in the period of the structure of the incommensurate phase with temperature occurs in jumps, and the incommensurate phase is a temperature sequence of long-period commensurate phases. In our case the role of temperature is played by the external magnetic field on account of the strong spin–orbit interaction, when the electron moment is considered as the total moment, without dividing it into spin and orbital parts. Apparently the parameters of the crystal vary in a definite way, and in a resonance or magnetic experiment at low temperatures in an external magnetic field one observes a superstructure in which regions of commensurability are separated by very narrow regions of ''incommensurability'' (phase solitons).[10] The spatial symmetry of the crystal lattice of $KTm(MoO_4)_2$ admits the existence of a Lifshitz gradient invariant. Therefore, the thermodynamic potential contains a term that can give rise to a modulated spatial structure. The additional absorption observed in the intermediate phase is of a relaxational character, and its onset is probably due to the formation of a superstructure of the lattice.

If our assumptions are correction, the incommensurate structure may appear as a consequence of the dynamic interaction of the electronic branch due to excitation of the Tm^{3+} ions to the first Stark level and the acoustic phonon branch of the crystal. The low-frequency vibrational spectrum of binary alkali–rare-earth molybdates is formed on account of vibrations of the layers as a whole.[13] Starting from the data

FIG. 2. Field dependence of the magnetic susceptibility χ of the compound $KTm(MoO_4)_2$ ($T = 1.7$ K, $f = 1$ kHz, $H\|a$). The arrows indicate the direction of change of the external magnetic field.

presented in Ref. 14 and the width of the gap between the ground level and first excited Stark level of the Tm^{3+} ions, one can estimate the value of the wave vector at which the crossover of the vibrational and electronic modes occurs:

$$K_0 = \Delta E / V,$$

where ΔE is the energy distance to the first Stark level of the Tm^{3+} ion ($2.3\,cm^{-1}$), and V is the speed of sound in the $KTm(MoO_4)_2$ crystal (2×10^3 m/s). Estimates show that $K_0 = 2.2 \times 10^8\,m^{-1}$, which corresponds to 16 unit cell parameters in the direction perpendicular to the layer packets of the crystal. The interaction of the electronic and phonon modes results in a softening of the phonon branch in the region of K_0.

As indirect evidence supporting the correctness of our ideas about the formation of superstructure in $KTm(MoO_4)_2$, we can point to the observation of a modulated incommensurate lattice structure in the isostructural compound $KDy(MoO_4)_2$ in the region of a structural phase transition of the cooperative Jahn–Teller type by the authors of Refs. 11 and 12.

It is possible that there is another physical mechanism on which one can base an explanation of the observed experimental results, such as the formation of regular domains or the formation of new phase nuclei. However, we prefer the mechanism examined here because of the strict periodicity of the steps and their heights and the appearance of an additional absorption line, although it is extraordinarily difficult to assess the relative merits of these mechanisms.

We conclude with the following note. We have reported only preliminary experimental results. Our proposed physical explanation for the observed features of the resonance absorption is only of a qualitative nature at this stage. Clearly only direct methods of measurement (x-ray, neutron) can give an unambiguous answer as to the presence of a modulated structure. On the other hand, the experimental results obtained here, in our opinion, do permit the assumption that the sequence of structural phase transformations in $KTm(MoO_4)_2$ under the influence of an external magnetic field are accompanied by the formation of a modulated superstructure of the lattice.

*E-mail: kobets@ilt.kharkov.ua

[1] V. I. Kut'ko, V. A. Pashchenko, and M. I. Kobets, Fiz. Nizk. Temp. **19**, 1354 (1993) [Low Temp. Phys. **19**, 962 (1993)].

[2] M. J. Leask and A. S. Tropper, J. Phys. C **14**, 3481 (1981).

[3] E. N. Khatsko, M. I. Kobets, and V. A. Pashchenko, *Seventh International Seminar on Ferroelastic Physics* [in Russian], Kasan (1997).

[4] E. N. Khatsko, M. I. Kobets, and Ju. V. Pereversev, Ferroelectrics **221**, N1-2 (1999).

[5] B. G. Vekhter, Fiz. Tverd. Tela (Leningrad) **29**, 2492 (1987) [Sov. Phys. Solid State **29**, 1434 (1987)].

[6] Yu. V. Pereverzev, Fiz. Nizk. Temp. **22**, 289 (1996) [Low Temp. Phys. **22**, 226 (1996)].

[7] V. G. Vekhter, É. A. Kozeĭ, M. D. Kaplan, and Yu. F. Popov, JETP Lett. **54**, 578 (1991).

[8] R. F. Klevtsova and S. V. Borisov, Dokl. Akad. Nauk SSSR **117**, 1334 (1967) [*sic*].

[9] I. E. Dzyaloshinskiĭ, Zh. Éksp. Teor. Fiz. **47**, 992 (1964) [Sov. Phys. JETP **30**, 665 (1965)].

[10] V. A. Golovko and D. G. Sannikov, Zh. Éksp. Teor. Fiz. **82**, 959 (1982) [Sov. Phys. JETP **55**, 562 (1982)].

[11] Yu. N. Kharchenko, Fiz. Nizk. Temp. **22**, 394 (1996) [Low Temp. Phys. **22**, 306 (1996)].

[12] N. F. Kharchenko, Yu. N. Kharchenko, R. Szymczak, and M. Baran, Fiz. Nizk. Temp. **24**, 915 (1998) [Low Temp. Phys. **24**, 689 (1998)].

[13] V. N. Kut'ko, Yu. N. Kharchenko, N. M. Nesterenko, and A. A. Gurskaas, Fiz. Nizk. Temp. **22**, 785 (1996) [Low Temp. Phys. **22**, 603 (1996)].

[14] V. Heine and D. C. McConnel, J. Phys. C: Solid State Phys. **17**, 1199 (1984).

Translated by Steve Torstveit

LATTICE DYNAMICS

Thermal expansion of single-crystal fullerite C$_{60}$ at liquid-helium temperatures

A. N. Aleksandrovskii, V. B. Esel'son, V. G. Manzhelii, and B. G. Udovidchenko

B. I. Verkin Institute for Low Temperature Physics and Engineering, National Academy of Sciences of Ukraine, 47 Lenin Ave., 310164, Kharkov, Ukraine*

A. Soldatov

Umea University, Department of Experimental Physics, 90187 Umea, Sweden Forschungszentrum Karlsruhe, INFP, Postfach 3640, 76021 Karlsruhe, Germany**

B. Sundqvist

Umea University, Department of Experimental Physics, 90187 Umea, Sweden***

The thermal expansion of single-crystal fullerite C$_{60}$ has been studied in the range of liquid-helium temperatures (2–10 K). At temperatures below $\sim$4.5 K the thermal expansion of fullerite C$_{60}$ becomes negative, in agreement with the previous results on polycrystalline materials. A qualitative explanation of the results is proposed.   © *2000 American Institute of Physics.* [S1063-777X(00)01201-9]

1. INTRODUCTION

One of the characteristic features of fullerite C$_{60}$ is the essential influence of the orientational states of its molecules on the physical properties of the crystal. A molecule of fullerite C$_{60}$ is shaped as a truncated icosahedron, whose surface forms 20 hexagons and 12 pentagons. The noncentral interaction between the globular molecules of C$_{60}$ is much weaker than the central interaction and fullerene molecules show reorientational motion at temperatures at which the interaction between the globular molecules of C$_{60}$ is weaker than the thermal energy. At condensation, fullerite C$_{60}$ forms a face-centered-cubic (fcc) lattice with space group $Fm3m$ through the action of the central van der Waals interaction. As shown by experimental studies (see, for example, Ref. 1), the rotation of molecules in this phase is slightly hindered. Upon decreasing the temperature, a structure-orientational phase transition into a less symmetrical, simple cubic (sc), low-temperature phase of $Pa3$ symmetry takes place at $T \approx 260$ K. This transition is accompanied by partial orientational ordering of the rotation axes of the C$_{60}$ molecules. Calculations of the intermolecular interaction in C$_{60}$ crystals with a Lennard–Jones type potential show that this phase should be orthorhombic.[2,3] Lu *et al.*[4] obtained a simple cubic structure corresponding to the real low-temperature phase of solid C$_{60}$ by adding a Coulomb term to the Lennard–Jones potential. This additional Coulomb interaction between the neighboring molecules arises because of the effective charges at the single and double bonds of molecules in the ordered phase at low temperatures. When passing from the fcc phase to a sc phase, the almost free rotation of molecules changes into rotation around a space diagonal $\langle 111 \rangle$. As the temperature decreases further in the $Pa3$ phase, the rota-

tional motion of the molecules around the $\langle 111 \rangle$ axes slows down. The lowest interaction energy of two neighboring molecules of C$_{60}$ is found for the orientational state when double bonds on the molecules are facing the centers of pentagons on a neighboring molecule (the ''pentagon'' configuration). A less-deep energy minimum occurs when the double bonds approach the centers of hexagons on a neighboring molecule (the ''hexagon'' configuration). The difference in the depths of the potential wells for these configurations is $\Delta \approx 10$ meV per intermolecular bond, and the energy barrier separating them is $U \approx 0.3$ eV (Ref. 5). Changes in the orientational states in fullerites have a cooperative character. At the temperature $T \approx 90$ K the rotation of molecules around the $\langle 111 \rangle$ axes is hindered almost entirely, and a complete orientational ordering is never reached. An orientational glass is formed in this manner. The glass is characterized by a fixed ratio of pentagon (83.3%) and hexagon (16.7%) orientations of C$_{60}$ molecules. This ratio of the number of molecules in each orientational state is fixed down to liquid-helium temperatures.[6] The local energy states of neighboring molecules are the base of a phenomenological model of two-hole orientational states which are widely used to describe a sc-phase of C$_{60}$ fullerite.

Models of orientational glasses formed by highly symmetric molecules with weak noncentral interaction are comparatively simple. It is easier to consider theoretically such glasses than other types of glasses and to interpret the experimental results.[7] This circumstance raises the hope that an adequate model for C$_{60}$ fullerite in the state of orientational glass can be constructed. Despite a considerable body of evidence about the physical properties of fullerites, data on their thermal expansion at low temperatures are scanty. At the

same time, it is only at low temperatures the peculiarities characteristic of orientational glasses can be expected to appear in the behavior of the thermal expansion of C_{60} fullerite.

In the present work we continue the low-temperature thermal expansion studies of C_{60}, in which we recently found[8] that at temperatures below ~3.4 K the thermal expansion of a compressed C_{60} powdered sample becomes negative and unusually large in magnitude. In order to rule out a possibility that the effects observed by us are due to the polycrystalline structure of the material, such as grain boundaries or surface impurities brought into the sample by compression, we have now repeated the thermal-expansion studies in the same temperature range on a very large single crystal of C_{60} fullerite of high purity (see below). Special attention was given to the purity of both the polycrystalline[8] and single-crystal samples, because low-temperature measurements (1.4–20 K) of the heat capacity of C_{60} (Ref. 9) showed a contribution linear in temperature that should be characteristic of a glass. It turned out,[10] however, that the magnitude of the linear contribution was connected with the presence of impurities in the test samples since it was much smaller in pure are samples.

2. EXPERIMENTAL ASPECTS

The low-temperature thermal expansion of C_{60} fullerite should be isotropic because it has a cubic lattice. Thus, in principle, both single-crystal and polycrystalline C_{60} can be used in thermal-expansion studies.

We previously[8] studied polycrystalline samples prepared from sublimated C_{60} powder with a nominal purity no worse than 99.98%, which was obtained from Term USA, Berkeley, CA, USA. X-ray powder diffraction of the material at room temperature showed sharp peaks of the fcc structure with a lattice constant $a = 14.13$ Å. In an atmosphere of dry argon the C_{60} powder was loaded in a small piston-cylinder device used for the sample preparation. After subsequent compacting of the powder at about 1 GPa, the sample was immediately transferred into a glass tube and dried under dynamic vacuum 10^{-6} for about 16 h. The glass tube was sealed thereafter. The compacting procedure was done in air and did not exceed 15 min. The resulting sample had the shape of a pellet 6 mm in diameter and about 6 mm in height. The sample was then taken out of the mold and inserted into a glass tube, which was evacuated to about 10^{-6} Torr and sealed off. It was stored in darkness under these conditions for three months before the beginning of the measurements. However, after this time it was found that the sample had broken down into several pieces. Only one of them, 6 mm in diameter and about 2.4 mm in height, was suitable for thermal-expansion studies and we made measurements only on this piece.[8]

The self-destruction of the sample indicates the presence of large, inhomogeneous, internal stresses which could affect the results of the dilatometric studies. Another possibility is that the results are affected by air molecules adsorbed on grain surfaces during the compression and locked after the compression into the samples, where they might either collect at the grain boundaries or diffuse into the crystal lattice.
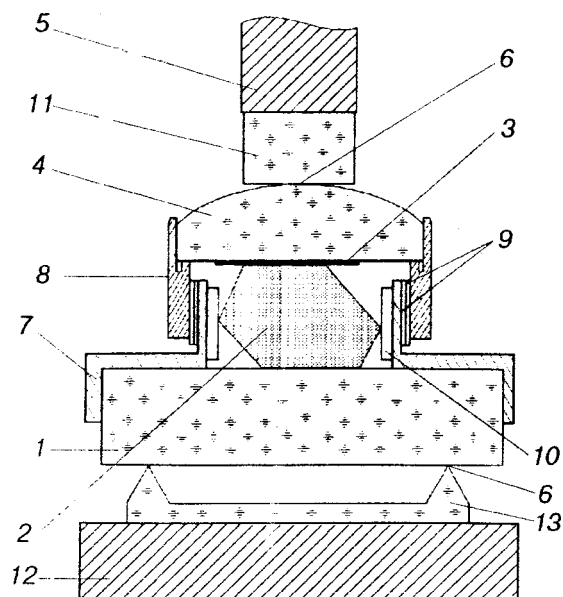

FIG. 1. Schematic drawing of the measuring cell of the dilatometer.

To exclude the possibility that the results are influenced by the factors discussed above we thought it necessary to carry out additional measurements of the thermal expansion on a single crystal which was not subjected to compression and mechanical treatment. We therefore obtained a very large C_{60} single crystal ($\sim 6.5 \times 4.3 \times 3.1$ mm) from Dr. M. Haluska, Vienna. This crystal was grown by the sublimation method in a cell under vacuum from Hoechst Super Gold Grade C_{60}. The crystal was not exposed to air or oxygen after growing was completed, but was transferred from its growth tube in argon atmosphere into a glass cell, which was then evacuated before sealing. Before putting the single-crystal sample into a measuring cell of the dilatometer, the glass cell with the sample was opened in the argon atmosphere under small extra pressure (about 200 Torr). The time required to put the sample into the measuring cell of the dilatometer was no more than 20 min. During this process the sample was blown over by a dry argon flow, and the cell was immediately evacuated after the mounting was completed. In the process of measuring thermal expansion the vacuum in the measuring cell with the sample was held at a pressure of 10^{-6} Torr.

The procedure for mounting the sample in the dilatometer and the measurement procedure were similar to those described earlier for the polycrystal.[8] The linear thermal expansion was measured using a capacitive dilatometer[11] with a resolution 2×10^{-9} cm, which was specially modified for measuring fullerite samples. The dilatometer was constructed in such a way that all elements capable of affecting the measured results for the linear thermal expansion of the sample because of their own thermal expansion were in a liquid-helium bath at a constant temperature. Thus, they could not affect the measuring results. The sample temperature was measured by a reference germanium resistance thermometer and good thermal insulation was provided by holding the sample in a vacuum. The measuring cell of the dilatometer is shown schematically in Fig. 1. A thermometric block (not

shown in Fig. 1), consisting of a measuring thermometer, a thermometer for regulating the temperature, and a sample heater, was mounted on the object table (*1*) of the dilatometer and established a reliable heat contact with this table. The fullerite test sample (*2*) was placed on the same table. The temperature drop along the sample was measured by a differential thermocouple (gold with iron-copper alloy). This thermocouple measured the temperature difference between the object table (*1*) of the dilatometer and a strip of thin aluminum foil (*3*), 0.02 mm in thickness and 7 mm wide, placed between the upper part of the sample and the sapphire hemisphere (*4*). The copper rod (*15*), the copper base (*12*), and sapphire support (*13*) are at the helium bath temperature. Thermal decoupling of the object table of the dilatometer from the structural elements of the device and from the rod (*5*) of the capacitive displacement gauge [the lower end of copper rod (*5*) ends in a sapphire tip (*11*)] is made by sapphire-sapphire point contacts (*6*). Because of the hardness and thermal conductivity of the single-crystal sapphire, such contacts showed good performance in dilatometers,[12,13] providing the necessary construction hardness and a large point thermal resistance. According to the data of Ref. 12, the thermal expansion of single-crystal sapphire along a direction inclined by 60° with respect to its hexagonal axis is $\alpha = 1.2T^{2.2} \times 10^{-11} \, \mathrm{K}^{-1}$ in the temperature range of interest here. For the direction along the axis the magnitude is probably still less, since at room temperature the linear thermal expansion of sapphire along the hexagonal axis is an order of magnitude lower than the linear thermal expansion in the base plane.[14] Therefore, to reduce thermal expansion of the sapphire to a minimum, cuts were made from artificial single-crystal sapphire, so that the direction along which the thermal expansion measurements were made would coincide with the direction of the hexagonal axis of the single crystals. Additional studies were made to determine the true contribution of the sapphire elements and of the aluminum foil to our thermal expansion studies of fullerite C_{60}. From the data obtained we find that this contribution is less than the resolution of our setup in the whole temperature range studied (see below). Sample temperatures below 4.2 K were reached by the Wheatley camera,[15] which has a thermal contact with the sample. The dilatometer element sensitive to small displacements (the capacitive displacement gauge) is a two-terminal capacitance gauge connected into an oscillator circuit based on a tunnel diode. The block consisting of the displacement gauge and the oscillator was also placed in a liquid-helium bath at a constant temperature.

The single crystal studied by us was probably unique in size and had a complex geometric shape. All the faces of the sample had essentially different areas and axes drawn through the geometric centers of parallel faces and were not perpendicular to these planes. Therefore, none of the pairs of plane-parallel faces provided a stable position of the hemisphere (*4*) on the sample (*2*). There was a danger that the sample (*2*) and the hemisphere (*4*) would slip with respect to one another in the process of measuring the thermal expansion. To overcome this difficulty, an adjustable fixture, which kept the positions of the sample (*2*) and of the sapphire hemisphere (*4*) fixed with respect to the table (*1*), was

designed. The adjustable fixture consists of a stationary adjustable ring (*7*) and a moving ring (*8*), onto which the sapphire hemisphere (*4*) supported on the sample (*2*) was firmly mounted. The parts (*7*) and (*8*) were made of copper. Good adjustment during the measurements and good sliding of the moving ring (*8*) with respect to the stationary ring (*7*) are reached because a gap of ~0.1 mm between adjacent cylindrical surfaces of the rings is filled by two ring Teflon gaskets (*9*). One of the gaskets fits on the external cylindrical surface of ring (*7*), the other fits on the inner surface of ring filled by two ring Teflon gaskets (*9*). One of the gaskets fits on the external cylindrical surface of ring (*7*), the other fits on the inner surface of ring (*8*). The thickness of each gasket is 0.05 mm. A gap between these gaskets provides a slight sliding of the Teflon-Teflon surfaces and a good alignment when ring (*8*) moves. The construction which is described here excludes seizing at the displacements of ring (*8*) at liquid-helium temperatures and provides the needed coaxiality of the object table (*1*), the sapphire hemisphere (*4*), and the rod (*5*) of the capacitive displacement gauge. The single crystal studied by us had a complex form. The largest dimension was 6.5 mm and the smallest was 3.1 mm. The sample in the stationary adjusting ring (*7*) was aligned by a split Teflon ring (*10*) also by decreasing the friction of the sample against the walls of ring (*7*) upon lowering or raising the temperature. Since there was a danger of destroying the sample when it was tightened with a rod (*5*) of the capacitive displacement gauge, we measured the thermal expansion perpendicular to two parallel sample planes with maximum areas despite the fact that their geometric centers were displaced with respect to each other. The distance between these planes was 3.1 mm and this was therefore the initial length of the sample; the change in the length was determined in the experiment. We note in this connection that after completing the experiment we did not find signs of destruction of the sample. The change in the sample length was determined when the temperature was raised or lowered. Changes in temperature and sample length were recorded once a minute and processed by a computer in real time. The sample temperature was determined to be $T_s = T_r + 0.5T_t$, where T_s is the temperature of the sample, T_r is the temperature of the object table as determined by a germanium resistance thermometer, and T_t is the temperature difference between the temperature of the object table and that of the upper part of the sample. T_t was determined by a differential thermocouple, as discussed above. Typical values of T_t were on the order of 0.1 K. The thermal expansion of C_{60} fullerite was measured by a step change technique as follows. First, the sample was held at a constant temperature T_1, where its temperature and the output of the capacitive displacement gauge of the dilatometer were read. The temperature of the object table with the sample was then changed to a temperature T_2, which was held constant. When the temperature drift of the sample did not exceed 0.01 K for 10 min, we determined the change in its length due to the change in temperature from T_1 to T_2. During the measurements the steps from T_1 to T_2 were 0.1–0.3 K, depending on the temperature range.
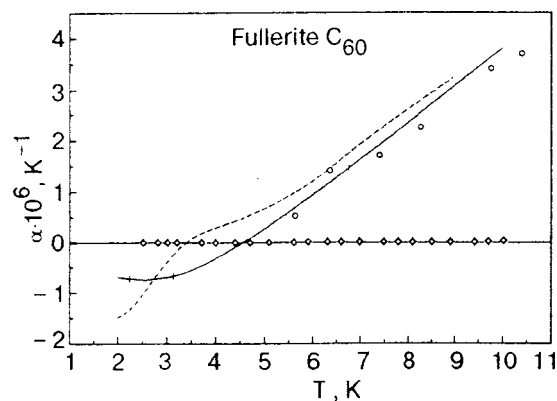
FIG. 2. Linear thermal expansion coefficients of fullerite C_{60}: polycrystal ($\cdots$): single crystal, this work (———); single crystal, private communication of the authors of Ref. 16 ($\bigcirc$); the results of the check experiment ($\diamond$).

FIG. 3. Schematic drawing of the measuring cell of the dilatometer for experiment to check the results.

3. EXPERIMENTAL RESULTS

The thermal expansion of single-crystal fullerite was determined in the temperature range 2–10 K. As reported elsewhere,[8] we previously made eight series of thermal-expansion measurements on a polycrystalline sample of C_{60} in the temperature range below 4.2 K, when the temperature was raised and when it was lowered, plus three similar series in the temperature range above 4.2 K. We have now added nine similar series of measurements on the C_{60} single crystal, five of them in the temperature range below 4.2 K. The linear thermal expansion coefficient α was obtained by differentiation with respect to T of the temperature dependence of the relative elongation $\Delta L/L$ of the samples. Figure 2 shows the temperature dependence $\alpha(T)$ of single-crystal fullerite (solid line). This figure also shows the mean-square errors in determining α. The results of our measurements on polycrystalline C_{60} (Ref. 8) are given by the dashed line. We compare the values obtained for the thermal expansion with the data of Gugenberger *et al.*,[16] who measured the thermal expansion of single-crystal fullerite in the temperature range 5–300 K (circles). From this figure it is clear that the results of our studies agree satisfactorily with the previous data on single crystals in the temperature range where they overlap. It is also clear that the polycrystal and the single crystal give very similar results. The most interesting result of our study is the negative thermal expansion obtained for both polycrystalline[8] and single-crystal fullerite C_{60} at temperatures below 3.4 K for the polycrystal and below 4.5 K for the single-crystal sample.

Since we consider the results of our studies of thermal expansion of fullerite far from being trivial, we have made the following additional experiment to check the results. We again mounted the measuring cell of the dilatometer in the way shown in Fig. 3. The notation in this figure is the same as in Fig. 1. From Fig. 3 it is clear that the sapphire hemisphere (4), which has a height of 3 mm, and the aluminum foil (3), upon which a thermocouple is placed, play the role of the samples. The thermal expansion measured in such a case is the sum of all spurious contributions from the components of the setup to the thermal expansion of fullerite. From this experiment it is clear that any extra contribution to
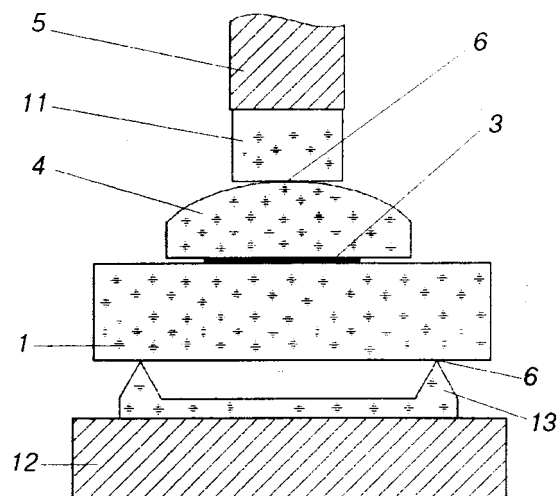
the thermal expansion does not exceed 2.5×10^{-8} K^{-1} in the whole temperature range studied by us. The measuring technique was the same as in the case of measuring the thermal expansion of fullerite. The only difference was a temperature step ΔT, which was 0.1–0.3 K when studying fullerite, and in the experimental check it was about 1 K. The results of this experimental check are shown in Fig. 2 by the rhombi. The figure shows that the magnitude of any spurious contribution to the measured value is negligible compared to the measured thermal expansion of fullerite. This experimental check testifies to the reliability of the values of the thermal expansion coefficients of fullerite which we measured.

4. DISCUSSION

A possible mechanism for the negative thermal expansion of fullerite C_{60} might be rotational tunnelling between energy-equivalent orientational states of molecules. Sheard[17] was first to suggest that rotational tunnelling of molecules can lead to a negative thermal expansion. This problem was considered in detail by Freiman,[18] as applied to the thermal expansion of solid methane. Because of rotational tunnelling, the energy level of a rotational ground state (whose degeneration is equal to the number of molecular orientations with identical energies) splits into several sublevels, whose number is determined by the lattice symmetry. At sufficiently low temperatures the contribution from excitations of intramolecular vibrations, phonons, and librons to the free energy of a crystal can be disregarded. In this case the free energy can be represented as a sum of the potential energy, the zero vibration energy, and a contribution F_t arising from the tunnel states. The contribution F_t can be written as

$$F_t = NkT \ln \sum_i a_i e^{-\Delta_i/kT}, \tag{1}$$

where the summation is made over the tunnel states i, a_i is the degeneration of the ith state, and Δ_i is the excess energy of this state above the energy of the ground state. The quan-

tity Δ_i depends exponentially on the height of the barrier U which separates the energy-equivalent orientations,

$$\Delta_i \sim e^{-bU(V)}, \qquad (2)$$

where b is a constant. A decrease in the volume V of the crystal leads to an increase in U and a decrease of the values Δ_i. Based on the dependence of U on V and on Eqs. (1) and (2) it can be shown, in general, that the thermal expansion contributed by the tunnel states is negative.[18]

This is particularly clear in the Grüneisen approximation $\alpha \sim \gamma C$, where α is the thermal expansion coefficient, C is the heat capacity, and γ is the thermal Grüneisen coefficient $\gamma_i = -(d \ln \Delta_i)/(d \ln V)$, which for tunnel levels are negative. Since the heat capacity is always positive, negative values of γ_i immediately imply negative values for the thermal expansion coefficient. In principle, the negative thermal expansion should be observed for all solids consisting of particles with rotational degrees of freedom. In most cases, however, because high barriers prevent molecular rotation, the tunnel splitting Δ_i is very small and the thermal expansion becomes negative at very low temperatures, which are at present hard to reach in dilatometric experiments.

Note one further important peculiarity of tunnel states. The dependence of the splitting of tunnel levels Δ_i on the height of the barrier (2) and the strong dependence of U on volume testifies that Grüneisen coefficients for tunnel levels should be very large in magnitude. It should be noted here that Grüneisen coefficients for the phonon and libron spectra of molecular crystals usually are on the order of one. The Grüneisen parameter for the low-temperature simple cubic phase of C_{60} was analyzed by White *et al.*[19] in the temperature range 10–200 K. To calculate the value γ of single-crystal fullerite C_{60} at $T < 10$ K we used the thermal expansion coefficients obtained in our work, data on the heat capacity from Ref. 10, where a pure polycrystal sample C_{60} was studied in the range 1.5–20 K, and the values of molar volume are $V = 416.77 \, cm^3 \cdot mole$ and the bulk modulus $B = 14 \, GPa$. The present value for the molar volume was determined by recalculating the value $V = 416.93 \, cm^3 \cdot mole$ measured directly by the x-ray method on single-crystal C_{60} (Ref. 20) at $T = 30$ K to ~ 4.2 K. The recalculation was made using data on thermal expansion from Ref. 16. No compressibility measurements of C_{60} have, to the best of our knowledge, been carried out at liquid-helium temperatures. The value of the bulk modulus given above corresponds to an average of values measured at 60 and 70 K (Ref. 21), and we assume that the temperature dependence of the compressibility $\chi = B^{-1}$ can be ignored in the ''glassy'' (orientationally frozen) state below about 90 K. Figure 4 shows the temperature dependence of γ obtained here. If we recalculate the values of the Grüneisen coefficient for the case of bulk modulus $B = 10.3 \, GPa$ (Ref. 22), then our values of γ at 10 K will correspond to the values of γ given in Ref. 19. At temperatures below 4.5 K for single-crystal C_{60} and below 3.4 K for polycrystalline C_{60} the Grüneisen coefficients are negative and reach large values. The unusually large negative values of γ testify in favor of the assumption that the negative thermal expansion is of a tunneling nature.[30]
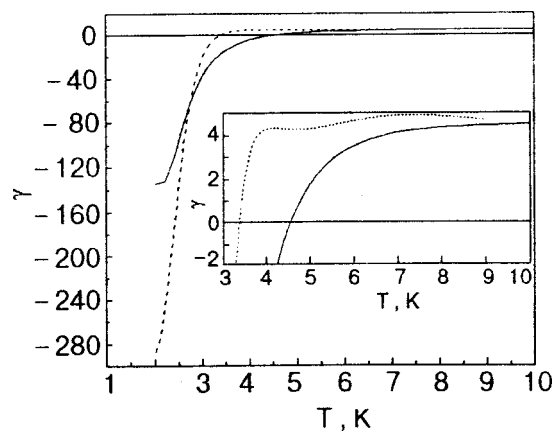

FIG. 4. Grüneisen parameter of fullerite C_{60}.

The negative contribution to the thermal expansion of C_{60} is very large and dominates at liquid-helium temperatures, but we cannot estimate its temperature dependence very accurately. It is impossible to extract a linear term in the temperature dependence of the thermal expansion coefficient, such as would be characteristic of a glass. However, according to Ref. 10, the contribution of the linear term to the heat capacity of sufficiently pure fullerite C_{60} is comparatively small.

The large moment of inertia of the C_{60} molecule and the rather large barrier heights preventing the molecule rotation in a lattice[5] are strong objections to the assumption of a tunneling nature of the negative thermal expansion coefficient of C_{60} fullerite. It should be noted, however, that in the vicinity of lattice defects the barriers can be reduced substantially. Such a lattice deformation of C_{60} fullerite can be caused by the frozen-in orientational disorder observed below 90 K, by impurities, and by the defects caused by compression of the powder or by the growth of the single crystal. Kveder *et al.*[23] studied photoluminescence and optical absorption spectra of rather large (2–3 mm), pure crystals of C_{60} fullerite. It turned out that the concentration of defects, which functioned as deep traps for exitons, was $10^3 – 10^{-4}$ of the number of C_{60} molecules. Since these crystals were prepared from a very pure material subjected to repeated resublimation in vacuum, the authors concluded that the effects discussed were natural defects of the crystal and were not connected with impurities. The authors did not rule out that these defects appeared as a result of plastic deformation of crystals during growth under the influence of their weight, since at the growth temperature (about 450–470°) the crystals were very plastic. The single crystal studied by us was some times larger than that in Ref. 23, and probably because of plastic deformation, the concentration of defects in our sample was therefore not smaller. The type of defects and their concentration are undoubtedly different for the single crystal and the polycrystalline samples studied by us. The dependence $\alpha(T)$ of these samples should therefore not be expected to be identical (Fig. 2).

Another possible explanation can be formulated in terms of librational motion of the molecules. At low temperatures, the majority of molecules are oriented in the pentagon orien-

tation in which each molecule nominally points a double C–C bond toward the center of a carbon atom pentagon on its neighbor. This configuration accounts for a rather large intermolecular distance, and the alternative hexagon orientation has a significantly smaller molecular volume, and hence smaller average intermolecular distance. For geometric reasons, librational motion of a molecule in the pentagon state might theoretically enable the molecules to come closer together. However, a strong argument against such a model is that librational modes have energies of 2–4 meV (Ref. 24) and should therefore freeze out at the low temperatures considered here.

Based on the present results we suggest that it would be useful to study also the thermal expansion of fullerite when different gases are introduced (intercalated) into the lattice, since the intermolecular interaction and the defect structure in this case undergo changes.[25–28] Note, in this connection, that in Ref. 29 argon which was introduced into the fullerite lattice was found to strongly influence the mechanical properties of fullerite. For example, the microhardness and Young's modulus of fullerite stored in argon atmosphere for 45 h at room temperature increased almost 100 fold.

*E-mail: aalex@ilt.kharkov.ua
**E-mail: alex.soldatov@infp.fzk.de
***E-mail: bertil.sundqvist@physics.umu.se

[1] J. D. Axe, S. C. Moss, and D. A. Neumann, in *Solid State Physics: Advances in Research and Applications*, edited by H. E. Ehrenreich and F. Spaepen, Academic Press, New York, Vol. 48, (1994), p. 149.
[2] Y. Guo, N. Karasawa, and W. A. Goddard III, Nature (London) **351**, 464 (1991).
[3] G. Ghosh, V. S. Sastry, and T. S. Radhakrishnan, Phys. Rev. B **57**, R13969 (1998).
[4] J. P. Lu, X.-P. Li, and R. M. Martin, Phys. Rev. Lett. **68**, 1551 (1992).
[5] V. D. Natsik and A. V. Podolskiy, Fiz. Nizk. Temp. **24**, 523 (1998) [Low Temp. Phys. **24**, 523 (1998)].
[6] W. I. F. David, R. M. Ibberson, T. J. S. Dennis, J. P. Hare, and K. Prassides, Europhys. Lett. **18**, 219 (1992); 735 (1992).
[7] V. G. Manzhelii, M. I. Bagatskii, I. Ya. Minchina, and A. N. Aleksandrovskii, J. Low Temp. Phys. **111**, 257 (1997).
[8] A. N. Aleksandrovskii, V. B. Esel'son, V. G. Manzhelii, B. G. Udovidchenko, A. V. Soldatov, and B. Sundqvist, Fiz. Nizk. Temp. **23**, 1256 (1997) [Low Temp. Phys. **23**, 943 (1997)].
[9] W. B. Beyermann, M. F. Hundley, J. D. Thompson, F. N. Diederich, and G. Grüner, Phys. Rev. Lett. **68**, 2046 (1992).
[10] W. P. Beyermann, J. D. Thompson, M. F. Hundley, and G. Grüner, Phys. Rev. Lett. **69**, 2737 (1992).
[11] A. M. Tolkachev, A. N. Aleksandrovskii, and V. I. Kuchnev, Cryogenics **15**, 547 (1975).
[12] R. H. Carr and C. A. Swenson, Cryogenics **4**, 76 (1964).
[13] K. O. McLean, C. A. Swenson, and C. R. Case, J. Low Temp. Phys. **7**, 77 (1972).
[14] Enziclopedic Dictionary of Physics [in Russian], Sovetskaja Enziklopedia. Moscow, Vol. 2 (1962).
[15] L. E. De Long, O. G. Symko, and J. C. Wheatley, Rev. Sci. Instrum. **42**, 147 (1971).
[16] F. Gugenberger, R. Heid, C. Meingast, P. Adelmann, M. Brawn, H. Wuhl, M. Haluska, and H. Kuzmany, Phys. Rev. Lett. **69**, 3774 (1992).
[17] F. W. Sheard, in *AIP Conference Proceedings, N3, Thermal Expansion-1971*, edited by M. G. Graham and H. E. Hagy, New York (1972), pp. 151–154.
[18] Yu. A. Freiman, Fiz. Nizk. Temp. **9**, 657 (1983) [Sov. J. Low Temp. Phys. **9**, 335 (1983)].
[19] M. A. White, C. Meingast, W. I. F. David, and T. Matsuo, Solid State Commun. **94**, 481 (1995).
[20] N. A. Aksenova, A. P. Isakina, A. I. Prokhvatilov, and M. A. Strzhemechny, Fiz. Nizk. Temp. **25**, 964 (1999) [Low Temp. Phys. **25**, 724 (1999)].
[21] B. Sundqvist, Physica B **265**, 208 (1999).
[22] B. Sundqvist, O. Andersson, A. Lundin, and A. Soldatov, Solid State Commun. **93**, 109 (1995).
[23] V. V. Kveder, V. D. Nedrii, E. E. Shteiman, A. N. Izoto, Yu. A. Osip'yan, and R. K. Nikolaev, Zh. Éksp. Teor. Fiz. **113**, 734 (1998) [JETP **87**, 412 (1999)].
[24] L. Pintschovius, S. L. Chaplot, R. Heid, B. Renker, M. Haluska, and H. Kuzmany, in *Electronic Properties of Fullerenes*), edited by H. Kuzmany, J. Fink, M. Mehring, and S. Roth, Springer-Verlag, Berlin (1993), p. 162.
[25] S. V. Lubenets, V. D. Natsik, L. S. Fomenko, A. P. Isakina, A. I. Prokhvatilov, M. A. Strzhemechny, N. A. Aksenova, and R. S. Ruoff, Fiz. Nizk. Temp. **23**, 338 (1997) [Low Temp. Phys. **23**, 251 (1997)].
[26] Yu. A. Ossipyan, V. S. Bobrov, Yu. S. Grushko, R. A. Dilanyan, M. A. Lebyodkin, and V. Sh. Sheckhtman, Appl. Phys. A: Solids Surf. **56**, 413 (1993).
[27] V. S. Bobrov, R. A. Dilanyan, L. S. Fomenko, M. A. Lebyodkin, S. V. Lubenets, and V. I. Orlov, in Solid State Phenom. **35**, **36**; J. Rabier, A. George, Y. Brechet, and L. Kubin (eds.) (1994), p. 519.
[28] V. S. Bobrov, R. A. Dilanyan, L. S. Fomenko, Yu. L. Iunin, M. A. Lebyodkin, S. V. Lubenets, V. I. Orlov, and Yu. A. Ossipyan, J. Supercond. **8**, 1 (1995).
[29] M. Haluska, M. Zehetbauer, M. Hulman, and H. Kuzmany, in *Materials Science Forum. 210–213, Part I. Nondestructive Characterization of Materials II*, A. L. Bartos, R. E. Green, Jr., and C. O. Ruud (eds.), Transtec. Publ., Switzerland (1996), p. 267.
[30] J. N. Dobbs, M. C. Foote, and A. C. Anderson, Phys. Rev. B **33**, 4178 (1986).

Phase transitions in antiferromagnetic cobalt fluoride

G. K. Cherpurnykh, O. G. Medvedovskaya, and O. A. Nikitina

Institute of Applied Physics, National Academy of Sciences of Ukraine, ul. Petropavlovskaya 58, 244030 Sumy, Ukraine*

The phase transitions in cobalt fluoride (at $T \ll T_N = 38$ K) in a longitudinal magnetic field are investigated theoretically, and it is shown that the field-induced transition of the magnetic subsystem from an antiferromagnetic phase can occur only to a canted phase and that it is a first-order transition. The character of this transition is due to the ''sign'' of the Dzyaloshinskiĭ interaction, and this affords an opportunity to determine experimentally the ''sign'' of the Dzyaloshinskiĭ interaction. The field of the transition to the spin-flop phase (when the total magnetic moment becomes parallel to the easy axis) coincides with the field of the transition to the spin-flip phase (when the antiferromagnetism vector becomes equal to zero). © *2000 American Institute of Physics.* [S1063-777X(00)01301-3]

The antiferromagnet (AFM) CoF_2 ($T_N = 38$ K) has been the subject of many studies for a few decades now (see, e.g., Ref. 1–8). It was noted in these works that one of the things that complicates the theoretical investigations of CoF_2 and thus makes it difficult to explain the experimental data is the absence of a small parameter on account of the large magnetic anisotropy of the crystal. The ratio of the anisotropy field H_a to the exchange field H_e does not satisfy the usual condition $H_a/H_e \ll 1$. In addition, a common problem[9,10] for AFMs with the Dzyaloshinskiĭ interaction (DI) is the experimental determination of the ''sign'' of the DI, which is of fundamental importance from the standpoint of the microscopic theory of the DI. According to Ref. 9, an answer to this question can be given by determining experimentally the direction of rotation of the antiferromagnetism vector **l** around the magnetic field **H** in the geometry $\mathbf{H} \perp EA \| \mathbf{d}$, where EA is the easy axis and **d** is a constant vector whose components characterize the value of the DI. However, as was pointed out in Ref. 10, a Mössbauer experiment[9] on easy-axis hematite did not give an unambiguous result (see also Ref. 11). It is therefore of interest to look for other experimental possibilities for answering this question.

Here it must be taken into consideration that, owing to the DI the rotation of the vector **l** around the ferromagnetic vector **m** occurs not only for $\mathbf{H} \perp EA$; it is sufficient that the component $\mathbf{H}_\perp \neq 0$ (see the phase diagram in Fig. 5 of Ref. 10). The condition $\mathbf{H}_\perp \neq 0$ plays a dual role: it brings about the rotation of the antiferromagnetic vector **l** and creates anisotropy in the basal plane, which tends to fix the ferromagnetic vector and, hence, to fix the plane of rotation of the antiferromagnetic vector **l**.

However, in tetragonal AFMs, a class which includes CoF_2, the DI itself creates anisotropy in the basal plane. For this reason (as we shall show below) a rotation of the vector **l** in a certain plane occurs in CoF_2 even in the case $\mathbf{H} \| EA$.

Therefore, the proposed study would undertake to study phase transitions in the AFM CoF_2 in a longitudinal magnetic field, in which case the fact that the condition H_a/E_e

$\ll 1$ does not hold has no bearing on the correctness of the conclusions; here one would make use of the basal plane anisotropy created by the DI. We use the thermodynamic potential E and the set of variables determining the configuration of the magnetic subsystem from Ref. 6. Therefore

$$E = (2M_0)[(1/2)E\mathbf{m}^2 + (1/2)G(\mathbf{m} \cdot \mathbf{1})^2 - D(m_x l_y + l_x m_y)$$
$$+ F(\mathbf{m} \cdot \mathbf{1})l_x l_y - \mathbf{m} \cdot H + (1/2)A_1(l_x^2 + l_y^2)$$
$$- (1/4)A_2(l_x^2 + l_y^2)^2], \qquad (1)$$

where $\mathbf{l} = (\mathbf{M}_1 - \mathbf{M}_2)/2M_0$; $\mathbf{m} = (\mathbf{M}_1 + \mathbf{M}_2)/2M_0$, $EA \| 0Z$.

The condition $\mathbf{m} \cdot \mathbf{l} = 0$ does not hold. We note that in expression (1) a minus sign as been chosen in front of the Dzyaloshinskiĭ constant D. A minus sign has also been chosen in front of the constant A_2, and in this case $A_2 > 0$.

Using the necessary conditions for the existence of a minimum of (1) as a function of the variables θ, φ, and **m** (see Fig. 1), we obtain the system of equations

$$\partial E/\partial \theta = 0, \quad \partial E/\partial \varphi = 0, \quad \partial E/\partial m = 0. \qquad (2)$$

Sufficient conditions for the existence of a minimum of (1) reduce to the condition that all the principal minors of the matrix $\hat{A} = (a_{ik})$, where

$$a_{ik} = \frac{\partial^2 E}{\partial x_i \partial x_k}$$

$$(x_1 = \theta, \quad x_2 = \varphi, \quad x_3 = m_x, \quad x_4 = m_y, \quad x_5 = m_z)$$

must be strictly positive. Equations (2), like Eqs. (8) and (10) in Ref. 6, admit the solutions

$$\cos \theta = 0, \quad \sin 2\varphi = 0. \qquad (3)$$

However solution (3) does not satisfy the sufficient conditions given above. Therefore, we are left with the case $\cos 2\varphi = 0$. This means that under the influence of a field $\mathbf{H} \| EA$ the rotation of the vector **l** occurs in a plane passing through the easy axis and the [110] direction.
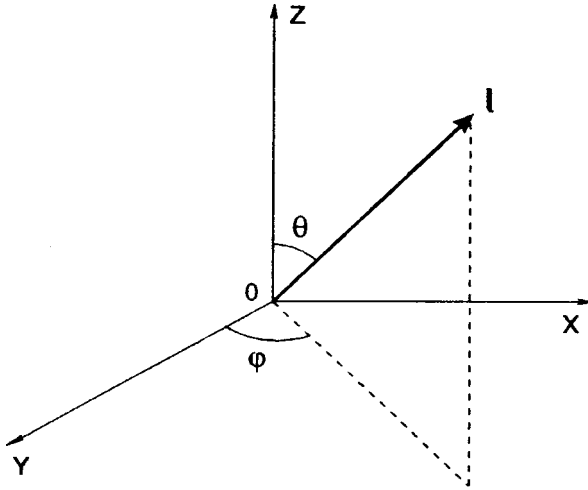
FIG. 1. Orientation of the antiferromagnetism vector **l** for **H**‖0Z‖EA. θ and φ are the polar and azimuthal angles of the vector **l**.

Using the sufficient conditions for the existence of a minimum of (1), we find that the greatest value of the magnetic field H_c at which the state

$$\sin\theta=0, \quad \cos 2\varphi=0 \tag{4}$$

is realized is determined by the condition

$$H_c=\sqrt{(E/G)(A_1E+A_1Gl^2-D^2+DFl^2+F^2El^2/4G)}$$
$$+Dl+FEl^2/2G. \tag{5}$$

Using the formula[6] for the field H_{tr} of the equilibrium transition between the phases $\theta=0$ and $\theta\neq0$ and taking into account that the angle $\theta\ll1$ in the neighborhood of a tricritical point, we obtain an expression for the difference

$$H_c-H_{tr}=\frac{1}{4}\left[\frac{\sqrt{E/G}(E+Gl^2)l^2(F^2/2G+A_2)}{\sqrt{A_1E+A_1Gl^2-D^2+DFl^2+F^2El^2/4G}}\right.$$
$$\left.+2Dl^2+\frac{FEl}{G}\right]\theta^2. \tag{6}$$

In writing formulas (5) and (6) we have used the notation (8) taken from Ref. 6, i.e.,

$$d=Dl, \quad f=Fl^3, \quad a_1=A_1l^2, \quad a_2=A_2l^4.$$

the first-order phase transition occurs if $H_c-H_{tr}>0$, and the second-order transition occurs if $H_c-H_{tr}\leqslant0$. The sign of the difference H_c-H_{tr} is determined by the sign of the expression in the square brackets in front of θ^2. Therefore it should be kept in mind that the potential (1) is written in such a way that all the constants in it have positive values. In addition, since the critical field H_c can only be real, the expression in front of the square root in (5) and, hence, in (6) can only be positive. It follows that $H_c-H_{tr}>0$ and, so the transition between the antiferromagnetic and the canted phases is a first-order transition. Here, however, it is necessary to keep the following circumstance in mind. In Fig. 1 the direction $[\bar{1}10]$ is the axis of rotation of the vector **l**, and in deriving formula (6) we took into account that, if one looks counter to the $[\bar{1}10]$ direction, the vector **l** is rotated clockwise from the

Z axis (angle $\varphi=\frac{1}{4}\pi$). If the vector **l** is rotated counterclockwise (angle $\varphi=1\frac{3}{4}\pi$), then a minus sign appears in front of the term $2Dl^2$ in formula (6) (and also in front of the DFl^2 term in the expression under the radical). In that case, for determining the sign of the difference H_c-H_{tr} it is necessary to use the numerical values of the constants of the potential (1) (we note that since $(A_2/A_1)^2\ll1$ and the product A_2E is substantially smaller than D^2, one expects that the condition $H_c-H_{tr}<0$ will be satisfied). Even though the sets of numerical values of the constants of the thermodynamic potential (1), determined from experiment by different authors, are different (the reason for this is the lack of a consistent theory), these data nevertheless permit one to assume that in this case the difference $H_c=H_{tr}<0$ and, hence, that the transition between the phases $\theta=0$ and $\theta\neq0$ will be a second-order transition. Thus we see that by determining experimentally the character of the transition between the antiferromagnetic and canted phases (in spite of the insignificance of the jump in magnetization at the first-order transition), one can thereby determine the ''sign'' of the DI.

To determine the subsequent behavior of the magnetic subsystem as the magnetic field increases, we use the equation for the angle θ at $\varphi=\pi/4$:

$$\sin\theta\left\{\cos\theta\left[-\frac{H^2G}{E(E+Gl^2)}+\frac{2HGl}{E(E+Gl^2)}\left(D+\frac{FE}{2G}\right)\right.\right.$$
$$\times\cos\theta-A_2l^2\sin^2\theta+A_1-\frac{D^2}{E}+\frac{1}{2E}$$
$$\times\left(\frac{G}{E+Gl^2}(Fl^3-2Dl)^2-Fl^2(Fl^2-4D)\right)\sin^2\theta\right]$$
$$\left.-\frac{HGl}{E(E+Gl^2)}\left(D+\frac{FE}{2G}\right)\sin^2\theta\right\}=0. \tag{7}$$

It follows from Eq. (7) that the state $\theta=\pi/2$ is realized for $l=0$, i.e., the field of the spin-flop and spin-flip transitions coincide. This conclusion agrees with the experimental data of Ref. 6, in which it was shown that the frequency dependence of the antiferromagnetic resonance is independent of field between the threshold field H_c and the field of the spin-flip transition. The strong growth of the magnetization observed above the threshold field H_c in Ref. 6 can be explained by the dependence of the angle θ on the field, which we have previously calculated[12] on a computer. According to the calculations, in fields $H>H_c$ there occurs a sharp increase in the angle θ with increasing magnetic field, and at $H\cong(5/4)H_c$ the angle θ already satisfies the condition $\pi/2-\theta\ll1$. For this reason, as the field is increased further one observes a linear dependence of the magnetization on the field.[6]

*E-mail: iapuas@gluk.apc.org

[1] V. G. Shapiro, V. I. Ozhogin, and K. G. Gurtovoĭ, Phys. Part. Nuclei **36**, 1559 (1972).

[2] O. N. Gufan, E. N. Kocharyan, A. S. Prokhorov, and E. G. Rudashevskiĭ, Zh. Èksp. Teor. Fiz. **66**, 1155 (1974) [Sov. Phys. JETP **39**, 555 (1974)].

[3] M. E. Lines, Phys. Rev. **137**, A982 (1965).

[4] V. N. Loktev and V. S. Ostrovskiĭ, Fiz. Tverd. Tela (Leningrad) **20**, 3257 (1978) [Sov. Phys. Solid State **20**, 1878 (1978)].

[5] N. F. Kharchenko, V. V. Eremenko, and A. I. Belyĭ, Zh. Èksp. Teor. Fiz. **82**, 827 (1972) [*sic*].

[6] K. G. Gurtovoĭ, A. S. Lagutin, and V. I. Ozhogin, Zh. Èksp. Teor. Fiz. **83**, 1941 (1982) [Sov. Phys. JETP **56**, 1122 (1982)].

[7] P. L. Richards, J. Appl. Phys. **35**, 850 (1964).

[8] P. Martel, R. A. Cowley, and R. W. H. Stevenson, Can. J. Phys. **46**, 1344 (1968).

[9] V. I. Ozhogin, S. S. Yakimov, R. A. Voskanyan, and V. Ya. Galitskiĭ, JETP Lett. **8**, 157 (1968).

[10] V. I. Ozhogin, Author's Abstract of Doctoral Dissertation [in Russian], Moscow (1974).

[11] R. Z. Levitin and V. A. Shchurov, in *Physics and Chemistry of Ferrites* [in Russian], Izd. MGU, Moscow (1973), p. 162.

[12] G. K. Chepurnykh, O. G. Medvedovskaya, and O. A. Nikitina, Fiz. Tverd. Tela (St. Petersburg) **38**, 1641 (1996) [Phys. Solid State **38**, 907 (1996)].

Translated by Steve Torstveit